Synthesis, Photophysics and Photocatalysis of [FeFe] Complex Containing Dyads and Bimolecular Systems

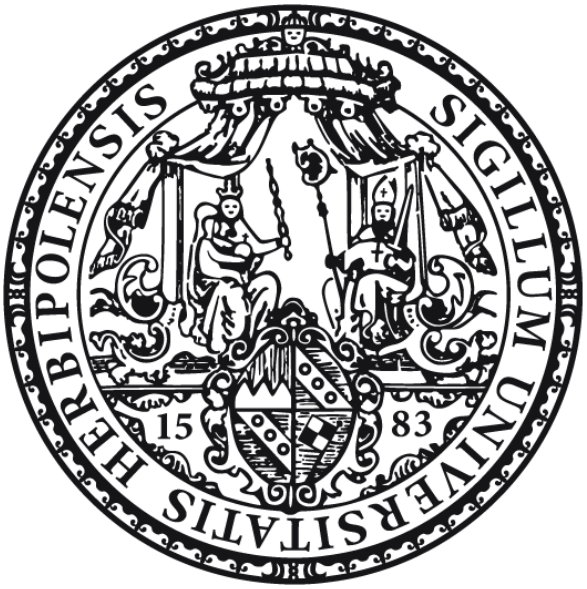

Dissertation zur Erlangung
des naturwissenschaftlichen Doktorgrades der
Julius-Maximilians-Universität Würzburg

vorgelegt von

Markus Roos
aus Marktheidenfeld

Würzburg 2021

Eingereicht bei der Fakultät für Chemie und Pharmazie am

25.01.2021

Gutachter der schriftlichen Arbeit

1. Gutachter: Prof. Dr. Christoph Lambert

2. Gutachter: Prof. Dr. Matthias Lehmann

Prüfer des öffentlichen Promotionskolloquiums

1. Prüfer: Prof. Dr. Christoph Lambert

2. Prüfer: Prof. Dr. Matthias Lehmann

3. Prüfer: Prof. Dr. Udo Radius

Datum des öffentlichen Promotionskolloquiums

24.03.2021

Doktorurkunde ausgehändigt am

Die vorliegende Arbeit wurde in der Zeit von Februar 2015 bis Dezember 2020 am Institut für Organische Chemie der Universität Würzburg angefertigt.

Mein besonderer Dank gilt

Herrn Prof. Dr. Christoph Lambert

dafür, dass ich dieses abwechslungsreiche, vielseitige und anwendungsnahe Thema bearbeiten durfte, sowie für die mit vielen Anregungen und Diskussionen verbundene Betreuung dieser Arbeit.

COPYRIGHT

Parts of this thesis have already been covered by the following bachelor theses (supervised by Markus Roos and Prof. Dr. Christoph Lambert):

1. *Synthese und Charakterisierung von [FeFe]-Hydrogenase-Imitatoren mit unterschiedlichen Phosphinliganden*, D. Polzin, Bachelor thesis, Julius-Maximilians-Universität (Würzburg), **2016**.

2. *Synthese und Charakterisierung einer photokatalytisch wirksamen biomimetischen Ruthenium(bipyridin)-[FeFe]-Hydrogenase-Dyade*, L. Haley; Bachelor thesis, Julius-Maximilians-Universität (Würzburg), **2018**.

CONTENTS

ABBREVIATIONS

2CS	two-component system
3CS	three-component system
Ac	acetyl
Boc	*tert*-butyloxycarbonyl
BODIPY	4,4-difluoro-4-bora-3a,4a-diaza-*s*-indacene
bpy	2,2′-bipyridine
Cat	(hydrogen evolution) catalyst
CE	counter electrode
CV	cyclic voltammetry
Cys	cysteine
DCC	*N*,*N*'-dicyclohexylcarbodiimide
DCM	dichloromethane
DFT	density-functional theory
DMAP	4-dimethylaminopyridine
DMF	*N*,*N*-dimethylformamide
DMS	dimethyl sulphate
$E_{1/2}$	half-wave potential
EA	ethyl acetate
EI	electron impact ionisation
E_{pa}	anodic peak potential
E_{pc}	cathodic peak potential
ESA	excited state absorption
ESI	electrospray ionisation

ET	electron transfer
Fc/Fc^+	ferrocene/ferrocenium
Fig.	figure
GC	gas chromatography
GPC	gel permeation chromatography
GSB	ground state bleach
h	hour(s)
H_2A	ascorbic acid
HEC	hydrogen evolution catalyst
ILCT	interligand charge transfer
isomeris.	isomerisation
LC	ligand centred
LED	light emitting diode
LMCT	ligand-to-metal charge transfer
M	mol l^{-1}
*m*CPBA	*meta*-chloroperoxybenzoic acid
MeCN	acetonitrile
min	minute(s)
MLCT	metal-to-ligand charge transfer
MO	molecular orbital
MOF	metal organic framework
OQ	oxidative quenching
pdt	propyldithiolate
PE	petrol ether
ppy	2-phenylpyridine

PS	photosensitiser
PTFE	polytetrafluoroethylene
pyr	pyridyl
r.t.	room temperature
RQ	reductive quenching
sat.	saturated
SD	sacrificial electron donor
SDS	sodium dodecyl sulphate
SEC	spectroelectrochemistry
TA	transient absorption
TBAHFP	tetrabutylammonium hexafluorophospate
TEA	triethylamine
TEOA	triethanolamine
TFA	trifluoroacetic acid
THF	tetrahydrofuran
TLC	thin layer chromatography
TOF	turnover frequency
TON	turnover number
WE	working electrode
WOC	water oxidation catalyst

1 INTRODUCTION

In the light of the steadily increasing global energy demand and the climate change that is already taking place, there is not only increasing interest but also considerable pressure to find a regenerative and environmentally friendly producible energy carrier that can reduce global dependence on fossil fuels. Hydrogen has the potential to become such an energy carrier, because, in addition to its very high energy density compared to fossil fuels, only water is released when it is used to generate electricity in a fuel cell or burned directly as a fuel.[1] For this purpose, however, an environmentally friendly production is mandatory. Today, hydrogen is usually obtained from natural gas through the greenhouse gas-releasing steam reforming process.[2] A more environmentally friendly alternative to this is the extraction from water by electrolysis, but this is very energy-intensive and, additionally, the energy provided should ideally have been generated in a climate-friendly manner. Since this would drive the energy demand even further and a comprehensive renewable energy supply has not yet been expanded everywhere, there is a great research interest in the photocatalytic water splitting, in which hydrogen and oxygen are obtained from water by irradiation with light.[3] In a practical application, this environmentally friendly energy carrier production could be realised, for example, with the help of sunlight and water as inexhaustible sources of energy and natural resources.

As explained in the following chapter, however, it is very difficult to create an artificial molecular system for full photocatalytic water splitting, because on the one hand many different components with different tasks are required for a functioning system and on the other hand because their material properties such as their redox potentials need to be attuned with one another. For this reason, in research on hydrogen evolution, only proton reduction is considered as the corresponding half-reaction of the full water splitting.[3] A so-called three-component system typical for photocatalytic proton reduction usually consists of a photosensitiser, a catalyst and a sacrificial electron donor. The material properties within this system must also be aligned with one another so that the intended photocatalytic redox process, which actually represents an electron cascade between the individual components induced by light irradiation, can take place under thermodynamic conditions.[3] However, the photocatalytic performance of the catalysts used in such systems does not usually come close to their natural role models, the so-called hydrogenase enzymes, to the active sites of which many hydrogen evolution catalysts refer.[4,5] Therefore, in recent years, many research groups have intensively researched system optimisations such as new components with better adapted material properties, better reaction conditions, optimised solvent mixtures or improved component compositions.[5] However, the use of photocatalytic dyads, which combine the

functionality of the photosensitiser and catalyst in one molecule and thus replace the previously intermolecular electron transfer processes with potentially faster intramolecular ones, has been relatively little explored. Accordingly, relatively little is known about the exact functioning and the performance compared to three-component systems from the few examples of such dyad containing photocatalytic systems.[6] For this reason, this thesis aims to examine, among other things, the component properties and the electronic processes of such dyad containing systems during photocatalysis and compare them with those of the corresponding bimolecular multi-component systems in order to gain new insights and thus to obtain the opportunity to further optimise such photocatalytic systems.

First, however, the theoretical principles on this topic are explained in more detail in the following chapter.

2 THEORETICAL PRINCIPLES AND STATE OF RESEARCH

2.1 Principles of Photocatalytic Water Splitting

The photocatalytic hydrogen generation using molecular systems has been a subject of great interest in research for the past 40 years and in particular since the structure of the active site of the very efficient [FeFe]-hydrogenase enzyme has been elucidated.[4,5,7-9] Before going into the basic principles of this process, it is important to understand that the proton reduction with hydrogen as its formation product is only a half-reaction of the entire water splitting procedure. Analogous to the splitting of the general hydrolysis equation into a water oxidation and a proton reduction process shown in equation 1 and 2, this can also be applied to the much more complex photocatalytic water splitting.

$$H_2O \longrightarrow \tfrac{1}{2}\, O_2 + 2\, H^+ + 2\, e^- \qquad (1)$$

$$2\, H^+ + 2\, e^- \longrightarrow H_2 \qquad (2)$$

The photocatalytic variant is also essentially a redox process, in which water is ideally employed as the starting material and in the course of which elemental oxygen is formed by oxidation and hydrogen is released by a reduction process. However, these operations are supposed to take place under photocatalytic conditions, which is why, as shown in **Fig. 1a**, a number of different process participants each with a distinct task are required.[3]

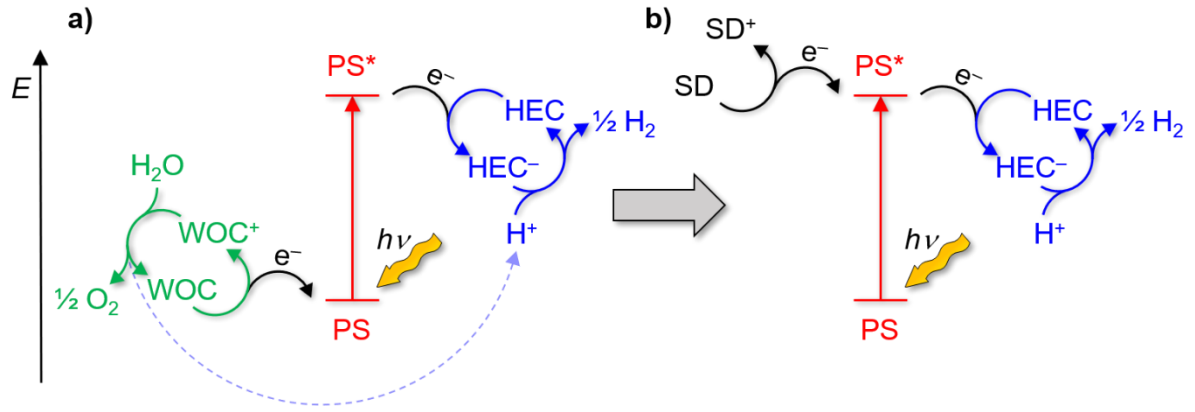

Fig. 1 Simplified scheme of **a)** the ideal photocatalytic water splitting process using a photosensitiser (PS), a water oxidation catalyst (WOC) and a hydrogen evolution catalyst (HEC) and of **b)** the photocatalytic proton reduction using a photosensitiser (PS), a hydrogen evolution catalyst (HEC) and a sacrificial electron donor (SD).

First of all, a photosensitiser (PS) is needed, which, as the linchpin of the overall reaction, delivers the required electrons for the proton reduction or absorbs the released electrons of the water oxidation in the corresponding redox reactions. In order to participate with the appropriate redox potentials, the photosensitiser additionally absorbs the energy required in

the form of light radiation and thus keeps the catalytic cycle going. Therefore, it represents the central link between water oxidation and proton reduction. Apart from this, as shown in the simplified scheme in **Fig. 1a**, the sub-processes just mentioned take place more or less independently of one another. For the water oxidation a water oxidation catalyst (WOC) is required, which usually reacts in its oxidised form with water and on which the actual oxidation of water to oxygen takes place. As described above, the electrons taken up during that process are then released by the WOC to the photosensitiser in order to be available again for a further reaction with water. Analogously, the proton reduction also takes place in such a catalytic cycle. Here a hydrogen evolution catalyst (HEC) is first reduced by the activated photosensitiser in order to subsequently generate hydrogen with a proton in the actual reduction. The thus oxidised catalyst is then reduced again by the activated photosensitiser in order to start the cycle again. Both half-reactions and the use of the photosensitiser therefore take place under catalytic conditions and are regenerated again and again within the process and are not consumed. While water oxidation provides the electrons required for proton reduction, this in turn ensures that the released electrons are captured.[3]

However, it must be pointed out that the system just described and shown in **Fig. 1a** represents an ideal system of the combined full water splitting, which in reality can only be fulfilled by very few and in most cases photoelectrochemical systems.[3,10-13] The reason for this is that for a functioning system, the redox potentials of all components involved must be matched to one another so that the successive electron transitions can take place. For the goal of an overall photocatalytic system, in which all processes can run without applying an additional external voltage, there must also be a sufficient thermodynamic driving force for the ongoing electron cascade. Therefore, it is extremely difficult to find or synthesise suitable components that are adjusted in their properties for the entire process. Instead, the focus is currently on researching and optimising the individual half-reactions.[3] Even though this means that the advantage of a self-contained system with self-sufficient half-reactions of the full water splitting is lost, this has the advantage that the properties of the components involved in the corresponding sub-process no longer have to be adapted to the overall process with all of its participants, but rather this only has to be done within the respective partial reaction. In addition, this means that the half-reactions and with them the containing individual electron transfers can also be optimised much better by increasing the scope for adapting the properties of individual components and thereby achieving much higher efficiencies for the water oxidation or proton reduction, respectively.[3] Nevertheless, full photocatalytic water splitting remains the ultimate goal of research in this area, not only because it is basically an artificial and environmentally friendly counterpart to natural photosynthesis, but also because it is a process that combines water oxidation and proton reduction with one another and provides the required electron flow for both sub-processes.[3]

When changing from the full photocatalytic water splitting to the photocatalytic proton reduction, as shown in **Fig. 1b**, the water oxidation must be replaced, which, in addition to the protons, primarily provided the electrons required for the reduction. This task is performed by a sacrificial electron donor (SD). In contrast to the actual water oxidation and proton reduction, which take place in a catalytic cycle, the sacrificial electron donor is actively consumed during the photocatalysis and must therefore be added in excess. The required properties of the individual components are discussed in more detail in the next section, but it is obvious from its task that only a material with a comparatively high reducing power can be used for this purpose.[14] Ideally, the SD is a reducing acid, such as ascorbic acid, because it also provides the protons for hydrogen generation. However, numerous examples of photocatalytic proton reduction systems without acid additions or that run in alkaline, show that on the one hand the solvent can serve as a sufficient proton source in many cases and on the other hand that the proton reduction, contrary to what its name suggests, can also takes place with HO^- containing solutions.[3,14]

2.2 Structure and Basics of Photocatalytic Three-Component Systems

A molecular photocatalytic three-component system (3CS), which is supposed to generate hydrogen under the influence of light by proton reduction, basically consists of a photosensitiser, a hydrogen evolution catalyst and a sacrificial electron donor.

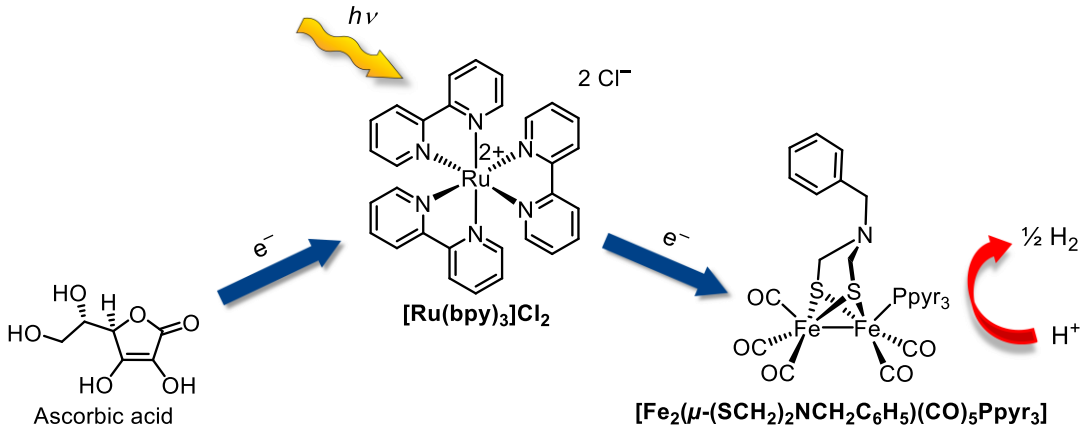

Fig. 2 Example of a photocatalytically active three-component system (3CS) with **$[Ru(bpy)_3]Cl_2$** as photosensitiser, **$[Fe_2(\mu\text{-}(SCH_2)_2NCH_2C_6H_5)(CO)_5Ppyr_3]$** as catalyst and ascorbic acid as sacrificial electron donor. The system was tested by Sun and Åkermark in a 1:1 (*v*/*v*) mixture of acetonitrile and water (pH = 3.7) and achieved after 3 h of irradiation with light < 25000 cm^{-1} (> 400 nm) a catalytic productivity of TON = 4.3.[15]

Fig. 2 shows an example of such a classic 3CS, which in this case is made up of a ruthenium photosensitiser, a [FeFe]-hydrogenase biomimic as catalyst and ascorbic acid as sacrificial electron donor. This system was developed and examined by Sun and Åkermark as part of

their study to investigate diiron complex containing photocatalysis systems.[15] In the following, the functionality, properties and examples of the corresponding individual components of a photocatalytic 3CS are discussed in detail.

2.2.1 The Photosensitiser

As already explained in the previous section, the primary task of the photosensitiser is to provide the catalyst with the electrons required for the reduction process. It itself recovers the emitted electrons through the sacrificial electron donor. In order to be able to participate in both processes with the required redox potentials and thus to be able to provide the energy required for proceeding the overall process, the photosensitiser absorbs the corresponding energy which is provided by light irradiation. Generally, organometallic complexes, such as **$[Ru(bpy)_3]Cl_2$** (bpy = 2,2'-bipyridine) in the example shown in **Fig. 2**, are used for this, since they have favourable properties as photosensitisers.[16-18] As a rule, they are able to occupy several different oxidation levels, which predestines them as a connecting element between several redox processes. Furthermore, because of the relatively strong interaction with their often cyclometalated ligands and the thus resulting charge-transfer absorption bands or the often expanded π-system, these complexes usually absorb in the visible spectral range, which also makes them practical for the use as photosensitisers.[16,17,19,20] As a further important feature, many transition metal complexes are triplet emitters due to possible intersystem crossing and a pronounced spin-orbit coupling.[16,21] Since the transition from a triplet state to the singlet ground state is spin-forbidden, this usually results in relatively long-lived excited states of that complexes. This is advantageous with regard to the redox processes taking place in photocatalysis, in which the photosensitiser is involved in the excited state, since it is more likely for the system to react with the corresponding reaction partner if the lifetime is long. Additionally, numerous uses as photosensitisers in very different systems have shown that the redox potentials of these complexes are very variable through synthetic customisation and adaptable to the corresponding conditions and used components. Thus, in addition to various ruthenium complexes, diverse iridium, rhenium, cobalt, zinc, and copper complexes have already been utilised as molecular photosensitisers in photocatalytic proton reduction.[5,9,18,22-26] In conjunction with [FeFe] biomimetic catalysts (see below), especially ruthenium and iridium complexes were often used as sensitisers in the past due to the well-matched redox potentials.[3,5,9] Another important aspect of a photosensitiser is its stability. In contrast to the material properties explained so far, which essentially have an influence on the catalytic activity, the chemo and photostability of the used complex affects above all the catalytic productivity of the overall system. How the catalytic activity and productivity as the decisive two parameters of the performance of a photocatalytic system are related to each other in detail and in particular to the material properties of the system components will be explained

below. In various studies, the complexes **[Ru(bpy)$_3$]Cl$_2$** and **[Ir(ppy)$_2$bpy]PF$_6$** (ppy = 2-phenylpyridine) used in this work as photosensitisers each showed different stability behaviour. While the ruthenium complex was found to be extremely stable to thermal and photochemical decomposition in the ground state as well as in its reduced and oxidised form,[23] this is only true to a limited extent for the cyclometalated iridium complex in the ground state. As Bernhard *et al.* were able to show, **[Ir(ppy)$_2$bpy]PF$_6$** tends to split off its bpy ligand and this tendency increases considerably in its oxidised or reduced form, which appears to be problematic with regard to the use in photocatalysis.[24,25,27-29] However, further studies with photocatalytic systems consisting of iridium photosensitisers and [FeFe] biomimetic catalysts have shown that the photo-instability of the iridium complexes tends to be comparable to the decomposition of the diiron complexes during photocatalysis.[30] Thus, the use of iridium photosensitisers in photocatalysis should at least not pose a significant problem for the overall productivity of the respective system. Interestingly, non-metal containing complexes can also be utilised as sensitising compounds. For instance, Eosin Y as a purely organic xanthene dye could be employed as a photosensitiser for hydrogen generation.[31] However, such organic compounds tend to be the minority for this purpose.

2.2.2 The Hydrogen Evolution Catalyst

The actual proton reduction with the formation of hydrogen takes place on the catalyst in a photocatalytic 3CS. As already mentioned above, an electron is transferred from the photosensitiser to the catalyst in the course of photocatalysis. For a functioning system, therefore, the reduction potential of the catalyst must match the corresponding redox potential of the photosensitiser. For a photocatalytic performing system, this means that, on the one hand, the energetic distance should not be too large and, on the other hand, that there must be a thermodynamic driving force between both so that the intended electron transfer can take place exergonically, i.e. without the additional supply of energy. Since the photocatalysis can basically take place *via* two different quenching mechanisms (see below) and it depends on this mechanism under which oxidation level and energetic state the photosensitiser reacts with the catalyst, knowledge of the mechanism involved is crucial for the thermodynamic assessment of the corresponding electron transfer. Furthermore, it is important for a good system performance that the catalyst shows a preferably high activity in hydrogen generation. As is well known, the natural hydrogenase enzymes show very high activities in the production of hydrogen. For instance, [NiFe]-hydrogenases can achieve up to 700 turnovers per second and molecule and are even outshone by the [FeFe]-hydrogenases with 6000–9000 turnovers per second and molecule.[4] The latter represent therefore the highest levels of natural hydrogen producing enzymes, which is why there is an interest in transferring their performance to an artificial system. To do this, the active site of the [FeFe]-hydrogenases found

in the two bacteria *Clostridium pasteurianum* and *Desulfovibrio desulfuricans* had to be elucidated.[4] In the late 1990s, this was achieved using gene sequencing and X-ray crystallography.[32] **Fig. 3a** shows the obtained structure of the active site. It essentially consists of the typical "butterfly" Fe_2S_2 subunit and a cubic cysteine-linked $[Fe_4S_4]$ complex, through which the electrons required for proton reduction are mediated. In addition, at the diiron centre there are two cyanide ligands responsible for anchoring the complex in the surrounding peptide matrix and three carbonyl ligands, one of which occupies a bridging position between the two iron atoms.[4,32]

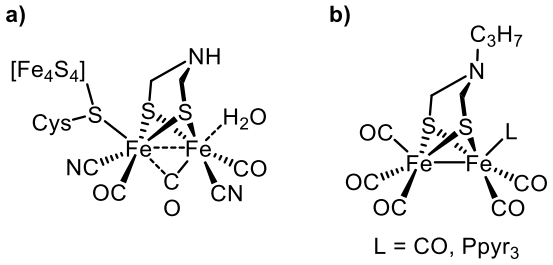

Fig. 3 **a)** Active site of [FeFe]-hydrogenase with characteristic "butterfly" Fe_2S_2 subunit and cysteine-linked $[Fe_4S_4]$ cluster for electron intermediation.[32] **b)** Typical [FeFe]-hydrogenase biomimic with an azadithiolate ligand synthesised by Rauchfuss *et al.* and Sun *et al.*, respectively.[15,33]

As can be seen in **Fig. 3b**, with the knowledge of the structure of the active site, numerous biomimics were synthesised, which as the key structural unit also has the characteristic Fe_2S_2 unit and up to six carbonyl ligands. Furthermore, these synthesised diiron compounds also show catalytic activity for proton reduction, even if this is generally significantly lower than that of their natural role model.[34,35] Although the quality of the photocatalytic performance of such a 3CS depends on a large number of factors and conditions and not only on the hydrogen evolution performance of the catalyst used, knowledge of the actual reaction mechanism of proton reduction with [FeFe]-hydrogenase biomimics is very important for further optimising the corresponding complexes. However, this is still not known in every detail. Experimental evidence of various intermediates and DFT calculations, nonetheless, have led to the conclusion of important intermediate stages and possible reaction pathways, which are shown in **Fig. 4**.[36,37]

A total of at least two electrons and two protons have to be contributed to the formation of one hydrogen molecule. This means that at least two full catalytic cycles in the 3CS are necessary for product formation. In addition, it could be demonstrated by UV/Vis and IR spectroscopy that the proton added to the [FeFe] complex first accumulates as a bridged hydride between the two iron atoms in the course of the first reduction process (see **Fig. 4**).[38] It could therefore be concluded that the electron density at the diiron core of the complex has a decisive influence on its reactivity. Hence, a higher electron density facilitates the attachment of a proton and thus increases the protophilicity of the complex.[9]

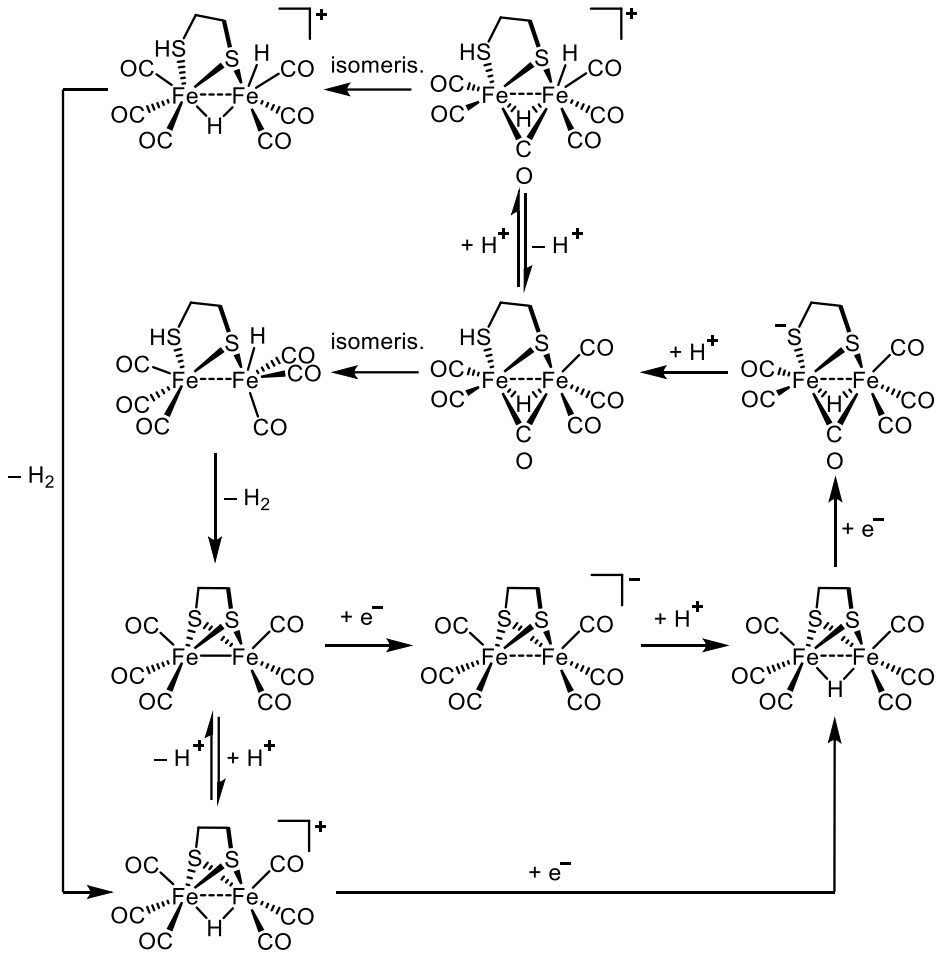

Fig. 4 Proposed mechanism of hydrogen evolution at a [FeFe]-hydrogenase biomimic.[36,37]

However, the electron density at the diiron core also has an opposite effect on the reduction potential, which is important for the envisaged electron cascade. If this experiences a large cathodic shift due to a high electron density, there is a risk that it no longer matches the corresponding redox potential of the photosensitiser and, as a result, the electron transfer can only take place to a limited extent or not at all.[9] On the other hand, it was found that diiron complexes with comparatively very positive and therefore mild reduction potentials, as a consequence of corresponding substituents, show a distinctly lower stability.[9] Aside from the fact that [FeFe] complexes exhibit generally relatively low reduction potentials (usually below –1.50 V *vs.* Fc/Fc^+),[39] this would have negative effects especially on the catalytic productivity of the respective systems and makes the use of these diiron compounds as a catalyst for hydrogen generation considerably more difficult. This must be taken into account when considering structural changes on the catalyst which can influence its electronic properties.

From the mechanism shown in **Fig. 4** it can also be seen that the sulphur atoms of the dithiolate bridge presumably also play an important role as an internal acid/base during proton reduction. Therefore, what has just been described about the electron density at the diiron core of the complex basically also applies to the dithiolate ligand. Especially since the dithiolate bridge, along with the carbonyl ligands, represents the main option for synthetically feasible structural

changes in the [FeFe] complexes. One possibility for effecting the electronic properties would be for example the attachment of additional functional groups directly to the iron core by simply substituting the carbonyl ligands. In particular, phosphine ligands have been established in the literature as such functionalities.[5] Due to their electron-donating effect and because they are in comparison with the carbonyl ligands relatively weak π-acceptors, they can increase the electron density and thus the protophilicity of the [FeFe] complexes.[40] However, as described above, this can also have a negative effect on the reduction potential. The electronic impact of the phosphines depends on the nature of their inner substituents. For instance, with less electron-donating substituents the π-acidity of the phosphines can be increased as a result of the lower σ^* antibonding orbitals within the ligand compounds.[41] The phosphine $Ppyr_3$, which is equipped with three pyrrole substituents, showed the best results in terms of the electrochemical and photocatalytic properties of the corresponding complexes.[9] Obviously, a $Ppyr_3$ substitution means that on the one hand the electron density at the diiron core is increased, but on the other hand only a comparatively small cathodic shift in the reduction potential is induced.

In addition to the [FeFe]-hydrogenase biomimics, other complexes can also be used as hydrogen generation catalysts. Various monoiron, triiron, nickel, and ruthenium containing compounds can also catalyse the proton reduction.[5,10,42] However, the most significant representatives in addition to the diiron compounds are cobalt complexes. In particular, the cobaloximes derived from vitamin B_{12} are often used, which mostly consist of a cobalt(III) central atom with an octahedral geometry and four nitrogen containing ligands in the equatorial plane.[43] **Fig. 5** shows an example of such a cobalt compound in a tetraazamacrocyclic complex. The actual hydrogen evolution catalysis takes place at one of the two coordination points, often equipped with leaving groups, outside the equatorial plane.[43,44] In contrast to the [FeFe] complexes, cobaloximes generally have milder reduction potentials, which means that there should be fewer problems due to unsuitable redox potentials of the photosensitiser used.[43] However, both types of compounds have potential in terms of their photocatalytic performance, since four-digit TON values have already been achieved in molecular photocatalytic systems with [FeFe] complexes as well as with cobaloximes.[5,45]

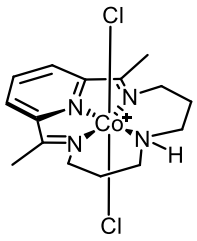

Fig. 5 Example for a cobaloxime hydrogen evolution catalyst consisting of a tetraazamacrocyclic complex.[46]

2.2.3 The Sacrificial Electron Donor

The sacrificial electron donor in the photocatalytic 3CS replaces the water oxidation and supplies the photosensitiser with the electrons required for the reduction. Accordingly, it is the only component that is actively consumed during catalysis and must therefore be added in excess. In addition to a relatively high reducing power, a compound must also have other properties in order to be used as a sacrificial electron donor. Naturally, for a thermodynamically feasible electron transfer to the photosensitiser, the oxidation potential of the sacrificial electron donor must be more negative than the corresponding reduction potential of the photosensitiser. As already mentioned in the section on the photosensitiser, it depends largely on the existing quenching mechanism of the respective system, under which oxidation level and electronic state the sensitiser reacts with the sacrificial electron donor. In addition, it must be ensured that after the electron transfer has taken place, the oxidised sacrificial electron donor does not act as an oxidising agent and triggers an electron back transfer. On the one hand, this can be ensured by converting the oxidised form of the sacrificial electron donor into inert molecules preferably in a quick and irreversible reaction. On the other hand, the compound must have a high so-called cage escape yield η_{CE}. This describes the ability to overcome the Coulomb interaction of the ion pair formed by the electron transfer from oxidised sacrificial electron donor and reduced photosensitiser.[14]

In addition to amines and thiols, organic carboxylic acids are also used as sacrificial electron donors. In the aqueous medium, ascorbic acid is very often utilised. The last two representatives have the additional advantage that, as acids, they serve not only as electron donors, but also as proton suppliers in the hydrogen evolution reaction. Ascorbic acid has an oxidation potential of 0.07 V *vs.* Fc/Fc^{+}[47] and is therefore suitable in combination with most known photosensitisers, provided that they are soluble in the aqueous medium. Triethylamine (TEA) and triethanolamine (TEOA) are most commonly used for the aliphatic amines. With an oxidation potential of about 0.29 V *vs.* Fc/Fc^{+}[14] for both compounds, they are somewhat more limited than ascorbic acid when it comes to combining them with photosensitisers, but their oxidation potential is sufficient for many known photosensitisers such as the $[Ru(bpy)_3]^{2+}$ and $[Ir(ppy)bpy]^{+}$ species. In addition, both amines are soluble in both aqueous and many organic solvents, which enormously increases their possible uses.[14]

As just described, a fast and preferably irreversible degradation is crucial to avoid an electron back transfer. **Fig. 6** shows the degradation pathway of ascorbic acid after deprotonation and oxidation occurred. The radical $HA^{\bullet}$ thus formed, as a strong acid, deprotonates quickly and almost irreversibly to the corresponding radical anion $A^{\bullet-}$, which then disproportionates into the inert dehydroascorbic acid A and ascorbate A^{2-}.[14]

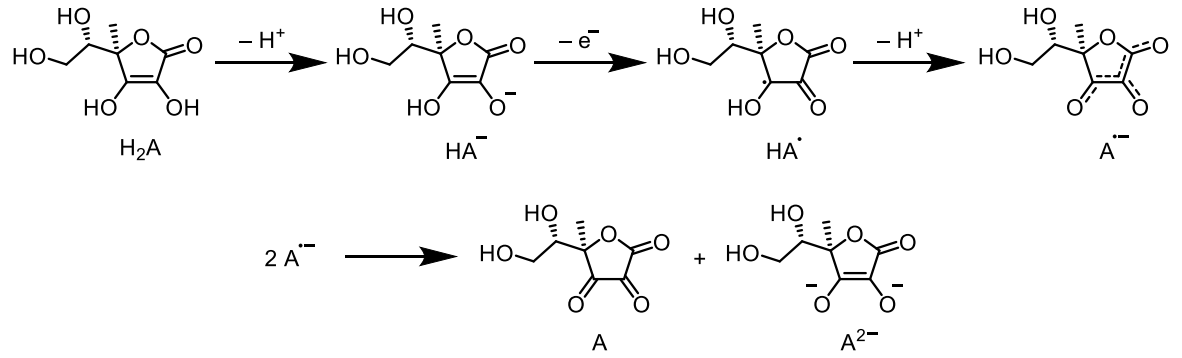

Fig. 6 Degradation pathway of ascorbic acid after deprotonation and oxidation.[14]

Both the effect as proton donor as well as the degradation of ascorbic acid are therefore strongly pH-dependent. The same also applies to the ability as an electron donor, but with the opposite sign. With increasing pH value, the concentration of ascorbate HA^- as the actual reducing agent in the reaction solution decreases, which consequently reduces the overall reducing power.[48] Since both the function of the electron donor and that of the proton donor are decisive for the course of the photocatalysis, there is always an optimal pH range for an ascorbic acid containing system in which both functions are least hampered.

The degradation pathway of TEA after oxidation is shown in **Fig. 7**. It consists in the first step of a rapid deprotonation of the formed aminyl radical by another TEA molecule, which is present in excess. This prevents possible and undesired back electron transfer from the now reduced photosensitiser to the aminyl radical. Then, the carbon-centred radical thus formed can basically reduce a photosensitiser molecule again, which additionally supports the formation of PS^- in the solution. Finally, the resulting iminium ion decomposes to diethylamine and acetaldehyde under water exposure.[14]

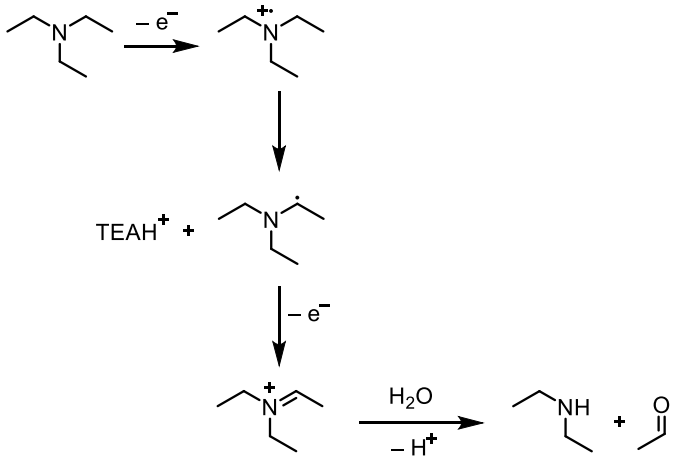

Fig. 7 Degradation pathway of triethylamine after oxidation.[14]

On the one hand, the pathway shows that water is essential for a complete degradation. For this reason, it is advantageous for TEA containing photocatalytic systems in organic solutions

to contain a certain amount of water. Such systems are therefore often operated in organic-aqueous solutions.[5] On the other hand, the reaction path shown in **Fig. 7** also results in a certain pH dependence. As a decisive difference between the amines used as sacrificial electron donors and the other compounds mentioned above, they operate optimally in alkaline medium. In an acid environment, however, the important deprotonation step would not take place after oxidation and the high oxidising power of the aminyl radical would presumably cause a back electron transfer.[14]

2.3 Catalytic Activity and Productivity

The performance of a photocatalytic hydrogen evolution system depends on several factors. In addition to the specific properties of the components involved, which are explained in the previous sections, this also relies upon other measurement parameters such as the pH value of the solution used, the composition of the substances or the time span for collecting the measurement data. Basically, the question arises how to adequately characterise the performance of such a system. In the course of the investigation of catalytic systems, two important performance characteristics have emerged: the catalytic activity and the catalytic productivity.

First of all, it is important to clarify the difference between the two expressions. Both of them contribute to the overall performance, but their dependencies from the molecular properties and their effects on the actual hydrogen production differ from each other. The catalyst related catalytic activity describes the production rate of the catalyst compound, that is the velocity of product turnover and is therefore dependent on mechanistic aspects, the electronic properties of the components used and on their structural design, in the sense of the promotion of intermediates or reactions steps by certain structural units. In addition, the activity of a catalytic system is also largely dependent on the thermodynamic and kinetic conditions with regard to the processes taking place. If there is a thermodynamic driving force and only low energy barriers for the respective process, a system should therefore also exhibit a relatively high catalytic activity. It is explicitly not dependent from any stability aspects. That means that a species, which would produce hydrogen with a high rate, but for stability reasons, not for a long timespan, would, however, be called a catalytic very active species. Although the overall amount of produced hydrogen would not be very high. Usually the catalytic activity is described by the turnover frequency (TOF), which stands for the actual turnover of produced molecules per catalyst molecule and time unit, so the actual production rate of a catalyst (or a photosensitiser in case of sensitiser related catalytic activity).

Furthermore, the catalyst related catalytic productivity describes the amount of produced molecules per catalyst molecule and is therefore mainly dependent on the stability of a system.

That means that in terms of a photocatalytic system especially the photostability of the concerned compounds plays a crucial role. However, chemostability during photocatalysis is also very important in such a system, especially considering that some hydrogen evolution catalysts such as [FeFe] complexes tend to decompose in such processes.[9] A system which shows a high stability and produces therefore for a very long time hydrogen under light irradiation, but exhibits at the same time a low production rate, is still a catalytic very productive system. In general, the catalytic productivity is described by the turnover number (TON), which stands for the ratio of produced hydrogen molecules per catalyst molecule before it gets inactive.

Apparently, it is important to consider about these different performance factors and differentiate accordingly. Nevertheless, there is a particular dependence between both factors, which should be considered, too. More precisely, if a system shows a better catalytic activity for example by means of a higher thermodynamic driving force in consequence of modified electronic properties, this should also be reflected in a higher catalytic productivity. For the reason that a more active catalyst produces under the assumption of a similar complex stability a higher amount of product in the same time window, which leads automatically to a higher productivity of the system. Since structurally very similar systems are often compared with one another in catalytic studies and one can assume comparatively similar compound stabilities for them, this is one reason why in literature the overall performance of a catalytic system is often characterised by TON only.[5,9] This practice has its limits, of course. In particular, since most of the side and decay reactions of the substances used are currently unknown and as a rule they are not investigated further. For instance, it is assumed that the often used phosphine ligands have a stabilising effect in [FeFe] complexes.[9] However, neither the exact reason for this on the molecular scale nor its quantitative extent is known. As a result, the TOF should actually be determined in addition to the usual TON specification for adequate distinction. In this case, however, both values would increase for the reasons mentioned above.

In this work, a distinction is explicitly made between the catalytic productivity and activity at certain points and in particular when examining the planned photocatalytic dyad systems (see below), which will also be investigated accordingly. In general, however, analogous to the literature, catalytic productivity is also used as a measure of the overall performance of the systems examined, especially in the preliminary study of different [FeFe]-hydrogenase biomimics which will also be evaluated under this aspect. This should be justifiable in view of the fact that the complex stabilities usually do not change fundamentally due to the planned structural changes and, therefore, should not have a serious impact on the TON values determined in the for the measurements considered relatively small time window.

2.4 Quenching Mechanisms of Photocatalysis

A photocatalytic multi-component system can basically run under two different quenching mechanisms. The term "mechanism" is probably somewhat misleading at this point, because in contrast to the reaction mechanism explained above on a [FeFe] biomimetic catalyst (see chapter 2.2.2), it is not the exact mechanistic sequence of a reaction that is meant, but basically the sequence of the successive redox processes during photocatalysis. As already mentioned in the previous sections, the quenching mechanism has a decisive influence on under which redox levels and electronic states the photosensitiser acts as the link between the sacrificial electron donor and the catalyst. Knowledge of the proceeding mechanism is therefore of crucial importance when it comes to the thermodynamic assessment of the redox cascade in progress. **Fig. 8** shows the two possible quenching mechanisms, which are explained in more detail below.

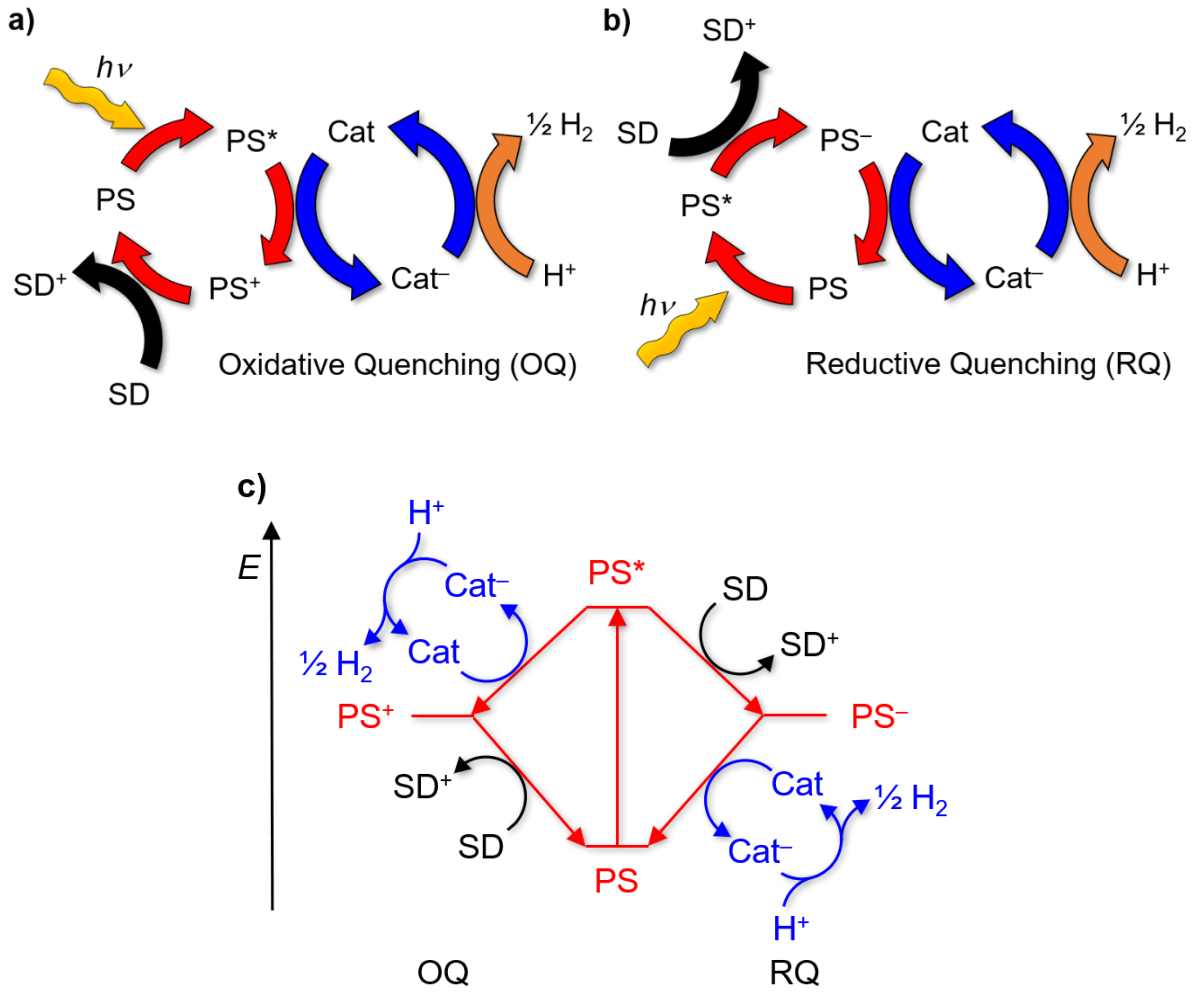

Fig. 8 Simplified schemes for the two mechanistic pathways possible in photocatalytic proton reduction: **a)** catalytic cycle-scheme for oxidative quenching (OQ) mechanism[8], **b)** catalytic cycle-scheme for reductive quenching (RQ) mechanism[8] and **c)** both processes on the energetic scale[9]. PS stands for the photosensitiser, Cat for the catalyst and SD for the sacrificial electron donor.

The two quenching mechanisms are the so-called oxidative quenching (OQ) and reductive quenching (RQ), named after the oxidation level the photosensitiser passes during the respective process. In both mechanisms, the photosensitiser is first excited by light irradiation. In the OQ mechanism, an electron is then transferred from the excited photosensitiser to the catalyst, where the actual proton reduction takes place. In the next step, the now oxidised photosensitiser is reduced back to its original state by the sacrificial electron donor. In the RQ mechanism, once the photosensitiser has been excited, it is first reduced by the sacrificial electron donor, whereupon the then reduced photosensitiser reduces the catalyst in order to return to the initial state. In order that the individual redox processes can run exergonically under photocatalytic conditions, the redox potentials of the components involved must meet certain thermodynamic conditions. Basically, the oxidation potential of the reducing agent must be more negative than the reduction potential of the oxidising agent. Starting with the RQ mechanism, this means for the initial electron transfer from the sacrificial electron donor to the excited photosensitiser:[9,14]

$$E^{0'}\,[SD^{+}/SD] < E^{0'}\,[PS^{*}/PS^{-}] \tag{3}$$

The subsequent reduction of the catalyst by the reduced photosensitiser must meet the following condition:[14]

$$E^{0'}\,[PS/PS^{-}] < E^{0'}\,[Cat/Cat^{-}] \tag{4}$$

In the OQ mechanism, electron transfer from the excited photosensitiser to the catalyst takes place first. This thermodynamic condition must therefore be fulfilled:[14]

$$E^{0'}\,[PS^{+}/PS^{*}] < E^{0'}\,[Cat/Cat^{-}] \tag{5}$$

The final reduction of the oxidised photosensitiser by the sacrificial electron donor must meet the following condition:[14]

$$E^{0'}\,[SD^{+}/SD] < E^{0'}\,[PS^{+}/PS] \tag{6}$$

Equations 3 to 6 result in several accompanying conditions for the considered system. The initial redox processes of both mechanisms (see equations 3 and 5) can only work if the photosensitiser simultaneously gains in oxidation or reduction power when it is excited by light. Accordingly, the following must apply to the photosensitiser in the RQ mechanism:[14]

$$E^{0'}\,[PS^{*}/PS^{-}] > E^{0'}\,[PS/PS^{-}] \tag{7}$$

This means that the excited photosensitiser is more likely to gather an electron from the sacrificial electron donor than it would be in its ground state. In the OQ mechanism, the following accordingly applies to the photosensitiser:[14]

$$E^{0'}\,[PS^{+}/PS^{*}] < E^{0'}\,[PS^{+}/PS] \quad (8)$$

This implies that the excited photosensitiser is more likely to reduce the catalyst than it would be in its ground state. Both facts indicate that the photosensitiser has a decisive influence on which mechanism takes place in a photocatalytic system. Indeed, the redox potentials of the other system components also influence the type of quenching mechanism. Furthermore, it can also depend on other parameters like the pH value, the concentration of the components or the used solvent.[14] Similar to the system's performance, the type of quenching mechanism usually depends on a large number of parameters, some of which are mutually dependent. This makes an accurate prediction of the quenching mechanism very difficult. Nevertheless, some indications can be derived from the discussed thermodynamic conditions. Thus, the RQ mechanism can be regarded as somewhat preferred over the OQ mechanism, since the reduced photosensitiser PS^{-} is usually a stronger reducing agent than the excited photosensitiser PS*. RQ systems can therefore handle a larger number of catalysts with more cathodic reduction potentials.[14] In addition, the OQ mechanism is observed especially in systems with photosensitisers, which are comparatively mild oxidising agents. Interestingly, the very popular $[Ru(bpy)_3]^{2+}$ photosensitiser is a kind of chameleon in this regard, since it uses both the OQ and the RQ mechanism depending on the used reaction conditions and reaction partners.[18,24,25,49-51]

2.5 Photocatalytically Active Dyads

Research on artificial systems that can generate hydrogen under the influence of light has made great progress since the 1970s. The great majority of researchers focused on the classic three-component systems (3CS) described in chapter 2.2.[34,35,52-54] In addition to many different possibilities for optimising such a system, there is an option in the synthesis and integration of photocatalytically active dyads in systems for hydrogen generation. These dyads consist of a photosensitiser that is covalently linked to a hydrogen generation catalyst. In a photocatalytic 3CS the sacrificial electron donor is the only component that is actively consumed during photocatalysis, so only the photosensitiser can meaningfully be linked to the catalyst in a corresponding dyad. The development of a dyad, which consists of a different combination of components or a corresponding triad, is therefore excluded. The main advantage of a dyad containing two-component system (2CS) is that the intermolecular electron transfer between the photosensitiser and the catalyst in a 3CS is replaced by an intramolecular process in the 2CS. Since in a 3CS the electron transfers can, in the best case, take place in a diffusion-controlled manner, this would no longer apply in the 2CS at least for the corresponding transfer between the photosensitiser and the catalyst. Thus, dyads have enormous optimisation potential and could significantly increase the performance of a photocatalytic system.

The first photocatalytic dyad was realised by Sun and Åkermark in 2003. As can be seen in **Fig. 9**, it consisted of a propyldithiolate [FeFe] catalyst which was covalently linked *via* the dithiolate bridge to a ruthenium tris-bipyridin photosensitiser.[55,56] As spacer unit between the photosensitiser and catalyst moieties a benzene ring was used, which was linked by an amide bond to one bipyridine ligand of the ruthenium complex and by an ester bond to the [FeFe] complex. This particular structure was chosen in order to mimic the active site of the hydrogenase from the *Desulfovibrio vulgaris* bacterium.[57] Regrettably, the dyad was not tested for hydrogen evolution and there are therefore no information given about its photocatalytic performance. In the following year, Åkermark, Hammarström and Sun created a dyad, which consisted of a ruthenium bis-terpyridine photosensitiser that was linked *via* an acetylene bond to a phenyl azadithiolate bridged diiron catalyst.[58] This system was also not tested for its photocatalytic performance.

In 2006 Hammarström and Ott followed a different attempt for a photocatalytic dyad design by linking a ruthenium tris-bipyridine photosensitiser *via* an acetylene bond directly to a tris-phenyl phosphine ligand of a propanedithiol bridged diiron compound (see **Fig. 9**).[59] The special aspect of this system was the connection *via* a phosphine ligand of the diiron core, whereby the improved stability of this diiron complex induced by the assembly of such a phosphine ligand was exploited.[9] Two years later, Sun published an approach which was very similar to the first one in 2003, in which the same ruthenium photosensitiser and spacer combination was linked directly to an azadithiolate bridge of the used diiron catalyst compound.[60] Again, this system was not tested in photocatalysis. This changed in the same year, when Fontecave *et al.* coupled a ruthenium photosensitiser to a cobaloxime complex *via* the quasi supramolecular bonded pyridine base of the catalyst, which was covalently linked to the oxazolophenanthroline ligand of the ruthenium complex (see **Fig. 9**).[50] This dyad was utilised in a photocatalytic 2CS using TEA as sacrificial electron donor and acetone as solvent and achieved a maximum catalyst related TON of 103 after 15 h of irradiation with a CdI-doped mercury lamp.

In 2012, the first [FeFe]-hydrogenase biomimic containing dyad was photocatalytically tested by Chen *at al.*, who linked for this purpose an iridium bis-phenylpyridine bipyridine photosensitiser by an amide bonded benzene ring spacer to a phosphine substituted [FeFe]-hydrogenase catalyst (see **Fig. 9**). Basically, this is a similar approach as the one mentioned above by Hammarström and Ott.[6] The dyad showed in photocatalysis a maximum catalyst related TON of 127 after 4 h of irradiation with light < 25000 cm^{-1} (> 400 nm). A mixture of acetonitrile and water (*v*/*v* = 9:1) was used as solvent and TEA was employed as the sacrificial electron donor. Noteworthy, the corresponding 3CS was also tested under the same conditions

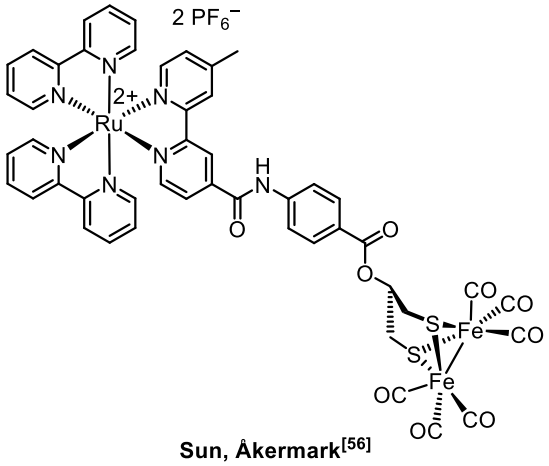

Sun, Åkermark[56]
2003
TON = n.a.

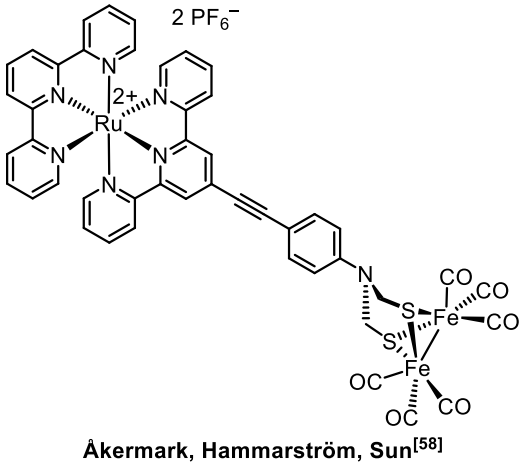

Åkermark, Hammarström, Sun[58]
2004
TON = n.a.

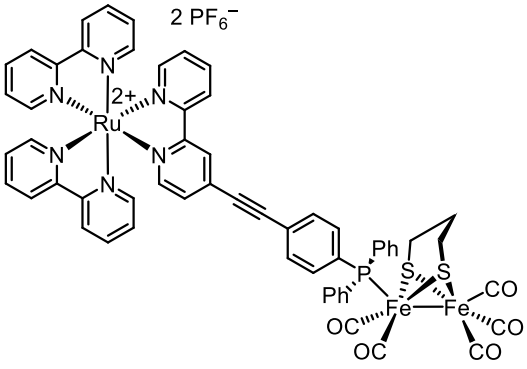

Hammarström, Ott[59]
2006
TON = n.a.

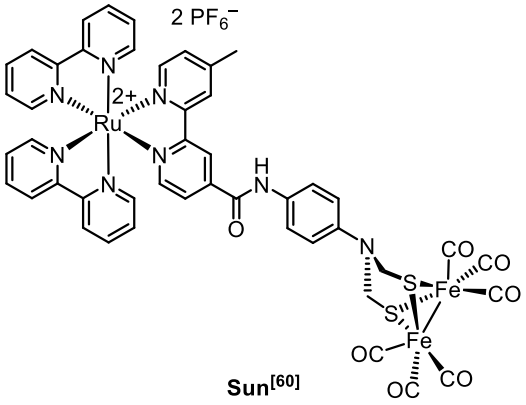

Sun[60]
2008
TON = n.a.

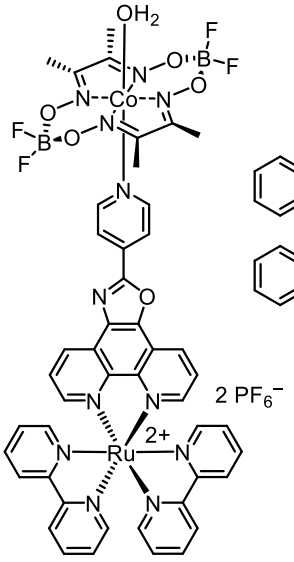

Fontecave[50]
2008
TON = 103 (15 h)

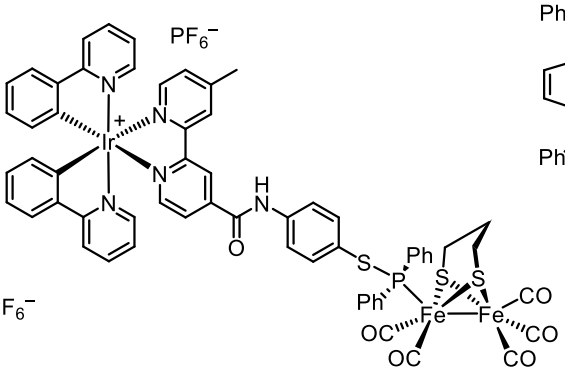

Chen[6]
2012
TON = 127 (4 h)

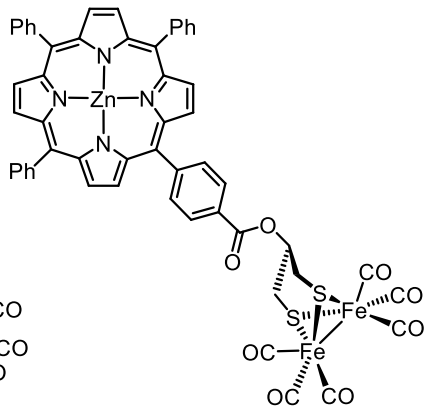

Song, Chen[61]
2014
TON = n.a.

Fig. 9 Important photocatalytic dyads from research up to 2014.

and showed with TON = 138 a better performance than the 2CS.[6] Interestingly, Sun *et al.*, who also observed such a behaviour of several photocatalytic dyads in comparison with their bimolecular 3CS, argued that in general a 3CS would benefit more from a reductive quenching mechanism than a 2CS and that this leads to this difference in performance.[9]

In 2014, Song and Chen developed photocatalytic dyads, each of which consisted of a [FeFe] complex covalently connected to a zinc porphyrin as the photosensitiser *via* their dithiolate bridges (see **Fig. 9**). Unfortunately, the photocatalytic performance of these supramolecular dyads was not tested in this work.[61] Two years later, Rau *et al.* also designed and synthesised a photocatalytic dyad with a supramolecular structure. This consisted of a ruthenium bis-tetrabutylpyridine photosensitiser, which was connected to a Rh(Cp*) centre *via* a tetrapyridophenazine ligand (see **Fig. 10**).[62] The latter acted as a proton reduction catalyst. Thus, this work represents the first dyad with such a rhodium complex as catalytic centre. This dyad was also investigated photocatalytically. A mixture of acetonitrile, water and TEA was used as solvent, while the latter also acted as the sacrificial electron donor. However, this photocatalytic system did not show a comparatively high performance. After 670 hours of irradiation with light at 21300 cm^{-1} (470 nm), only a TON of 17 could be achieved.[62]

In 2015, Luo and Wu were the first to present a dyad that did not build on a transition metal in its sensitiser part. Their system consisted of a thienyl-substituted BODIPY photosensitiser, which was bound to a cobaloxime catalyst *via* a pyridine bridge.[63] This system showed a TON of 73 in an acetonitrile-water mixture (pH = 8.5) with TEOA as sacrificial electron donor after it had been irradiated with light < 23800 cm^{-1} (> 420 nm) for 10 hours. Furthermore, also in the catalyst part, new structures apart from the common [FeFe] complexes and cobaloximes could be successfully installed and tested in photocatalytic dyads. In 2016, Rau and Streb succeeded in covalently binding a bipyridine-functionalised Anderson-type polyoxometalate, which acted as a proton reduction catalyst, to two iridium 2-phenylpyridine complexes (see **Fig. 10**).[64] Under photocatalytic conditions, the dyad built up in this way was able to achieve a TON of 80 after seven days of light irradiation at 21300 cm^{-1} (470 nm). During the experiments DMF was used as solvent and TEA and acetic acid as sacrificial electron and proton donor, respectively. In addition, the corresponding 3CS was also examined for its photocatalytic performance in this study. The 2CS showed a much higher TON than the 3CS (TON = 6) under the same conditions.[64] The authors suspected that a significantly favoured electron transfer within the dyad was responsible for this. This system also served as the basis for the dyad published by Dietzek in 2018, which consisted of a Keggin-like polyoxometalate as the catalyst part and a ruthenium bis-terpyridine photosensitiser (see **Fig. 10**).[65] With this system, the main problem of the previous system by Rau and Streb, namely the short lifetime of the charge-separated

state after light excitation due to the rapid charge recombination, could be eliminated. Unfortunately, this system has not been tested for its photocatalytic performance.

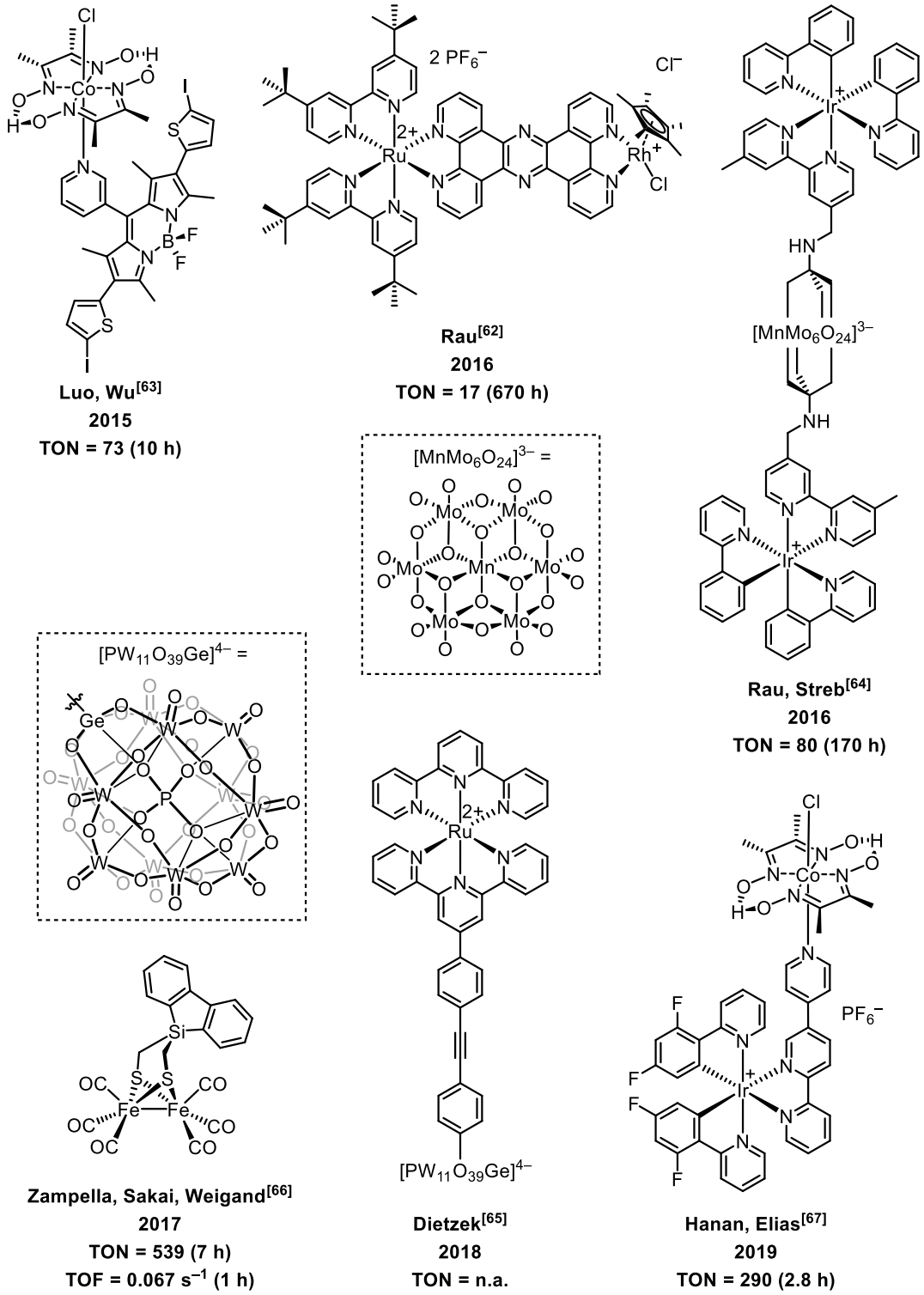

Fig. 10 Important photocatalytic dyads of recent research since 2015.

In recent years, new [FeFe] complex containing dyads have also been developed. In 2017, for example, Zampella, Sakai and Weigand were able to covalently link several fluorene and silafluorene sensitisers each with a [FeFe] complex.[66] The silafluorene dyad shown in **Fig. 10**

achieved the highest photocatalytic performance with TON = 539 and TOF = 0.067 s^{-1} within the first hour of light irradiation. The experiments were carried out in an aqueous cetrimonium bromide micelle solution, with TEA as the sacrificial electron donor and TFA as the proton source.

As one of the most recent results in the field of photocatalytic dyads, Hanan and Elias were able to present a dyad in 2019, which consisted of a fluorine-substituted iridium 2-phenylpyridine photosensitiser, which was covalently linked to a cobaloxime catalyst *via* a bipyridine ligand.[67] After 2.8 hours of irradiation with light at 22100 cm^{-1} (452 nm), this dyad showed a TON of 290 in acetonitrile with TEOA as the sacrificial electron donor and HBF_4 as proton source.

2.6 Photocatalysis in Pure Water

As mentioned in section 2.1, the development of an artificial system of full water splitting is a fundamental goal of research in this area, in order to possibly make a decisive contribution to environmentally friendly energy carrier production. To do this, such a system should work in pure water. Most of the researched photocatalytic systems for hydrogen evolution usually work either in pure organic solvents or in aqueous-organic solvent mixtures for reasons of solubility.[3,5,9] However, there are also examples that work in pure water.[45,68-70] In order to ensure the functionality of a system in water, all water-insoluble components must first be brought into solution in an aqueous environment. There are basically several options for this. One is, for example, to increase the hydrophilicity of the corresponding compound through synthetic changes or the addition of solubilising substituents. For instance, Wu *et al.* was able to ensure the solubility of a [FeFe]-hydrogenase biomimic in water by attaching a hydrophilic sulfonic acid group to its dithiolate bridge, as can be seen in **Fig. 11**.[68] Furthermore, the dentritic [FeFe] complex developed by Zheng, Yang and Li shows an example of a synthetically even more complex attachment of corresponding substituents.[34] This consisted of a [Fe_2(μ-$S_2$$(CO)_6$] complex, which was embedded by two attached Fréchet-type dendrons (see **Fig. 11**). In this specific example, the water solubility of the complex should not be guaranteed by the substituents used, but this would be entirely conceivable by slight changes in the dendrons used. In addition to the synthetic effort, which has become very clear in this example, this solubilisation method also has the disadvantage that the addition of substituents often also changes the electronic properties of the corresponding compounds, which are very important for the overall functionality of that systems.

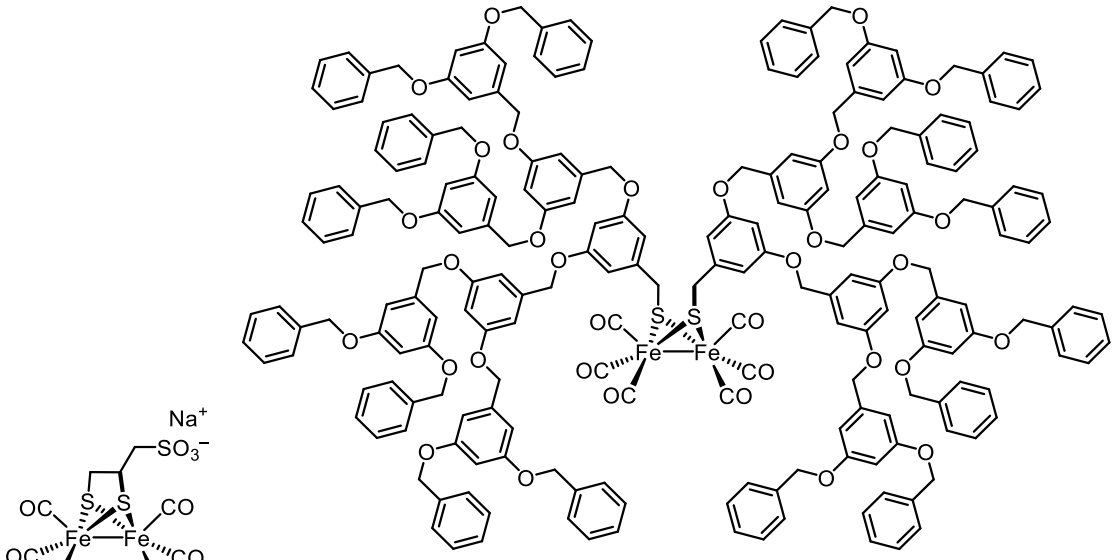

Fig. 11 Examples of the synthetic insertion of functional groups on [FeFe] complexes as an option to influence their solubility.

Another method consists of adding solubilising agents which either bring only the correspondingly insoluble components or the entire photocatalytic system into solution by appropriate action. These amphiphilic additives usually form soluble structures or entire networks by often supramolecular interactions with one another, in which the insoluble compounds can then be embedded. Thus, the corresponding compounds are not structurally changed themselves. In addition, either through suitable voids in the rigid structures or through the motile character of the supramolecular interactions between the additives, an exchange of substances from the interior of the cavities formed into the surrounding solution and *vice versa* is ensured. This is of crucial importance for the functioning of a photocatalytic system.

An example of the application of solubilising additives is the use of supramolecularly formed micelles in an aqueous environment. In 2010, Wu *et al.* were able to bring a photocatalytic system consisting of a rhenium photosensitiser, a [FeFe] catalyst and ascorbic acid into solution in pure water with the help of SDS micelles (see **Fig. 12**).[70] With this work they could show that hydrogen conversion is possible in such an environment, albeit on a very small scale. One advantage was that the production of the micelle solution was relatively simple. All that was needed was to bring the water-insoluble components into a DCM solution with a specific SDS concentration and then to evaporate the organic solvent. After the subsequent addition of water, the amphiphilic SDS molecules interacted with one another and formed micelles. Due to the hydrophobic effect, the water-insoluble components were included in the micelles. The

problem with this solubilising agent used, however, was its relatively low loading capacity in the range of 10^{-3} M to 10^{-5} M, which was also very molecularly selective.[70]

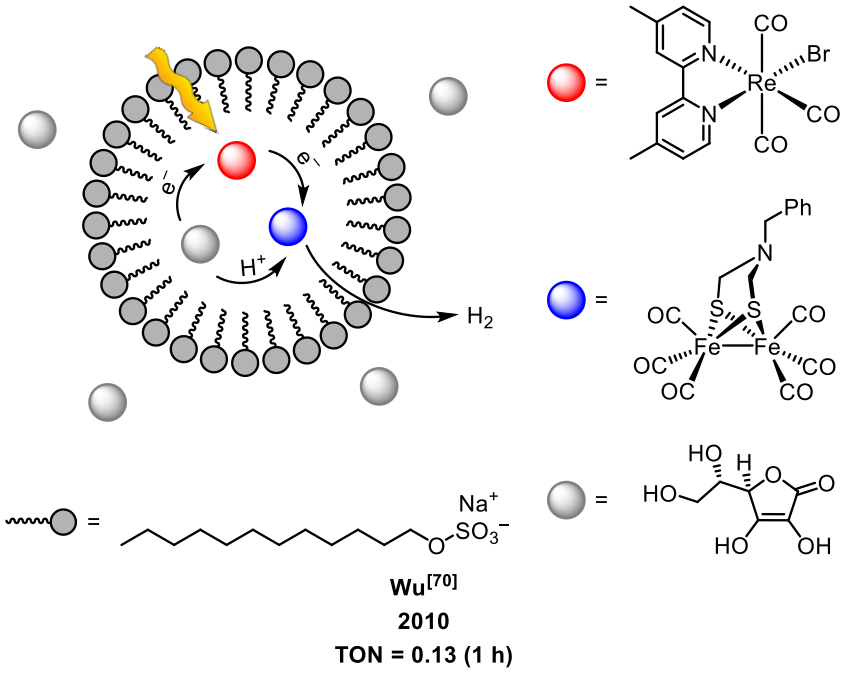

Fig. 12 Solubilisation of a photocatalytic system in water by SDS micelles.

Sun and Wang took a different approach in 2012. They used an oligosaccharide consisting of cyclodextrin to solubilise a system consisting of a xanthene dye photosensitiser, a [FeFe] catalyst and TEA in water (see **Fig. 13**).[71] The oligosaccharide had a pronounced hydrophobic cavity which, through special host-guest interactions, was able to include the corresponding substances. The photocatalytic components used in this study were specially equipped with hydrophilic substituents beforehand in order to be able to make a direct comparison between the system integrated in cyclodextrin and the system that was freely soluble in water. Surprisingly, the cyclodextrin system showed a significantly higher catalytic productivity than the free system. It was thus possible to show that solubilisation can have a positive effect on the stability of the components used.[71] In 2013, Cohen and Ott integrated a [FeFe] complex into a metal-organic framework (MOF) and were able to show that this exhibits photocatalytic activity in an aqueous solution containing a ruthenium photosensitiser and ascorbic acid.[72] Strictly speaking, this is not an example of the use of a solubilising additive. Nevertheless, the MOF also enables the water-insoluble catalyst to be solubilised by integrating the [FeFe] complex. Even if this is an extremely complex synthetic method compared to the other examples. In 2014 Yu and Li were able to show that a molecular sieve can also serve as a solubilising additive. Accordingly, they were able to immobilise a [FeFe] complex in a K^+-exchanged molecular sieve by simply adding the molecular sieve to a hexane solution of the catalyst.[69] Together with an iridium photosensitiser and TEA in water, a photocatalytic system could be formed and hydrogen generated under light irradiation.

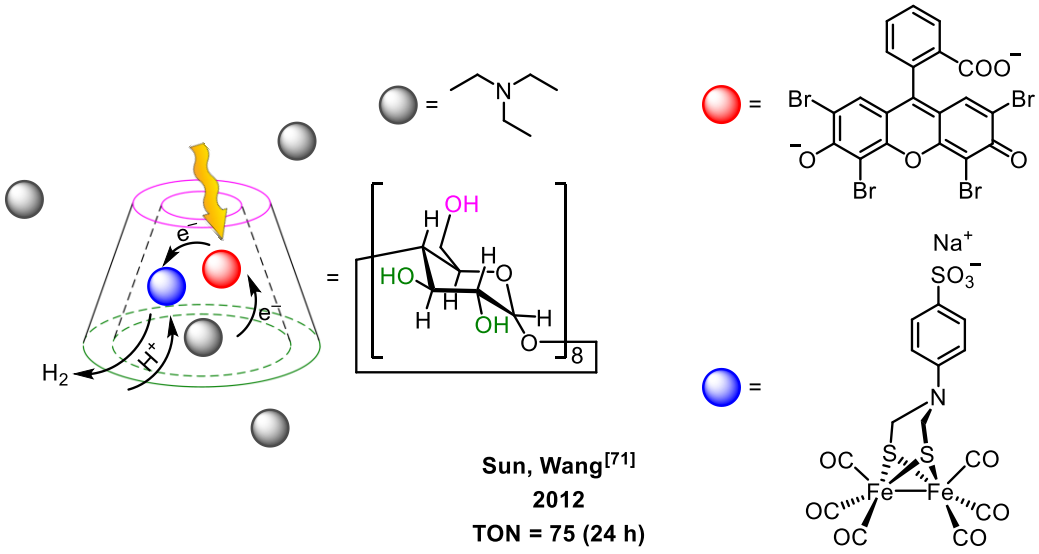

Fig. 13 Solubilisation of a photocatalytic system in water by a cyclodextrin cavity.

Polymers can also be used as a solubilising additive. Luxenhofer *et al.* developed a poly(2-oxalzoline) substance which, like SDS, can form micelles in water.[73-75] In order to establish the amphiphilicity of the corresponding polymer, short-chain methoxy side groups for the hydrophilic and long-chain butoxy side groups for the lipophilic properties were added to the corresponding amide binding sites on the polymer backbone (see **Fig. 14**). The decisive advantage of polymer micelles over, for example, simple SDS micelles, is that the properties of the polymer can be influenced by the synthesis of the corresponding monomers and the polymerisation of the entire compound. Through block polymerisation, hydrophilic and lipophilic blocks can be created in the polymer chain in a targeted manner, which are crucial for micelle formation, since the hydrophilic blocks are to be found in the outer areas of the micelle and the lipophilic blocks in the inner areas. Thus, not only the amphiphilic character of the entire polymer can be fine-tuned, but also the properties of the later micelles in aqueous solution and the conditions required for their formation. The methoxy- and butoxy-functionalised poly(2-oxazoline) block copolymers, mentioned above, show comparatively low critical micelle formation concentrations (between 100 mg l^{-1} and 6 mg l^{-1}) and low critical solution temperatures, which makes their utilisation in possible applications much easier.[74] In addition, the micelles formed from them show an excellent charge capacity of up to 50 wt-%.[75] This enables them for the solubilisation of entire complex systems. So far, poly(2-oxazolines) have only been used in the area of drug delivery.[74-77] However, in the course of a cooperation between the Lambert group and the Luxenhofer group, water-insoluble organometallic complexes together with organic compounds could easily be brought into solution with the help of this polymer in unpublished preliminary studies. The polarity of the micellar inner cavity is roughly comparable to that of acetonitrile. Thus, poly(2-oxazoline) micelles offer a further promising possibility to operate water-insoluble photocatalytic systems in water.

3 AIM OF THE WORK

In this thesis, photocatalytic two-component and three-component systems based on [FeFe]-hydrogenase biomimics should be investigated with regard to their spectroscopic, electrochemical and electronic properties. In addition, also their photocatalytic performance regarding hydrogen generation and the photophysics during photocatalysis should be analysed. In preparation for the development of a corresponding dyad system, several different diiron catalysts were first screened in a study for their spectroscopic and electrochemical properties and their photocatalytic performance was compared with one another. The desired dyad systems were then developed from the top-performing system.

For the photocatalytic proton reduction in this preliminary study on various [FeFe] catalysts, it was intended that it should, if possible, take place in pure water, since such performing systems are comparably rare in literature and would contribute to the long-term goal of a full water splitting reaction in water. Additionally, the knowledge gained from this should then also be applied to the dyad systems. In the study, **$[Ru(bpy)_3]Cl_2$** was used as a water-soluble photosensitiser and ascorbic acid as the sacrificial electron donor. In combination with various [FeFe]-hydrogenase biomimics, this component combination could already be used very often successfully in photocatalytic systems in the past, which indicates the comparatively well-adjusted redox potentials of the individual components.[5,9] In order to bring the water-insoluble diiron catalysts into solution in an aqueous environment, the poly(2-oxazoline) polymer shown in **Fig. 14**, which was thankfully made available by the Luxenhofer group as part of a cooperation, was utilised as a polymeric micelle-forming agent. The easy-to-use film hydration method was used to solubilise the catalysts, in which the water-insoluble substance was first dissolved in DCM together with poly(2-oxazoline).[74] Then, a polymeric thin film was generated by evaporation of the solvent. After adding water, the corresponding solubilising micelle solution was finally formed.

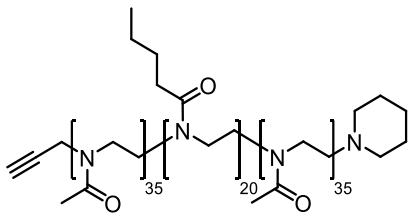

Propargyl-MeO_{x35}-*n*BuO_{x20}-MeO_{x35}-piperidine

Fig. 14 Poly(2-oxazoline) polymer used for solubilisation of water insoluble compounds in this work.

In order to investigate the influences of the different structural units of the [FeFe]-hydrogenase biomimics on their compound properties and also on the photocatalytic performance of the

corresponding systems, fourteen different [FeFe] complexes were synthesised and examined within the scope of the study. The corresponding diiron compounds are displayed in **Fig. 15**.

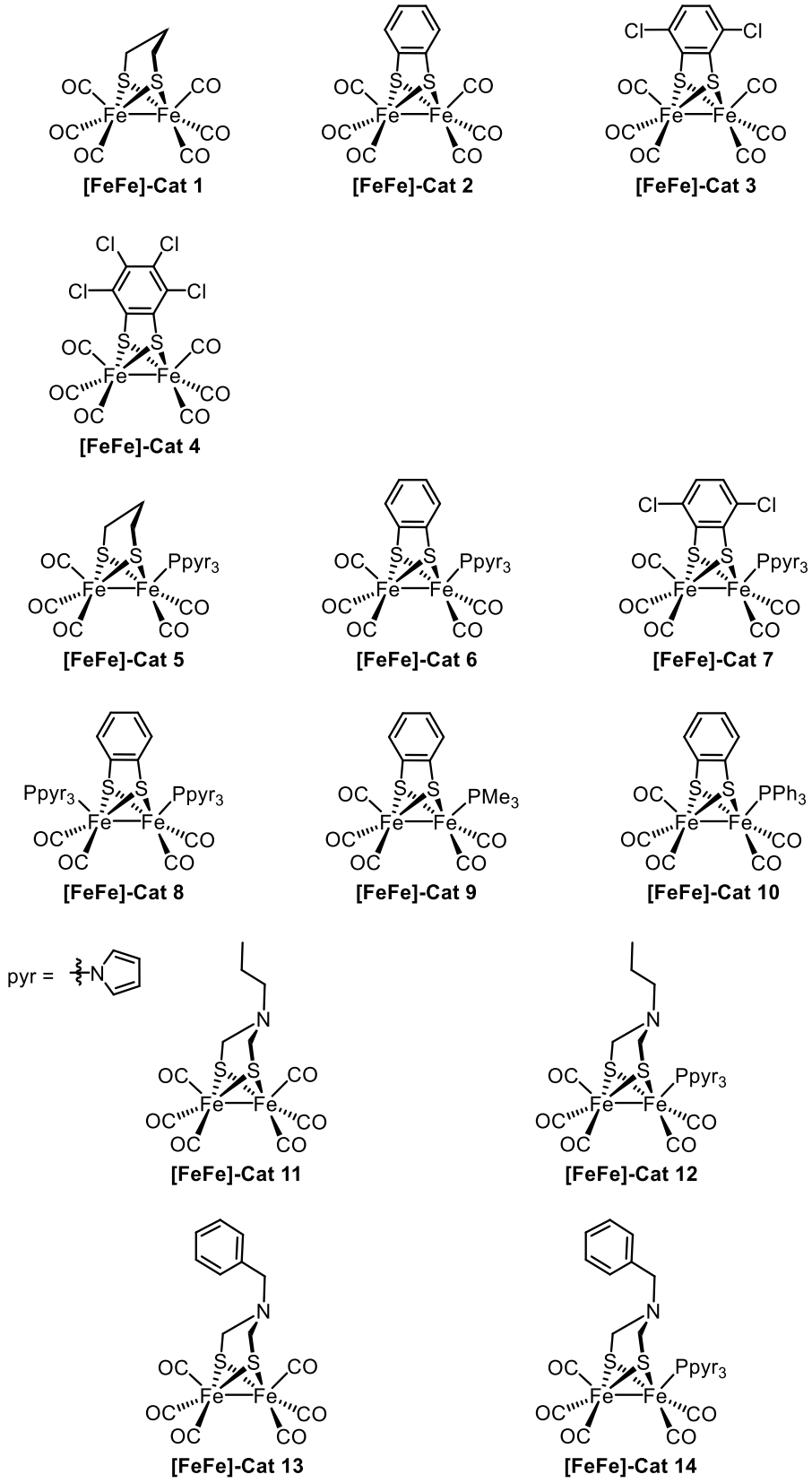

Fig. 15 Envisaged [FeFe] complexes for diiron hydrogenase biomimic studies.

From the compounds depicted it is apparent that in particular the dithiolate moiety and carbonyl or phosphine ligands of the [FeFe] complexes are varied in order to investigate the effects of their structural change on the electronic properties and possibly also on the photocatalytic output of the corresponding system. In addition to the simple propyldithiolate containing complex **[FeFe]-Cat 1**, the benzyldithiolate complex **[FeFe]-Cat 2**, the dichlorobenzyldithiolate complex **[FeFe]-Cat 3** and the tetrachlorobenzyldithiolate complex **[FeFe]-Cat 4** were compared with one another in order to obtain diiron compounds that have an increasingly electron-withdrawing dithiolate ligand. With **[FeFe]-Cat 11** and **[FeFe]-Cat 13** two azadithiolate containing compounds were also synthesised in order to check whether the additional contained nitrogen atom in the dithiolate ligand, as an internal acid/base, has a positive effect on the photocatalytic performance. Furthermore, all diiron complexes mentioned were also equipped with a $Ppyr_3$ ligand. In the case of the benzyldithiolate containing complex, compounds with a PMe_3 and a PPh_3 ligand were also synthesised in order to investigate the effects of the corresponding phosphine ligands on the material properties and the photocatalysis.

As mentioned above, a photocatalytic dyad should be developed and synthesised from the top-performing system of the diiron compound study by covalently linking the corresponding catalyst with the ruthenium photosensitiser. The aim was to build on the bioinspired photocatalytic dyad constructed by Sun and Åkermark in 2003 (see **Fig. 16**), since it comprises two π-conjugation blockers in form of an amide and an ester bond.[56] These are intended to hamper a too strong electronic coupling between the photosensitiser and the catalyst moiety within the dyad and thus prevent any possible electron back transfer. In order to investigate the influence of the bridge or the distance between the two dyad constituents on the material and system properties, an extended dyad was additionally produced that uses a biphenyl unit instead of a benzyl ring as the corresponding spacer unit (see **Fig. 16**). In addition to these dyads, the associated single components should also be synthesised in order to form the corresponding 3CS. In this way it should be possible to examine the dyad containing 2CS with the associated 3CS not only with regard to their spectroscopic and electrochemical properties, but also to be able to directly compare their photocatalytic performance. In addition, the thermodynamic and kinetic properties of the corresponding systems and, in particular, the type of quenching mechanisms that take place should be investigated. With this knowledge, the observations made by Sun *et al.* with regard to the performance of photocatalytic dyad systems in direct comparison with their bimolecular multicomponent systems can possibly be evaluated.[9] Time-resolved spectroscopic investigations should also provide further information on the photophysics of the photocatalysis in these systems and the influence of the dyadic bridging unit on the overall process.

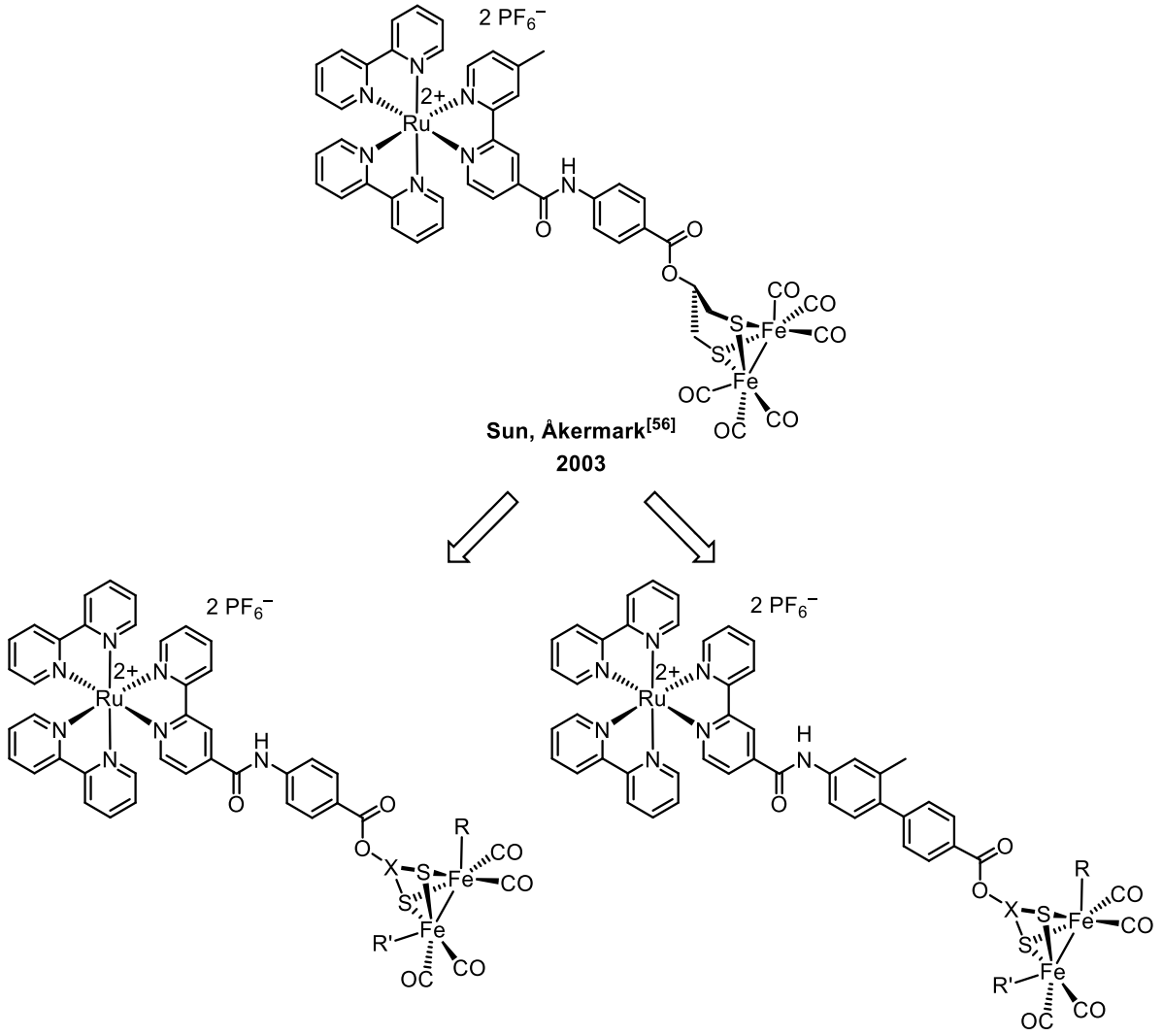

Fig. 16 Envisaged photocatalytic dyads, which are based on the work published by Sun and Åkermark in 2003.[56] The structure of the dithiolate ligand (marked as X) as well as of the iron ligands R and R' depends on the results of the preceding diiron hydrogenase biomimic studies.

4 DIIRON HYDROGENASE BIOMIMIC STUDIES

The following study will investigate the catalytic performance of [FeFe]-hydrogenase biomimics for generating hydrogen, embedded in a photocatalytic system in pure water. Because of their insolubility in water, they should be solubilised in aqueous solution using poly(2-oxazoline) (see **Fig. 14**). Although numerous [FeFe] complex containing multicomponent systems have been investigated in the past, these have generally been studied in organic solvents or aqueous-organic mixtures.[5,9] On the other hand, relatively little is known about systems in pure water that work with the help of solubilisers. For this reason and in preparation for the subsequent investigation of photocatalytic dyad systems in pure water, several [FeFe] complexes were synthesised in the following and characterised both spectroscopically and electrochemically. In order to determine whether the resulting findings also have an impact on the photocatalytic performance of the corresponding systems in the aqueous micelle environment, the corresponding [FeFe] catalysts with **$[Ru(bpy)_3]Cl_2$** as photosensitiser and ascorbic acid as sacrificial electron donor were then examined for their performance under photocatalytic conditions.

To determine possible structure-property relationships, two structural units of the [FeFe] complexes were varied in the study. In addition to different dithiolate bridges, each with different electronic properties, various phosphine ligands were also attached to the diiron complexes. Various influences of such structural changes on the electronic properties of such [FeFe] complexes are already known from the literature.[39] However, since the photocatalytic performance of multicomponent systems depends on a large number of influences, it is essential for the characterisation of such systems to test them under the above-mentioned photocatalytic conditions.[3,9] Only in this way conclusions can be drawn from the structural change in the catalysts used to a changed performance of the system. Last but not least, these findings should also be used for the development of a functioning dyad system, so the top-performing system in this study should also form the basis for a corresponding dyad.

4.1 Synthesis

As described above, a series of different diiron hydrogenase mimics (see **Fig. 15**) was synthesised in order to get a deeper understanding of the influence of the particular molecular building blocks on the photocatalytic performance. In particular, the photocatalytic productivity in systems with pure water as solvent in combination with the necessary use of a surfactant should be investigated. Considering the active site of the [FeFe]-hydrogenase and its simplest mimic **[FeFe]-Cat 1** (see **Fig. 15**), two major molecular building blocks are apparent. On the one hand, the dithiolate bridging unit, which is linked by the two sulphur atoms to the diiron

core and, on the other hand, the six carbonyl ligands. While modification at the carbonyl ligands is normally accompanied by an exchange with other ligand compounds, the dithiolate bridge opens the field for extensive modifications and the assembly of many different moieties to the catalyst. Since, these modifications usually come along with a change of the electronic properties of the whole compound, it was desired to analyse this impact on the basis of a series of compounds with different dithiolate bridges: going from the slight electron pushing propyldithiolate over the mesomeric stabilising benzenedithiolate to the strong electron-withdrawing 3,4,5,6-tetrachlorobenzene-1,2-dithiolate. In addition to that, diiron compounds with bioinspired azadithiolate ligands were also synthesised, for the reason that in literature this moiety is known as an indispensable component of the [FeFe]-hydrogenase enzyme and subserves as an internal acid/base with the task to transfer the protons from the surrounding solution to the diiron core. It should therefore also be investigated whether the azadithiolate ligand has a positive influence on the proton reduction mechanism and catalytic performance in the designated systems under the abovementioned conditions.

The synthesis of the desired [FeFe] complexes basically followed two different synthetic routes, as it is depicted in **Fig. 17**. Most of the abovementioned biomimics could be easily constructed by the well-known conversion of triiron dodecacarbonyl with the corresponding dithiol in boiling THF. The consequent formation of a $[Fe_2(\mu\text{-}S_2R)(CO)_6]$ species by the treatment of ironcarbonyl compounds with organothiols was already discovered in the beginning of the last century.[78-84] However, the exact mechanism of this formation is not entirely certain. Although, in the late 1970s and early 1980s first insights on that topic were made.[85,86] It was assumed that during the reaction first one thiol function binds to an active iron atom. For that purpose, a reactive "$Fe(CO)_4$" intermediate of whatever kind was postulated as the active species of $Fe_3(CO)_{12}$, which is formally a $Fe(CO)_4$-adduct. After that, two of the formed $RSFe(CO)_4$ species would build the $[Fe_2(\mu\text{-}S_2R)(CO_6)]$ product by a mutually attack of the sulphur atoms on the iron core of the corresponding reaction partner. Thereby, two molecules of CO would be released.[85] The fact that a three-core iron compound of the form $[Fe_3(\mu\text{-}S_2R)_2(CO)_7]$ was found as a side product of this conversion additionally supported in principle the CO displacement mechanism of the sulphur atoms.[86] Besides, the formation of this side product could be minimised by adjusting the stoichiometric ratio of the starting material. In this work, a ratio of 1.1 equivalents of the corresponding dithiol to 1.0 equivalents of $Fe_3(CO)_{12}$ was used for the most conversions. Compared with alternative syntheses starting from toxic compounds like iron pentacarbonyl, the advantages of this reaction are, beside a simple product separation by column chromatography, the comparatively harmless starting materials and the relatively high product yield. For the compounds synthesised in this work, the propyldithiolate and benzyldithiolate containing diiron complexes showed the highest yields. In the latter case, a yield of 91 % could be achieved, which perhaps could be ascribed

to a favoured steric pre-configuration and the hence spatial proximity of the sulphur atoms at the benzene ring. In the literature known synthesis of **[FeFe]-Cat 2** by Ott *et al.* only 57 % yield could be achieved.[87] In the otherwise analogous synthesis, the starting materials were used in a less favourable equimolar ratio, which probably led to the lower yield. The formation of **[FeFe]-Cat 1** gave a yield of 76 %. Seyferth *et al.* were able to achieve for the same synthesis a comparable yield of 78 %.[88] However, the conversions of the chlorine-substituted benzyldithiolate containing complexes gave a different picture. Here, yields of only 21 % for **[FeFe]-Cat 3** respectively 14 % for **[FeFe]-Cat 4** could be accomplished (see **Fig. 17a**).

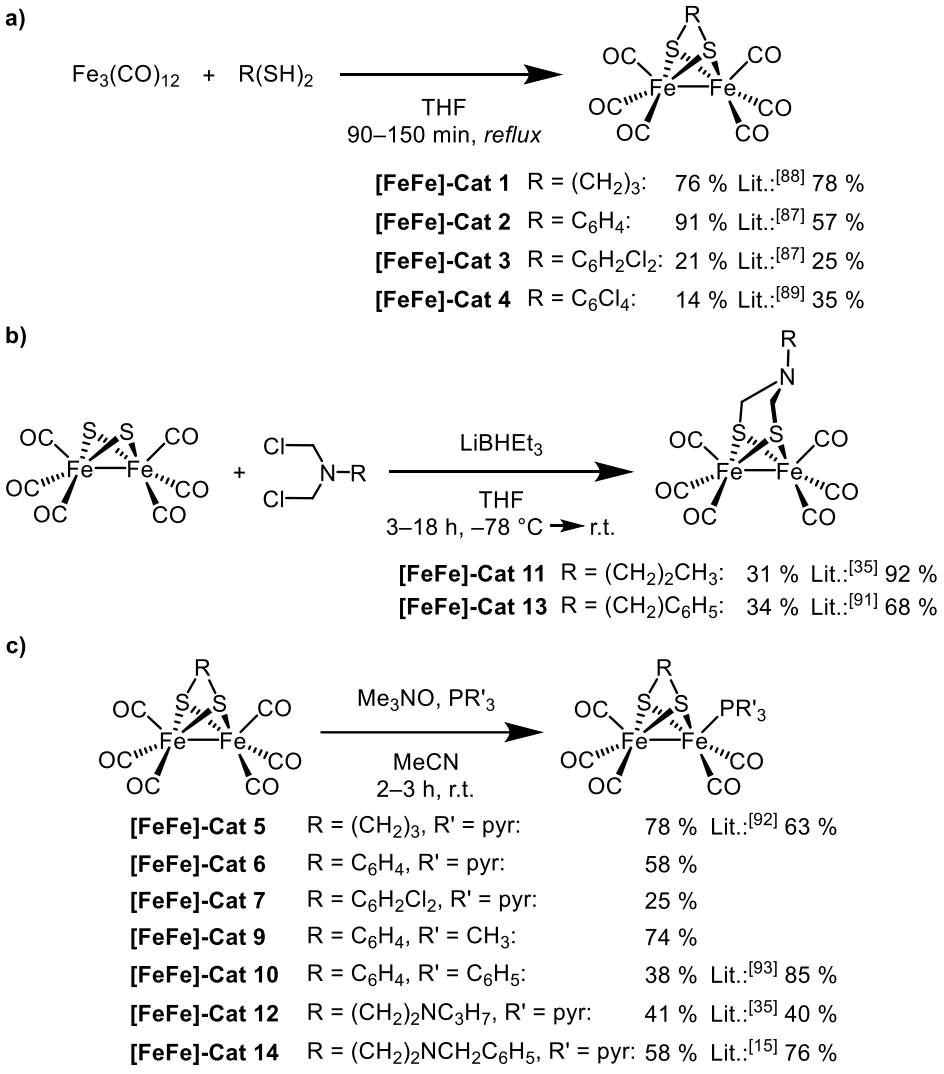

Fig. 17 a) Synthesis of propyldithiolate and benzyldithiolate containing [FeFe]-hydrogenase biomimics in this work by the reaction of $Fe_3(CO)_{12}$ with the corresponding dithiol in THF. **b)** Synthesis of the azadithiolate bridged [FeFe]-hydrogenase biomimics by reaction of **$[Fe_2(\mu\text{-}S_2)(CO)_6]$** with $LiBHEt_3$ and the corresponding *N*,*N*-bis(chloromethyl)alkyl amine. **c)** Ligand exchange reaction of a [FeFe] complex with trimethylamine *N*-oxide and the corresponding phosphine.

It seems that the electron-withdrawing effect of the chlorine substituents within the benzyldithiolate bridge had a significant negative influence on the nucleophilic attack of the sulphur atoms during the reaction. The quantity of the involved chlorine atoms accordingly had

the effect that the reaction of the fourfold chlorinated benzyldithiolate compound gave the lowest yield. Accordingly, the literature known synthesis of **[FeFe]-Cat 3** by Ott *et al.*, which again differs only in the equimolar ratio of the starting materials, gave a comparably low yield of 25 %.[87] In contrast, Felton *et al.* were able to achieve in their synthesis of **[FeFe]-Cat 4** a significantly higher yield of 35 %. Although they used the supposedly less favourable equimolar ratio of the starting material, too.[89]

As described above, not all the desired [FeFe]-hydrogenase mimics were approachable *via* the reaction of $Fe_3(CO)_{12}$ with the corresponding dithiol. For the complexes with an azadithiolate bridging unit, this route did not work due to a deficient synthesis of the azadithiols from *N*,*N*-bis(chloromethyl)alkyl amines. Additionally, the subsequently conversions of the azadithiols with $Fe_3(CO)_{12}$ yielded not the desired [FeFe] complexes. Instead, an approach in which first the sulphur atoms were enclosed directly at the diiron core and then followed by the build-up of the azadithiolate bridging unit was pursued. Therefore, first **$[Fe_2(\mu\text{-}S_2)(CO)_6]$** was synthesised by the literature known reaction of iron pentacarbonyl with sulphur in a methanol potash lye mixture.[90] The yield of this reaction was with 43 % barely satisfying, but represents a clear improvement over the literature yield of only 10 %. In addition to the toxicity of $Fe(CO)_5$ as the starting material, the relatively poor output constitutes the disadvantage of this synthetic route in comparison with the abovementioned syntheses. In the further course, the azadithiolate [FeFe] complex was constructed by a nucleophilic attack of the *in situ* with lithium triethylborohydride reduced **$[Fe_2(\mu\text{-}S_2)(CO)_6]$** on the corresponding *N*,*N*-bis(chloromethyl)alkyl amine (see **Fig. 17b**). The moderate yields of this conversion with 31 % for **[FeFe]-Cat 11** and 34 % for **[FeFe]-Cat 13** could be probably explained by the electron-donating effect of the amino function in the *N*,*N*-bis(chloromethyl)alkyl amines and the therefore reduced electrophilicity of these reactants. However, in the corresponding literature known reactions of **[FeFe]-Cat 11** and **[FeFe]-Cat 13** by Yang and Li, or Ott and Lomoth significantly higher yields of 92% and 68% could be achieved.[35,91] During the syntheses of both complexes in this work, the actual conversions proceeded almost quantitatively, which could be determined by means of TLC controls. The low yields thus resulted from the work-up steps for the respective crude products. Here both complexes were found to be relatively temperature and moisture sensitive. Despite adapting the corresponding work steps and intermittent cooling, major yield losses could not be prevented at this point. The *N*,*N*-bis(chloromethyl)alkyl amines for the reactions, namely ***N*,*N*-bis(chloromethyl)propan-1-amine** and ***N*,*N*-bis(chloromethyl)benzene-methanamine** were accessible *via* the conversion of propan-1-amine or phenylmethanamine with paraformaldehyde in DCM to form the corresponding (alkylimino)dimethanol intermediate, which was then chlorinated by addition of thionyl chloride.[33]

In addition to the abovementioned investigation on the influence of different dithiolate ligands on the catalytic performance, it was also an aim of this work to examine the impact of an exchanged carbonyl ligand sphere. Namely, a substitution of one carbonyl ligand with a phosphine ligand was envisaged. In literature it could be shown that especially a substitution with a phosphine ligand with its relatively strong electron-donating ability induced an increase of the electron density at the iron core, which has in principle a positive effect on the protophilicity of the [FeFe] catalyst and with that supports the apposition of protons during the catalysis mechanism.[9] Still, the altered electron density has also an impact on the reduction potential, which is obviously a crucial factor for the overall redox process. To investigate this phosphine impact, it was decided to synthesise different [FeFe] complexes containing the more common PMe_3 and PPh_3, and also $Ppyr_3$ as ligand and additionally to vary the quantity of the inserted ligands. The ligand exchange reaction used for this purpose is a fairly simple and straightforward method. It is based on the literature known synthesis of **[FeFe]-Cat 14** by Sun and Åkermark and has been adapted with regard to the molar ratios of the starting materials and the reaction time.[15] In the first step of this phosphination the corresponding [FeFe] complex was mixed with trimethylamine *N*-oxide in acetonitrile in order to initiate a decarbonylation. In contrast to the equimolar ratio in the literature, a slight excess of 1.2 equivalents of the decarbonylating agent was used for the syntheses in this work. As a result of the CO dissociation, the now accessible coordination position at the iron core quickly gets occupied by an acetonitrile molecule due to the binding character of the solvent. According to the literature, an equivalent of the corresponding phosphine was then added, as a result of which the weakly bound solvent molecule was substituted by a nucleophilic attack. Noteworthy, this reaction needs a preferably complete exclusion of oxygen and moisture due to the oxophilicity of the phosphine compounds.

As displayed in **Fig. 17c**, the product yields exhibited a quite big range depending on the dithiolate bridge as well as on the ligands of the introduced phosphine. The propyldithiolate and pyrrolyl phosphine containing complex **[FeFe]-Cat 5** could be prepared in 78 % yield. Its literature known synthesis by Hou and Peng was only able to achieve a yield of 63 %.[92] This is presumably due to the fact that in their procedure the *in situ* decarbonylation by trimethylamine *N*-oxide was omitted and instead the [FeFe] complex was reacted directly with $Ppyr_3$. In contrast, **[FeFe]-Cat 10** could only be synthesised with a 38 % yield. Chiang *et al.* were able to produce this compound in 85 % yield.[93] They used DCM instead of acetonitrile as solvent and extended the reaction time of the initial decarbonylation to one hour. The azadithiolate containing complex **[FeFe]-Cat 12** could also be synthesised with a similarly low yield of 41 %, but thus confirmed the literature value of 40 % by Yang and Li for their synthesis of this compound.[35] **[FeFe]-Cat 14** could be produced with a yield of 58 %. Sun and Åkermark achieved a yield of 76 % in their synthesis of the [FeFe] complex, but used an equimolar

amount of trimethylamine *N*-oxide and allowed the reaction mixture to react for twice as long, as mentioned above.[15] The literature unknown substances **[FeFe]-Cat 6**, **[FeFe]-Cat 7** and **[FeFe]-Cat 9** could be synthesised with a yield of 58 %, 25 % and 74 %, respectively. Generally, the complexes with a larger bridging unit, like the dichlorobenzyldithiolate or the azadithiolate ligands, showed a lower yield probably due to the increased steric hindrance. This factor should get even more pronounced with a sterically more demanding phosphine. Still, the electronic properties of these nucleophilic compounds also play an important role, as can be seen in the formation of **[FeFe]-Cat 6** compared with that of **[FeFe]-Cat 9**. While the methyl phosphine substituents support the nucleophilicity of the reactant, the pyrrolyl side groups, as somewhat weaker electron-donating substituents, show at least a lower tendency of assistance, which condensed in a lower product yield. In the case of the phenyl phosphine substituents also both factors come into play, due to the slight electron-withdrawing effect of the aromatic phosphine side groups and their steric hindrance. Whereby, the latter presumably tipped the balance to the lowest output of 38 % in the direct comparison of the different phosphine ligands. Finally, by simply treating the onefold $Ppyr_3$-substituted benzyldithiolate complex **[FeFe]-Cat 6** with $Ppyr_3$, the doubly substituted and literature unknown complex **[FeFe]-Cat 8** could be obtained in 20 % yield.

4.2 Steady-State Absorption Spectroscopy

Absorption spectra of the synthesised diiron compounds (see **Fig. 15**) were recorded in DCM solution (ca. $5 \cdot 10^{-5}$ M) at 298 K. To get a better overview, the following study is divided in three parts, whereas in the first one the spectroscopic aspects of **[FeFe]-Cat 1**, **[FeFe]-Cat 2**, **[FeFe]-Cat 3**, **[FeFe]-Cat 4**, **[FeFe]-Cat 5**, **[FeFe]-Cat 6** and **[FeFe]-Cat 7** are discussed and compared to apprehend the influence of the different dithiolate and the $Ppyr_3$ phosphine ligands on the energetic properties. Then, the absorption spectra of **[FeFe]-Cat 8**, **[FeFe]-Cat 9** and **[FeFe]-Cat 10** are investigated to observe the impact of the different phosphine ligands. Finally, the absorption spectra of the azadithiolate containing compounds **[FeFe]-Cat 11**, **[FeFe]-Cat 12**, **[FeFe]-Cat 13** and **[FeFe]-Cat 14** are surveyed.

As it is depicted in **Fig. 18**, the absorption spectrum of **[FeFe]-Cat 1**, as a typical example of such a diiron biomimetic compound, shows a dominant signal at 30400 cm^{-1} (329 nm) and a weak low-energy absorption ranging in the visible region from 17500 cm^{-1} (571 nm) to 25000 cm^{-1} (400 nm). With the help of spin-restricted DFT calculations, Fiedler and Brunold could show that the first, dominant absorption band can be assigned to an electronic transition from the so-called Fe(σ) molecular orbital to the antibonding Fe(σ^*) molecular orbital.[94] The weak, low-energy absorption band, on the other hand, can be ascribed to the transition from the Fe(t_{2g}) to the Fe(σ^*) molecular orbital.[94] For a better overview, the corresponding MO

diagram of **[FeFe]-Cat 1** is shown in **Fig. 19a**. The MO labelling refers to the corresponding principal contributing atom. At this point it must be pointed out that despite the larger energetic distance between the participating molecular orbitals, the Fe(t_{2g})-Fe(σ^*) transition appears at lower energy than the Fe(σ)-Fe(σ^*) transition in the absorption spectrum of **[FeFe]-Cat 1** due to electronic relaxation in the excited state.[94]

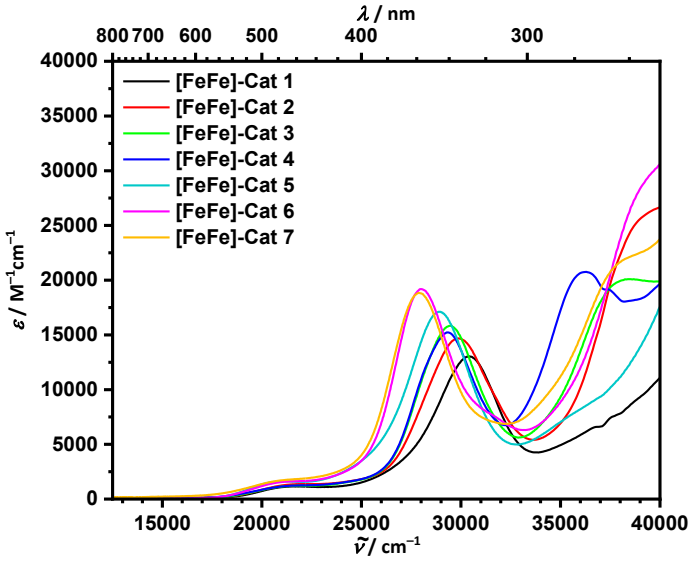

Fig. 18 UV/Vis absorption spectra of **[FeFe]-Cat 1**, **[FeFe]-Cat 2**, **[FeFe]-Cat 3**, **[FeFe]-Cat 4**, **[FeFe]-Cat 5**, **[FeFe]-Cat 6** and **[FeFe]-Cat 7** measured in DCM at 298 K.

In comparison with **[FeFe]-Cat 1**, the absorption spectrum of **[FeFe]-Cat 2** shows an additional and intense high-energy extinction at 40000 cm^{-1} (250 nm), which obviously belongs to the benzene-centred π-π^* excitation of the altered dithiolate ligand. Furthermore, the Fe(σ)-Fe(σ^*) transition at 29900 cm^{-1} (334 nm) exhibits a bathochromic shift of 500 cm^{-1} (5 nm) and a slightly higher molar extinction coefficient, which speaks for a change of the electronic properties at the iron core as a consequence of the varied dithiolate ligand. More precisely, the slight electron-withdrawing effect of the benzene ring should cause a lowered electron density at the sulphur atoms, which in turn induces a change in the electronic structure of the directly adjacent iron-centred orbitals. Noteworthy, the weak Fe(t_{2g})-Fe(σ^*) transition offers no significant difference, which presumably indicates an effect on mainly the Fe(σ) orbital. With two or four chlorine atoms on the benzene dithiolate ligand, **[FeFe]-Cat 3** and **[FeFe]-Cat 4** have an even stronger electron-withdrawing effect on the iron core. Therefore, the absorption spectrum of **[FeFe]-Cat 3** exposes for the Fe(σ)-Fe(σ^*) excitation at 29500 cm^{-1} (339 nm) an additional bathochromic shift of 400 cm^{-1} (5 nm) and a somewhat higher extinction coefficient in comparison with **[FeFe]-Cat 2**. In addition, the π-π^* transition at 38400 cm^{-1} (260 nm) also shows a bathochromic shift and a decrease in intensity as a result of the differed electronic character within the benzene ring. Surprisingly, the spectrum of **[FeFe]-Cat 4** does not differ

much from that of **[FeFe]-Cat 3** concerning the iron-centred transitions. Obviously, the additional two chlorine atoms do not have such a big effect on the electron-withdrawal of the dithiolate ligand. However, they do influence the benzene-centred π-π^* transition at 36200 cm^{-1} (276 nm), which experienced a quite distinct bathochromic shift of 2200 cm^{-1} (16 nm).

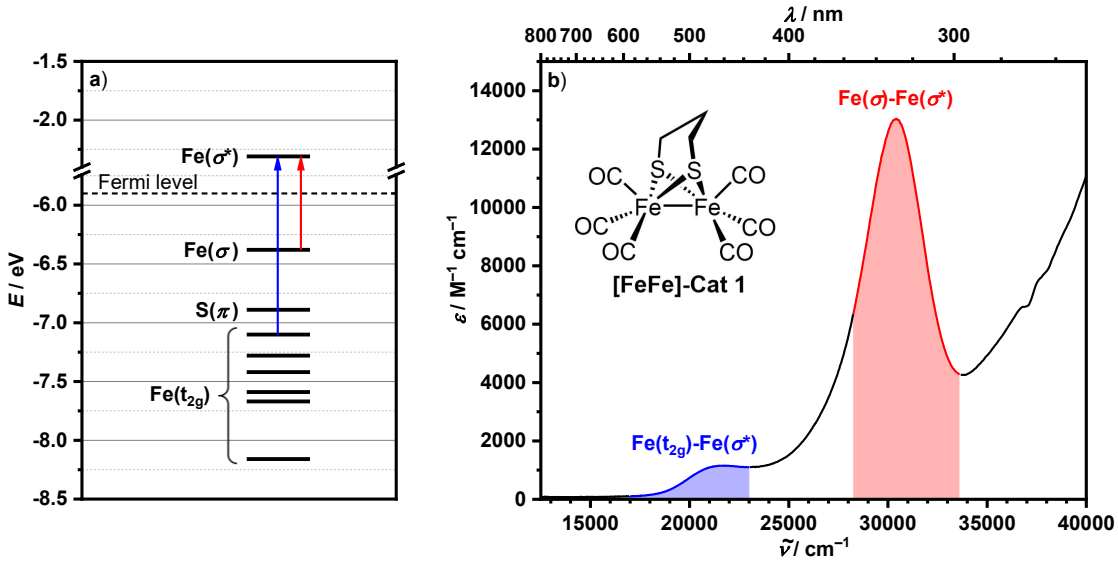

Fig. 19 a) Excerpt from the MO diagram of **[FeFe]-Cat 1** obtained from spin-restricted DFT calculations by Fiedler and Brunold.[94] The MO labelling refers to the corresponding principal contributing atom. The Fe(t_{2g})-Fe(σ^*) transition is marked with a blue and the Fe(σ)-Fe(σ^*) transition with a red arrow. **b)** UV/Vis absorption spectrum of **[FeFe]-Cat 1** measured in DCM at 298 K. The aforementioned electronic transitions are marked with the appropriate colours. Due to electronic relaxation in the excited state, the Fe(t_{2g})-Fe(σ^*) transition appears in the absorption spectrum at lower energy than the Fe(σ)-Fe(σ^*) transition.[94]

The exchange of one CO ligand by a phosphine reveals an even more intense influence on the electronic character of the diiron compound as the absorption spectrum of **[FeFe]-Cat 5** illustrates in **Fig. 18**. In comparison with the all-CO compound **[FeFe]-Cat 1** the dominant iron-centred Fe(σ)-Fe(σ^*) excitation exhibits a distinct bathochromic shift of 1500 cm^{-1} (17 nm) to 28900 cm^{-1} (346 nm). Here the influence of the phosphine ligand as a relative strong σ-donor and π-acceptor ligand is visible. Depending on the nature of their inner substituents, the phosphines are in relation to the carbonyl ligand slightly weaker π-acceptors.[40] Nevertheless, with less electron-donating substituents the π-acidity of the phosphines gets strengthened as a result of the lower σ^* antibonding orbitals within the ligand compounds.[41] For that reason the pyrrole substituents of the utilised $Ppyr_3$ phosphine should afford the latter to still react as a relatively good π-acceptor. Although, the ligand exchange does influence the electronic properties of the iron core, as the spectral shift indicates. It seems that the higher electron density at the iron atoms caused by the lower π-acidity of the phosphine destabilises the Fe(σ) orbital and therefore induces the distinct bathochromic shift in the absorption spectrum.

Meanwhile, also the weaker Fe(t_{2g})-Fe(σ^*) transition is obviously affected by this, indicated by a somewhat wider range into the low-energy spectral region. Nevertheless, this effect turns out not as intensely as for the preceding iron-centred absorption. The abovementioned influences of the benzene dithiolate and dichlorobenzene dithiolate ligands also come into play here in the spectra of **[FeFe]-Cat 6** and **[FeFe]-Cat 7**. Both compounds show very similar absorptions and exhibits with the Fe(σ)-Fe(σ^*) transition at 28000 cm^{-1} (357 nm) for **[FeFe]-Cat 6** or 27900 cm^{-1} (358 nm) for **[FeFe]-Cat 7** the energetically lowest lying signals in this series of diiron complexes. As it was the case for the all-CO compound **[FeFe]-Cat 3**, the benzene-centred π-π^* transition of the chlorinated complex **[FeFe]-Cat 7** at 38000 cm^{-1} (263 nm) experienced a decrease in intensity and a slight bathochromic shift compared to **[FeFe]-Cat 6**.

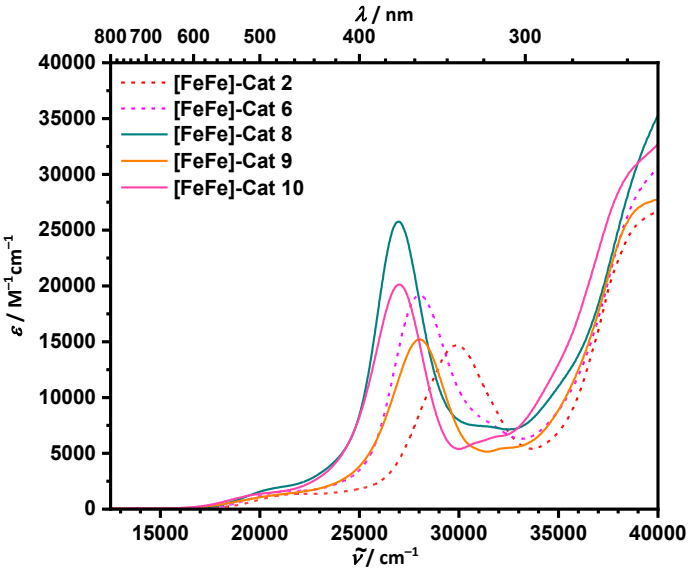

Fig. 20 UV/Vis absorption spectra of **[FeFe]-Cat 8**, **[FeFe]-Cat 9** and **[FeFe]-Cat 10** measured in DCM at 298 K. For comparison, the absorption spectra of **[FeFe]-Cat 2** and **[FeFe]-Cat 6** measured in DCM at 298 K are given in dotted lines.

The impact of different kinds and numbers of phosphine ligands on the spectral absorption features of the corresponding diiron complexes are illustrated in **Fig. 20**. **[FeFe]-Cat 8** with its two $Ppyr_3$ ligands shows in comparison with the mono-phosphinated **[FeFe]-Cat 6** an intense red-shifted and dominant iron-centred Fe(σ)-Fe(σ^*) transition at 27000 cm^{-1} (370 nm) and a more intense benzene-based π-π^* transition presumable right beyond the edge of the measuring window at 40000 cm^{-1} (250 nm). The red shift of the central iron-based extinction is at that point 1000 cm^{-1} (13 nm) and 2900 cm^{-1} (36 nm) compared with the all-CO compound **[FeFe]-Cat 2**, which again underlines on the one hand the previously discussed weaker π-acidity and therefore more electron-donating effect of the $Ppyr_3$ ligand and, on the other hand, its additivity. Although, the impact of the second phosphine ligand turned out less forcefully. Interestingly, **[FeFe]-Cat 8** shows a slight higher extinctions coefficient for the weak Fe(t_{2g})-

Fe(σ*) transition, which is at the same time somewhat elongated in the low-energy direction. The absorption spectrum of **[FeFe]-Cat 9** displays the typical Fe(σ)-Fe(σ*) absorption at 28000 cm^{-1} (357 nm) and the π-π* transition of the benzenedithiolate ligand as a shoulder signal at 39300 cm^{-1} (254 nm). In comparison with the $Ppyr_3$ substituted **[FeFe]-Cat 6**, the decrease of intensity for both features is mainly apparent. However, the absence of spectral shifts is a little bit unexpected because of the predicted lower π-acidity of the alkyl substituted PMe_3 phosphine compared with $Ppyr_3$ and the therefore expected bathochromic shift of the Fe(σ)-Fe(σ*) transition in the absorption spectrum. The PPh_3 phosphinated **[FeFe]-Cat 10** exhibits the dominant Fe(σ)-Fe(σ*) absorption at 27000 cm^{-1} (370 nm), which is the same as for **[FeFe]-Cat 8**, and the π-π* transition at a shoulder signal at 28600 cm^{-1} (350 nm), so red-shifted compared with $Ppyr_3$ substituted **[FeFe]-Cat 6**. Obviously, one phenyl substituted phosphine ligand has a comparable impact on the iron-centred spectroscopic features than two $Ppyr_3$ ligands. This is probably a result of the sterically demanding phenyl ligands, which cause, despite their weak electron-withdrawing effect, a weakening of the π-acidity due to an unfavourable phosphine geometry.[40]

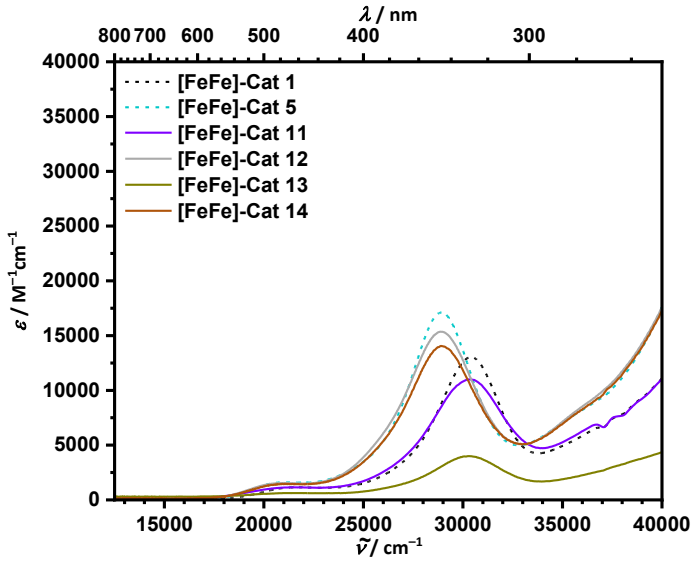

Fig. 21 UV/Vis absorption spectra of **[FeFe]-Cat 11**, **[FeFe]-Cat 12**, **[FeFe]-Cat 13** and **[FeFe]-Cat 14** measured in DCM at 298 K. For comparison, the absorption spectra of **[FeFe]-Cat 1** and **[FeFe]-Cat 5** measured in DCM at 298 K are given in dotted lines.

The absorption spectra of the azadithiolate containing [FeFe] complexes are illustrated in **Fig. 21**. At the first glance there are no significant spectral differences between **[FeFe]-Cat 11** and **[FeFe]-Cat 1**, which can be attributed as the corresponding diiron complex with no containing tertiary amino function. The only difference is the smaller extinction coefficient of the central Fe(σ)-Fe(σ*) absorption. The same picture is emerging by looking at the $Ppyr_3$ substituted complex **[FeFe]-Cat 12** in comparison with the corresponding compound **[FeFe]-Cat 5**. The same is true for the benzyl substituted **[FeFe]-Cat 13** and **[FeFe]-Cat 14**, whereas the

tremendous intensity decrease of the former is traceable to the comparably poor solubility of the compound in DCM. In order to achieve a better comparability with the previous measurements, this solvent was nevertheless used for this complex. However, by reference to the lower extinction coefficient of **[FeFe]-Cat 14** compared to **[FeFe]-Cat 12** the basic tendency of an additional extinction decrease of these benzyl substituted azadithiolate [FeFe] complexes is visible. Apparently, the inserted amino function does not influence the energetic character of the complexes at all, but shrinks the extinction of the iron-centred Fe(σ)-Fe(σ^*) transition.

In summary, the investigation of the absorption spectroscopy of the different [FeFe] complexes illustrated in **Fig. 15** demonstrated the influence of the dithiolate bridging unit as well as of a phosphine ligand on the electronic properties especially at the iron core of the catalysts. With increasing electron-withdrawing character of the dithiolate ligand, the central Fe(σ)-Fe(σ^*) transition gets more red-shifted, which presumably could be attributed to a decrease of electron density at the sulphur atoms and a therefore destabilising effect on the Fe(σ) orbital because of the coincidently unaffected Fe(t_{2g})-Fe(σ^*) absorption. The insertion of a phosphine ligand in place of a former carbonyl ligand showed a more direct impact on the electronic character. The phosphines increase the electron density at the iron atoms as electron-donating ligands due to the weaker π-acidity compared to the CO substituents. Therefore, both iron-based spectral features showed a bathochromic shift, but the lion's share of the effect occurred at the central Fe(σ)-Fe(σ^*) absorption. As expected from observations in the literature, $Ppyr_3$ showed, as opposed to PMe_3 and PPh_3, the lowest red-shift due to the compact three pyrrole substituents with a weaker electron-donating character. In respect of the proton reduction mechanism, this is important, because of the higher protophilicity as a consequence of the increased electron density at the iron core. For this purpose, PMe_3 and PPh_3 would naturally be the better ligands, but, contrary to the other phosphines, $Ppyr_3$ has the possibility to elicit only small cathodic shifts in the reduction potential of the catalyst. However, the azadithiolate ligands showed no impact on the electronic character of the diiron complexes. This makes them interesting as versatile supporting structural unit during catalysis, as previously mentioned, which has no negative effect on electronic properties of the desired [FeFe] complex.

4.3 Electrochemistry

The alignment of the redox potentials is crucial for the photocatalysis, as described above. It not only controls weather the desired electron cascade occurs at all but also affects the system's performance. That is why the redox potential determination of the synthesised [FeFe] catalyst (see **Fig. 15**) *via* cyclic voltammetry is substantial. However, there is a well-known complication with this measuring method and the diiron complexes resulting from the relative

strong interaction of the compounds with ligating solvents like MeCN. This causes the formation of side products during the oxidation or reduction process due to the addition or a ligand exchange with solvent molecules and, therefore, chemically an irreversible redox process in cyclic voltammetry measurement.[95,96] The irreversibility makes the exact determination of the underlying redox potential impossible, in fact the cyclic voltammograms can give only a rough estimations. Since, all of the investigated [FeFe] complexes were affected by this issue, a comparison within this study would still be possible. Unfortunately, Lewis basic solvents also have the property to solute the [FeFe] compounds best, which is, besides the better comparability with literature values, why it was nevertheless decided to measure the electrochemical experiments in acetonitrile. In order to get a better overview and to investigate the influence of the phosphine ligands on the redox potentials of the [FeFe] complexes, we compared in the following the cyclic voltammograms of the unsubstituted all-CO compounds and very similar catalysts with those of the corresponding phosphinated [FeFe] complexes. The outcomes of **[FeFe]-Cat 1** and **[FeFe]-Cat 5** are illustrated in **Fig. 22**, those of **[FeFe]-Cat 2**, **[FeFe]-Cat 6**, **[FeFe]-Cat 8**, **[FeFe]-Cat 9** and **[FeFe]-Cat 10** in **Fig. 23**. The cyclic voltammograms of **[FeFe]-Cat 3**, **[FeFe]-Cat 4** and **[FeFe]-Cat 7** are depicted in **Fig. 24**. **Fig. 25** shows the results for the azadithiolate containing compounds **[FeFe]-Cat 11**, **[FeFe]-Cat 12** and **[FeFe]-Cat 13**, **[FeFe]-Cat 14**, respectively. The corresponding data are reported in **Table 1**.

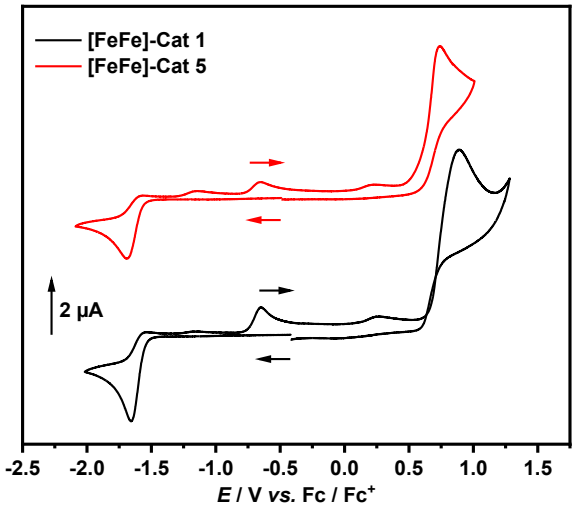

Fig. 22 Cyclic voltammograms of **[FeFe]-Cat 1** (1 mM) and **[FeFe]-Cat 5** (1 mM) in an acetonitrile solution (0.1 M TBAHFP) at 298 K. Experimental setup: Pt as WE, Pt as CE, Ag/AgCl as reference, scan rate: v = 100 mV s^{-1}.

As it was expected, both **[FeFe]-Cat 1** and **[FeFe]-Cat 5** show in the cyclic voltammogram the characteristic irreversible behaviour for the iron-centred oxidation, which refers to the $Fe^{II}Fe^{I}/Fe^{I}Fe^{I}$ redox couple, as well as for the reduction, which refers to the $Fe^{I}Fe^{I}/Fe^{0}Fe^{I}$ redox

couple. In addition, both compounds exhibit on the return of the reduction process an anodic peak potential at –0.65 V *vs.* Fc/Fc$^+$, which arises from a side product formed during reductive degradation and is therefore disregarded for the further contemplations. Interestingly, the phosphine ligand obviously has an influence on the reduction potential as well as on the oxidation potential, whereas the letter is affected more intensely as the data in **Table 1** offer. Thus, the reduction potential of **[FeFe]-Cat 1** at –1.66 V *vs.* Fc/Fc$^+$ has experienced only a relative small cathodic shift of 0.04 V due to the phosphination, which resulted in a reduction potential of **[FeFe]-Cat 5** at –1.70 V *vs.* Fc/Fc$^+$. On the contrary, the oxidation potential of **[FeFe]-Cat 1** at 0.90 V *vs.* Fc/Fc$^+$ has shifted 0.16 V in cathodic direction to the oxidation potential of **[FeFe]-Cat 5** at 0.74 V *vs.* Fc/Fc$^+$.

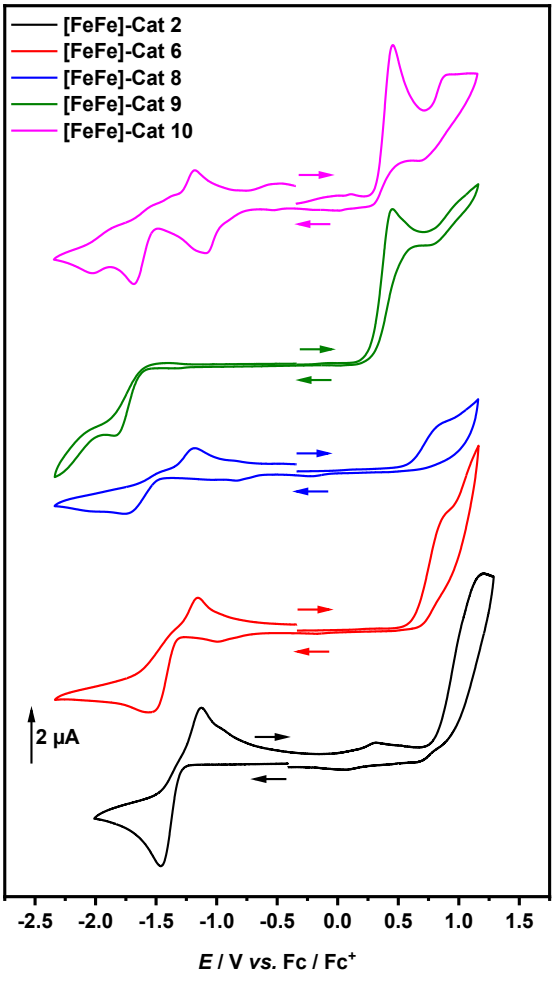

Fig. 23 Cyclic voltammograms of **[FeFe]-Cat 2** (1 mM), **[FeFe]-Cat 6** (1 mM), **[FeFe]-Cat 8** (1 mM), **[FeFe]-Cat 9** (1 mM) and **[FeFe]-Cat 10** (1 mM) in an acetonitrile solution (0.1 M TBAHFP) at 298 K. Experimental setup: Pt as WE, Pt as CE, Ag/AgCl as reference, scan rate: v = 100 mV s^{-1}.

The cyclic voltammograms of the [FeFe] complexes with the benzenedithiolate ligands vary in parts significantly. Whereas those of **[FeFe]-Cat 2** and the Ppyr$_3$ substituted compounds look

very similar in their features, the electrochemical curves of **[FeFe]-Cat 9** and **[FeFe]-Cat 10** each show a very different character. The curves of **[FeFe]-Cat 2**, **[FeFe]-Cat 6**, **[FeFe]-Cat 8** and **[FeFe]-Cat 10** display on the return of the reduction process anodic peak potentials at –1.13 V *vs.* Fc/Fc^+, –1.15 V *vs.* Fc/Fc^+, –1.18 V *vs.* Fc/Fc^+ and again –1.18 V *vs.* Fc/Fc^+, respectively, which correspond to irreversible formed side products during reduction, as it was the case for the previously discussed [FeFe] complexes, and will also be disregarded for the further contemplation. In addition, the cyclic voltammogram of **[FeFe]-Cat 10** shows especially at cathodic potentials multiple features of which the quite intense cathodic peak potential at –1.09 V *vs.* Fc/Fc^+ also revealed as a signal descending from a side product formed during oxidation. This insight was found out by measuring only the reduction curve of **[FeFe]-Cat 10** on which this signal was lacking. Therefore, this feature will also be disregarded. As can be seen in **Table 1**, **[FeFe]-Cat 2** exhibits a reduction potential at –1.46 V *vs.* Fc/Fc^+ and an oxidation potential at 1.21 V *vs.* Fc/Fc^+. Compared with the values of **[FeFe]-Cat 1**, the slight electron-withdrawing effect of the benzenedithiolate ligand seems to shift the redox potentials of the diiron compound into anodic direction, which also should therefore have an impact on the catalytic performance of the system. Furthermore, the $Ppyr_3$ ligand of **[FeFe]-Cat 6** shows a comparable effect as already discussed above which leads to a decrease (0.10 V) of the reduction potential to –1.56 V *vs.* Fc/Fc^+ compared to that of the corresponding all-CO compound **[FeFe]-Cat 1** and to a decrease (0.29 V) of the oxidation potential to 0.92 V *vs.* Fc/Fc^+. Obviously, the phosphine ligand in the benzenedithiolate containing [FeFe] complexes has a greater impact on the redox potentials than in the propanedithiol compounds. An even bigger shift at least for the reduction potential is observable by the addition of a second $Ppyr_3$ ligand in **[FeFe]-Cat 8**. Here, the cathodic peak potential for the reduction is –1.76 V *vs.* Fc/Fc^+ and with this 0.20 V lower than that of **[FeFe]-Cat 6**. However, for the oxidation the anodic peak potential of **[FeFe]-Cat 8** is 0.89 V *vs.* Fc/Fc^+ and thus only 0.03 V lower in value than that of **[FeFe]-Cat 6**. The cyclic voltammogram of the PMe_3 substituted **[FeFe]-Cat 9** differs beside the potential values also in shape and number of the redox signals. It is alongside the below-mentioned curves of the azadithiolate complexes the only one with no signals arising from side products formed during the redox processes. The reduction potential at –1.85 V *vs.* Fc/Fc^+ has experienced a cathodic shift of 0.39 V compared to the corresponding all-CO compound **[FeFe]-Cat 1** and the oxidation potential at 0.45 V *vs.* Fc/Fc^+ a cathodic shift of 0.76 V. This constitutes a tremendous difference to the $Ppyr_3$ substituted compound and illustrates the effect of the pyrrole substituents within the phosphine ligand on the redox potential in contrast to the PMe_3 substituted diiron complex. The cyclic voltammogram of the PPh_3 substituted **[FeFe]-Cat 10** displays four redox signals. Compared to the data of **[FeFe]-Cat 9**, it must be assumed that the cathodic peak potential at –1.69 V *vs.* Fc/Fc^+ and the anodic peak potential at 0.46 V *vs.* Fc/Fc^+ are referred to the iron-centred reduction and oxidation,

respectively. Therefore, the cathodic peak potential at –2.03 V *vs.* Fc/Fc^+ and the anodic peak potential at 0.91 V *vs.* Fc/Fc^+ presumably arise from redox processes based on the benzene substituents of the PPh_3 phosphine ligand. Thus, the Fe^IFe^I/Fe^0Fe^I reduction of the PPh_3 substituted [FeFe] complex also has experienced a cathodic shift (0.23 V) compared to the unsubstituted compound **[FeFe]-Cat 1**, but it is not as big as that of the PMe_3 substituted complex. For the $Fe^{II}Fe^I/Fe^IFe^I$ oxidation, there is nevertheless a similar cathodic shift (0.75 V) in relation to the unsubstituted complex **[FeFe]-Cat 1** as it was the case for the PMe_3 compound.

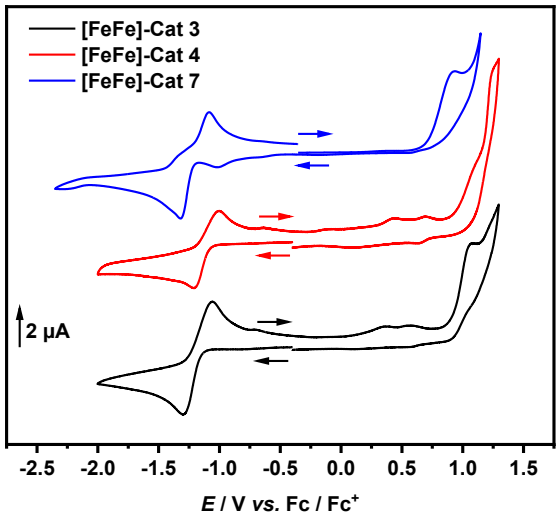

Fig. 24 Cyclic voltammograms of **[FeFe]-Cat 3** (1 mM), **[FeFe]-Cat 4** (1 mM) and **[FeFe]-Cat 7** (1 mM) in an acetonitrile solution (0.1 M TBAHFP) at 298 K. Experimental setup: Pt as WE, Pt as CE, Ag/AgCl as reference, scan rate: v = 100 mV s^{-1}.

The cyclic voltammograms of the chlorobenzenedithiolate [FeFe] complexes **[FeFe]-Cat 3**, **[FeFe]-Cat 4** and **[FeFe]-Cat 7** are very similar in shape. As was the case for the most of the previously discussed curves, all display a signal for a side product formed during the iron-centred reduction (–1.06 V *vs.* Fc/Fc^+ for **[FeFe]-Cat 3**, –1.00 V *vs.* Fc/Fc^+ for **[FeFe]-Cat 4** and –1.09 V *vs.* Fc/Fc^+ for **[FeFe]-Cat 7**). Again, these features will be disregarded for the further contemplation. The cathodic peak potential of **[FeFe]-Cat 3** at –1.30 V *vs.* Fc/Fc^+ for the Fe^IFe^I/Fe^0Fe^I reduction has experienced an anodic shift (0.16 V) compared with that of **[FeFe]-Cat 2**, which is obviously a result of the stronger electron-withdrawing effect of the chlorine substituted benzenedithiolate ligand and the therefore reduced electron density at the [FeFe] complex. Interestingly, the oxidation potential has shifted at the same time towards lower potentials (1.08 V *vs.* Fc/Fc^+ for **[FeFe]-Cat 3** compared to 1.21 V *vs.* Fc/Fc^+ for **[FeFe]-Cat 2**). The extension of two additional chlorine atoms to the chlorobenzenedithiolate ligand leads by contrast to an anodic shift for both redox potentials (–1.21 V *vs.* Fc/Fc^+ for the Fe^IFe^I/Fe^0Fe^I reduction of **[FeFe]-Cat 4** and 1.14 V *vs.* Fc/Fc^+ for the $Fe^{II}Fe^I/Fe^IFe^I$ oxidation

of **[FeFe]-Cat 4**). The electrochemical curve of the $Ppyr_3$ substituted **[FeFe]-Cat 7** shows a cathodic peak potential for the iron-centred reduction at –1.32 V *vs.* Fc/Fc^+ and an anodic peak potential for the corresponding oxidation at 0.94 V *vs.* Fc/Fc^+. Here, the phosphination induced only relatively small cathodic shifts compared to the unsubstituted compound **[FeFe]-Cat 3** (0.02 V for the Fe^IFe^I/Fe^0Fe^I reduction and 0.14 V for the $Fe^{II}Fe^I/Fe^IFe^I$ oxidation).

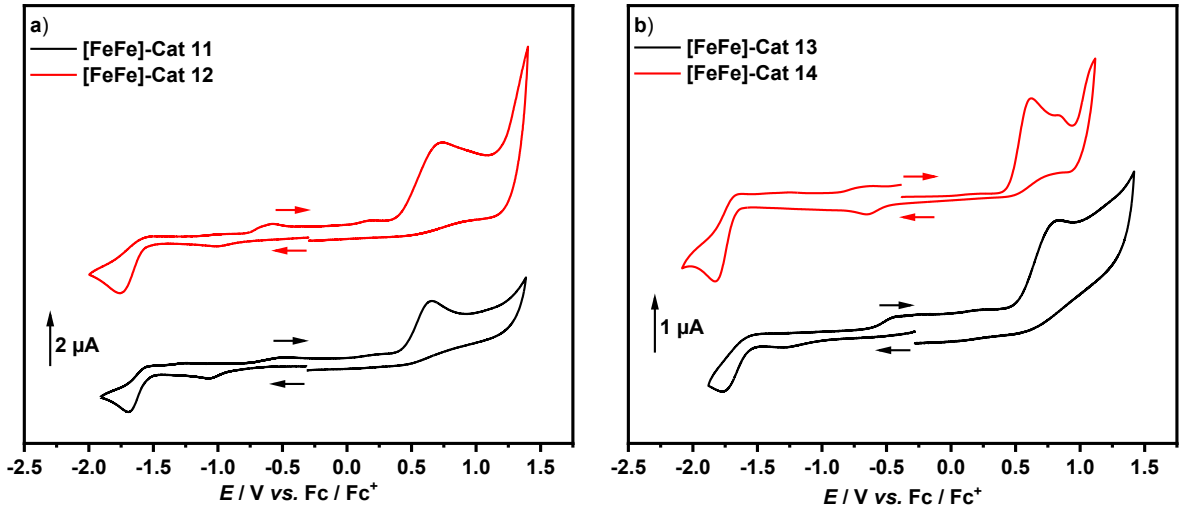

Fig. 25 Cyclic voltammograms of **a) [FeFe]-Cat 11** (1 mM) and **[FeFe]-Cat 12** (1 mM), **b) [FeFe]-Cat 13** (1 mM) and **[FeFe]-Cat 14** (1 mM) in an acetonitrile solution (0.1 M TBAHFP) at 298 K. Experimental setup: Pt as WE, Pt as CE, Ag/AgCl as reference, scan rate: v = 100 mV s^{-1}.

The cyclic voltammograms of the azadithiolate containing [FeFe] complexes **[FeFe]-Cat 11** and **[FeFe]-Cat 12** are very similar in shape. The all-CO compound shows the iron-centred reduction at –1.70 V *vs.* Fc/Fc^+ and the $Ppyr_3$ substituted one at –1.76 V *vs.* Fc/Fc^+. This means a small cathodic shift of only 0.06 V in potential caused by the phosphination. Surprisingly, the $Fe^{II}Fe^I/Fe^IFe^I$ oxidation at 0.65 V *vs.* Fc/Fc^+ of the unsubstituted compound lies 0.08 V beneath the corresponding potential of the $Ppyr_3$ substituted complex at 0.73 V *vs.* Fc/Fc^+, which is an unexpected behaviour generated by phosphination in comparison with all of the previously discussed compounds. In addition, it is apparent by comparing the relative position on the potential scale especially of the reduction potentials with that of the propanedithiolate and benzenedithiolate containing complexes that an electron-withdrawing structural unit usually induces an anodic potential shift and in contrast the azadithiolate ligand does not. This underlines the observations we made during the absorption spectroscopy (see above) which implied that the amine containing ligand does obviously not reduce the electron density at the core of the [FeFe] complex on a larger scale. The same is of course true for **[FeFe]-Cat 13** and its $Ppyr_3$ substituted equivalent **[FeFe]-Cat 14**. Here, the benzyl substituent within the azadithiolate ligand induces even a further decrease in value of the redox potentials. However, the cathodic potential shift induced by the $Ppyr_3$-phosphination could be observed in this case

for both redox potentials and was 0.05 V for the $Fe^{I}Fe^{I}/Fe^{0}Fe^{I}$ reduction (–1.78 V *vs.* Fc/Fc^{+} for **[FeFe]-Cat 13** and –1.83 V *vs.* Fc/Fc^{+} for **[FeFe]-Cat 14**) and 0.22 V for the $Fe^{II}Fe^{I}/Fe^{I}Fe^{I}$ oxidation (0.84 V *vs.* Fc/Fc^{+} for **[FeFe]-Cat 13** and 0.62 V *vs.* Fc/Fc^{+} for **[FeFe]-Cat 14**). Additionally, a weak second anodic peak potential at 0.84 V *vs.* Fc/Fc^{+} presumably deriving from the additional benzene ring of the azadithiolate ligand could be observed during the measurement.

In summary, the electrochemical study of the [FeFe] complexes depicted in **Fig. 15** revealed on the one hand the influence of electron-withdrawing structural units on the redox potentials, more precisely an anodic potential shift as a consequence of the reduced electron density at the core of the [FeFe] complex. Expectably, the benzenedithiolate containing compounds and among them the double chlorine substituted **[FeFe]-Cat 4** showed the biggest effect regarding this matter. However, the azadithiolate containing diiron complexes did not show such an effect, which is in line with the observations of the absorption spectroscopy study (see above). On the other hand, the experiments illustrated the varying influences of the different phosphine ligands. Whereas the benzene substituted PPh_3 ligand and to a greater extent the methyl substituted PMe_3 ligand induced a tremendous cathodic potential shift in the redox potentials (up to 0.39 V for the $Fe^{I}Fe^{I}/Fe^{0}Fe^{I}$ reduction and 0.76 V for the $Fe^{II}Fe^{I}/Fe^{I}Fe^{I}$ oxidation), the $Ppyr_3$ ligand demonstrated in comparison only small cathodic shifts (between 0.02 V and 0.10 V for the $Fe^{I}Fe^{I}/Fe^{0}Fe^{I}$ reduction and between 0.03 V and 0.29 V for the $Fe^{II}Fe^{I}/Fe^{I}Fe^{I}$ oxidation). Again, this emphasises the stronger π-acidity of the $Ppyr_3$ ligand as opposed to the other investigated phosphines caused, on the one hand, by the in comparison with PMe_3 less electron-donating effect of the pyrrole substituents and, on the other hand, by the in comparison with PPh_3 more favourable geometry of the ligand, which overall moderates the electron-donating character of the phosphine.[40] This is very important for the photocatalysis, because $Ppyr_3$ seems to be the only ligand which on the one hand increases the electron density at the iron core of the catalyst and with this also the protophilicity, but does on the other hand not induce a big cathodic shift in the for the catalytic mechanism important reduction potential, which would probably cause a mismatch with the redox potentials of the photosensitiser. This is especially important for those complexes with particularly negative reduction potentials, since in this way the thermodynamic driving force of the electron transfer on the catalyst can also be largely preserved.[9] Certainly, this should positively affect the overall photocatalytic performance of the systems with $Ppyr_3$ substituted catalysts in contrast to such with PMe_3 substituted, PPh_3 substituted or even unsubstituted catalysts.

Table 1 Electrochemical data of [FeFe] complexes for diiron hydrogenase biomimic studies measured by cyclic voltammetry in acetonitrile solutions with 0.1 M TBAHFP at 298 K.

Compound	E_{red} (V *vs.* Fc/Fc$^+$)		E_{ox} (V *vs.* Fc/Fc$^+$)	
	E_{pc-2}	E_{pc-1}	E_{pa-1}	E_{pa-2}
[FeFe]-Cat 1		–1.66	0.90	
[FeFe]-Cat 5		–1.70	0.74	
[FeFe]-Cat 2		–1.46	1.21	
[FeFe]-Cat 6		–1.56	0.92	
[FeFe]-Cat 8		–1.76	0.89	
[FeFe]-Cat 9		–1.85	0.45	
[FeFe]-Cat 10	–2.03	–1.69	0.46	0.91
[FeFe]-Cat 3		–1.30	1.08	
[FeFe]-Cat 4		–1.21	1.14	
[FeFe]-Cat 7		–1.32	0.94	
[FeFe]-Cat 11		–1.70	0.65	
[FeFe]-Cat 12		–1.76	0.73	
[FeFe]-Cat 13		–1.78	0.84	
[FeFe]-Cat 14		–1.83	0.62	0.84

4.4 Photocatalysis

The abovementioned investigations were able to highlight the effects of the particular [FeFe] structural units on the electronic character and also on the redox potentials of the catalysts. As already mentioned, the electron density especially at the iron core of the complexes and the reduction potential have a decisive influence on the catalytic process, because they affect the protophilicity and the desired electron transfer on the catalyst respectively and adjudicate therefore whether the whole process of the photocatalysis proceeds or not. In the literature a large number of publications on photocatalysis using [FeFe] catalysts can be found. In some of them also the effects of different structural units on the photocatalysis were discussed. Due to the solubility behaviour of the catalysts, however, the majority of them deal with reactions in organic solvents or in organic-aqueous mixtures.[5,9,39,53,97] For the desired photocatalytic conversion in pure water as medium an additive is therefore needed to ensure the solubilisation of the diiron complex. As mentioned before, a poly(2-oxazoline) polymer which forms micelles in aqueous solution is attended to be used for this purpose.[74,75,77] Since the polarity of the cavity formed is roughly comparable to that of acetonitrile, the desired solubilisation should therefore occur if the polymer concentration used is above the critical micelle formation concentration. This is intended to be examined in the following. However, it is not only the aim to clarify whether a solubilisation of the [FeFe] complexes shown in **Fig. 15** is possible, but much more whether an entire photocatalytic system consisting of **[Ru(bpy)$_3$]Cl$_2$** as photosensitiser, the corresponding solubilised diiron complex and ascorbic acid as sacrificial electron donor works in such an environment. This implicates that the desired electron cascade

between the different involved components proceeds during light irradiation and hydrogen is being produced. In addition, it also should be determined whether the knowledge gained from absorption spectroscopy, cyclic voltammetry and possibly given literature conformity are also reflected in the performance of the photocatalysis of the individual compounds examined under these new conditions.

The preparation of the aqueous micelle solutions with the aid of the poly(2-oxazoline) polymer shown in **Fig. 14** could easily be carried out for all [FeFe] complexes by using the film hydrogenation method[74] described above. The polymeric thin films were produced in the process by starting from DCM solutions. The polymer concentration used in the final photocatalytically active solutions was based at least on the 25 times mass excess in relation to the compound to be solubilised to ensure a concentration above the critical micelle formation concentration and a sufficient solubilisation. In order to be able to compare the prepared photocatalytically active solutions with one another, the polymer concentration in all batches was 5.6 mg ml^{-1}. The successful inclusion in the formed poly(2-oxazoline) micelles could be ascertained in all cases by streak-free and turbidity-free aqueous solutions. Exemplary, UV/Vis absorption spectra of **[FeFe]-Cat 5** in DCM and aqueous polymer solution, of **$[Ru(bpy)_3]Cl_2$** in water and of the corresponding photocatalytic system in aqueous polymer solution were recorded, as can be seen in **Fig. 26**. All absorption features, especially them of the water insoluble diiron complex, are clearly visible in the spectrum of the photocatalytic system in aqueous solution. Therefore, the first goal, the solubilisation of the [FeFe] complex, was successfully achieved.

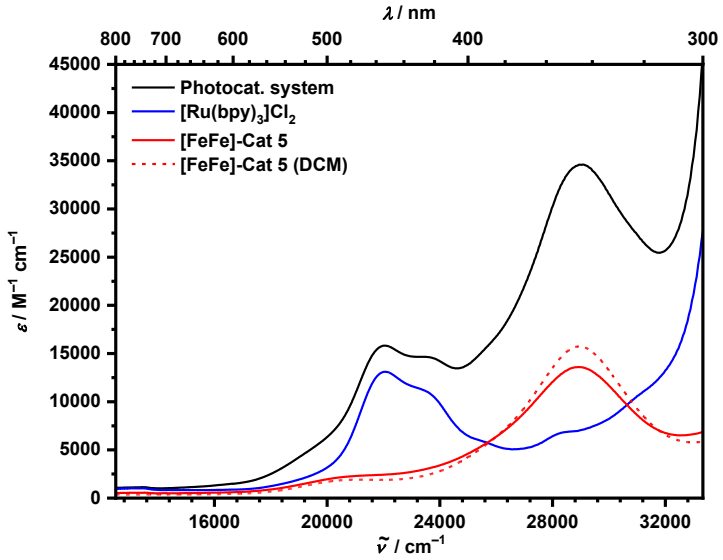

Fig. 26 UV/Vis absorption spectroscopy of photocatalytically active system containing **$[Ru(bpy)_3]Cl_2$** ($5.00 \cdot 10^{-5}$ M), **[FeFe]-Cat 5** ($9.84 \cdot 10^{-5}$ M) and ascorbic acid (0.20 M) as well as of its components in water at 298 K. The photocatalytic system and **[FeFe]-Cat 5** were measured in an aqueous poly(2-oxazoline) solution (2.0 mg ml^{-1}). For comparison, **[FeFe]-Cat 5** in DCM ($9.91 \cdot 10^{-5}$ M) is depicted in dashed line.

In order to investigate the catalytic performance, more precisely the catalytic productivity, of the different systems, the photocatalytic hydrogen evolution using the ruthenium photosensitiser in combination with the corresponding diiron catalyst with ascorbic acid as the sacrificial electron donor was performed in water (pH = 3) with a poly(2-oxazoline) concentration of 5.6 mg ml^{-1} each. For the photosensitiser and the corresponding diiron catalyst equimolar amounts (0.30 mM) were used. The concentration of ascorbic acid was 0.20 M for each solution. After irradiation of the samples with light at 21500 cm^{-1} (465 nm) from a LED source (10 LEDs @ 3.0 V and 1.58 A, for emission spectrum see **Fig. 74**) for 5 h, the gas phase over the solutions was investigated by gas chromatography. With the amount of produced hydrogen, the TON referring to the amount of deployed catalyst could be calculated. The results for the systems with the [FeFe] compounds depicted in **Fig. 15** are illustrated in **Fig. 27**.

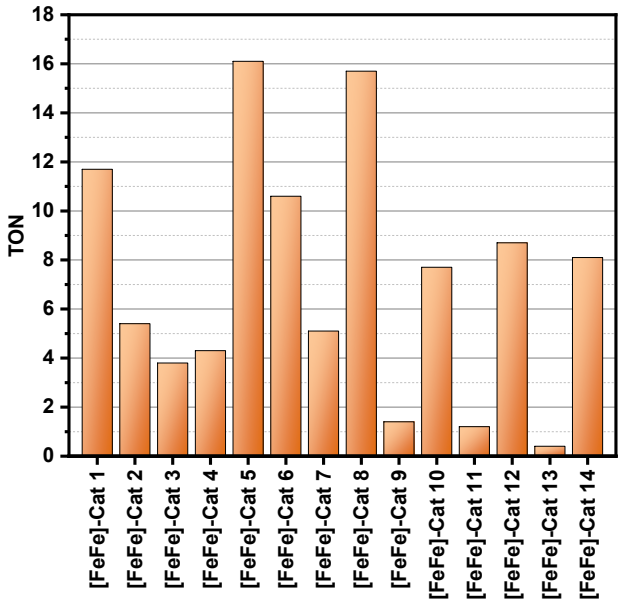

Fig. 27 Photocatalytic hydrogen evolution in aqueous poly(2-oxazoline) solution (pH = 3, polymer concentration: 5.6 mg ml^{-1}) at 293 K after 5 h irradiation with light at 21500 cm^{-1} (465 nm). Stoichiometric proportions: 0.30 mM [FeFe] catalyst, 0.30 mM **$[Ru(bpy)_3]Cl_2$** and 0.20 M ascorbic acid.

In the row of the all-CO compounds **[FeFe]-Cat 1**, **[FeFe]-Cat 2**, **[FeFe]-Cat 3** and **[FeFe]-Cat 4** the propyldithiolate containing complex shows with a TON of 11.7 by far the highest productivity. In contrast, the other benzenedithiolate containing complexes exhibit only comparable small differences between their key figures. With its pure benzene ring within this dithiolate ligand, **[FeFe]-Cat 2** still offers with a TON of 5.4 a somewhat more productive performance than both chlorine substituted representatives with a TON of 3.8 and 4.3, respectively. From this it can be deduced that in principle a rather electron-donating dithiolate ligand, like the propyldithiolate one, increases the catalytic productivity much more than an electron-withdrawing moiety like benzenedithiolate. As previously mentioned, in the absorption

spectroscopy study, the electronic character of the dithiolate ligand presumably plays an important role on the electron density at both sulphur atoms. Due to their function for restoring the initial state of both iron atoms by reconnecting with them during the catalysis mechanism, a higher electron density on their position should therefore enhance the catalytic activity as well as the stability of the catalyst to some extent.[4,98] Noteworthy, the actual strength of the electron-withdrawal is obviously immaterial for the productivity of the all-CO compounds, as can be seen from the results of the chlorobenzenedithiolate containing catalysts. Unfortunately, in literature there are only very few photocatalytic studies about [FeFe] complexes with different dithiolate ligands and especially their effect on the catalytic performance. Although, there are numerous examples for systems with such different catalysts, but often recorded under different conditions which makes a comparison very difficult to impossible.[5,9,99] Therefore, no reference to literature values will be given at this point.

By comparison with the single $Ppyr_3$ substituted diiron complexes, an in parts tremendous increase of the TON up to almost doubling is visible, which demonstrates the important impact of the direct bonded phosphine ligand. The biggest increase registered the pure benzendithiolate containing **[FeFe]-Cat 6**. However, the corresponding propyldithiolate catalyst **[FeFe]-Cat 5** still shows the highest performance with a TON of 16.1, which additionally constitutes the highest output for all investigated systems in this study. Furthermore, the dichlorodithiolate substituted **[FeFe]-Cat 7** exhibits with a TON of 5.1 only a quite small increase compared with the corresponding all-CO compound. This illustrates in addition the now much higher impact of the dithiolate ligand on the catalytic performance in conjunction with presence of the $Ppyr_3$ phosphine ligand. Here, the dichlorobenzenedithiolate moiety with its stronger electron-withdrawing character presumably inhibits or consumes the increase in performance introduced by the electron-donating phosphine ligand. As one might expect, a second $Ppyr_3$ ligand brings an additional TON boost illustrated by **[FeFe]-Cat 8**. With a TON of 15.7, the increasement is in the course of this almost additive. By comparing the performance of the catalysts with different phosphine ligands, once again the importance of the electronic character of the phosphine ligand on the system's productivity is obvious. Whereas the PMe_3 substituted catalyst shows with a TON of only 1.4 the smallest output within this row, the corresponding PPh_3 catalyst distinctly surpasses this by an achieved TON of 7.7, which, however, is still not even the three-fourths of the output of the $Ppyr_3$ substituted **[FeFe]-Cat 6** with a TON of 10.6. Here, clearly the influence of the corresponding reduction potential is apparent. As the electrochemistry experiments showed above, the reduction potential of the $Ppyr_3$ substituted complex is the most positive one, followed by the more cathodic shifted potential for the PPh_3 substituted catalyst and finally the PMe_3 compound exhibited by far the most negative potential, which is a consequence of the different π-acidities of the phosphines caused by the different electronic and steric character of their inner substituents (see above).

In combination with the reduction potential of the **[Ru(bpy)$_3$]Cl$_2$** photosensitiser of –1.76 V *vs.* Fc/Fc$^+$[24] and under the assumption of a reductive quenching mechanism, obviously only the reduction potentials of the Ppyr$_3$ and PPh$_3$ substituted diiron catalysts (–1.56 V *vs.* Fc/Fc$^+$ for **[FeFe]-Cat 6** and –1.69 V *vs.* Fc/Fc$^+$ for **[FeFe]-Cat 10**, see **Table 1**) match to the in equation 4 listed requirement for a thermodynamic feasible electron transfer from the reduced photosensitiser to the catalyst:

$$E^{0'}\,[PS/PS^-] < E^{0'}\,[Cat/Cat^-] \qquad (4)$$

On closer consideration, the more anodic shifted potential of **[FeFe]-Cat 6** fits essentially better to that of the photosensitiser than the corresponding potential of **[FeFe]-Cat 10.** The latter is presumably to near for generating a sufficient driving force, not considering the additional shifts generated by solvent change from acetonitrile to water. These insights are therefore in line with the result from the photocatalysis. However, the abovementioned performance of the system with the double Ppyr$_3$ substituted **[FeFe]-Cat 8** is not. Its reduction potential (–1.76 V *vs.* Fc/Fc$^+$, see **Table 1**) is equal to that of **[Ru(bpy)$_3$]Cl$_2$**. Thus, the distinct performance increase presumably has to be ascribed to the second important effect of the phosphine ligands on the core of the [FeFe] complexes: its electron-donating ability. In this case the two phosphine ligands would lead to an additionally higher protophilicity at the iron core due to the increased electron density there, which would compensate the negative influence of the simultaneously cathodic shifted reduction potential of the complex. This would be an additional improvement for the catalytic mechanism, in which one of the first steps is the addition of a proton at both iron atoms.[98,100]

In general, the Ppyr$_3$ ligand seems to pre-eminently increase the system's catalytic activity by increasing the protophilicity of the complex and at the same time by adjusting the reduction potential of the catalyst to that of the used **[Ru(bpy)$_3$]Cl$_2$** photosensitiser. This correlation was already discussed by Sun *et al.* for systems in an acetonitrile-water mixture and also appears to be true for the systems under the environment investigated in this work.[9] However, as the distinct higher turnover numbers of the Ppyr$_3$ substituted complexes in relation to the unsubstituted ones show, the phosphine ligand leads additionally to an enhanced catalytic productivity. In literature also an enhancement of the catalysts stability by the phosphine ligands was discussed.[9] Since, the exact impact of the phosphines on the stability of all different [FeFe] compounds used in this study is not certain, it is difficult to argue how much exactly the impact of these ligands on the catalytic activity and productivity is. Nevertheless, under the previously mentioned assumptions of more or less comparable photo instabilities of the used components and the usage of the same reaction conditions throughout the experiments, it is presumable that the phosphine ligands also enhance, beside the stability of the catalyst and with this the catalytic productivity, the activity of the systems in a crucial

manner. Particularly by considering the abovementioned increased protophilicity and matching reduction potential of the [FeFe] complexes. Furthermore, the adverse effect of very positive reduction potentials of the [FeFe] catalysts on their stability, which was also discussed by Sun *et al.*[9], could be confirmed in this study, too. The diiron compounds with reduction potentials above –1.50 V *vs.* Fc/Fc^+ showed, with the exception of the unsubstituted azadithiolate complexes, the lowest TON values. This is particularly noticeable in view of the supposedly higher thermodynamic driving force of these complexes. However, to what extent the complex stabilities or possibly their electronic properties had an influence on this could not be further elucidated at this point.

On consideration of the azadithiolate containing [FeFe] complexes multiple aspects strike the eye by comparing their results of the photocatalysis. First, there is no big difference between the catalysts with the benzyl substituted azadithiolate ligands and them with the respective propyl substituents. This speaks for a just small influence of this residual at the nitrogen atom on the overall system's performance. Obviously, the distance to the decisive [FeFe] complex core is too far. Furthermore, there is a tremendous difference between the performance of the systems with the respective all-CO complexes and them with the $Ppyr_3$ substituted compounds. The minor output of the former (TON = 1.2 for **[FeFe]-Cat 11** and TON = 0.4 for **[FeFe]-Cat 13**) could be explained with reference to the corresponding reduction potentials (see **Table 1**). Whereas that of **[FeFe]-Cat 11** scarcely fulfils the thermodynamic requirement stated in equation 4, **[FeFe]-Cat 13** does not, leading to an even worse catalytic output. The potential mismatch in both cases exacerbates the catalytic process considering the insufficient thermodynamic driving force. Both phosphine substituted azadithiolate catalysts show in contrast a comparable high performance with a TON of 8.7 for **[FeFe]-Cat 12** and a TON of 8.1 for **[FeFe]-Cat 14**. Again, this demonstrates the ability of $Ppyr_3$ to compensate a potential mismatch with its electronic influence on the catalyst, as it was the case for **[FeFe]-Cat 8**. However, the results for the all-CO azadithiolate compounds impressively show that the initially envisaged function of the nitrogen atom as an internal acid/base does not crucially contribute to the photocatalytic performance of that systems.

To investigate the reproducibility of the obtained results from the photocatalytic measurements, the system consisting of **[FeFe]-Cat 5**, **$[Ru(bpy)_3]Cl_2$** and ascorbic acid was measured a total of four times under the optimal conditions determined in this work (see below). The respective reaction solutions were prepared anew each time in order to incorporate the inaccuracies occurring during the preparation of the solutions. The series of measurements showed a variation coefficient of 11 %. This procedure was then repeated with two other photocatalytic systems. With these, values of 11 % and 12 % could be determined. It can therefore be assumed that with the measurement method used in this thesis to determine the photocatalytic

productivity, the results obtained show on average a relative standard deviation of somewhat over 10 %.

In summary, this study about the photocatalytic performance of systems with different [FeFe] catalysts depicted in **Fig. 15** and solubilised in water with poly(2-oxazonline) micelles demonstrated the influences of important structural units of the diiron complexes under this new environment. Especially, the effects of the phosphine ligands on the system's performance could be highlighted, which appear to be very similar to that already discussed in literature for similar systems in an aqueous-organic solvent mixture.[9] Hence, it can be assumed that the impact of the individual structural units, like the dithiolate or a phosphine ligand, behave at least qualitatively in the aqueous micellar solution in a similar way to the already known systems. Furthermore, based on the results of the absorption spectroscopy and electrochemical investigations, certain correlations in the performance of the diiron complexes could be determined. For instance, it was found that an electron-withdrawing dithiolate ligand has a negative effect on catalytic productivity, which is incidentally only noticeable in combination with a phosphine ligand. This fact indicates that the low electron density at the two sulphur atoms of the dithiolate caused by the electron-withdrawal negatively influences the catalytic process and this only comes into play when the catalytic mechanism as a whole is favoured by the increased protophilicity caused by the phosphine ligand. As expected, it was also shown that suitable redox potentials are a crucial prerequisite for high productivity. In some cases, however, unsuitable redox potentials could be compensated by particularly strong electron pressure generated by inserted phosphine ligands, and a relatively high turnover number could nevertheless be achieved. It is striking that the findings from both absorption spectroscopy and cyclic voltammetry, especially exhibit an impact on the photocatalytic activity. This in turn suggests the previously mentioned assumption that a higher catalytic productivity is not only the consequence of an enhanced component stability but also the result of an improved system's activity under the given precondition of the same experimental conditions and a consistent period of time. However, since it is uncertain how the individual molecular units affect the respective stability of the components during photocatalysis, it is therefore also unknown how high the influence on the activity and productivity is.

As already described above, the system consisting of **[FeFe]-Cat 5**, **$[Ru(bpy)_3]Cl_2$** and ascorbic acid was able to achieve a maximum turnover number of 16.1 in the aqueous medium with the aid of the poly(2-oxazoline) micelles. However, it was questionable whether this was already the maximum of what such a catalyst was capable of. As is known, catalytic productivity does not only depend on the stability of the components used, but also significantly on other experimental conditions such as the concentration of the constituents or in this case especially the pH of the solution. Therefore, the top-performing system just described should

be further optimised in terms of its productivity. The results of this purpose are described in the following.

A key parameter is the ratio or the concentration of the individual components in the photocatalytic system. Changing the concentration of a component not only changes the composition of the system and the constituent's ratio, but in particular also the roles as a limiting factor in the system. In a system in which, for example, a relatively photo-unstable photosensitiser represents in the course of photocatalysis the limiting factor due to the permanent light irradiation, the catalyst can all at once become the limiting factor by significantly increasing the photosensitiser concentration. Since a deficit of sensitiser molecules due to radiation-induced degeneration can now easily be compensated because of the sheer excess of them in solution and, as a consequence thereof, the increased probability of the presence of non-decomposed species. At the same time, from the catalyst's point of view, the oversupply of potential reaction partners could lead to a higher workload and thus possibly to faster catalyst degeneration. However, the limitation that applies to photosensitisers in particular is that they can only participate in the electron cascade after light excitation and that, if the concentration is too high, this will no longer be possible for all existing molecules due to the simultaneously increasing absorption cross section and decreasing irradiation depth of the solution.[24] Such a change naturally has a decisive impact on the system's turnover numbers. In general, ruthenium complexes exhibit a higher photostability compared to the diiron complexes, which is why it can be assumed for the previously examined photocatalytic systems that the corresponding catalysts can also be regarded as limiting factors with reference to the molecular stability.[24] In order to determine the maximum limit of the [FeFe] catalyst, several batches were examined photocatalytically, each of which gradually increased the photosensitiser-catalyst ratio. The results are depicted in **Fig. 28**.

In order to raise the photosensitiser-catalyst ratio, two different approaches were used during the experiments. Based on the equimolar composition, the photosensitiser concentration was gradually increased in one method, while the catalyst concentration was gradually decreased in the other approach. As can be seen in **Fig. 28**, both methods partially showed significant differences in the outcome. With the corresponding 1:0.25 ratio, the largest TON of 31.4 could be achieved, which corresponds to a fourfold photosensitiser excess and almost a doubling of productivity compared to the equimolar system. Furthermore, it was shown that in all cases a reduction in the catalyst concentration gave better results than the corresponding increase in the photosensitiser concentration. This is very likely related to the constant concentration of the sacrificial electron donor in the solutions. As the photosensitiser concentration increases, the ratio between ascorbic acid and **$[Ru(bpy)_3]Cl_2$** decreases, which obviously has a negative effect on the associated electron transfer during photocatalysis. On the other hand, reducing

the catalyst concentration does not change this ratio and therefore does not lead to the described negative effects.

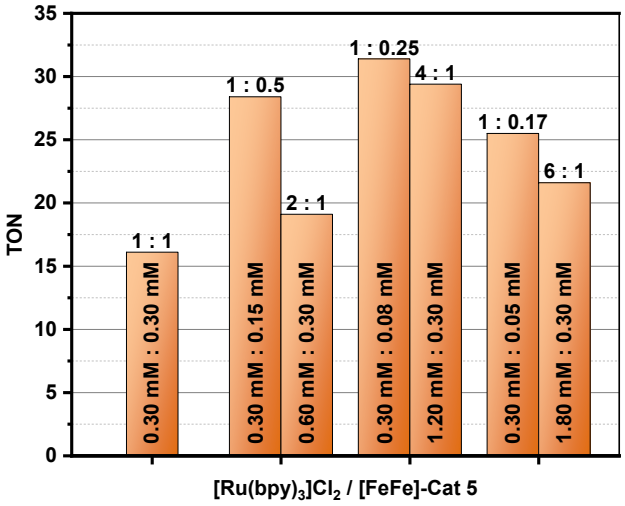

Fig. 28 Photocatalytic hydrogen evolution in aqueous poly(2-oxazoline) solution (pH = 3, polymer concentration: 5.6 mg ml^{-1}, ascorbic acid concentration: 0.20 M) under different **[Ru(bpy)$_3$]Cl$_2$** : **[FeFe]-Cat 5** ratios at 293 K after 5 h irradiation with light at 21500 cm^{-1} (465 nm). The concentrations of **[Ru(bpy)$_3$]Cl$_2$** and **[FeFe]-Cat 5** used in the respective reaction solutions are indicated on the columns.

Another decisive factor for the turnover number is the prevailing pH-value of the reaction solution, especially in aqueous environments. This consequently plays mainly a role in systems with pH sensitive components. In the previously examined photocatalytic compositions, especially ascorbic acid used as the sacrificial electron donor plays this role. Interestingly, for this molecule two antagonistic effects bring to bear, since ascorbic acid is a protonic acid as well as a reducing agent. For instance, a decrease in pH would enhance the acidity on the one hand, but lower the reducing power on the other. This is due to the fact that ascorbate, as the deprotonated form of ascorbic acid, constitutes the actual reducing agent of the system. Its proportion in the reaction solution becomes therefore smaller and lower as the pH decreases.[48] Furthermore, the effect of the [FeFe] complex as a proton reduction catalyst is also pH dependent to a certain degree, since it has to be protonated several times to produce hydrogen during the catalytic process.[3,97,99,100] Accordingly, increased acidity should favour catalytic protonation on the diiron complex. However, it should be remarked at this point that the [FeFe] complexes can quite work catalytically under alkaline conditions, as numerous publications e.g. in combination with amines as sacrificial electron donors showed.[5,53,69] In addition, the consumption of the sacrificial electron donor itself also influences the pH of the solution and thus all of the effects listed above. This is why pH-independent sacrificial electron donors, e.g. 1,3-dimethyl-2-phenylbenzimidazoline (BIH), was already used for photocatalytic proton reduction.[14,101] For reasons of comparability between the examined systems and for the sake of simplicity, this problem was not considered further below. Nonetheless, these partly

opposite dependencies should therefore lead to a certain optimal pH range for the overall system in which the best conditions prevail for the individual components without the negative aspects predominating. To determine this range, several photocatalytic experiments were carried out with systems consisting of **[FeFe]-Cat 5**, **[Ru(bpy)$_3$]Cl$_2$** and ascorbic acid in aqueous poly(2-oxazoline) solutions, each with a different pH-value adjusted by the addition of hydrochloric acid and sodium hydroxide solution, respectively. The outcome is depicted in **Fig. 29**.

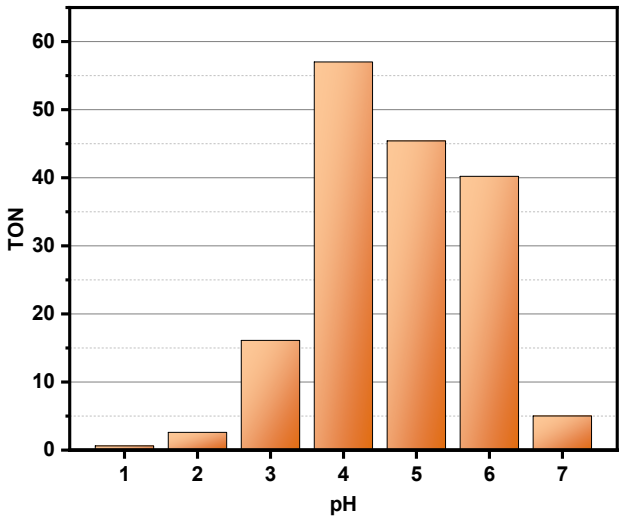

Fig. 29 Photocatalytic hydrogen evolution in aqueous poly(2-oxazoline) solution (polymer concentration: 5.6 mg ml^{-1}) under different pH values at 293 K after 5 h irradiation with light at 21500 cm^{-1} (465 nm). Stoichiometric proportions: 0.30 mM **[FeFe]-Cat 5**, 0.30 mM **[Ru(bpy)$_3$]Cl$_2$** and 0.20 M ascorbic acid.

The system investigated showed the highest turnover of 57.0 at a pH of 4. At lower pH values, the tests exhibited a rapid drop in productivity, so the system only offered a TON of 16.1 at pH = 3 and even only a TON of 2.6 at pH = 2. In this region there is presumably not enough ascorbate in the reaction mixture due to the too low pH-value to effectively deliver adequately electrons needed for the photocatalysis. At higher pH values, there was at first a certain performance plateau. So, the productivity at pH = 5 only decreased to 45.4 and further to 40.2 at pH = 6. Thus, the system was able to keep its turnover to approx. 70 % in a relatively small pH range (4–6). After that, also in the neutral solution (pH = 7), the turnover dropped dramatically to just 5.0. Here, the acidity of the solution is supposedly too weak to effectively protonate the catalyst during the catalytic mechanism.

In summary, the optimisation attempts of a photocatalytic system, containing a [FeFe] catalyst, a bipyridine-ruthenium complex as photosensitiser and ascorbic acid as sacrificial electron donor, in an aqueous poly(2-oxazoline) solution in terms of component ratio and pH-value gave optimal conditions for a system with a 1:0.25 ratio between photosensitiser and catalyst and a

pH-value of the aqueous solution of 4. This knowledge is applied to all such systems in the following.

4.5 Conclusion

In summary, in this study it was possible to synthesise fourteen different [FeFe]-hydrogenase biomimics with various dithiolate and phosphine ligands (see **Fig. 15**) and examine as well as compare their spectroscopic, electrochemical and photocatalytic properties. On the one hand, the effects of various dithiolate ligands as the characteristic structural unit of these diiron complexes and also of added phosphine ligands on the properties of the overall complexes should be investigated and analysed. On the other hand, it should be determined whether these water-insoluble catalysts can be incorporated into pure water in a photocatalytic system using poly(2-oxazoline) as a solubiliser and can release hydrogen in photocatalysis. In addition, if employed successfully, the photocatalytic performance of the various catalysts should be tested and, based on the productivity determined, possibly conclusions drawn about the effects of structural units and material properties previously determined.

The spectroscopic investigations showed that the electron-withdrawing dithiolate ligands especially destabilise the Fe(σ) orbital. However, this effect was not nearly as severely as that of the phosphine ligands bound directly to the iron core of the complexes. These ligands increase the electron density at the [FeFe] complex, which was shown by the bathochromic shift of all iron-based spectral features. Among the phosphines, $Ppyr_3$ had the weakest effect due to the less sterically demanding and less electron-donating pyrrole substituents.[40] A property that was also noticeable in the electrochemical and photocatalytic investigations. The azadithiolate ligands, on the other hand, showed no noteworthy influence on both the spectral and the electrochemical properties of the corresponding compounds. The cyclic voltammetry investigations of the remaining compounds offered that electron-withdrawing dithiolate ligands caused an anodic shift in the redox potentials, which could be expected given the results of the investigations on absorption spectroscopy. Furthermore, the phosphine ligands showed varying influences on the redox potentials of the compounds. A relatively strong cathodic shift in redox potentials was registered for complexes with a PPh_3 ligand and especially for those with a PMe_3 ligand, but only a small cathodic shift for $Ppyr_3$ ligands. This results from a stronger π-acidity of $Ppyr_3$ as a consequence of the implemented pyrrole substituents, which therefore moderates the electron-donating character of the phosphine.[9] Moreover, this insight confirms the findings in literature about common phosphine ligands like PMe_3,[95] PMe_2Ph,[102] PPh_3, $P(OEt)_3$[103] or $P(OMe)_3$[104] which would lead to a cathodic shift in the reduction potential of the [FeFe] complex, as it would be expected from an electron-donating moiety, and therefore to a bigger mismatch to the oxidation potential of the applied photosensitiser. This means that $Ppyr_3$

is in the row of the tested phosphine ligands in this work the only one which has the ability to enhance protophilicity by increasing the electron density within the complex without simultaneously inducing a strong cathodic shift in the redox potentials. Both aspects are important in terms of the presumed catalytic mechanism and with that also for the system's catalytic performance. Therefore, this was also reflected in the results of the photocatalytic investigation of the compounds. Although, an increased protophilicity and adjusted redox potentials of the components primarily should enhance the catalytic activity of the systems, the productivity was also improved, as the measured turnover numbers proved. The effects of the corresponding structural units shown in the previous experiments could stabilise intermediates formed during the photocatalysis or have a fundamentally stabilising influence on the complexes and thus lead to higher productivity. However, these influences on the complex stabilities cannot be verified further at this point. Furthermore, the higher turnover numbers could also be a consequence of the presence of several preconditions like the usage of the same measurement conditions, in particular the irradiation period under consideration, the use of the same system components and a presumably comparable photostability of the catalysts examined. As a result, the irradiation time and the associated degradation of the catalysts after a certain time would equally be the limiting factor for all systems, which would have the consequence that a higher catalytic activity in the period under consideration would also lead to higher productivity. Since, as already mentioned, it is not known to what extent the abovementioned effects of the corresponding structural units have an influence on the compound stability, it is not possible to go into further detail here on their proportional influence on activity and productivity. Nevertheless, certain dependencies of specific structural units on the catalytic performance could be recognised. For instance, the effects of the phosphine ligands were very similar to the relationships already discussed in the literature for similar systems in aqueous-organic solvent mixtures.[9] Even in the new aqueous environment, the phosphine ligands brought about a very significant improvement in productivity, despite the fact that the catalysts were encased in micelles. In some cases, an existing discrepancy in the reduction potential of the **[Ru(bpy)$_3$]Cl$_2$** photosensitiser and the corresponding catalyst used could be compensated by phosphination. In addition, the electron-withdrawing dithiolate ligands had a negative impact, but only in combination with a phosphine ligand. Which in turn suggests that the dithiolate unit has a quasi-secondary influence on the catalytic process, which only comes into play when the conversion as a whole is activated by the phosphine ligand. It was assumed that in particular the electron density on both sulphur atoms is influenced by the electronic properties of the dithiolate ligand. In an assumed mechanism,[4,98] these are responsible for the regression of the parent compound in one of the last steps, which would support the presumption just mentioned.

In the context of this study, the photocatalytic performance of systems with a ruthenium photosensitiser and a biomimetic [FeFe]-hydrogenase complex in pure water was determined and their dependence on structural units of the catalyst was also investigated. This concept and the knowledge gained was used in the following to research photocatalytic dyad complexes.

5 PHOTOCATALYTIC DYADS AND BIMOLECULAR SYSTEMS

As already discussed in the chapter on the theoretical principles, three different components are required for a functioning system for the photocatalytic generation of hydrogen. In addition to the photosensitiser, which is responsible for absorbing the energy required for the ongoing electron cascade, the catalyst, on which the actual proton reduction takes place, and a sacrificial electron donor are used to provide the required electrons. In the past, research has mainly focused on the study of such three-component systems (3CS).[3,5,8,9] As shown in chapter 4, there are several options for optimising the photocatalysis of such 3CS, such as changing the stoichiometric composition of the system or changing process parameters such as the pH value. Another option is to influence the process itself through structural changes. Several intermolecular electron transfers take place in a 3CS during photocatalysis. Depending on the thermodynamic and kinetic conditions, these may represent process-critical energy barriers. In the best case, however, they would take place in a diffusion-controlled manner. One way to possibly avoid this is to use photocatalytically active dyads. Since, as already mentioned, the sacrificial electron donor is actively consumed as the only component, it cannot be integrated covalently. This leaves only the possibility of covalently linking the photosensitiser to the catalyst to form a photocatalytically active dyad. In this way, one intermolecular electron transfer can possibly be replaced by a potentially faster intramolecular process. For the development of such a dyad containing two-component system (2CS), similar to the 3CS, care must be taken to ensure that the material properties of the components within the dyad are adjusted to one another in order to enable proton reduction as efficiently as possible. In the following, photocatalytically active dyad systems based on an existing 3CS were synthesised and investigated regarding their spectroscopic, electrochemical and photocatalytic properties.

In addition, mechanistic aspects of the systems synthesised should also be investigated, since these also have an impact on the performance of such 2CS. Sun *et al.* already described in 2011 that in the 2CS examined so far it was noticeable that such systems, which performed *via* the oxidative quenching mechanism (OQ), showed an increase in performance compared to the corresponding 3CS.[9] The exact reasons for this behaviour are not certain. The initial electron transfer may play a crucial role for the overall performance, since in case of OQ this differs fundamentally between 2CS and 3CS. If, on the other hand, the systems perform *via* reductive quenching (RQ), then 2CS and 3CS do not differ accordingly in their first step. A possible advantage due to stronger electronic coupling between the dyad components would then only be limited to the supposedly less important second electron transfer. However, such weighting of the redox processes occurring in the respective mechanisms cannot be carried

out without including the electronic data. Whether a step e.g. as a rate-determining step is decisive for the overall performance of the catalysis is precisely determined by these electronic properties and can therefore not be declared as important or unimportant in advance. Presumably, the bridge unit built into the dyads and the influence of their electronic properties on that of the entire molecule therefore have a decisive impact. For this reason, in addition to the question of the mechanism that takes place in the dyad systems, this should also be discussed in the following investigations.

5.1 Ruthenium Containing Systems

In the following, photocatalytically active dyad systems should be synthesised and characterised. The synthetic construction of such a system can be considerably simplified by using already known components of systems that work under the desired conditions and environments. Furthermore, with regard to the analytical characterisation, it is also advantageous if a corresponding 3CS is available as a reference system for a comparison of essential system properties. Since, as shown in the previous chapter, various [FeFe]-hydrogenase biomimics in combination with a tris(bipyridine)ruthenium(II) photosensitiser in an aqueous poly(2-oxazoline) solution in some cases show a high photocatalytic performance, the targeted dyad systems in the following should be based on these known systems and examined as well as compared with regard to their spectroscopic, electrochemical and photocatalytic properties with the corresponding bimolecular systems. For a photosensitiser-catalyst dyad, the choice of the bridge building block that covalently connects the photosensitiser part to the catalyst part is crucial for the properties of the molecule and thus also for the properties of the overall photocatalytic system. In addition, the bridge component naturally also has an impact on the synthetic route for the construction of such a molecule, which will be discussed in more detail in the following section. The bridge building block also has a decisive influence on the electronic coupling between the two functionalities and thus contributes, on the one hand, to how likely an intramolecular electron transfer between the two molecular components is and, on the other hand, how likely a possible electron back transfer is. This back transfer would have a negative effect on the lifetime of the reduced catalyst and thus ultimately on the photocatalytic performance of the overall system. To avoid this and to reduce the electronic coupling between the dyad components, a bridge building block with two π-conjugation blockers (see **Fig. 30**) was used. In addition, two dyads, each with different lengths of the bridge building blocks, were produced and examined in order to investigate the influence of the bridge length on the performance of the overall system. A longer bridge between the dyad components should further minimise the electronic coupling.

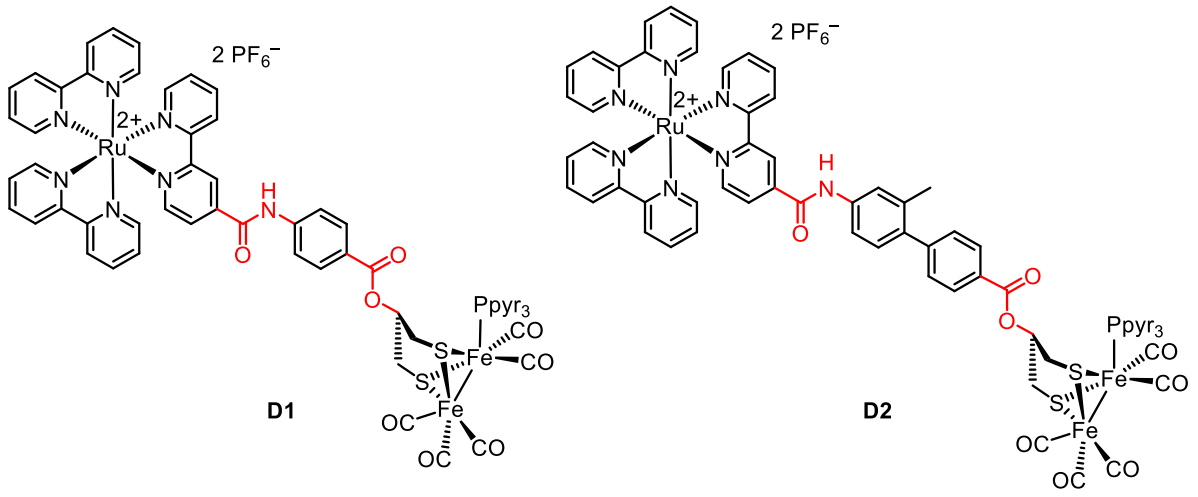

Fig. 30 Photocatalytically active dyads **D1** and **D2**. The amide and ester bonds within the molecules act as π-conjugation blockers and are highlighted in red.

Following the considerations just described, the photocatalytically active dyads **D1** and **D2** shown in **Fig. 30** are synthesised and examined below. These are based on the one hand on the 3CS with the highest photocatalytic performance investigated in the previous chapter, which consists besides the **[Ru(bpy)$_3$]Cl$_2$** photosensitiser and the ascorbic acid sacrificial electron donor of the Ppyr$_3$ phosphinated complex **[FeFe]-Cat 5** catalyst with a propanedithiolate ligand. On the other hand, these molecules are based on the work of Sun and Åkermark, who presented a very similar dyad in 2003 (see **Fig. 31**) and thus showed a viable synthetic route for the dyad systems desired in this work.[56]

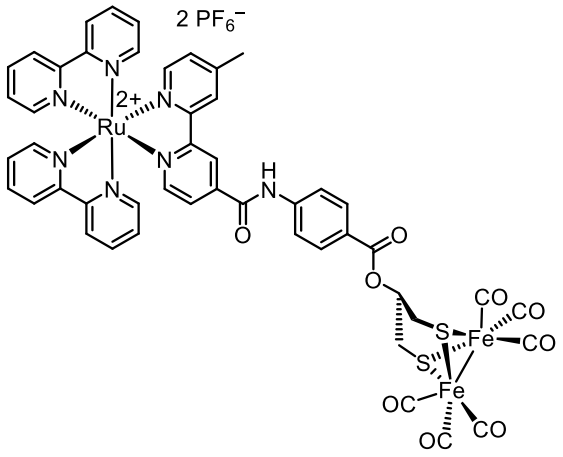

Fig. 31 Photocatalytic dyad developed by Sun and Åkermark in 2003.[56]

Similar as in the literature system, in **D1** and **D2** the bridge spacer is covalently connected *via* an amide bond to one of the three bipyridine ligands of the ruthenium complex and on the catalyst side *via* an ester bond to the dithiolate ligand of the [FeFe] catalyst. Both bonds act as π-conjugation blockers in the dyads to reduce the electronic coupling between the individual components. **D1** and **D2** differ structurally only in the number of phenyl rings installed in the

spacer and thus ultimately in the distance between the photosensitiser part and the catalyst part. In order to avoid a planar arrangement of the biphenyl spacer in **D2**, an additional methyl substituent was attached in the ortho position of a phenyl ring.

5.1.1 Synthesis

As mentioned above, the synthesis of the dyads **D1** and **D2** is based on that for a very similar molecule from Sun and Åkermark.[56] The advantage of this synthetic route is that not all of the individual components of the dyad molecule have to be at first synthesised individually and then linked together by coupling reactions, as one might expect from retrosynthetic considerations. Actually, the [FeFe] catalyst is built up directly on the bridge spacer, which also constitutes the starting point of the synthesis, and in the end only the ruthenium complex has to be connected by a simple amide linkage. To make this possible, at first an acid function in the 4-position must be attached to one bipyridine ligand of the ruthenium complex and then an appropriately acid-functionalised ruthenium complex has to be built up with this. The corresponding synthesis route for **D1** is shown in **Fig. 32**, **Fig. 33** and **Fig. 34**.

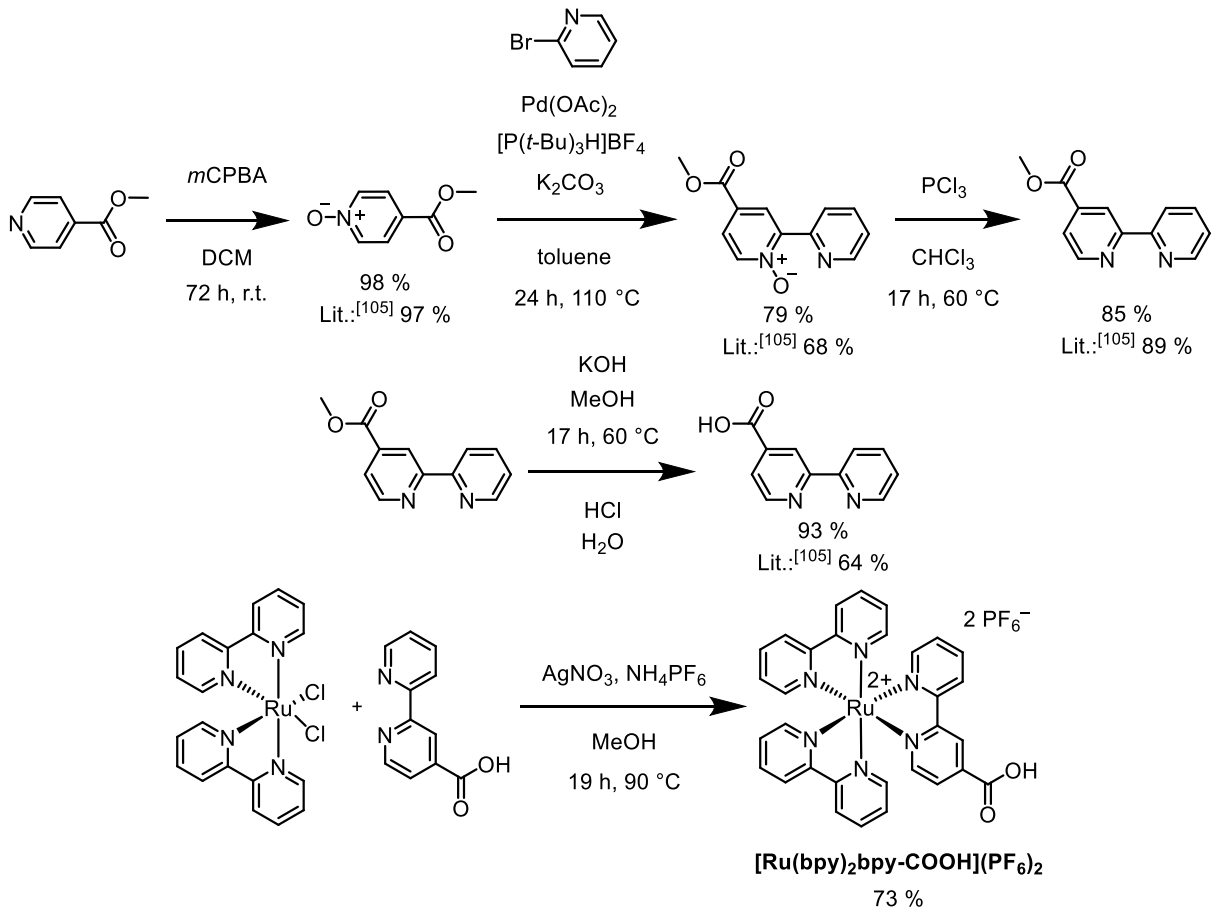

Fig. 32 Synthesis of acid-functionalised **[Ru(bpy)$_2$bpy-COOH](PF$_6$)$_2$**.

Starting with the synthesis of the ruthenium complex, the formation of the desired acid-functionalised 2,2'-bipyridine ligand followed the literature known procedure of Vasta and Raines.[105] First, methyl isonicotinate was oxidised by *meta*-chloroperoxybenzoic acid in a dry DCM solution at r.t. to form **4-(methoxycarbonyl)pyridine 1-oxide**. The yield of this reaction was with 98 % almost quantitative. **4-(Methoxycarbonyl)pyridine 1-oxide**, now equipped with the *N*-oxide as a strongly in the 2-position directing group, was subsequently linked with 2-bromopyridine to form **4-(methoxycarbonyl)-[2,2'-bipyridine] 1-oxide** in a palladium-catalysed cross-coupling reaction with a yield of 79 %. Then the molecule was reduced by trichlorophosphane to **methyl [2,2'-bipyridine]-4-carboxylate** in 85 % yield. Afterwards, the product was treated with potassium hydroxide in methanol in order to deprotect the carboxylic acid, which was finally reacidified by hydrochloric acid. A yield of 93 % could be achieved in this reaction. The actual ruthenium complex was then prepared by treating $[Ru(bpy)_2]Cl_2$ with silver nitrate and the subsequent addition of **(2,2'-bipyridine)-4-carboxylic acid** to form the red orange solid **$[Ru(bpy)_2bpy\text{-}COOH](PF_6)_2$** with a yield of 73 %. This reaction is based on similar ruthenium complex formations by Vauzeilles and Aukauloo, in which slightly different bipyridine ligands were added.[106]

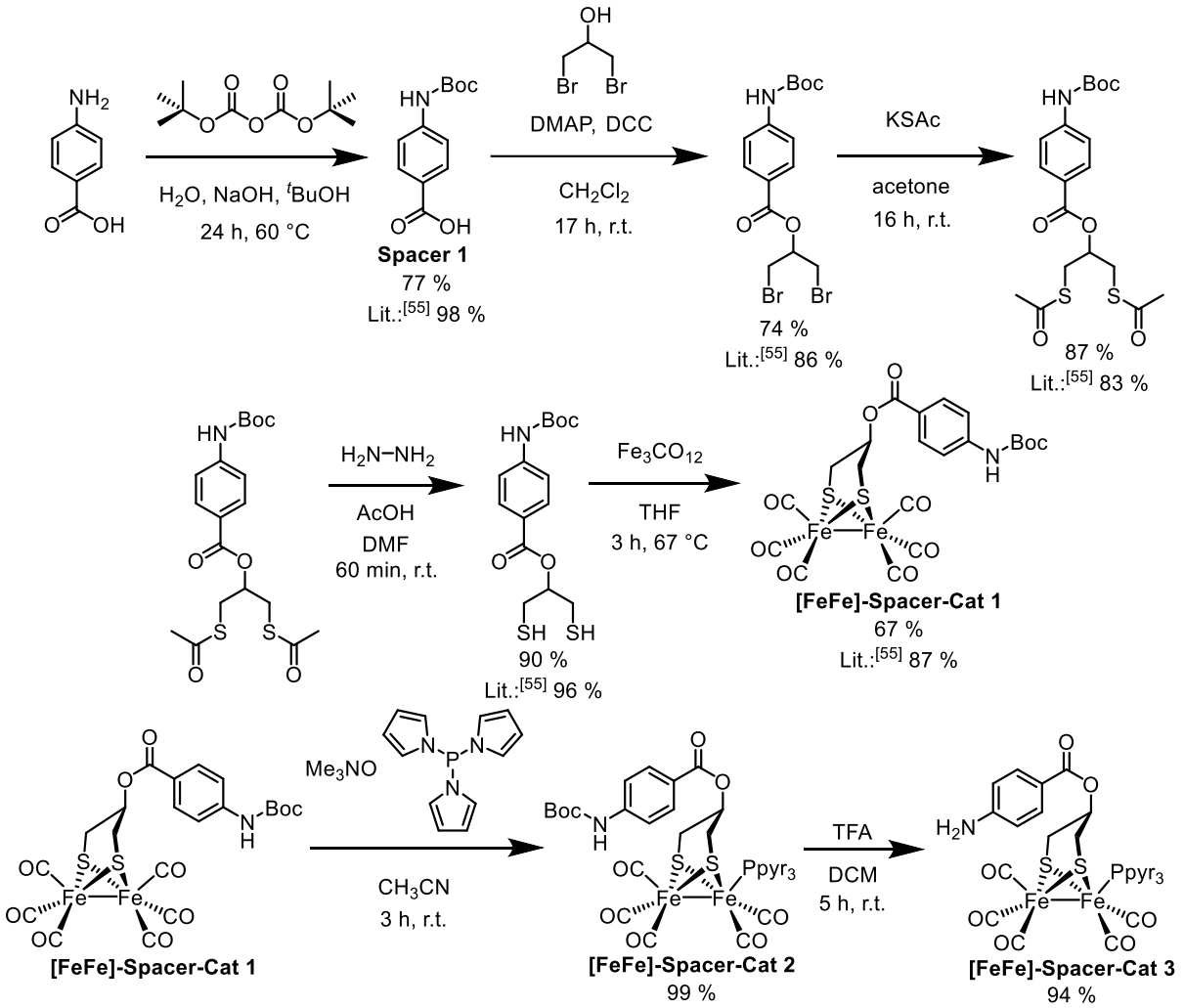

Fig. 33 Synthesis of **[FeFe]-Spacer-Cat 3**.

As mentioned above, after the synthesis of the ruthenium photosensitiser part, the [FeFe] catalyst moiety was built up directly on the bridge spacer. The synthetic route chosen largely followed that of Sun and Åkermark for a very similar molecule.[55] In order to implement the desired ester function between the bridge and the catalyst part, it was started from *p*-aminobenzoic acid. The first step in the synthesis was to protect the nucleophilic amino function by attaching a Boc protecting group in a reaction with di-*tert*-butyl dicarbonate under alkaline conditions. A yield of 77 % was achieved in this reaction. Then a Steglich esterification with 1,3-dibromopropan-2-ol took place with the catalytic use of DCC and DMAP to form the corresponding 1,3-dibromopropan-2-yl compound in 74 % yield. Subsequently, both bromine atoms were replaced by thioacetate groups in a nucleophilic substitution reaction with potassium thioacetate in 87 % yield. Thereafter, the dithioacetate molecule was treated with hydrazine in acetic acid solution, whereby the corresponding dithiol was obtained in 90 % yield. Analogous to the synthesis of the [FeFe]-hydrogenase mimics described in the previous chapter, the reaction of the dithiol in THF solution with triiron dodecacarbonyl gave **[FeFe]-Spacer-Cat 1** in 67 % yield. Deviating from the route of Sun and Åkermark, in the next step a CO ligand was initially cleaved by the action of trimethylamine *N*-oxide and was then replaced *in situ* by $Ppyr_3$ in the reaction with **tris(1*H*-pyrrol-1-yl)phosphine**. This phosphination reaction could be accomplished almost quantitatively and was based on the corresponding reactions described in the previous chapter for the synthesis of the [FeFe]-hydrogenase mimic compounds. In the last step, the Boc protecting group was finally cleaved off by the reaction with trifluoroacetic acid to give **[FeFe]-Spacer-Cat 3** in 94 % yield.

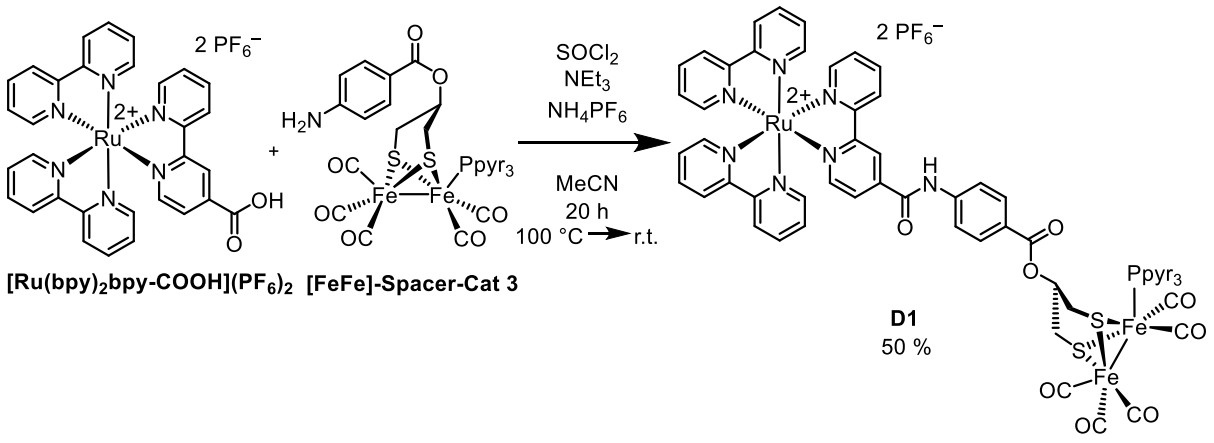

Fig. 34 Formation of photocatalytically active dyad **D1** by coupling of **[Ru(bpy)$_2$bpy-COOH](PF$_6$)$_2$** and **[FeFe]-Spacer-Cat 3**.

With the preparation of **[Ru(bpy)$_2$bpy-COOH](PF$_6$)$_2$** and **[FeFe]-Spacer-Cat 3** both building blocks for the dyad were synthesised. Now, the final step was the linkage of the two molecules under the formation of an amide bond, as it is shown in **Fig. 34**. To do this, the acid function of **[Ru(bpy)$_2$bpy-COOH](PF$_6$)$_2$** had to be first activated *in situ* by heating in thionyl chloride to

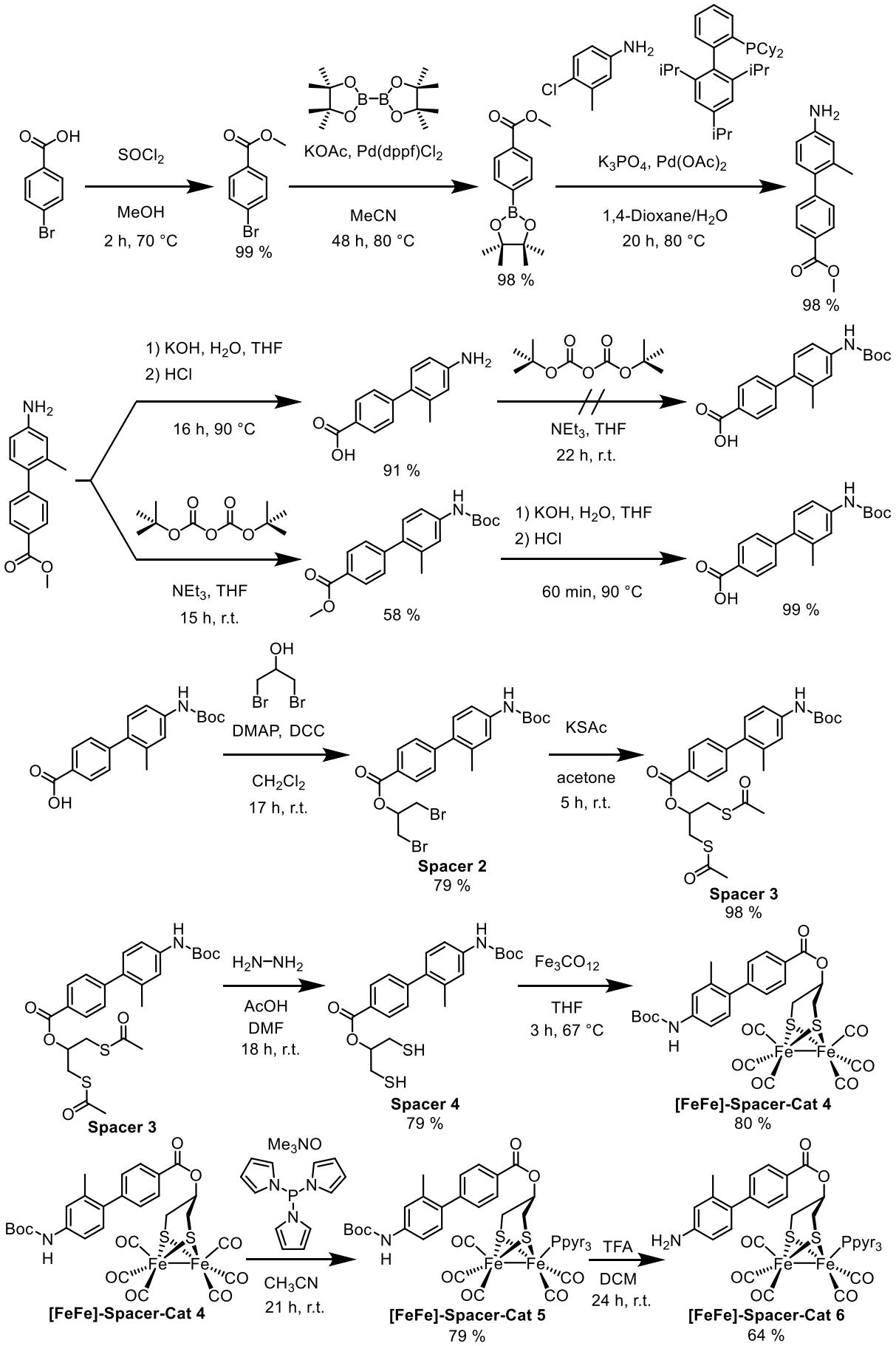

Fig. 35 Synthesis of **[FeFe]-Spacer-Cat 6**.

form the corresponding carboxylic acid chloride. After removing the excess thionyl chloride, **[FeFe]-Spacer-Cat 3** and triethylamine for trapping the resulting hydrogen chloride were added in acetonitrile as solvent. After stirring at r.t. for 20 hours, the formed crude product was purified by flash column chromatography using silica gel as stationary phase and a mixture of acetonitrile, water and sat. aqueous KNO_3 solution (*v*/*v*/*v* = 90:5:5) as eluent in order to assure a sufficient solubility of the cationic dyad molecule on the column. Finally, the red crystalline product was obtained by reprecipitation from aqueous NH_4PF_6 solution.

The synthesis of the elongated **D2** dyad was largely analogous to that of **D1** with the exception that the biphenyl spacer had to be constructed first. **Fig. 35** shows the corresponding synthetic route to **[FeFe]-Spacer-Cat 6** and **Fig. 36** the final coupling with **[Ru(bpy)$_2$bpy-COOH](PF$_6$)$_2$** to **D2**. The biphenyl unit was produced by Suzuki coupling of a correspondingly borylated methyl benzoate with 4-chloro-3-methylaniline, based on the procedure described by Levy *et al*.[107] The additional methyl group on the aniline should serve to twist both phenyl rings in such a way that they are as perpendicular as possible to one another, thus minimising the electronic interaction of the two π-systems and further decreasing the electronic coupling within the dyad by introducing this additional nodal plane. In preparation for the coupling reaction, the acid function of the commercially available 4-bromobenzoic acid was initially protected by the almost quantitative reaction of thionyl chloride in methanol. Whereby, the esterification was carried out by a nucleophilic attack of the solvent on the carboxylic acid chloride formed *in situ* with thionyl chloride. In the next step, the molecule prepared in this way was converted into the corresponding methyl benzoate boronate in a classic Miyaura borylation in 98 % yield. The reaction based on the proceeding of Li *et al*.[108] As just mentioned, the next step was to produce the biphenyl through a Suzuki coupling with 4-chloro-3-methylaniline. Palladium(II) acetate was used as a pre-catalyst in combination with XPhos as a Buchwald ligand. The latter makes the active catalyst extremely sterically demanding, which in turn leads to an increased stereoselectivity of the palladium-catalysed cross-coupling reaction. The yield of this coupling was markedly high at 98 %.

Analogous to the synthesis of **D1** and the method of Sun *et al.*,[56] the carboxylic acid function should first be deprotected and then the amino function be protected by a Boc protecting group. However, this procedure led to a problem when the protecting group was introduced. Only the *tert*-butyl ester product of the reaction of the free acid group with di-*tert*-butyl dicarbonate could be detected in this reaction. Since this decarboxylation takes place under acid catalysis,[109] the excess triethylamine added was apparently not sufficient to prevent this. For this reason, the order of the steps was reversed and the amino function was first protected by the reaction with di-*tert*-butyl dicarbonate in THF in the presence of triethylamine. The acid function, which was still protected, could not cause a side reaction this time. Nevertheless, the yield was

comparatively low at 58 %. The methyl ester was then saponified in almost quantitative yield by boiling in aqueous basic potassium hydroxide solution. During the final acidification with hydrochloric acid, however, care had to be taken to ensure that the solution did not become too acidic in order to avoid premature acid-catalysed removal of the Boc protecting group.

All subsequent reactions up to **[FeFe]-Spacer-Cat 6** were completely analogous to the **D1** synthesis. The yields of the individual reaction steps were good to very good, as shown in **Fig. 35**. Likewise, the amide linkage to the **D2** dyad was in accordance with the previous **D1** synthesis, as can be seen in **Fig. 36**. The achieved and comparatively lower yield of 42 % is probably due to the more sterically demanding diiron reagent.

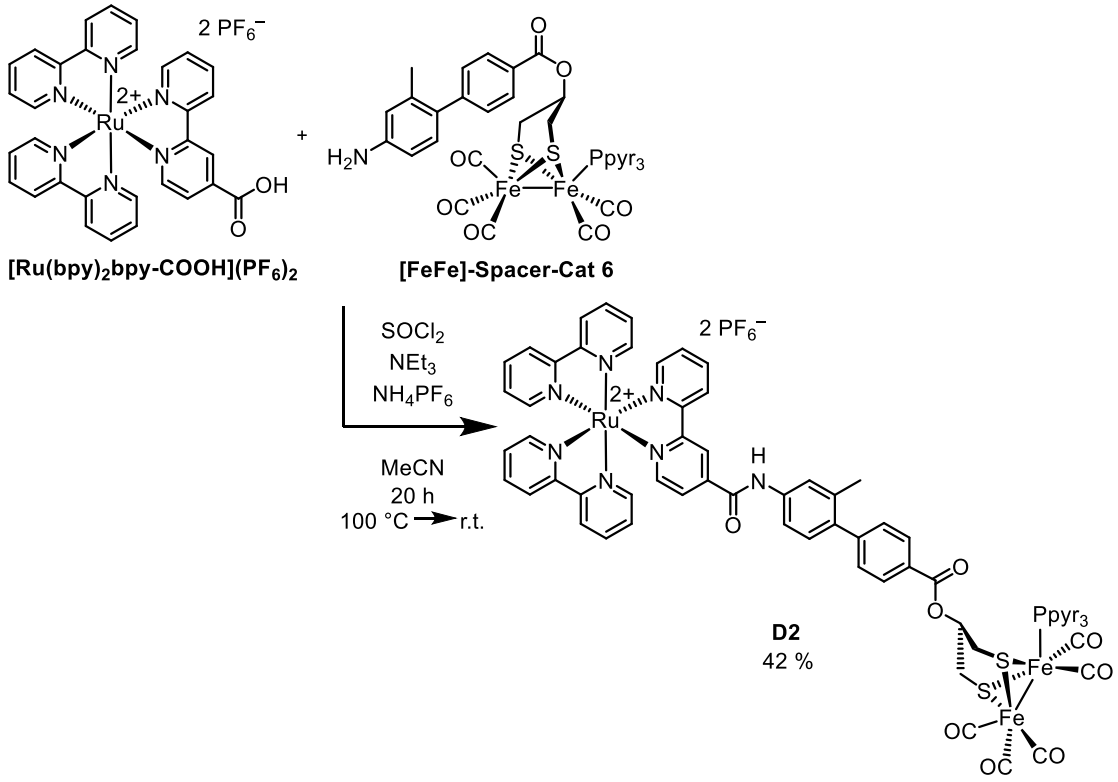

Fig. 36 Formation of photocatalytically active dyad **D2** by coupling **[Ru(bpy)$_2$bpy-COOH](PF$_6$)$_2$** and **[FeFe]-Spacer-Cat 6**.

5.1.2 Steady-State Absorption Spectroscopy

In order to characterise the spectroscopic features of both the dyads synthesised and the corresponding molecular components, UV/Vis absorption spectra of **[FeFe]-Spacer-Cat 2**, **[FeFe]-Spacer-Cat 5**, **[Ru(bpy)$_3$]Cl$_2$**, **D1** and **D2** in water were recorded. The Boc-protected [FeFe] complex precursors were used for reasons of chemostability. As in case of the dyad molecules, these were solubilised in poly(2-oxazoline) micelles so that they could be measured in aqueous solution and thus in the same environment as in photocatalysis. To prepare the $1 \cdot 10^{-5}$ M solutions, 20.0 mg of the polymer was used for each of the 10.0 ml solutions. The

spectra of **D1** and its corresponding components are depicted in **Fig. 37**, those of **D2** and the corresponding single molecules in **Fig. 38**. For a better comparison of the two systems, all spectra are compared in **Fig. 39**.

The absorption spectrum of **[FeFe]-Spacer-Cat 2** consists of two main features. On the one hand, there are the spectroscopic characteristics of the core [FeFe] complex with its intense iron-centred Fe(σ)-Fe(σ^*) transition at 29000 cm^{-1} (345 nm) and the weak Fe(t_{2g})-Fe(σ^*) transition ranging from 17000 cm^{-1} (590 nm) to 22500 cm^{-1} (444 nm). On the other hand, there is the dominant and quite broad π-π^*-transition of the phenyl spacer moiety at 36000 cm^{-1} (278 nm). The ruthenium photosensitiser shows a very intense absorption band at 35000 cm^{-1} (286 nm), which can be assigned to the ligand-centred (LC) π-π^* transition.[16] Furthermore, there is a relative broad characteristic absorption feature in the visible region ranging from 18000 cm^{-1} (556 nm) to 26600 cm^{-1} (376 nm) with a peak signal at 22000 cm^{-1} (455 nm) and a shoulder signal at 23400 cm^{-1} (427 nm). This feature can be assigned to metal-to-ligand charge transfer (MLCT) transitions, which are of particular importance for the processes examined in this work, since they represent in principle the first steps of the electron cascade from the photosensitiser to the catalyst. This is also the reason why the examined photocatalytic systems are excited with light within this spectral range (see chapter 5.1.7). The weak low-energy absorption tailing below 20000 cm^{-1} (> 500 nm) derives from the spin-forbitten ^{3}MLCT transition, whereas the prominent features above this value arise from the spin-allowed ^{1}MLCT transition.[16]

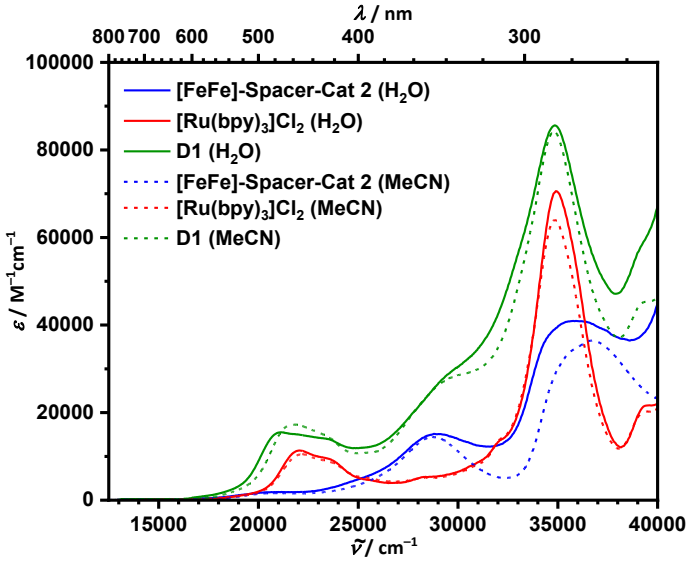

Fig. 37 UV/Vis absorption spectra of **[FeFe]-Spacer-Cat 2**, **[Ru(bpy)$_3$]Cl$_2$** and **D1** measured in water (solid lines) and acetonitrile (dashed lines) at 298 K. **[FeFe]-Spacer-Cat 2** and **D1** were solubilised by poly(2-oxazoline) micelles for the measurements in water.

The absorption spectrum of the dyad **D1** appears at first glance as the sum of its individual components. On closer inspection, however, there are some differences. In addition to a significant broadening and only a slight red shift of the dominant LC π-π^* absorption to 34800 cm^{-1} (287 nm) and a suspected red shift of the spacer-centred π-π^* excitation, due to the weakly formed shoulder at 36300 cm^{-1} (275 nm), especially the peak of the MLCT band shows a clear red shift to 21100 cm^{-1} (474 nm) and the iron-centred transition a blue shift under the shoulder at 29900 cm^{-1} (334 nm). It can be concluded from this that the underlying energy levels have changed due to an existing electronic coupling between the individual components within the dyad. In order to exclude an influence of the poly(2-oxazoline) micelles especially on the spectroscopic features of the ruthenium photosensitiser, which was not solubilised as single molecule but as part of the dyad, all compounds were additionally measured in acetonitrile without any polymer assistance. As can be seen in **Fig. 37**, all abovementioned effects emerge also without the use of the micelles. Although, some of them are more pronounced as in case of the red shifted spacer-centred π-π^* excitation and some are less intense as in case of the red shifted MLCT band. A smaller red shift and a weaker broadening can also be seen at the LC π-π^* transition. That demonstrates that the solubilisation has an impact on the energy levels of the components, which is evident, for example, by comparing both spectra of **[FeFe]-Spacer-Cat 2**. Nevertheless, the spectrum of the dyad molecule shows the same spectroscopic changes compared to those of its components, which clearly underlines the influence of the electronic coupling described above.

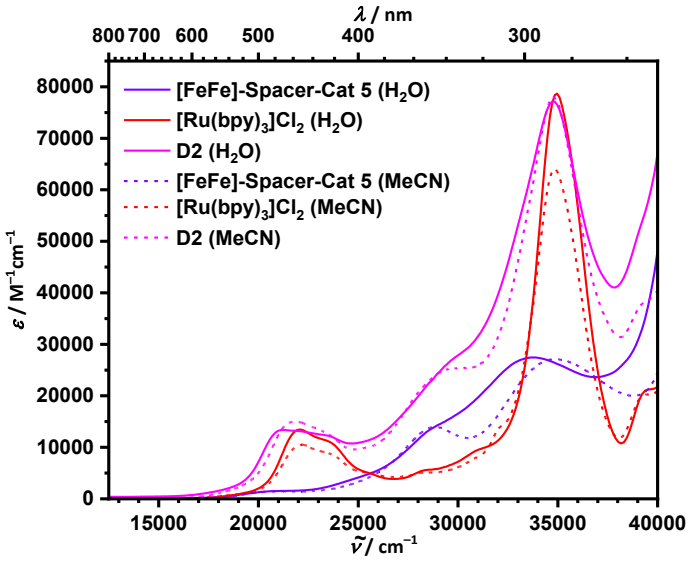

Fig. 38 UV/Vis absorption spectra of **[FeFe]-Spacer-Cat 5**, **$[Ru(bpy)_3]Cl_2$** and **D2** measured in water (solid lines) and acetonitrile (dashed lines) at 298 K. **[FeFe]-Spacer-Cat 5** and **D2** were solubilised in poly(2-oxazoline) micelles for the measurements in water.

As can be seen in **Fig. 38**, the same effects occur in the spectra for **D2** and its corresponding individual components. **[FeFe]-Spacer-Cat 5** shows at 28800 cm^{-1} (347 nm) the Fe(σ)-Fe(σ^*) transition as a shoulder signal and at 33800 cm^{-1} (296 nm) the intense and broad π-π^* transition of the biphenyl spacer moiety. The for a [FeFe] complex typical weak absorption band of the Fe(t_{2g})-Fe(σ^*) transition occurs between 17200 cm^{-1} (581 nm) and 22200 cm^{-1} (450 nm). The absorption spectrum of **D2** presents a quite strong red shifted MLCT absorption band ranging from 15100 cm^{-1} (662 nm) to 24700 cm^{-1} (405 nm) with a peak signal at 21200 cm^{-1} (472 nm). The iron-centred Fe(σ)-Fe(σ^*) transition appears as a blue shifted shoulder signal at 30000 cm^{-1} (333 nm). The dominant bipyridine-centred π-π^* transition at 34800 cm^{-1} (287 nm) is in relation to the corresponding absorption band of **$[Ru(bpy)_3]Cl_2$** slightly bathochromic shifted. Hence, all spectral features of the dyad show the same alterations in relation to the spectra of its components as it was the case for **D1**. As was to be expected, solubilisation also has an influence on the spectra, as the comparison to the absorption spectra in acetonitrile without the addition of poly(2-oxazoline) shows (see **Fig. 38**). Nonetheless, the solubilisation only causes a change in the already existing spectral shifts, which were certainly caused by the electronic coupling between the individual dyad components. This finding already gives a first insight into the influence of the extended bridge spacer and thus the increased distance between the photosensitiser part and the catalyst part of the dyad on the electronic coupling between these components. Obviously, despite the increased distance in **D2**, there is still a coupling between the components comparable to that in **D1**. In the following sections, further investigations will show whether this also manifests itself in other substance properties and how this affects the photocatalytic performance in particular.

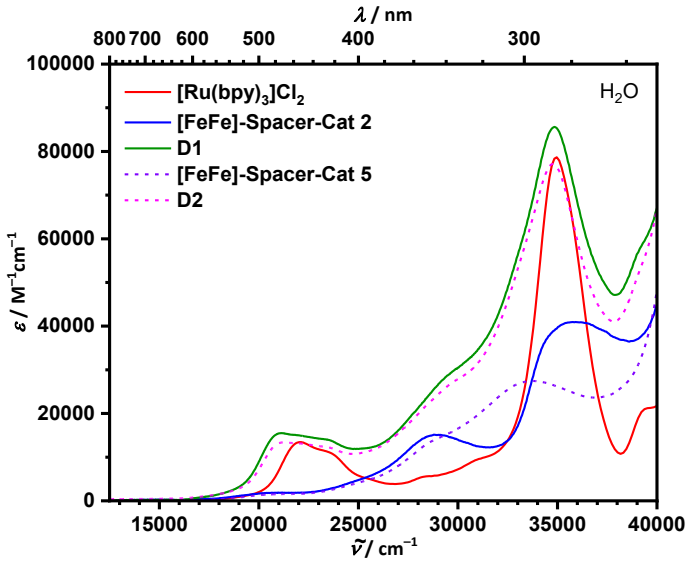

Fig. 39 UV/Vis absorption spectra of **[FeFe]-Spacer-Cat 2**, **[FeFe-Spacer-Cat 5**, **$[Ru(bpy)_3]Cl_2$**, **D1** and **D2** measured in water at 298 K. **[FeFe]-Spacer-Cat 2**, **[FeFe]-Spacer-Cat 5**, **D1** and **D2** were solubilised in poly(2-oxazoline) micelles.

The comparison between the absorption spectra of **D1** and **D2** or their individual components shown in **Fig. 39** can be used to examine the extent to which the expansion of the bridge spacer affects the spectral properties of the dyad molecule.

Apart from the somewhat weaker absorbance of **D2** and both a slight red shift in the LC π-π^* absorption of **D2** with respect to **D1** and a slight blue shift of the corresponding MLCT bands, the two spectra show no major differences. This is mainly due to the fact that the greatest spectral difference is completely overlaid by the broadened LC π-π^* absorptions in the dyad molecules. As can only be seen in the comparison between **[FeFe]-Spacer-Cat 2** and **[FeFe]-Spacer-Cat 5**, the extension of the bridge spacer by replacing the phenyl unit with a biphenyl unit causes a comparatively large bathochromic shift in the π-π^* transition of that moiety.

5.1.3 Electrochemistry

To determine the redox potentials of the dyad compounds and their corresponding individual components, **D1**, **D2**, **[Ru(bpy)$_3$]Cl$_2$**, **[FeFe]-Spacer-Cat 2** and **[FeFe]-Spacer-Cat 5** were examined by cyclic voltammetry. As solvent acetonitrile was used in all cases because, in addition to sufficient solubility of the substances examined, it also ensured a comparatively large measuring window. The cyclic voltammograms of **D1**, **[FeFe]-Spacer-Cat 2** and **[Ru(bpy)$_3$]Cl$_2$** are displayed in **Fig. 40**, them of **D2**, **[FeFe]-Spacer-Cat 5** and **[Ru(bpy)$_3$]Cl$_2$** in **Fig. 41**. The corresponding electrochemical data are reported in **Table 2**.

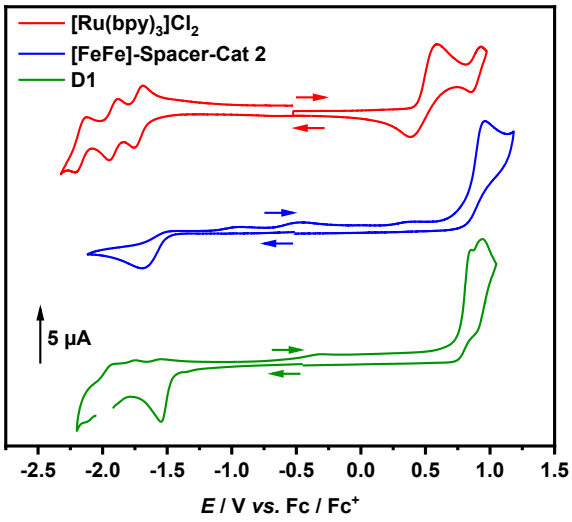

Fig. 40 Cyclic voltammograms of **[Ru(bpy)$_3$]Cl$_2$** (1 mM), **[FeFe]-Spacer-Cat 2** (1 mM) and **D1** (1 mM) in an acetonitrile solution (0.1 M TBAHFP) at 298 K. In the curve of **D1** an artefact at –2.0 V *vs.* Fc/Fc$^+$ caused by electrochemical processes at the cathode during measurement is omitted. Experimental setup: Pt as WE, Pt as CE, Ag/AgCl as reference, scan rate: v = 100 mV s^{-1}.

The recorded curve of **[Ru(bpy)$_3$]Cl$_2$** shows at negative potentials clearly the typical three reversible reduction waves, which arise each from the reduction of a bpy ligand.[16,19,110] Therefore, the first signal at –1.72 V *vs.* Fc/Fc$^+$ corresponds to the reduction of one bpy ligand,

the second signal at –1.91 V *vs.* Fc/Fc^+ to the further reduction of another ligand and the signal at –2.16 V *vs.* Fc/Fc^+ to the redox process which leads to a ruthenium complex with three reduced bpy ligands. At positive potentials there are two oxidation processes visible in the voltammogram. A pseudo-reversible wave at 0.49 V *vs.* Fc/Fc^+ and a reversible oxidation at 0.89 V *vs.* Fc/Fc^+. The latter can be assigned to a metal-centred oxidation process and thus referred to the Ru^{III}/Ru^{II} redox couple, whereas the pseudo-reversible signal derives from the oxidation of the two chloride anions and is therefore disregarded for further contemplations.[19,110,111] The cyclic voltammogram of **[FeFe]-Spacer-Cat 2** shows in contrast to that of the ruthenium species less features. At –1.69 V *vs.* Fc/Fc^+ there is an irreversible reduction which is typical for a [FeFe] complex and belongs to the Fe^IFe^I/Fe^0Fe^I redox couple. In direction of the anodic reversal potential there is an irreversible oxidation at 0.96 V *vs.* Fc/Fc^+ associated with the corresponding $Fe^{II}Fe^I/Fe^IFe^I$ redox couple.

The dyad **D1** shows in its cyclic voltammogram at first glance all features of both individual components examined before, as it was expected. However, on closer consideration all of these redox processes occur at different potentials compared to that of the corresponding single molecules. For instance, the irreversible Fe^IFe^I/Fe^0Fe^I reduction appears at –1.55 V *vs.* Fc/Fc^+ which means an anodic shift of 0.14 V in relation to the corresponding reduction of **[FeFe]-Spacer-Cat 2** and the $Fe^{II}Fe^I/Fe^IFe^I$ oxidation arises at 0.86 V *vs.* Fc/Fc^+ with a cathodic shift of 0.10 V. Also, the photosensitiser-based redox processes have experienced potential shifts. The somewhat weak reversible Ru^{III}/Ru^{II} oxidation at 0.92 V *vs.* Fc/Fc^+ appears with a relatively small anodic shift of 0.03 V. The three reversible bpy oxidations are at least visible but not very well resolved and partially overlaid by other features, so that a sufficient determination of the corresponding potentials is not possible at this point. Nevertheless, in a direct comparison with the curve of **$[Ru(bpy)_3]Cl_2$** slightly shifts of the corresponding waves are discernible. That means that the covalent bonding of both dyad parts influences the redox potentials in part intensely, which underlines the abovementioned findings of the absorption spectroscopic investigations. Although the determined potentials of the irreversible processes at the diiron units also depend on the corresponding diffusion coefficients, which for the individual [FeFe] catalysts will certainly differ significantly from those of the dyads.[112] A direct comparison between these values of the [FeFe] complexes and the dyads is therefore not possible. Nevertheless, especially the measured anodic shift of the iron-centred reduction of **D1** could probably indicate an increase of the corresponding $E^{0'}$ [D1-Cat/D1-Cat$^-$] redox potential, which is important for the photocatalytic process. The extent to which this is advantageous for photocatalysis also depends to a large degree on the energetic position of the redox potential of the excited photosensitiser, which is examined in more detail in the following sections.

The influence of increasing the intramolecular distance between the photosensitiser and the catalyst is examined below in the electrochemical analysis of **D2** and the corresponding individual components **[FeFe]-Spacer-Cat 5** and **[Ru(bpy)$_3$]Cl$_2$**.

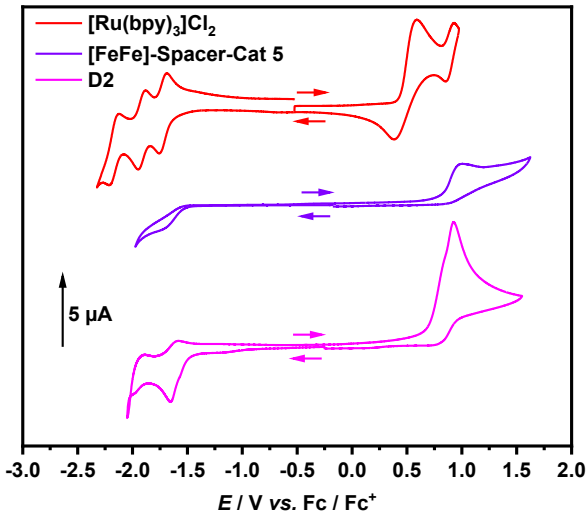

Fig. 41 Cyclic voltammograms of **[Ru(bpy)$_3$]Cl$_2$** (1 mM), **[FeFe]-Spacer-Cat 5** (1 mM) and **D2** (1 mM) in an acetonitrile solution (0.1 M TBAHFP) at 298 K. Experimental setup: Pt as WE, Pt as CE, Ag/AgCl as reference, scan rate: v = 100 mV s^{-1}.

The cyclic voltammogram of the diiron compound **[FeFe]-Spacer-Cat 5** shows the typical irreversible $Fe^{I}Fe^{I}/Fe^{0}Fe^{I}$ reduction at –1.77 V *vs.* Fc/Fc$^+$ and the irreversible $Fe^{II}Fe^{I}/Fe^{I}Fe^{I}$ oxidation at 0.99 V *vs.* Fc/Fc$^+$. Compared to that of **[FeFe]-Spacer-Cat 2**, a slightly cathodic shift for the reduction and a slightly anodic shift of the oxidation due to the exchange of the aromatic substituent within the dithiolate ligand can be observed. The recorded curve of the dyad **D2** exhibits at negative potentials the irreversible $Fe^{I}Fe^{I}/Fe^{0}Fe^{I}$ reduction at –1.65 V *vs.* Fc/Fc$^+$ and one of the reversible bpy-based reductions at –1.95 V *vs.* Fc/Fc$^+$. At positive potentials there is only the irreversible $Fe^{II}Fe^{I}/Fe^{I}Fe^{I}$ oxidation at 0.93 V *vs.* Fc/Fc$^+$ visible. However, based on the observations for **D1**, the oxidation located at the ruthenium core does not seem to be influenced as intensely as the iron-based redox processes by the covalent coupling of the photosensitiser part and the catalyst part. For this reason, the reversible Ru^{III}/Ru^{II} oxidation in **D2** is probably overlaid by the more intense iron-based oxidation. By comparing the redox processes of **D2** with those of **[FeFe]-Spacer-Cat 5**, the same effects can be observed as with **D1**, except that the shifts are slightly smaller in case of **D2**. The $Fe^{I}Fe^{I}/Fe^{0}Fe^{I}$ reduction has undergone an anodic shift of 0.12 V and the $Fe^{II}Fe^{I}/Fe^{I}Fe^{I}$ oxidation a cathodic shift of 0.06 V. This means that the redox potentials in **D2** are still significantly influenced by the coupling of the two dyad components, but not as strongly as for **D1**. The extent to which this is due to the greater distance between the dyad components in **D2** and the associated lower electronic coupling between them or to the changed diffusion coefficient cannot be discussed further at this point. However, the comparison between the

two dyads suggests that the iron-based $E^{0'}$ [D2-Cat/D2-Cat^{-}] redox potential, which is important for photocatalysis, is not reduced as much for **D2** as for **D1**, as can be seen in **Fig. 42**. As already mentioned above, the effect of this on photocatalysis still depends on the redox potential of the excited photosensitiser, which is examined in the following sections.

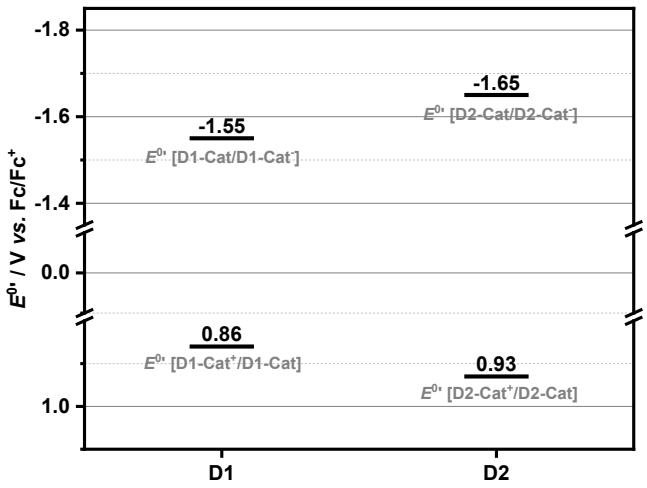

Fig. 42 Scheme of ground state redox potentials $E^{0'}$ of **D1** and **D2** referring to iron-based redox processes.

Table 2 Electrochemical data of **[Ru(bpy)$_3$]Cl$_2$**, **[FeFe]-Spacer-Cat 2**, **[FeFe]-Spacer-Cat 5**, **D1** and **D2** measured by cyclic voltammetry in an acetonitrile solution (0.1 M TBAHFP) at 298 K.

Compound	E_{red} (V *vs.* Fc/Fc$^+$)			E_{ox} (V *vs.* Fc/Fc$^+$)	
	E_{pc-3}	E_{pc-2}	E_{pc-1}	E_{pa-1}	E_{pa-2}
[Ru(bpy)$_3$]Cl$_2$	–2.16[a]	–1.91[a]	–1.72[a]	0.49[b]	0.89[a]
[FeFe]-Spacer-Cat 2			–1.69	0.96	
[FeFe]-Spacer-Cat 5			–1.77	0.99	
D1			–1.55	0.86	0.92[a]
D2		–1.95	–1.65	0.93	

[a] $E_{1/2}$ of reversible reduction resp. oxidation. [b] Pseudo-reversible oxidation.

5.1.4 Estimation of Excited State Redox Potentials

For assessing and classifying the redox processes that take place during photocatalysis in the 2CS and the dyad molecules contained therein in comparison to the corresponding 3CS, the redox potentials of the components involved play a decisive role. In order that the electron transfer steps between the individual components take place from a thermodynamic point of view, the corresponding redox potentials must meet the in chapter 2.4 listed conditions, which can also be used to compare different systems with one another. For a better overview, the relevant thermodynamic conditions are repeated at this point. Assuming reductive quenching (RQ), the following must apply to the corresponding initiative reduction of the excited photosensitiser (PS) by the sacrificial electron donor (SD):[14]

$$E^{0'}\,[SD^{+}/SD] < E^{0'}\,[PS^{*}/PS^{-}] \quad (3)$$

For the subsequent electron transfer from the reduced photosensitiser to the catalyst, the required thermodynamic condition can be described as follows:

$$E^{0'}\,[PS/PS^{-}] < E^{0'}\,[Cat/Cat^{-}] \quad (4)$$

For systems in which oxidative quenching (OQ) predominates, however, the excited photosensitiser reduces the catalyst in the first step, which can be described under thermodynamic conditions with the following stipulation for the redox potentials:

$$E^{0'}\,[PS^{+}/PS^{*}] < E^{0'}\,[Cat/Cat^{-}] \quad (5)$$

The conditions for the subsequent re-reduction of the oxidised photosensitiser by the sacrificial electron donor can accordingly be formulated as follows:

$$E^{0'}\,[SD^{+}/SD] < E^{0'}\,[PS^{+}/PS] \quad (6)$$

As can be seen from the equations above, a ranking comparison of several photocatalytically active systems requires not only the ground state redox potentials but also that of the excited photosensitiser inserted. Bernhard *et al.* applied a method in which it is possible to estimate these using the results from the electrochemical analysis and emission spectroscopic data.[24] The basis for this is that the 0-0 energy determined from the emission spectrum represents the energy gap between the ground state potentials and that of the excited state. Starting from the reduction potential of the photosensitiser $E^{0'}\,[PS/PS^{-}]$, the reduction potential of the excited state $E^{0'}\,[PS^{*}/PS^{-}]$ can be estimated by formally adding the energy gap. Accordingly, formal subtraction of the amount of the energy gap leads from the oxidation potential of the photosensitiser $E^{0'}\,[PS^{+}/PS]$ to the estimated oxidation potential of the excited state $E^{0'}\,[PS^{+}/PS^{*}]$.

The excited state redox potentials of **[Ru(bpy)$_3$]Cl$_2$** as well as of the photosensitiser parts of **D1** and **D2** were estimated using the emission spectra shown in **Fig. 43**. The 0-0 energies were determined using the tangential method by applying a tangent to the higher-energy side of the emission spectrum. The intersection with the x-axis gives the estimated 0-0 energy. The results are reported in **Table 3**.[113]

With the values thus estimated, the thermodynamic conditions of the individual systems listed above can be assessed. With an oxidation potential $E^{0'}\,[SD^{+}/SD]$ of ascorbic acid as sacrificial electron donor of 0.07 V *vs.* Fc/Fc^{+}[47] and assuming that the systems investigated perform the photocatalysis *via* the RQ mechanism, it follows that both the 2CS and the corresponding 3CS clearly meet the condition described in equation 3. Due to the very similar values of the reduction potential of the excited photosensitiser, the different systems differ only marginally

from one another. With $\Delta E_{RQ\text{-}1}$ values from 0.40 V to 0.49 V, all exhibit very high thermodynamic driving forces for the initial electron transfer. On the other hand, if it would be assumed that the systems operate under the OQ mechanism, then all considered systems with the values obtained from cyclic voltammetry definitely do not fulfil the condition for a thermodynamically feasible process shown in equation 5. Even if the value for $E^{0'}$ [D2-PS$^+$/D2-PS*] of **D2** could only be roughly estimated due to the overlapping of the Ru^{III}/Ru^{II} oxidation by the iron-based $Fe^{II}Fe^{I}/Fe^{I}Fe^{I}$ oxidation in the corresponding cyclic voltammogram and therefore ultimately the value of the latter process has to be used as the basis. From this it can be deduced that all systems examined here clearly prefer the RQ mechanism over the OQ mechanism for thermodynamic reasons.

Table 3 Excited state redox properties of ruthenium containing compounds.

Compound	$E^{0'}$ [PS$^+$/PS*] (V *vs.* Fc/Fc$^+$)	$E^{0'}$ [PS*/PS$^-$] (V *vs.* Fc/Fc$^+$)	0-0 energy[a] (eV)
[Ru(bpy)$_3$]Cl$_2$	–1.34	0.51	2.23
D1	–1.19	0.56	2.11
D2	–1.19	0.47	2.12

[a] Estimation from emission spectrum (see **Fig. 43**).

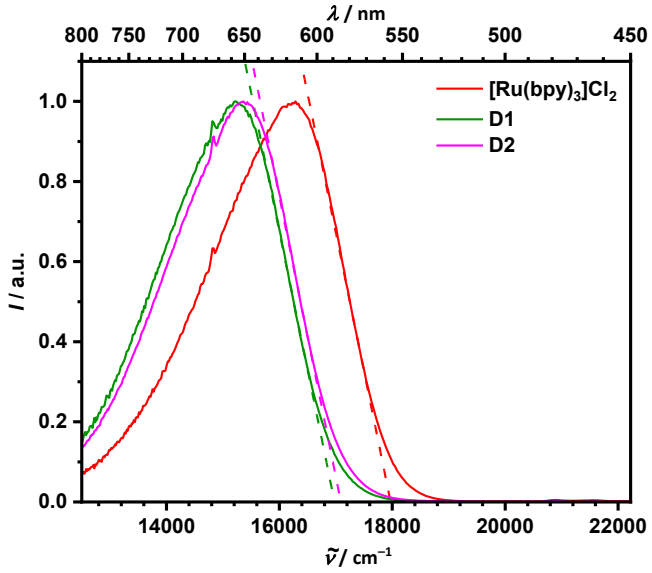

Fig. 43 Normalised emission spectra of **[Ru(bpy)$_3$]Cl$_2$**, **D1** and **D2** measured in degassed acetonitrile solution at 298 K. The samples were excited at λ_{ex} = 23900 cm^{-1} (419 nm). Tangents for the 0-0 energy estimation are given in dashed lines.

When considering the second electron transfer within the framework of the RQ mechanism, which represents the intramolecular transfer process in case of the dyad molecules, the systems behave differently than in the previously considered cases, as it was expected. The 3CS with **[FeFe]-Spacer-Cat 2** as catalyst fulfils the thermodynamic condition described in equation 4 relatively scarcely with $\Delta E_{RQ\text{-}2}$ = 0.03 V. In contrast, the corresponding values for the 3CS with **[FeFe]-Spacer-Cat 5** violate this condition just as closely with ΔE = –0.05 V. In

light of the fact that the values obtained from the cyclic voltammograms of the [FeFe] complexes are based only on irreversible redox processes and these only allow a rough estimate regarding the underlying redox potentials, it can only be said that in this case there is a significantly higher energy barrier in both systems for the second electron transfer than for the first one. This means that in case of the two 3CS, the first step represents the thermodynamic driving force of photocatalysis and the second step the rate-determining step within the electron cascade.

The situation is somewhat more difficult for the dyad molecules. On the one hand, there is also the restriction just mentioned that the observed irreversible redox processes of the diiron moieties only allow rough estimates of the underlying redox potentials. On the other hand, there is the problem with **D1** and **D2** that due to the poor resolution of the photosensitiser-based reductions in the corresponding cyclic voltammograms, it cannot be determined with certainty whether the signal for the first bpy reduction is overlaid by that of the $Fe^{I}Fe^{I}/Fe^{0}Fe^{I}$ reduction or whether the next signal in the cathodic direction represents that for the first bpy reduction. Due to the weakly pronounced anodic peak potential immediately above the irreversible [FeFe] reduction in **D1** and **D2** (see **Fig. 40** and **Fig. 41**), it was assumed that the signal for the first bpy reduction is superimposed by the $Fe^{I}Fe^{I}/Fe^{0}Fe^{I}$ reduction. At that point it can only be presumed that both reduction potentials are very similar and that a situation comparable to that in the corresponding 3CS results. Nevertheless, it can be deduced from this that both considered 2CS behave similarly to the corresponding 3CS with regard to the redox potentials involved. The first redox process represents the thermodynamic driving force and the second the rate-determining step of the photocatalysis. A decisive difference between **D1** and **D2** or between the corresponding 3CS could not be determined under the abovementioned conditions.

5.1.5 Emission Quenching Studies

Another method to prove that the photocatalysis in both the 2CS and the associated 3CS operates *via* the RQ mechanism is to investigate whether the photosensitiser emission is quenched by the sacrificial electron donor. In case of a present RQ mechanism, such emission quenching studies can also provide information about the kinetics of the initial electron transfer in the photocatalysis process and thus of the energy barrier of this crucial step. Therefore, the excited state quenching of the ruthenium compounds in combination with ascorbic acid as sacrificial electron donor and quencher was investigated. For this purpose, first the emission spectra and phosphorescence lifetimes of **$[Ru(bpy)_3]Cl_2$**, **D1** and **D2** were recorded in water. A 25-fold mass excess of the poyl(2-oxazoline) polymer (see **Fig. 14**) was used for both dyad compounds, on the one hand to ensure adequate solubilisation of the compounds in the aqueous environment and on the other hand to create conditions comparable to those in

photocatalysis. Ascorbic acid was then added to these solutions and the emission spectra as well as the time resolved phosphorescence decay curves were measured with subsequent increased quencher concentration. The spectra and selected decay traces thus obtained are shown in **Fig. 44** and **Fig. 45** and the corresponding lifetimes are reported in **Table 4**.

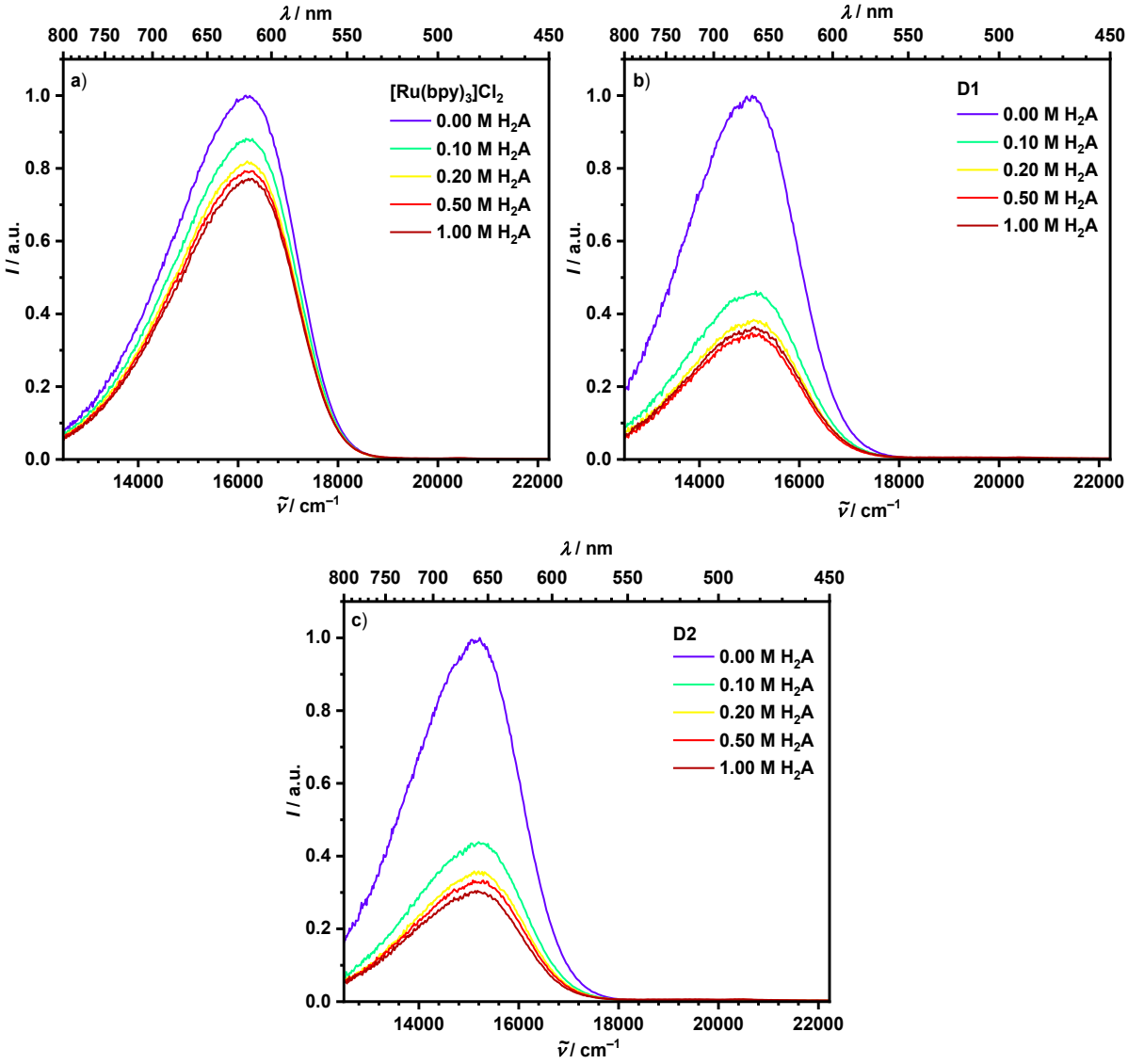

Fig. 44 Normalised emission spectra of **a) [Ru(bpy)$_3$]Cl$_2$**, **b) D1** and **c) D2** in degassed water with increasing amount of ascorbic acid (H_2A) as quencher at 298 K. **D1** and **D2** were solubilised with a poly(2-oxazoline) polymer (see **Fig. 14**). The samples were excited at λ_{ex} = 23900 cm^{-1} (419 nm).

Table 4 Phosphorescence lifetimes of **[Ru(bpy)$_3$]Cl$_2$**, **D1** and **D2** without and with subsequently increasing ascorbic acid (H_2A) concentration in water at 298 K. **D1** and **D2** were solubilised with a poly(2-oxazoline) polymer (see **Fig. 14**). The samples were excited at λ_{ex} = 23900 cm^{-1} (419 nm).

Compound	$c(H_2A)$ 0.00 M		0.10 M		0.20 M		0.50 M		1.00 M	
	τ_1 (ns)	τ_2 (ns)	τ_1 (ns)	τ_2 (ns)	τ_1 (ns)	τ_2 (ns)	τ_1 (ns)	τ_2 (ns)	τ_1 (ns)	τ_2 (ns)
[Ru(bpy)$_3$]Cl$_2$	286	768	215	528	182	473	156	369	144	320
D1	336	701	190	512	149	406	142	376	147	363
D2	317	781	215	528	182	473	156	369	147	322

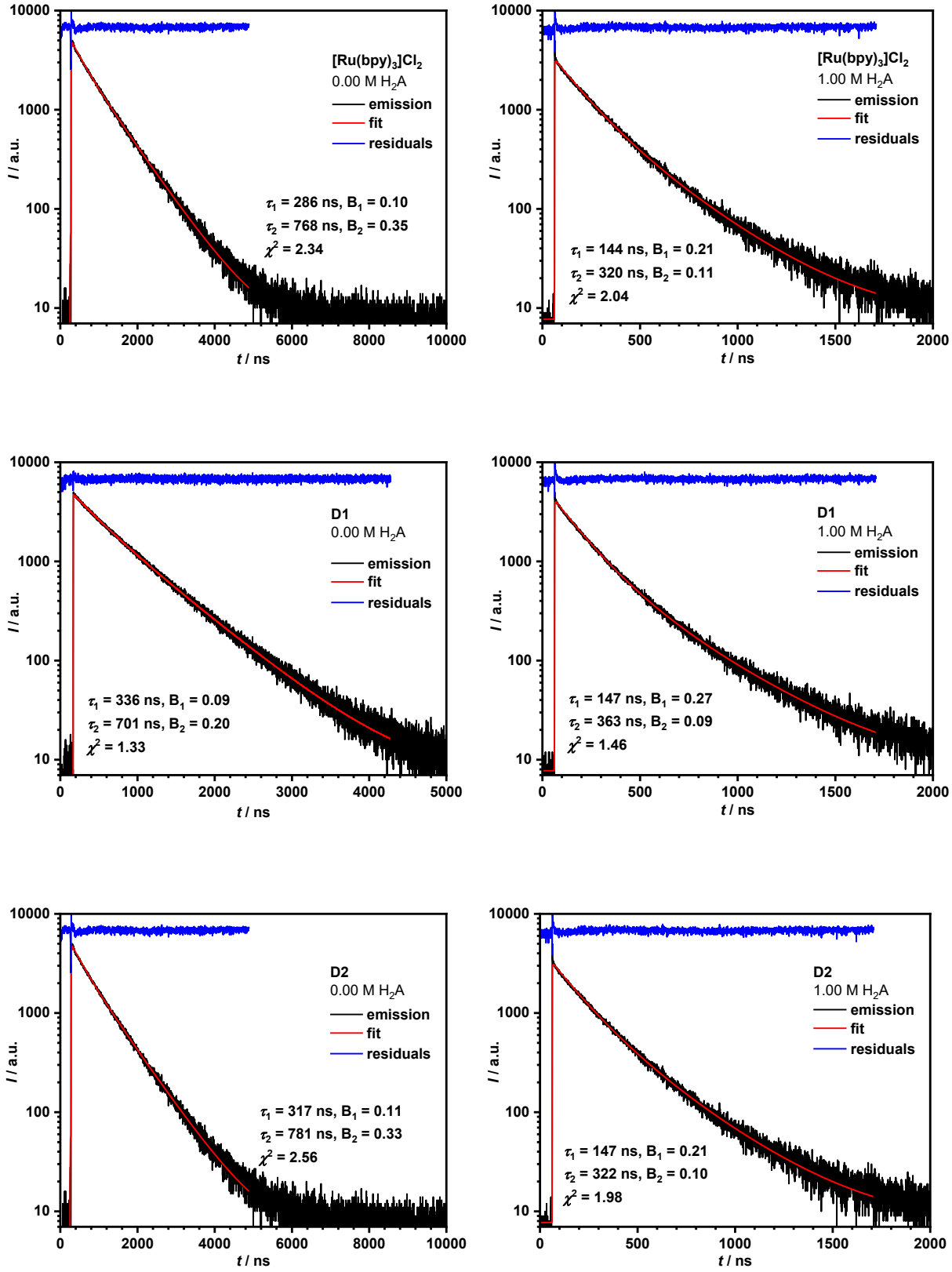

Fig. 45 Phosphorescence kinetics of **[Ru(bpy)$_3$]Cl$_2$** (first line), **D1** (second line) and **D2** (third line) without a quencher (left side) and with 1.00 M ascorbic acid (H_2A) (right side) in water at 298 K. **D1** and **D2** were solubilised with a poly(2-oxazoline) polymer (see **Fig. 14**). The samples were excited at λ_{ex} = 23900 cm^{-1} (419 nm). The kinetic traces were fitted to a second order decay by deconvolution.

In order to achieve the emission kinetics of the particular compounds, the corresponding phosphorescence decay curves obtained (see **Fig. 45**) were fitted by deconvolution using the following biexponential term:

$$R(t) = B_1 e^{\left(-\frac{t}{\tau_1}\right)} + B_2 e^{\left(-\frac{t}{\tau_2}\right)} \quad (9)$$

The values for the coefficients B, the lifetimes τ and the goodness of fit χ^2 of the individual fits can be found in the corresponding diagrams in **Fig. 45**.

All investigated ruthenium compounds exhibit two lifetimes and both of them are affected by ascorbic acid, which is why both were considered for this study. The one generated by a faster decay process ranges from 286 ns for **[Ru(bpy)$_3$]Cl$_2$** to 336 ns for **D2** in absence of a quencher and that caused by a slower mechanism accordingly ranges from 701 ns for **D1** to 781 ns for **D2**. Assuming dynamic quenching, the bimolecular rate constant for dynamic quenching k_d can be calculated with the ratio of lifetimes of non-quenched and quenched excited states (τ_0/τ) using the Stern-Volmer equation:

$$\frac{I_0}{I} = \frac{\tau_0}{\tau} = K_d[Q]+1 = k_d \tau_0[Q]+1 \quad (10)$$

By plotting τ_0/τ against the quencher concentration [Q], the Stern-Volmer constant K_d can be determined from the slope of the ideally linear curve. This can then be used to calculate k_d by using the unquenched lifetime τ_0. However, equation 10 only applies to dynamic quenching with a monoexponential emission decay, i.e. one that can be described by only one lifetime τ. Therefore, the measured lifetimes were first plotted individually in the corresponding Stern-Volmer plots shown in **Fig. 46**.

When looking at the diagrams shown in **Fig. 46**, it is striking that for all the ruthenium compounds considered, the ratio of lifetimes τ_0/τ plotted against the quencher concentration [Q] follows in its progression an exponential approximation instead of a linear regime which would be expected for classic dynamic quenching. This means that the systems still behave relatively common in the sense of the expected dynamic quenching and according to equation 10 at low quencher concentrations. At higher concentrations, however, the systems approach a state in which further addition of quencher molecules only leads to a reduced or no further attenuation of the phosphorescence. Since the emission do not shift in the course of the measurement series, as can be seen in **Fig. 44**, a possible decomposition of the reduced ruthenium species generated by ascorbic acid can be excluded. Static quenching can also be ruled out due to the fact that the emission lifetime changes when the quencher is added. In addition, the fact that when the plateau-quencher concentrations are reached, the phosphorescence is not completely quenched and thus unquenched ruthenium compounds

are still present in the solutions, speaks against the appearance of a type of saturation concentration at which all emitting molecules are quenched immediately by the quencher molecules. Rather, the observed behaviour indicates that the quenching cannot be adequately described with the simplified model of dynamic quenching on which the linear Stern-Volmer equation is based.

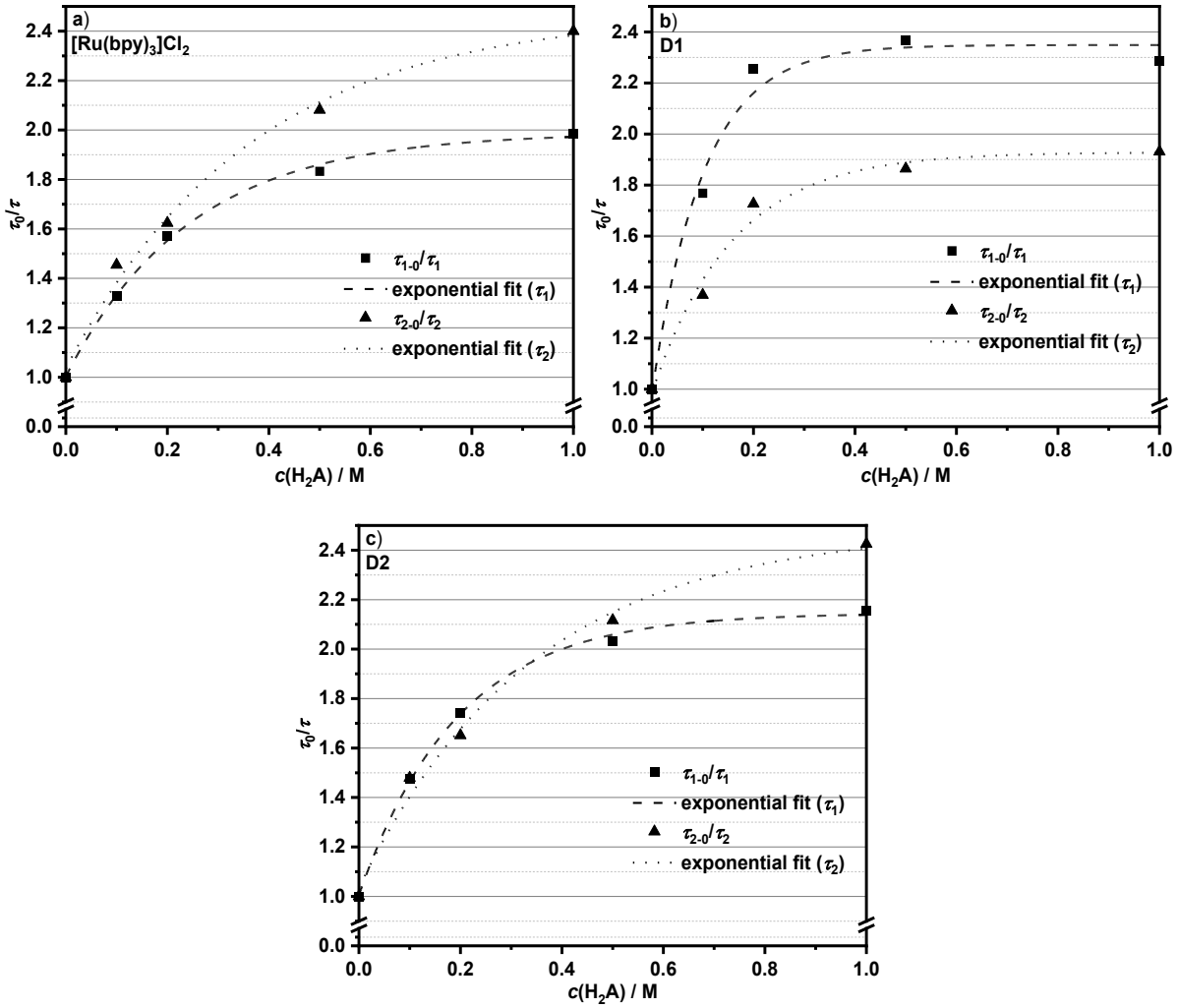

Fig. 46 Stern-Volmer plots of the measured lifetimes τ_1 and τ_2 of **a) [Ru(bpy)$_3$]Cl$_2$**, **b) D1** and **c) D2** in water with ascorbic acid (H_2A) as quencher. **D1** and **D2** were solubilised with a poly(2-oxazoline) polymer during the measurements (see **Fig. 14**). The non-linearity of the τ_0/τ ratios is illustrated with the help of exponential fits.

Similar behaviour has already been observed with ruthenium compounds in combination with oxygen as quencher, which were used as optical oxygen sensors.[114] Due to matrix effects, in which the corresponding molecules were embedded and immobilised, significantly more complex models had to be used to describe the quenching processes. Although the dyad molecules **D1** and **D2** were solubilised in water using poly(2-oxazoline) micelles, **[Ru(bpy)$_3$]Cl$_2$** also showed the same effects without the use of micelles, which is probably why they are not the cause of this behaviour. The origin is more likely to be found in the biexponential emission decay of the ruthenium compounds, because a non-linear course in the Stern-Volmer plot for

compounds with a multiexponential emission decay is not entirely unknown. On the one hand, Lakowicz *et al.*, for example, were also able to show a deviation from the linear Stern-Volmer behaviour through various emission quenching experiments with *p*-bis-[2-(5-phenyloxazolyl)]-benzene.[115] By comparing different quenching models, the authors were able to show that the multiexponential quenching behaviour can no longer only be described by the simple collisional quenching model, but that this is also influenced by other factors such as e.g. the fluorophore-quencher distance and transient effects. On the other hand, Sillen and Engelborghs were able to show mathematically using a simple model system with a biexponential emission decay that averaging the lifetimes can also lead to a non-linear course in the Stern-Volmer diagram.[116] Although the existence of three or four lifetimes of the ruthenium compounds could be excluded by negligibly small or negative values of the corresponding coefficients B during the fitting of the decay curves, this could nevertheless indicate that the lifetimes obtained are dependent on other factors in some way. However, these dependencies could not be resolved at this point.

Another problem that occurs in systems with multiexponential emission decay is that each lifetime often exhibits its own quenching rate constant k_d. When considering the initial slopes of the Stern-Volmer plots shown in **Fig. 46**, this also applies to the ruthenium systems considered in this work. In order to better deal with the results of this quenching study and to better classify them, a simplification would be advantageous. As already mentioned above, Sillen and Engelborghs have investigated precisely on this topic to what extent lifetimes can usefully be averaged without the results being falsified.[116] They were able to show that it is possible to calculate the average collisional quenching constant $\langle k_d \rangle_f$ with the help of the so-called intensity average lifetime $\langle \tau \rangle_f$. The deviation from the actual dynamic quenching constant k_d was minimal with this method. The intensity average lifetime $\langle \tau \rangle_f$ in a system with a biexponential emission decay is defined as follows:[116]

$$\langle \tau \rangle_f = \frac{B_1 \tau_1^2 + B_2 \tau_2^2}{B_1 \tau_1 + B_2 \tau_2} \tag{11}$$

It is formed from the two measured lifetimes τ_1 and τ_2 and the associated coefficients B_1 and B_2 and represents the average amount of time the emitting compound spends in the excited state. By including the coefficients B_1 and B_2, it is an average weighted by the contribution of the respective lifetime.[116] From equation 11 it follows that analogously to τ_1 and τ_2 also $\langle \tau \rangle_f$ is a function of [Q]. Therefore, the corresponding intensity average lifetime $\langle \tau \rangle_f$ was thus initially formed with the aid of equation 11 for each quencher concentration [Q]. The corresponding data for **[Ru(bpy)$_3$]Cl$_2$**, **D1** and **D2** are given in **Table 5** and the Stern-Volmer plots generated from them are shown in **Fig. 47**.

Table 5 Intensity average lifetimes $\langle\tau\rangle_f$ of **[Ru(bpy)$_3$]Cl$_2$**, **D1** and **D2** without and with subsequently increasing ascorbic acid (H_2A) concentration in water at 298 K. The data were calculated using equation 11 and the values from **Table 4**.

Compound	$c(H_2A)$ 0.00 M $\langle\tau\rangle_f$ (ns)	0.10 M $\langle\tau\rangle_f$ (ns)	0.20 M $\langle\tau\rangle_f$ (ns)	0.50 M $\langle\tau\rangle_f$ (ns)	1.00 M $\langle\tau\rangle_f$ (ns)
[Ru(bpy)$_3$]Cl$_2$	722	328	280	254	239
D1	636	307	250	234	245
D2	726	328	280	254	236

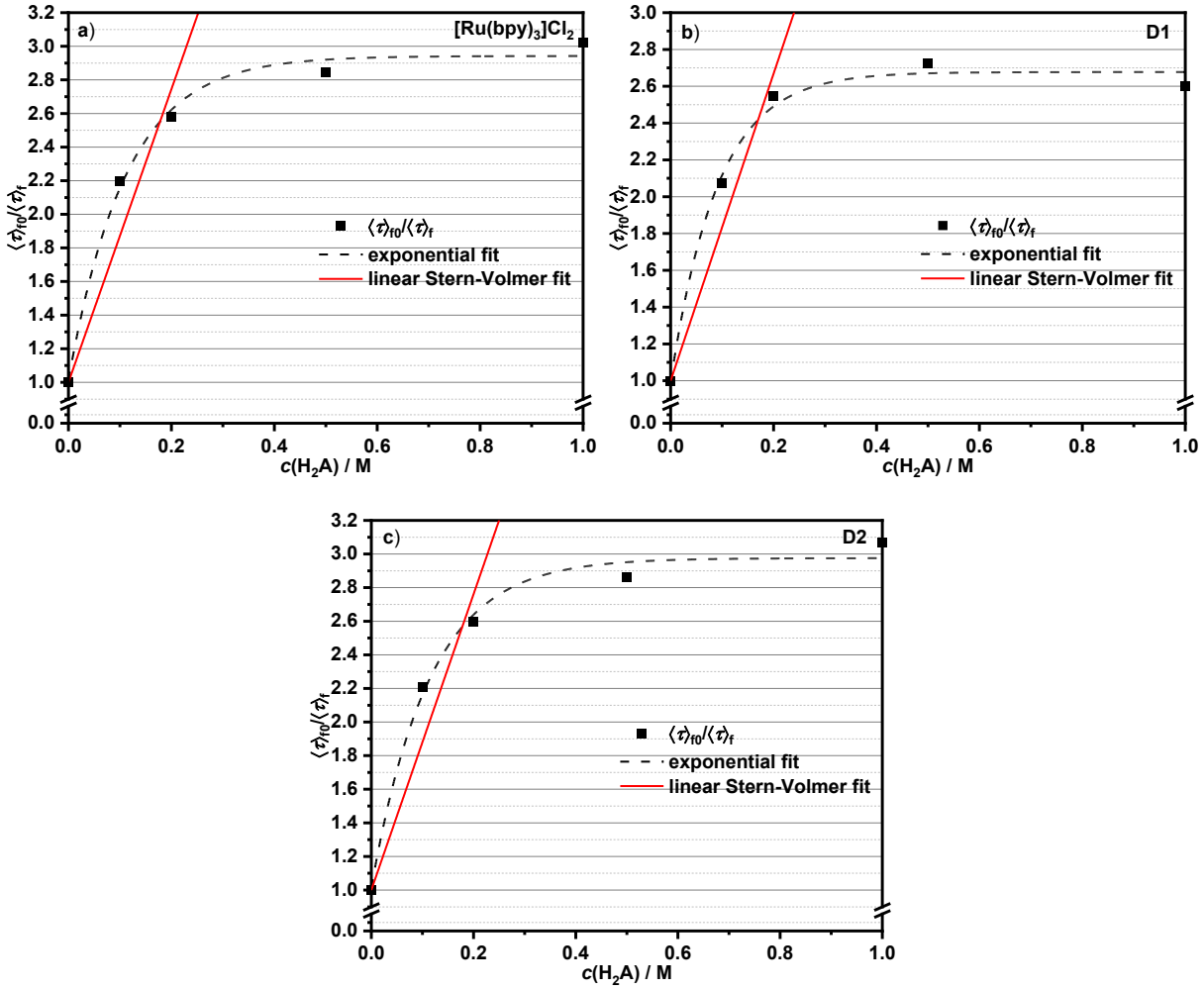

Fig. 47 Stern-Volmer plots of the intensity average lifetimes $\langle\tau\rangle_f$ of **a) [Ru(bpy)$_3$]Cl$_2$**, **b) D1** and **c) D2** in water with ascorbic acid (H_2A) as quencher. **D1** and **D2** were solubilised with a poly(2-oxazoline) polymer during the measurements (see **Fig. 14**). For linear Stern-Volmer fits (red lines) the first three data points were used. All linear fits in Stern-Volmer plots have $R^2 \geq 0.99$.

As was to be expected, all Stern-Volmer plots shown in **Fig. 47** exhibit the non-linearity previously observed for the individual lifetimes. Since the concentrations of ascorbic acid used as sacrificial electron donor in photocatalysis were located in the lower region of the range investigated in this study, the simple dynamic quenching model was nevertheless assumed for the sake of simplicity. As can be seen in the Stern-Volmer plots in **Fig. 47** and already

mentioned, the results obtained in these areas agree relatively well with this linear model. Though, this simplification must be taken into account in the results of this study, which is why they should only be regarded as an approximation rather than as fixed quantities.

Analogously to the relationship given in equation 10, the average Stern-Volmer constant $\langle K_d \rangle_f$ can be determined from the slope of the linear Stern-Volmer fit shown in **Fig. 47**. As Sillen and Engelborghs were able to show, the average collisional quenching constant $\langle k_d \rangle_f$ can now be calculated with the aid of the intensity average lifetime $\langle \tau \rangle_{f0}$ in absence of the quencher:[116]

$$\langle k_d \rangle_f = \frac{\langle K_d \rangle_f}{\langle \tau \rangle_{f0}} \tag{12}$$

The corresponding results for **[Ru(bpy)$_3$]Cl$_2$**, **D1** and **D2** are reported in **Table 6**.

Table 6 Average quenching kinetics of **[Ru(bpy)$_3$]Cl$_2$**, **D1** and **D2** with ascorbic acid as quencher in water at 298 K. **D1** and **D2** were solubilised with a poly(2-oxazoline) polymer (see **Fig. 14**).

Compound	$\langle K_d \rangle_f$[a] (M^{-1})	$\langle \tau \rangle_{f0}$ (ns)	$\langle k_d \rangle_f$ (M^{-1} s^{-1})
[Ru(bpy)$_3$]Cl$_2$	8.72	722	$1.21 \cdot 10^7$
D1	8.34	636	$1.31 \cdot 10^7$
D2	8.80	726	$1.21 \cdot 10^7$

[a] Determined from linear Stern-Volmer fit using the first three data points in the corresponding Stern-Volmer plot (see **Fig. 47**).

First of all, the results of the study clearly show that the luminescence of all investigated ruthenium compounds is reduced by the addition of ascorbic acid. This again emphasises the findings that could be obtained by considering the ground state redox potentials and that of the excited photosensitiser, which state that the examined systems operate the photocatalysis *via* the RQ mechanism. In addition, the determined rate constants $\langle k_d \rangle_f$ for dynamic quenching show that the values of the three compounds differ only slightly from each other. This is also in line with the findings from the previous section. **[Ru(bpy)$_3$]Cl$_2$** exhibits a $\langle k_d \rangle_f$ value of $1.21 \cdot 10^7$ M^{-1} s^{-1}, which matches quite well with the literature value obtained in water[16] and therefore basically confirms the abovementioned approximations made for this study. **D1** shows a $\langle k_d \rangle_f$ value of $1.31 \cdot 10^7$ M^{-1} s^{-1} and **D2** a $\langle k_d \rangle_f$ value of $1.21 \cdot 10^7$ M^{-1} s^{-1}. Since all these values are several orders of magnitude below the usual diffusion rates of such aqueous solutions (10^{10}–10^{11} M^{-1} s^{-1}),[117] this shows that the initial reduction of the photosensitiser by the sacrificial electron donor does not take place in a diffusion-controlled manner, but is determined by the corresponding electron transfer barriers of the components involved in this step. In general, the reduction barrier between the sacrificial electron donor and the ruthenium sensitiser in the 3CS and in the dyad system does not seem to differ significantly due to the very similar rate constants of the various systems investigated. Small differences only become apparent on closer inspection. The rate constant for the dyad **D1** is somewhat higher than for

the **[Ru(bpy)$_3$]Cl$_2$** system. Obviously, the spacer-catalyst moiety in **D1** attached *via* an amide function lowers the reduction barrier of the ruthenium complex in direct comparison to the individual **[Ru(bpy)$_3$]Cl$_2$** molecule. This could be explained by the fact that this residue withdraws electron density from the photosensitiser to a certain extent. This effect is apparently somewhat reduced by the extension of the spacer unit in **D2**. As a result, the elongated dyad **D2** exhibits the same electron transfer barrier than the **[Ru(bpy)$_3$]Cl$_2$** molecule. However, it must be pointed out again that, on the one hand, the differences obtained between the systems are very small and, on the other hand, due to the necessary simplifications described above, these results should rather be regarded as an approximation.

5.1.6 ns-Transient Absorption Spectroscopy

In order to gain a deeper insight into the processes during photocatalysis and in particular into the initial electron transfer of the assumed RQ mechanism, transient absorption (TA) spectroscopic investigations were carried out. This time-resolved pump-pulse laser spectroscopic analysis method allows a view on the intermediates formed within a certain time window and, by measuring their associated decay curves, also the determination of their lifetimes.

In this work TA measurements were carried out by using a ns-laser setup on **[Ru(bpy)$_3$]Cl$_2$** and the dyads **D1** and **D2** in previously degassed water. Due to the solubility behaviour of the dyad molecules in the aqueous medium, as in the previous sections, **D1** and **D2** were solubilised with the poly(2-oxazoline) polymer shown in **Fig. 14**. The concentrations of the respective substances were chosen so that their optical density at the excitation wavelength corresponded to approximately 0.2. To investigate the initial electron transfer of the photocatalysis, each substance was measured once without and once with ascorbic acid in excess (0.10 M) as sacrificial electron donor. In order to ensure the comparability of the corresponding measurements, the same concentration of the respective substance was used. The wavelength of the laser pump pulses was adjusted to 21700 cm^{-1} (460 nm) in order to directly excite the MLCT transition of the photosensitisers. As mentioned in the previous sections, this transition represents the starting point of the electron cascade of the entire photocatalysis process. The TA spectra of **[Ru(bpy)$_3$]Cl$_2$** without and with ascorbic acid are shown in **Fig. 48**. Those of **D1** and **D2** are depicted in **Fig. 50** and **Fig. 52**, respectively. **Fig. 49**, **Fig. 51** and **Fig. 53** show the TA decay curves at the wavelengths which are marked by dashed lines in the corresponding TA spectra.

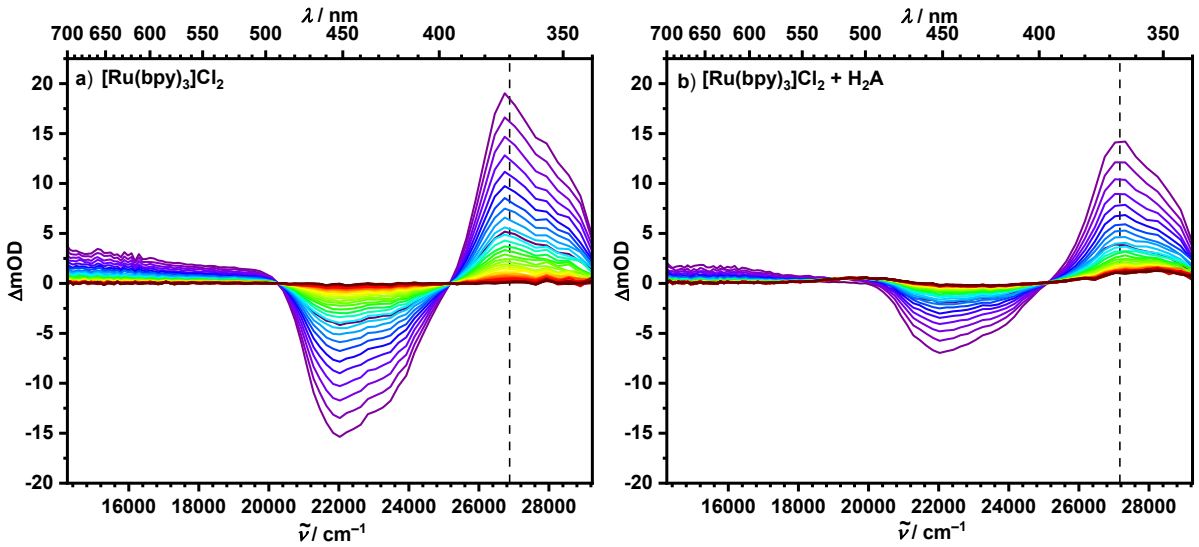

Fig. 48 UV/Vis transient absorption (TA) spectra of **a) [Ru(bpy)$_3$]Cl$_2$** ($1.35 \cdot 10^{-5}$ M) in water at 298 K and of **b) [Ru(bpy)$_3$]Cl$_2$** ($1.39 \cdot 10^{-5}$ M) and ascorbic acid (0.10 M) in water at 298 K. TA spectra were obtained between 0 ns (purple) and 3.44 µs (dark red) after excitation at λ_{ex} = 21700 cm^{-1} (460 nm). The time delay between each curve is 80.0 ns.

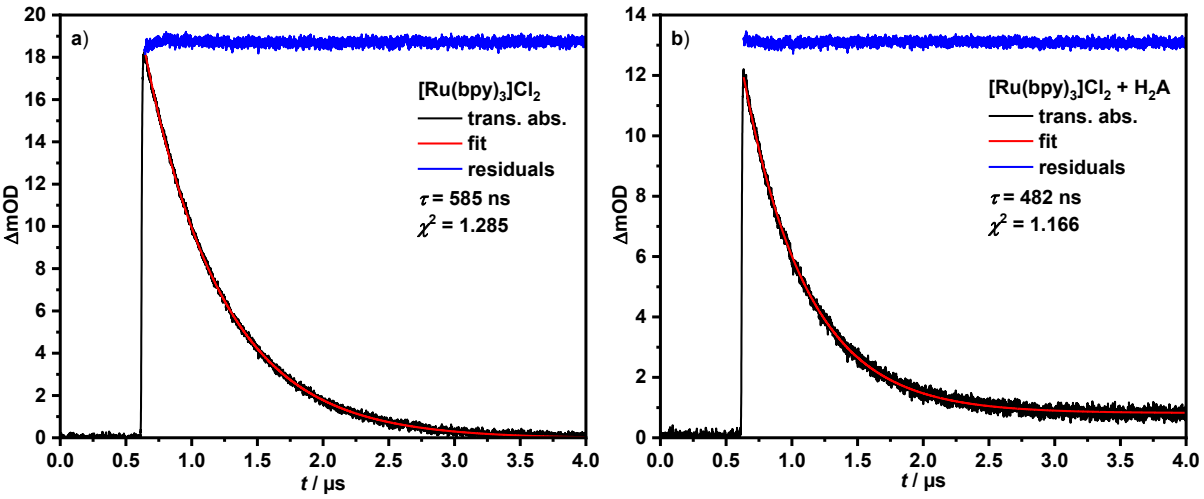

Fig. 49 Transient absorption (TA) kinetics of **a) [Ru(bpy)$_3$]Cl$_2$** ($1.35 \cdot 10^{-5}$ M) in water recorded at 27000 cm^{-1} (370 nm) and of **b) [Ru(bpy)$_3$]Cl$_2$** ($1.39 \cdot 10^{-5}$ M) and ascorbic acid (0.10 M) in water recorded at 27300 cm^{-1} (366 nm) at 298 K after excitation at λ_{ex} = 21700 cm^{-1} (460 nm). The TA kinetic traces were tail-fitted to a first-order decay with the data given in the chart.

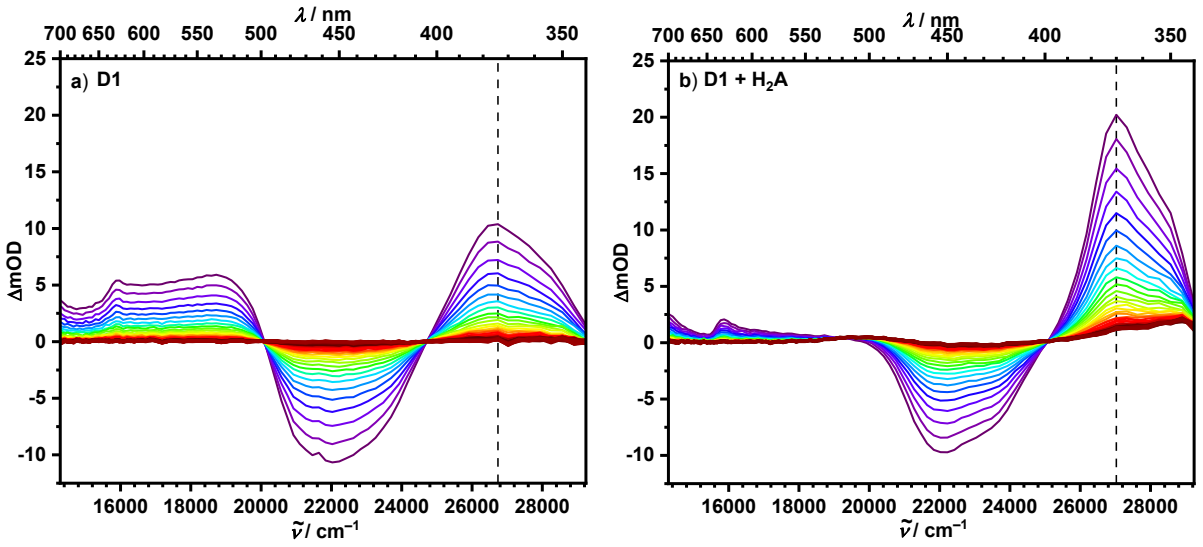

Fig. 50 UV/Vis transient absorption (TA) spectra of **a) D1** ($9.42 \cdot 10^{-6}$ M) in water at 298 K and of **b) D1** ($1.11 \cdot 10^{-5}$ M) and ascorbic acid (0.10 M) in water at 298 K. In both measurements **D1** was solubilised with a poly(2-oxazoline) polymer (see **Fig. 14**). TA spectra were obtained between 0 ns (purple) and 3.44 µs (dark red) after excitation at λ_{ex} = 21700 cm^{-1} (460 nm). The time delay between each curve is 80.0 ns.

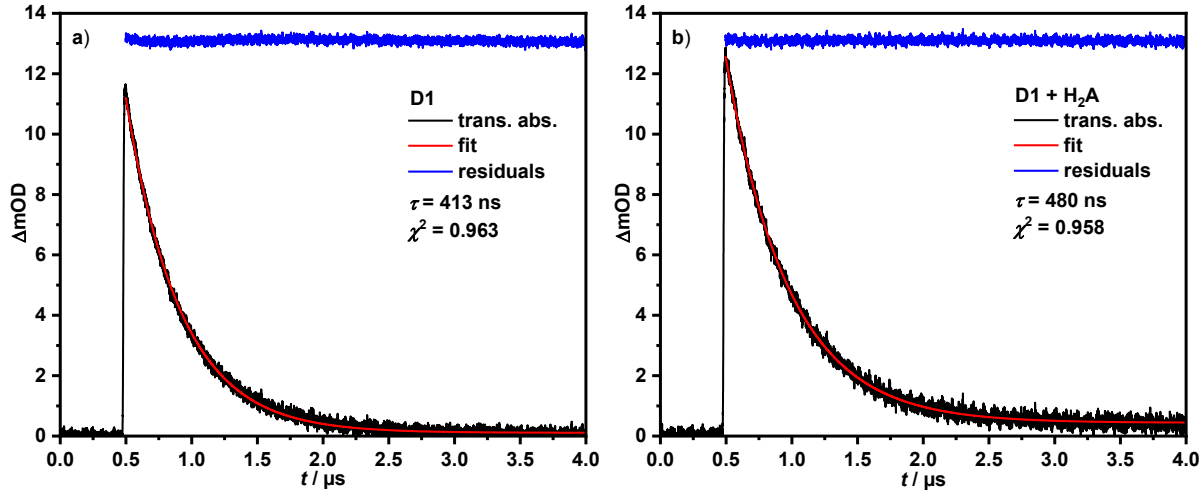

Fig. 51 Transient absorption (TA) kinetics of **a) D1** ($9.42 \cdot 10^{-6}$ M) in water recorded at 26700 cm^{-1} (374 nm) and of **b) D1** ($1.11 \cdot 10^{-5}$ M) and ascorbic acid (0.10 M) in water recorded at 27000 cm^{-1} (370 nm) at 298 K after excitation at λ_{ex} = 21700 cm^{-1} (460 nm). In both measurements **D1** was solubilised with a poly(2-oxazoline) polymer (see **Fig. 14**). The TA kinetic traces were tail-fitted to a first-order decay with the data given in the chart.

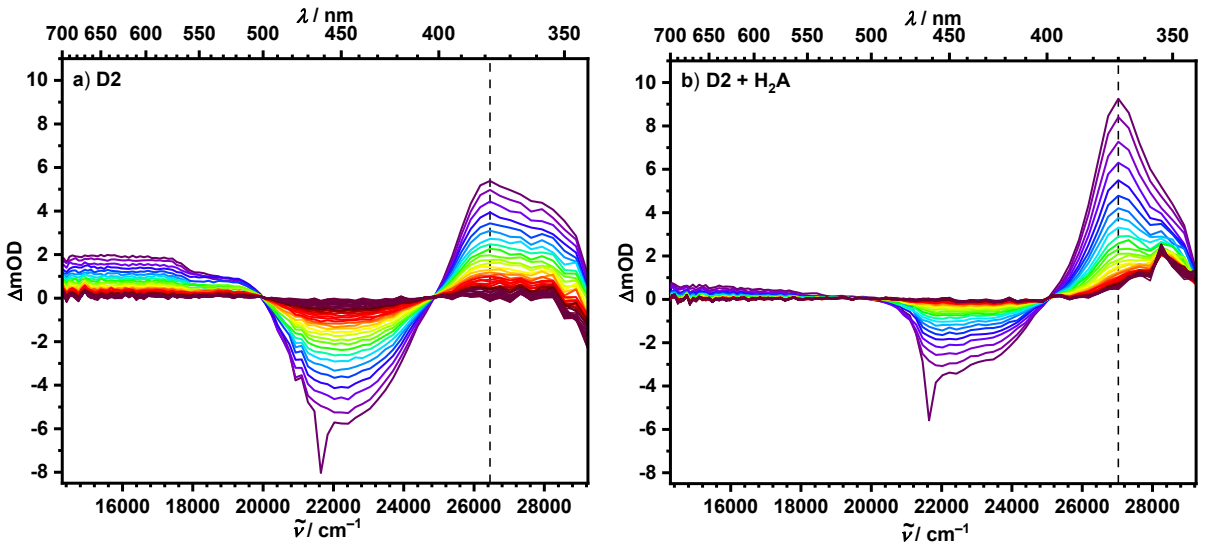

Fig. 52 UV/Vis transient absorption (TA) spectra of **a) D2** ($1.27 \cdot 10^{-5}$ M) in water at 298 K and of **b) D2** ($1.34 \cdot 10^{-5}$ M) and ascorbic acid (0.10 M) in water at 298 K. In both measurements **D2** was solubilised with a poly(2-oxazoline) polymer (see **Fig. 14**). TA spectra were obtained between 0 ns (purple) and 3.44 µs (dark red) after excitation at λ_{ex} = 21700 cm^{-1} (460 nm). The time delay between each curve is 80.0 ns.

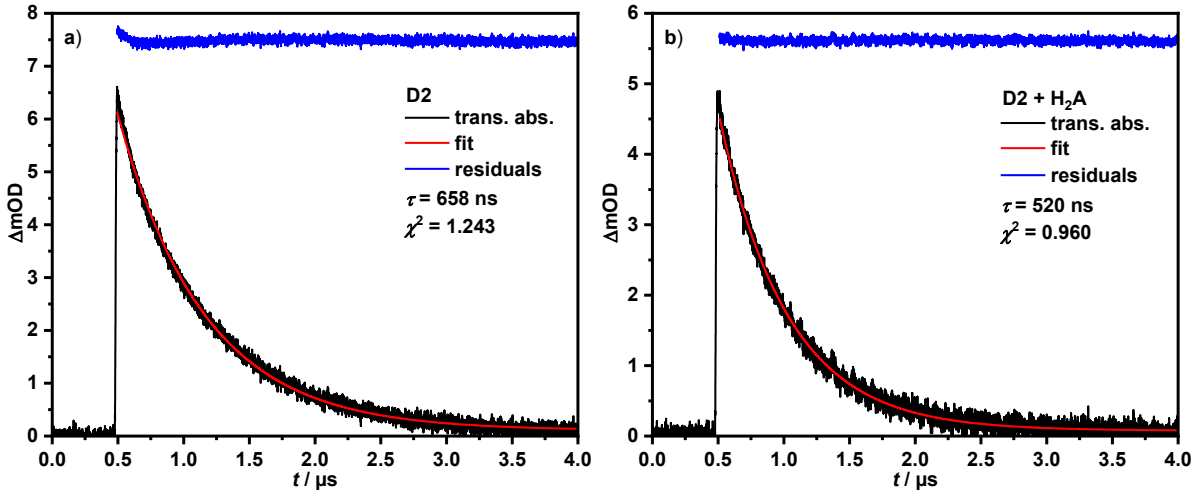

Fig. 53 Transient absorption (TA) kinetics of **a) D2** ($1.27 \cdot 10^{-5}$ M) in water recorded at 26500 cm^{-1} (378 nm) and of **b) D2** ($1.34 \cdot 10^{-5}$ M) and ascorbic acid (0.10 M) in water recorded at 27000 cm^{-1} (370 nm) at 298 K after excitation at λ_{ex} = 21700 cm^{-1} (460 nm). In both measurements **D2** was solubilised with a poly(2-oxazoline) polymer (see **Fig. 14**). The TA kinetic traces were tail-fitted to a first-order decay with the data given in the chart.

At first glance, the TA spectra of the investigated substances without ascorbic acid are very similar and therefore, due to the structural similarity of the organometallic ruthenium moiety, basically consist of the same three spectroscopic features, which differ from one another only in terms of their intensity and in some cases somewhat in terms of their spectroscopic position. At higher energies there is an intense positive signal which can be assigned to the excited

state absorption (ESA) of a reduced bpy ligand.[118] This signal shows a slight bathochromic shift in the series from **[Ru(bpy)$_3$]Cl$_2$** at 26900 cm^{-1} (372 nm) *via* **D1** at 26700 cm^{-1} (375 nm) to **D2** at 26500 cm^{-1} (378 nm), which illustrates the structural changes in the immediate vicinity of the bridging bpy ligand within the dyads. This is followed by an equally intense negative signal towards lower energies, which can be assigned to the ground state bleaching (GSB) of the excited MLCT transition.[118] As expected, the GSB shows its minimum for all three substances at 22100 cm^{-1} (452 nm). This is followed by a broad ESA signal in a range from 14300 cm^{-1} (700 nm) to 20000 cm^{-1} (500 nm). It is known that an ESA of the pure and neutral bpy ligand takes place at 16400 cm^{-1} (610 nm).[118] In addition, other processes, such as a ligand-to-metal charge transfer (LMCT) transition, i.e. the retransfer of an electron from the ligand to the ruthenium central atom, overlap in this broad band.[118] Accordingly, this excitation can only take place when Ru^{2+} has already been oxidised to Ru^{3+}, which is the case after excitation of the MLCT transition. All these signals indicate that, as expected, both in the single molecule **[Ru(bpy)$_3$]Cl$_2$** as well as in the dyads during the excitation in the spectroscopic region of the MLCT transition, the ruthenium central atom is oxidised from Ru^{2+} to Ru^{3+} and an electron is transferred to a bpy ligand. However, the recorded TA spectra cannot determine on which bpy ligand the electron is transferred to. Even if the bathochromic shift of the ESA of the reduced bpy ligand in the dyads indicates that the bridging bpy ligand within the dyads carries a not inconsiderable part of the charge. Hammarström *et al.* were able to show that for pure **[Ru(bpy)$_3$]Cl$_2$** the electron transferred to the ligand can no longer be assigned to one of the three ligands after just one picosecond.[118] It is assumed that this behaves relatively similarly in the dyad molecules, even if the negative charge on the bridging bpy ligand should be somewhat stabilised by the neighbouring and electron withdrawing amide group.

As already mentioned above, TA spectra of the substances already examined were afterwards recorded in combination with ascorbic acid as sacrificial electron donor to investigate the initial electron transfer of the assumed RQ mechanism during photocatalysis. As can be seen in **Fig. 48**, **Fig. 50** and **Fig. 52**, the presence of ascorbic acid has an effect on the spectral features, which have changed in a more or less similar manner for all substances on a closer consideration. Starting with the ESA of the reduced bpy ligand, it is noticeable that the intensity of the dyads has almost doubled, while the signal for **[Ru(bpy)$_3$]Cl$_2$** has lost some of its intensity. The signal has also shifted hypsochromically for all samples examined. **[Ru(bpy)$_3$]Cl$_2$** now shows the signal at 27300 cm^{-1} (366 nm), while it appears for **D1** and **D2** at 27000 cm^{-1} (370 nm). At the same time, the GSB has a lower intensity for all molecules in combination with the sacrificial electron donor and, moreover, in particular for the dyads has a hump at 23400 cm^{-1} (428 nm), whereupon the GSB minimum has accordingly shifted to 22200 cm^{-1} (451 nm). The biggest change, however, has experienced the broad ESA in the lower part of the energy range. Its intensity has decreased extremely in interaction with

ascorbic acid. In case of the two dyads, it is partially completely quenched. Accordingly, there is probably hardly any Ru^{3+} as an intermediate species that could participate in a LMCT process with a reduced bpy ligand. Furthermore, the increases in the ESA intensity of the reduced bpy ligand indicate that in the samples examined, ascorbic acid as the sacrificial electron donor probably reduced at least one other bpy ligand of the ruthenium complex. This probably also applies to the investigated **$[Ru(bpy)_3]Cl_2$** system, since here the signal's intensity has also increased in relation to the significantly weakened GSB despite the detected absolute decrease in intensity. The spectral shift of this ESA signal also speaks for a change in the electronic conditions, which could possibly have been caused by a reduction in an adjacent bpy ligand. All of these spectroscopic observations thus underline a reduction of the ruthenium photosensitiser by ascorbic acid and thus also the findings of the previous investigations regarding a RQ mechanism in the 2CS and the corresponding 3CS examined in this work during the photocatalysis. The observed changes in the GSB would also fit this finding, since the hump probably result from the GSB being overlaid with an ESA at 23400 cm^{-1} (428 nm). This ESA signal could accordingly descend from the $[Ru(bpy)_3]^+$ species, as Sun *et al.* have already observed for a similar 3CS.[119] Even if the band observed in the literature appeared at significantly lower energies. Since the hump especially appears in the case of the dyads and the TA measurements in the literature were carried out in another solvent, a direct comparison is not meaningful. However, the appearance of the reduced photosensitiser in the presence of ascorbic acid is a further evidence of the RQ mechanism.

In the TA spectra of all three substances examined, a relatively weak and broad ESA in the range from 26300 cm^{-1} (380 nm) to 29400 cm^{-1} (340 nm) appears at later times in combination with ascorbic acid, which cannot be assigned. For identification, a spectroelectrochemistry measurement of the ruthenium photosensitiser, which was synthetically expanded to include a methyl benzoate group *via* an amide bond on a bpy ligand, was carried out (see appendix). However, apart from the spectral features already listed, no further features could be detected. Additionally, due to the excess of ascorbic acid, the presence of a $[Ru(bpy)_3]^{3+}$ species can be ruled out. The signal may come from the [FeFe] catalyst moiety of the dyads. However, this signal also appears in the **$[Ru(bpy)_3]Cl_2$** measurement, albeit somewhat weakened. Due to the irreversible redox behaviour of the [FeFe] complex compounds in acetonitrile and the too small CV measurement window in an aqueous environment, no adequate spectroelectrochemistry measurement of the dyads or of the corresponding [FeFe] complexes could be carried out. Unfortunately, this signal can therefore not be assigned any further.

To make statements about the kinetics of the electron transfer, decay curves were recorded for all TA measurements at selected spectral positions. These curves were then tail-fitted to obtain the lifetimes of the corresponding species applying the following exponential equation:

$$R(t) = Be^{\left(-\frac{t}{\tau}\right)} \quad (13)$$

In **Fig. 49**, **Fig. 51** and **Fig. 53** the ESA decay curves of the reduced bpy ligand are exemplarily shown together with the corresponding kinetic data. However, the data obtained are difficult to interpret, e.g. the significant increase of the lifetime of pure **D2** compared to that of pure **D1**. Whereas the lifetime decrease of pure **D1** compared to that of pure **[Ru(bpy)$_3$]Cl$_2$** could be explained by the additional covalent attachment of the [FeFe] catalyst moiety as an electron acceptor within the dyad. In addition, the lifetimes change to different degrees by adding ascorbic acid. One reason for this could be the fact that several processes are responsible for the generation of this signal in the presence of ascorbic acid. However, it is challenging to quantify the individual processes involved with only the data from the TA measurements. Therefore, in order to get more solid knowledge about the kinetics during photocatalysis, it would be useful to analyse the $[Ru(bpy)_3]^+$-ESA because, as shown above, it is created exclusively by the impact of the sacrificial electron donor. In addition, this is particularly interesting with regard to the knowledge about the kinetics of the second electron transfer in the RQ mechanism from the reduced photosensitiser to the catalyst. Since the signal of the reduced ruthenium complex in aqueous solution overlaps with the GSB, further TA measurements of **D1** in different solvents were carried out. With acetone as an aprotic solvent, conditions were found under which the $[Ru(bpy)_3]^+$-ESA signal presumably shifted to 18900 cm^{-1} (528 nm) and therefore no longer overlapped with the GSB. Due to the hydrophilic properties of ascorbic acid, it had to be replaced by triethylamine (TEA) as the sacrificial electron donor.

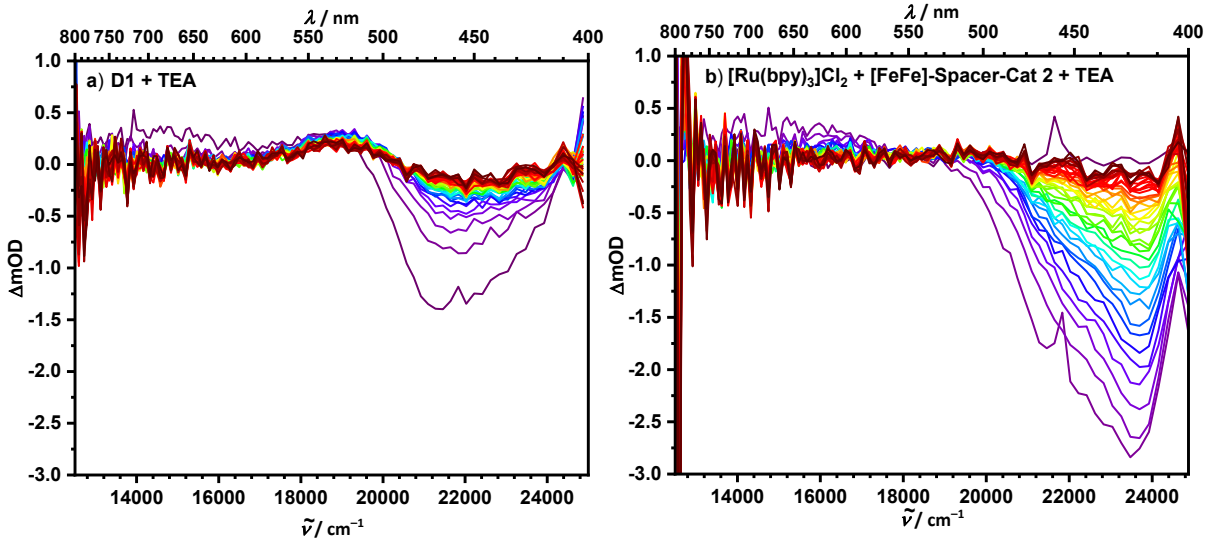

Fig. 54 UV/Vis transient absorption (TA) spectra of **a) D1** ($1.26 \cdot 10^{-5}$ M) and TEA (48.4 mM) in acetone at 298 K and of **b) [Ru(bpy)$_3$]Cl$_2$** ($1.30 \cdot 10^{-5}$ M), **[FeFe]-Spacer-Cat 2** ($1.22 \cdot 10^{-5}$ M) and TEA (31.4 mM) in acetone at 298 K. TA spectra were obtained between 0 ns (purple) and 3.44 µs (dark red) after excitation at λ_{ex} = 21700 cm^{-1} (460 nm). The time delay between each curve is 80.0 ns.

Fig. 54a shows the corresponding TA measurement of **D1**. Unfortunately, the assumed $[Ru(bpy)_3]^+$ signal in the corresponding 3CS, consisting of **$[Ru(bpy)_3]Cl_2$**, **[FeFe]-Spacer-Cat 2** and TEA in acetone, was probably overlaid by the GSB again, which suggests the distinctive shape of the GSB in **Fig. 54b**. It was therefore not possible to make a final comparison between the ruthenium complex containing 2CS and the associated 3CS regarding their kinetics during photocatalysis. At this point, however, the surprising durability of the assumed $[Ru(bpy)_3]^+$ signal of obviously at least several microseconds within the dyad with its integral electron acceptor must be emphasised.

5.1.7 Photocatalysis

To determine the photocatalytic performance of the ruthenium containing systems in this work, both dyads **D1** and **D2**, as well as the corresponding 3CS, consisting of **$[Ru(bpy)_3]Cl_2$** as photosensitiser and **[FeFe]-Spacer-Cat 2** or **[FeFe]-Spacer-Cat 5** as catalysts, were used in photocatalysis in combination with ascorbic acid as the sacrificial electron donor. The photocatalytic measurements were carried out in an aqueous medium at a pH of 4 using the findings from the investigations of the [FeFe] catalysts described in chapter 4.4. In contrast, the concentrations of the 3CS components were used in a 1:1 ratio for comparability with the corresponding 2CS. The photosensitiser and catalyst or dyad concentration was accordingly 0.30 mM for all systems. Ascorbic acid was used with 0.14 M in excess. Due to the poor solubility of the [FeFe] catalysts or dyads in water, they were sulubilised for photocatalysis using the poly(2-oxazoline) polymer shown in **Fig. 14** in a 25-fold mass excess. During the investigations, each sample was irradiated with light at 21500 cm^{-1} (465 nm) from 10 LEDs (@ 3.0 V and 1.58 A) for the specified period of time. In order to determine whether the systems treated this way have generated hydrogen and to characterise their photocatalytic productivity, the gas phases over the previously degassed aqueous solutions were then examined by means of gas chromatography. With the amount of hydrogen produced, the TON was then calculated referring to the catalyst or the combined photosensitiser-catalyst system. To determine the photocatalytic activity for the 3CS, consisting of **$[Ru(bpy)_3]Cl_2$** and **[FeFe]-Spacer-Cat 2**, and the **D1** containing 2CS, the gas pressure during the photocatalysis was additionally recorded in real time using pressure sensors. The increase in pressure is a measure of the turnover frequency. Due to the problem with sealing against hydrogen described below, it was not possible to receive suitable data using this procedure for the 3CS, consisting of **$[Ru(bpy)_3]Cl_2$** and **[FeFe]-Spacer-Cat 5**, and for the **D2** containing 2CS. The results of the examined systems are shown in **Fig. 55** and **Fig. 56** and reported in **Table 7**.

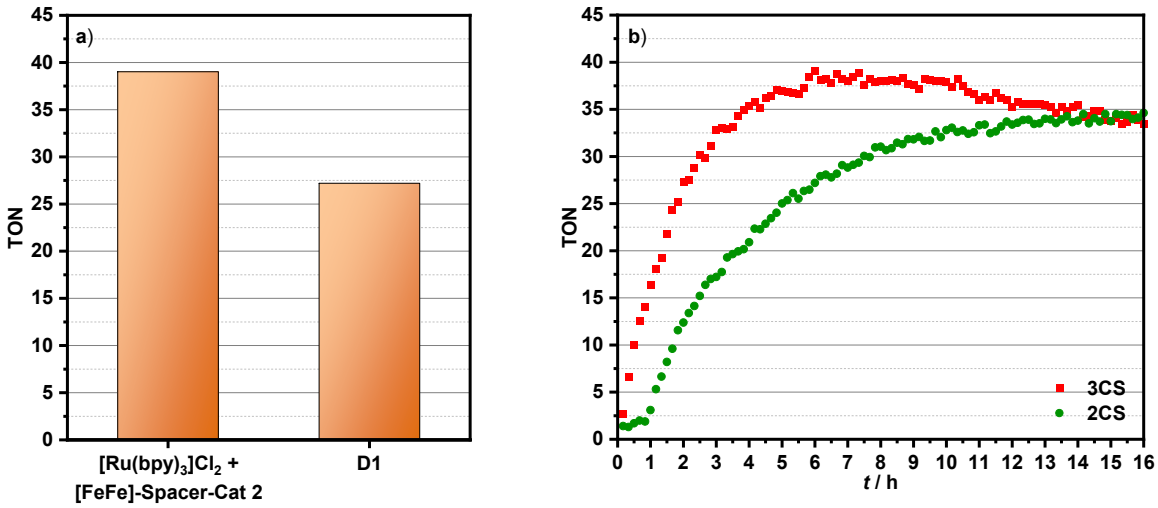

Fig. 55 Photocatalytic hydrogen evolution in aqueous poly(2-oxazoline) solution (pH = 4, polymer concentration: 6.2 mg ml^{-1}) at 293 K after irradiation with light at 21500 cm^{-1} (465 nm). **a)** Turnover numbers (TON) after 6 h of irradiation. Stoichiometric proportions: (left column) 0.30 mM **[Ru(bpy)$_3$]Cl$_2$**, 0.30 mM **[FeFe]-Spacer-Cat 2** and 0.14 M ascorbic acid; (right column) 0.30 mM **D1** and 0.14 M ascorbic acid. **b)** Temporal progress of hydrogen evolution reactions.

As can be seen in **Fig. 55**, both the 3CS, consisting of **[Ru(bpy)$_3$]Cl$_2$** and **[FeFe]-Spacer-Cat 2**, as well as the corresponding **D1** containing 2CS are photocatalytically active and generate hydrogen by light irradiation. As expected, this also applies to the other two systems, as can be seen in **Fig. 56**. The functionality of all components and their presence as a prerequisite for hydrogen generation could be additionally confirmed through control experiments carried out, in which one component of the respective system was removed and all of which proceeded without detectable hydrogen evolution. Compared to systems known from literature, the **[Ru(bpy)$_3$]Cl$_2$** and **[FeFe]-Spacer-Cat 2** containing 3CS with a TON of 39 and a TOF of 0.0044 s^{-1} achieved comparably high values after 6 h of irradiation.[5,9] For instance, Sun *et al.* reached with a very similar 3CS with **[Ru(bpy)$_3$]Cl$_2$** as photosensitiser and also a Ppyr$_3$ substituted [FeFe] catalyst only a TON of 4.3 after 3 h.[15] A mixture of equal parts of acetonitrile and water was used as solvent. Even if a direct comparison of different systems measured under various conditions is difficult, it can already be derived from these results that a comparatively high photocatalytic productivity can also be achieved using aqueous micellar solutions and that this productivity does not necessarily suffer from the possibly hindered mass transport from or into the micelles. However, with a TON of 27 and a TOF of 0.0027 s^{-1}, the **D1** containing 2CS shows a significantly lower photocatalytic performance than the associated 3CS. This is somewhat surprising given the results of the absorption spectroscopic and electrochemical investigations and especially that of the emission quenching studies. However, this result is in line with the findings of Sun *et al.*, which convey that photocatalytically active dyads in general, which operate *via* the RQ mechanism, would not benefit from the covalent bond between the photosensitiser and the catalyst and would hence perform worse than the corresponding multicomponent systems.[9] Since most of the investigations in the

previous sections suggest that the considered systems work according to the RQ mechanism, this would correspondingly apply here as well. Furthermore, the TA measurements already indicated that the transferred negative charge in the dyad **D1** apparently remains in the area of the ruthenium photosensitiser for a quite long time during photocatalysis. Although no comparison could be made with the corresponding 3CS, this finding indicates that the electron transfer from the sacrificial electron donor to the photosensitiser is probably not the rate-determining step. Furthermore, the bridging units built into **D1** and, accordingly, also in **D2**, could represent too high barriers for a sufficient electron transfer. Under this assumption, the dyads would not benefit from the covalent bond between the photosensitiser and the catalyst and would therefore behave analogously to the multicomponent systems during photocatalysis. The charge obtained would be transferred to the [FeFe] complex of a second dyad molecule instead of internally to the bound catalyst. The photocatalytic performance of the dyads would also suffer from the additional steric hindrance, which could explain the poorer values of **D1** compared to the 3CS.

A closer look at the temporal progress of the photocatalytic hydrogen evolution reactions shown in **Fig. 55b** reveals that the examined systems behave differently after reaching the for the photocatalysis typical pressure plateau. This can be attributed to leaks in the used PTFE seals against hydrogen, which can also be seen from the drop in the 3CS curve after reaching the plateau. This problem made the recording of a pressure curve and the associated determination of the photocatalytic activity of various systems extremely difficult during this work and led to many failed attempts, in which no increase in pressure could be detected despite the ongoing photocatalysis. Fortunately, in some cases, as with **D1**, adequate sealing has been achieved. In contrast, no meaningful values could be achieved for **D2** and the associated 3CS despite several attempts, which is why no statements can be made here regarding the photocatalytic activities of these systems. In some cases, such as the 3CS shown in **Fig. 55b**, a pressure curve could be recorded, but existing leaks in the seal caused the pressure built up to decrease during the photocatalysis. This resulted in the corresponding system reaching a lower pressure level than would be the case with a dense measuring system. Although the pressure profiles were scaled to the nominally correct height with the help of the TON values determined, this leakage problem definitely has an influence on the slope of the curves, which is decisive for determining the TOF values. For instance, it can be assumed that the 3CS shown in **Fig. 55b** would have an even steeper slope. Nonetheless, in the specific case, this would in no way affect the statements described above, but would actually reinforce them for intrinsically higher TOF values for the 3CS. Since these PTFE seals were only used in conjunction with the pressure sensors, this problem only affected the recording of some pressure profiles. This did not affect the determination of the photocatalytic productivity.

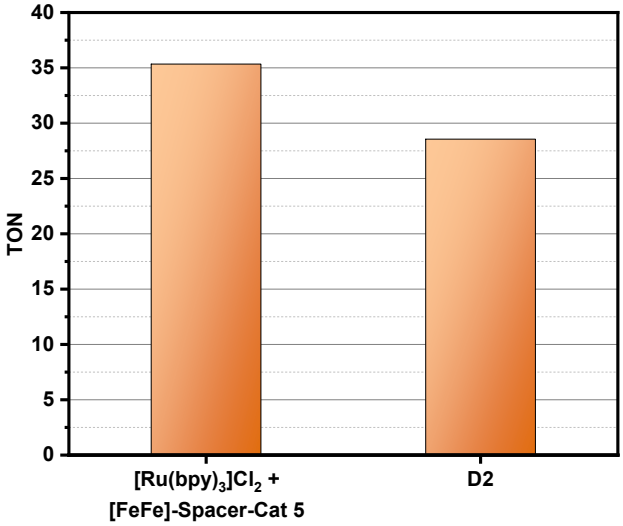

Fig. 56 Photocatalytic hydrogen evolution in aqueous poly(2-oxazoline) solution (pH = 4, polymer concentration: 6.2 mg ml^{-1}) at 293 K after 17 h irradiation with light at 21500 cm^{-1} (465 nm). Stoichiometric proportions: (left column) 0.30 mM **[Ru(bpy)$_3$]Cl$_2$**, 0.30 mM **[FeFe]-Spacer-Cat 5** and 0.14 M ascorbic acid; (right column) 0.30 mM **D2** and 0.14 M ascorbic acid.

As can be seen in **Fig. 56**, the 3CS consisting of **[Ru(bpy)$_3$]Cl$_2$** and **[FeFe]-Spacer-Cat 5** shows a TON of 35, while the corresponding **D2** containing 2CS exhibit a TON of 29. The values of the two systems therefore differ only marginally from those of the two previously considered. In view of the fact that both systems were irradiated longer than the systems described above, it can be assumed that the **D1** containing 2CS and the associated 3CS show a slightly better photocatalytic performance than the systems with the extended bridge building blocks. Surprisingly, this is particularly true for the corresponding 3CS, where this influence should actually be expressed less strongly. All in all, the influence of the bridge component has only a relatively weak effect. This finding has already become apparent in the investigations described in the previous sections. Rather, it also shows here, analogous to the two previously examined systems, that the 3CS exhibits a significantly higher productivity than the 2CS. Therefore, and due to the structural similarity, it can be assumed that the assumptions described above apply here as well.

Table 7 Photocatalytic hydrogen evolution data of the ruthenium containing 2CS and 3CS in water (pH = 4) at 293 K.

System	TON	TOF[a] (s^{-1})
3CS (**[Ru(bpy)$_3$]Cl$_2$+[FeFe]-Spacer-Cat 2**)	39[b]	0.0044
2CS (**D1**)	27[b]	0.0027
3CS (**[Ru(bpy)$_3$]Cl$_2$+[FeFe]-Spacer-Cat 5**)	35[c]	
2CS (**D2**)	29[c]	

[a] Determined by maximum slope in the temporal progress of hydrogen evolution reactions (see **Fig. 55b**). [b] After 6 h irradiation with light at 21500 cm^{-1} (465 nm). [c] After 17 h irradiation with light at 21500 cm^{-1} (465 nm).

5.1.8 Conclusion

In summary, two photocatalytically active dyads, **D1** and **D2**, each consisting of a $[Ru(bpy)_3]^{2+}$ photosensitiser and a covalently linked [FeFe] complex catalyst, could be synthesised in this study along with their corresponding catalyst components **[FeFe]-Spacer-Cat 2** and **[FeFe]-Spacer-Cat 5**. The compounds obtained were characterised together with the **$[Ru(bpy)_3]Cl_2$** photosensitiser by means of absorption spectroscopy and cyclic voltammetry. In addition, their photocatalytic performance was compared with ascorbic acid as the sacrificial electron donor in the corresponding dyad containing two-component systems (2CS) and bimolecular three-component systems (3CS), respectively. The absorption spectroscopy revealed an existing coupling between the components within the dyad molecules, which is reflected in spectral shifts of the photosensitiser-centred MLCT band, the iron-centred Fe(σ)-Fe(σ^*) band and in particular of the spacer-centred π-π^* transition in the direct comparison to those of the single molecules. In contrast, the elongation of the bridge building block, which is the decisive structural difference between the two dyad molecules **D1** and **D2**, has no significant influence on their spectral characteristics. These findings were also confirmed by the electrochemical investigations. The energetic position of the dyad redox potentials also exhibits significant shifts compared to that of the corresponding single molecules redox potentials indicating an appreciable coupling between the dyad components. Whereas the redox potentials of **D1** and **D2** show only small differences. However, the results of the CV investigations tend to indicate that, as expected, the coupling within the dyad decreases somewhat as the bridge unit is elongated. Surprisingly, the thermodynamic conclusions about the inner dyad coupling were not reflected in the results of the photocatalytic investigations. With a TON of 27 and a TOF of 0.0027 s^{-1}, the **D1** containing 2CS shows a significantly lower performance than the corresponding 3CS, consisting of **$[Ru(bpy)_3]Cl_2$** and **[FeFe]-Spacer-Cat 2**. The same applies to the **D2** containing 2CS which also shows a substantially lower photocatalytic productivity (TON = 29) than the corresponding 3CS (TON = 35), consisting of **$[Ru(bpy)_3]Cl_2$** and **[FeFe]-Spacer-Cat 5**. With these results, however, the systems examined confirm the observations of Sun *et al.* about the lower photocatalytic performance of dyad systems, which operate *via* the RQ mechanism, compared to the corresponding bimolecular systems.[9] TA measurements were carried out on the **D1** containing 2CS and the associated 3CS to further elucidate the electron transfer from the photosensitiser to the catalyst, which is the crucial step in this context. Unfortunately, with these TA examinations it was not possible to obtain meaningful results regarding the temporal sequence of the photocatalytic processes in the 3CS. Nevertheless, the results of the 2CS suggest that the electron remains on the ruthenium photosensitiser for a relatively long time after reduction by the sacrificial electron donor, despite the covalent bond to the [FeFe] catalyst present in the dyad. In combination with the output of the photocatalysis, this shows that the dyads obviously do not seem to benefit from the

covalent connection between the photosensitiser and the catalyst in the processes of the electron cascade.

As just mentioned, it is of crucial importance for the characterisation of the systems which quenching mechanism and thus the order in which the individual electron transfers take place during photocatalysis. Therefore, several kinetic studies including the characterisation of the excited state redox potentials of the ruthenium photosensitiser moieties and the emission quenching of them by ascorbic acid were carried out to investigate the electron transfer from the sacrificial electron donor to the photosensitiser. As a result, all studies confirmed the assumed RQ mechanism in the examined systems, which in turn affirms the relevance of the abovementioned observation by Sun *et al.* for these systems.[9]

The extension of the bridge building block within the dyad has, as already showed in the absorption spectroscopic and electrochemical investigations, no major influence either from thermodynamic or kinetic aspects. This relatively small structural change seems to have a too little impact on the material properties of the dyads in order to make a noticeable difference. It is suspected that the amide and ester bonds implemented in the dyads as connection points and π-conjugation blockers between the individual dyad components have a comparatively large influence on the electron transfers and possibly hinder them too much despite the existing electronic coupling. Due to the already mentioned problems of the examined ruthenium containing systems, especially with the TA measurements, it was unfortunately not possible to investigate this in more detail within the scope of this work and with the available analysis methods. However, this could probably be possible by replacing the ruthenium photosensitiser moiety by another suitable organometallic complex. Since iridium photosensitisers in particular are also investigated in the Lambert group, the characterisation of a corresponding iridium photosensitiser dyad will be dealt with in the following chapter.

5.2 Iridium Containing Systems

In the following, a photocatalytically active iridium photosensitiser [FeFe] complex dyad, based on the previously discussed ruthenium containing dyad molecules **D1** and **D2**, was synthesised and characterised. As described in the previous section, the structural composition of the dyad should basically be taken over from **D1** in order to investigate the influence of the amide and ester bonds as π-conjugation blockers on the intramolecular electron transfer. Only the photosensitiser unit is to be replaced by a cyclometalated iridium complex, to presumably enable a more detailed examination of the processes taking place during the photocatalysis. Two 2-phenylpyridine (ppy) ligands and one bipyridine (bpy) ligand were used as ligands for this organometallic complex, since on the one hand this resulting $[Ir(ppy)_2bpy]^+$ complex has already been successfully used in the literature as a photosensitiser in photocatalysis in

conjunction with [FeFe]-hydrogenase mimics.[5,9,34,53] On the other hand, by linking the bridge building block to the bipyridine ligand, it is possible to produce the dyad analogous to **D1** with just an adaption of the photosensitiser synthesis without changing the Spacer-[FeFe] complex synthesis. Taking into account the results from chapter 4, a $Ppyr_3$-substituted propyldithiolate [FeFe] complex was used as the catalyst moiety, which is connected to the photosensitiser moiety *via* a phenyl ring bridge bonded with the abovementioned amide and ester bonds. **Fig. 57** shows the desired iridium photosensitiser [FeFe] complex dyad **D3**. The amide and ester conjugation blockers are marked in red.

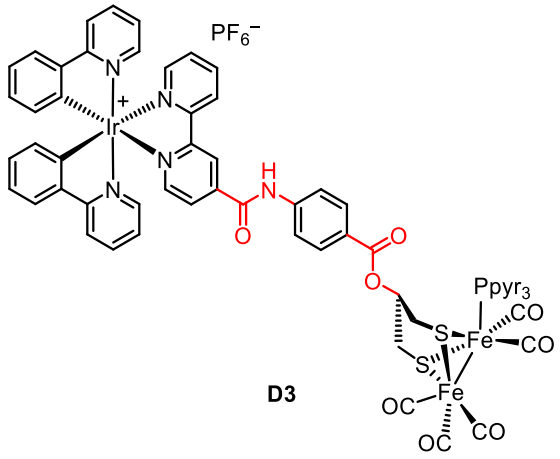

D3

Fig. 57 Photocatalytically active dyad **D3**. The amide and ester bonds within the molecule act as π-conjugation blockers and are highlighted in red.

Preliminary photocatalytic investigations (see below) have shown that $[Ir(ppy)_2ppy]^+$ photosensitisers show only relatively poor photocatalytic performance in combination with ascorbic acid as sacrificial electron donor and [FeFe] complexes as catalysts in the aqueous medium, presumably due to poorly matched redox potentials. Therefore, **D3** should be examined photocatalytically in a more suitable 2CS. Further investigations have shown that a high performing system can be built up using TEA as the sacrificial electron donor and with an acetonitrile-water mixture as the solvent (see below). In addition, this system was used as the basis for the investigations and measurements described in the following sections. For the classification of the results, again the corresponding 3CS, consisting of the **$[Ir(ppy)_2bpy]PF_6$** photosensitiser, **[FeFe]-Spacer-Cat 2** as the catalyst and TEA as sacrificial electron donor, should be used as a reference system. In this manner, the spectroscopic and electrochemical properties of **D3** should be investigated and compared with its corresponding single-molecular components. In addition, the electron transfers of the **D3** containing 2CS that take place during photocatalysis should be examined again with regard to their thermodynamic and kinetic aspects and compared with those of the associated 3CS. Preferably, insights into the intramolecular electron transfer in the 2CS should be gained, as mentioned at the beginning, so that conclusions can be drawn about the effects of the bridge building blocks used in the

dyad. Since no noteworthy effects on the material properties and the photocatalytic performance were observed in the previous chapter by an extension of the bridge moiety used in the dyad, there will be no comparison with a corresponding additional dyad in this study.

5.2.1 Synthesis

The synthesis of the photocatalytically active dyad **D3** and the associated constituents is based on the synthesis of **D1** described in the previous chapter on the ruthenium dyads. To a large extent, it is even identical to it, since in **D3**, as with **D1**, the structurally identical Spacer-[FeFe] catalyst moiety should be attached to the photosensitiser moiety *via* a bpy ligand (see **Fig. 57**). Thus, the **D3** synthesis is also based on the concept of Sun and Åkermark for the covalent linking of a [$Fe_2\mu$-pdt$(CO)_6$] (pdt = propyldithiolate) catalyst to a ruthenium tris-bipyridine photosensitiser *via* the dithiolate bridge of the [FeFe] complex and the associated introduction of two π-conjugation blockers in the form of an amide bond between the bpy ligand of the photosensitiser and the phenyl spacer and an ester bond between this and the pdt ligand of the diiron complex.[55,56] As previously with **D1** and **D2**, these units are intended to reduce the electronic coupling between the dyad components and thus prevent potential rapid back electron transfer during photocatalysis after the charge has been transferred from the photosensitiser to the catalyst. In addition, analogously to the ruthenium dyads, $Ppyr_3$ is to be attached to the catalyst moiety as a ligand, in order to enhance the stability and protophilicity of the catalyst by increasing the electron density on the iron core without simultaneously inducing a strong shift of the redox potential, as shown in chapter 4.[9]

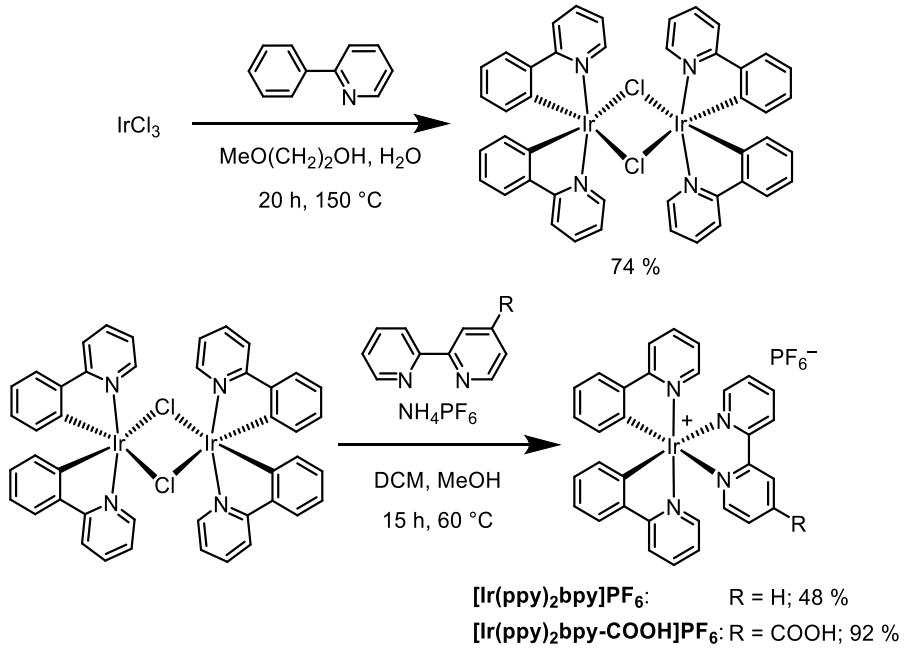

Fig. 58 Synthesis of the non-functionalised **[Ir(ppy)$_2$bpy]PF$_6$** photosensitiser and the acid-functionalised **[Ir(ppy)$_2$bpy-COOH]PF$_6$** photosensitiser.

The build-up of the photosensitiser moiety, which differs from the **D1** synthesis, is based on the syntheses of similar iridium complexes known from the literature.[120,121] **Fig. 58** shows the synthesis of the iridium photosensitiser **[Ir(ppy)$_2$bpy]PF$_6$** and of the acid-functionalised iridium photosensitiser **[Ir(ppy)$_2$bpy-COOH]PF$_6$**, respectively. First, the **[Ir(ppy)$_2$Cl]$_2$** dimer was prepared by treating iridium trichloride with 2-phenylpyridine in a mixed solvent of 2-ethoxyethanol and water at 150 °C overnight with a yield of 74 %. In the next step, it was possible to prepare with this intermediate both the **[Ir(ppy)$_2$bpy]PF$_6$** photosensitiser by reaction with 2,2'-bipyridine and the acid-functionalised **D3** precursor **[Ir(ppy)$_2$bpy-COOH]PF$_6$** by reaction with **(2,2'-bipyridine)-4-carboxylic acid**. The yield for **[Ir(ppy)$_2$bpy]PF$_6$**, which is to be used as the photosensitiser in the 3CS, was 48 %. In contrast, **[Ir(ppy)$_2$bpy-COOH]PF$_6$** could be produced almost quantitatively with a yield of 92 %.

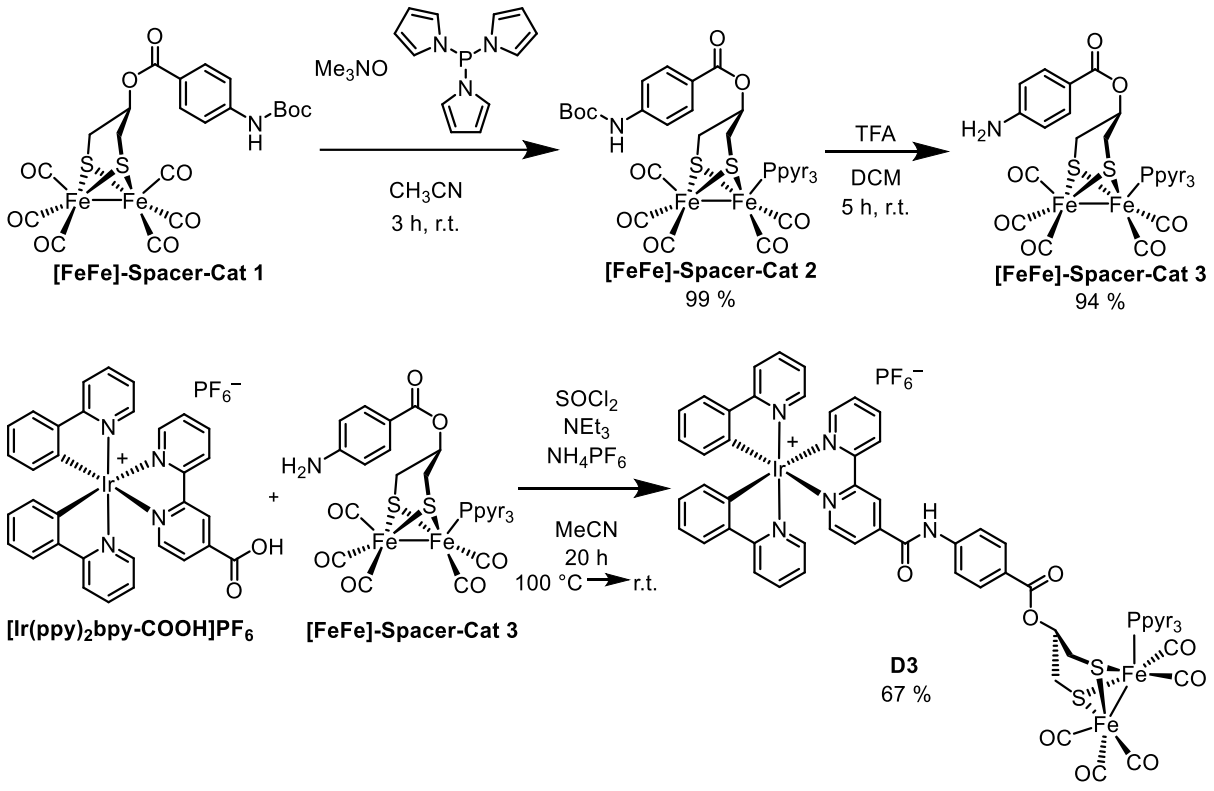

Fig. 59 Synthesis of **[FeFe]-Spacer-Cat 3** and formation of photocatalytically active dyad **D3** by coupling of **[Ir(ppy)$_2$bpy-COOH]PF$_6$** and **[FeFe]-Spacer-Cat 3**.

Since, as already mentioned, the synthesis of the second **D3** precursor **[FeFe]-Spacer-Cat 3** has already been described in the chapter on the ruthenium dyads, this will not be explained further here. The final preparation of the photocatalytic dyad **D3** was achieved by coupling **[Ir(ppy)$_2$bpy-COOH]PF$_6$** with **[FeFe]-Spacer-Cat 3** in a good yield of 67% (see **Fig. 59**). For this purpose, the acid-functionalised iridium precursor was first activated with thionyl chloride and then used without further purification for the subsequent reaction with **[FeFe]-Spacer-Cat 3** in acetonitrile. Triethylamine was added to trap the releasing hydrogen chloride during this reaction. The purification of the crude product obtained was again analogous to the **D1**

synthesis. First, the crude product was purified by flash column chromatography on silica gel in an aqueous acetonitrile/KNO_3 mixture (acetonitrile/water/$KNO_{3(aq)}$ = 90:5:5) to ensure the solubility of the cationic dyad. The product was then reprecipitated from a saturated aqueous NH_4PF_6 solution to obtain **D3** as a red solid.

The syntheses of the reference molecules **[FeFe]-Cat 5** and **Spacer** used in the next section have already been described in the chapter on the diiron hydrogenase biomimic studies (see **Fig. 17**) and in the chapter on the ruthenium dyads (see **Fig. 33**), respectively.

5.2.2 Steady-State Absorption Spectroscopy

For spectral characterisation, the Dyad **D3** was examined by absorption spectroscopy at 298 K. In addition, for better classification of the data obtained, absorption spectra of the single-molecule components **[FeFe]-Spacer-Cat 2**, **[Ir(ppy)$_2$bpy]PF$_6$**, as well as of the diiron catalyst without the spacer moiety and of **Spacer 1** were recorded. Acetonitrile was used as the solvent in order to measure under the same conditions as for photocatalysis. Due to the good solubility of all measured molecules in acetonitrile, no solubilising agent had to be added this time. The corresponding absorption spectra are shown in **Fig. 60**.

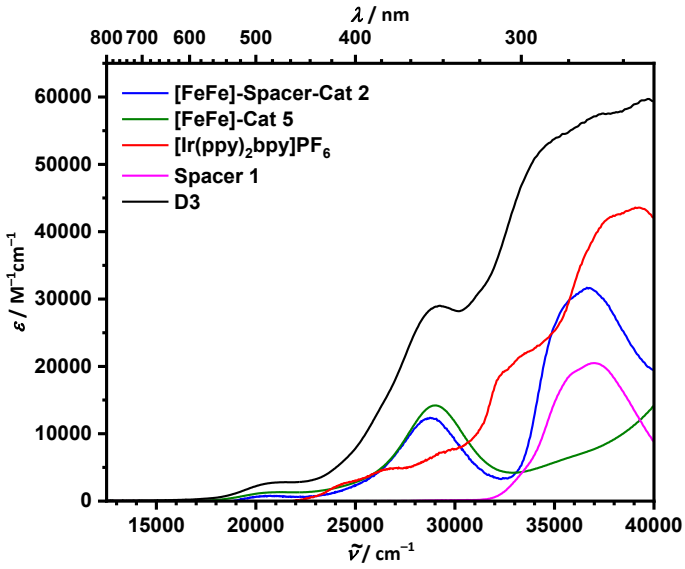

Fig. 60 Absorption spectra of **[FeFe]-Spacer-Cat 2**, **[FeFe]-Cat 5**, **[Ir(ppy)$_2$bpy]PF$_6$**, **Spacer 1** and **D3** measured in acetonitrile at 298 K.

All measured components show a relatively high extinction in the near-UV range with a towards longer wavelengths decreasing intensity, which extends into the visible. **Fig. 60** shows that the spectrum of **D3** is composed of the spectra of its components, with deviations in the range from 27800 cm^{-1} (360 nm) to 38500 cm^{-1} (260 nm). The relatively undefined and broad shoulder that occurs in the region between 30300 cm^{-1} (330 nm) and 38500 cm^{-1} (260 nm)

essentially consists of overlapping absorption bands of two structural units. As the comparison with the spectra of the corresponding compounds shows, the band is not only composed of the red-shifted and broadened π-π^* excitation of the aromatic spacer unit, but also of the bpy and ppy-centred ^{1}LC (ligand-centred) transition of the cyclometalated iridium complex.[20,122] The spectral shifts in this region are not surprising, since these structural units of the dyad have experienced the greatest effects and changes through the coupling of **[FeFe]-Spacer-Cat 3** with **[Ir(ppy)$_2$bpy]PF$_6$** forming **D3**. Otherwise, the spectrum of **D3** is mainly dominated by the just mentioned ^{1}LC bands at 39200 cm^{-1} (255 nm) and 37500 cm^{-1} (266 nm), as well as by the absorption band of the iron-centred Fe(σ)-Fe(σ^*) transition at 29000 cm^{-1} (345 nm), which is blue-shifted in comparison with that of **[FeFe]-Spacer-Cat 3**.[20,94,122] Despite the just described deviations of the dyad spectrum from that of the corresponding single components **[FeFe]-Spacer-Cat 2** and **[Ir(ppy)$_2$bpy]PF$_6$**, the spectral differences are somewhat smaller compared to the ruthenium dyads in the previous chapter. This indicates a comparatively smaller electronic coupling between the iridium photosensitiser and the [FeFe] catalyst within **D3**.

[FeFe]-Spacer-Cat 2 itself is a composite of the catalyst **[FeFe]-Cat 5** and the **Spacer 1** compound. The comparison of the corresponding absorption spectra reveals a similar situation to that of the Dyad **D3**. The spectrum of **[FeFe]-Spacer-Cat 2** is also composed of the bands of the corresponding individual components, which show some spectral shifts due to an existing electronic coupling within the composite. Both the iron-centred Fe(σ)-Fe(σ^*) absorption of **[FeFe]-Spacer-Cat 2** at 28800 cm^{-1} (347 nm) is slightly red-shifted compared to that of **[FeFe]-Cat 5**, as is the spacer-centred π-π^* excitation at 36700 cm^{-1} (273 nm) compared to that of the **Spacer 1** compound.[94] Hence, the ester bond as a π-conjugation blocker cannot completely prevent the coupling between the aromatic spacer moiety and the diiron complex within the composite. In addition, a weak low-energy absorption in the range from 17500 cm^{-1} (570 nm) to 23000 cm^{-1} (435 nm) occurs in all iron containing compounds, which can be assigned to the iron-centred Fe(t_{2g})-Fe(σ^*) transition.[94] It is known from literature that also the spin-forbidden and, therefore, very weak ^{3}MLCT transitions from one ppy ligand to the iridium central atom or from the bpy ligand to the iridium central atom in [Ir(ppy)$_2$bpy]$^+$ complexes are located in this low-energy region below 22200 cm^{-1} (> 450 nm).[20,122] Therefore, this should also apply to the **[Ir(ppy)$_2$bpy]PF$_6$** photosensitiser and the dyad **D3**. **Fig. 61** shows the corresponding section of the absorption spectra of both compounds in logarithmic scaling.

While for **D3** the corresponding weak absorption band is superimposed by the Fe(t_{2g})-Fe(σ^*) transition, **[Ir(ppy)$_2$bpy]PF$_6$** shows a band at 21500 cm^{-1} (465 nm) which can be associated to this transition. As already mentioned above, these charge transfer processes are crucial for the desired electron cascade during photocatalysis, since they represent the first step in

electron transfer from the photosensitiser to the catalyst. For this reason, in the hydrogen evolution reactions, the iridium containing samples were irradiated with blue light at 21500 cm^{-1} (465 nm). **Fig. 61** also shows an absorption of **[FeFe]-Spacer-Cat 2** in this spectral region. It can be seen from this that during photocatalysis the diiron complex is probably excited in equal parts as the photosensitiser. This represents a considerable disadvantage of this iridium system compared to the ruthenium systems considered previously, in which the absorbance of the corresponding MLCT bands at this wavelength is many times higher than that of the Fe(t_{2g})-Fe(σ^*) transition. It can be assumed that the excitation of the [FeFe] catalyst leads to a discrepancy in the redox potentials of the components involved and, thus, can considerably hinder the photocatalysis. The extent to which this affects the photocatalytic performance is discussed in chapter 5.2.7.

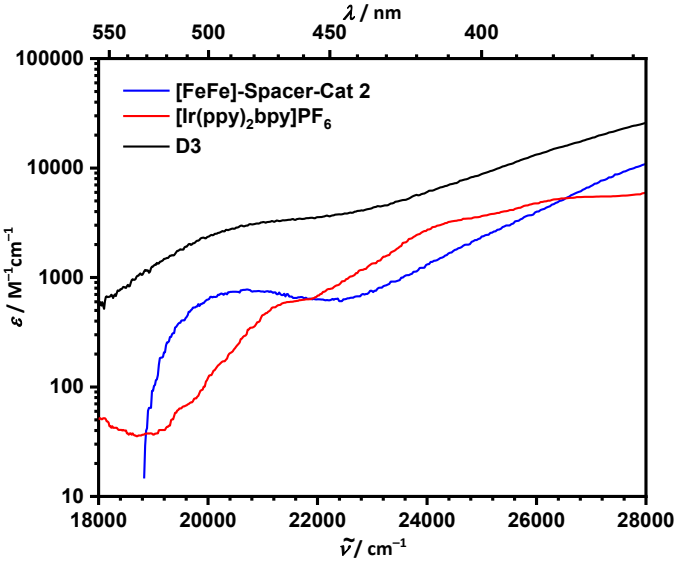

Fig. 61 Absorption spectra of **[FeFe]-Spacer-Cat 2**, **[Ir(ppy)$_2$bpy]PF$_6$** and **D3** measured in acetonitrile at 298 K in the spectral region associated to the iridium based ^{3}MLCT transitions in logarithmic scale.

5.2.3 Electrochemistry

Aligned redox potentials are a crucial prerequisite for functioning photocatalytic systems with its consecutive electron transfer processes.[3,9,39,123,124] Therefore, as in the previous chapters, cyclic voltammetry measurements were carried out to determine the redox potentials of the compounds investigated.

Fig. 62 shows the cyclic voltammograms of **[Ir(ppy)$_2$bpy]PF$_6$**, **[FeFe]-Spacer-Cat 2**, **[FeFe]-Cat 5** and **D3** in dry and degassed acetonitrile at 298 K. As before, when examining the ruthenium dyads, acetonitrile was used as the solvent in cyclic voltammetry, because on the one hand, as described above, this should be used as the main component of the solvent mixture in photocatalysis, and on the other hand because it provides good solubility and a

comparatively large electrochemical measurement window. The corresponding electrochemical data are reported in **Table 8**.

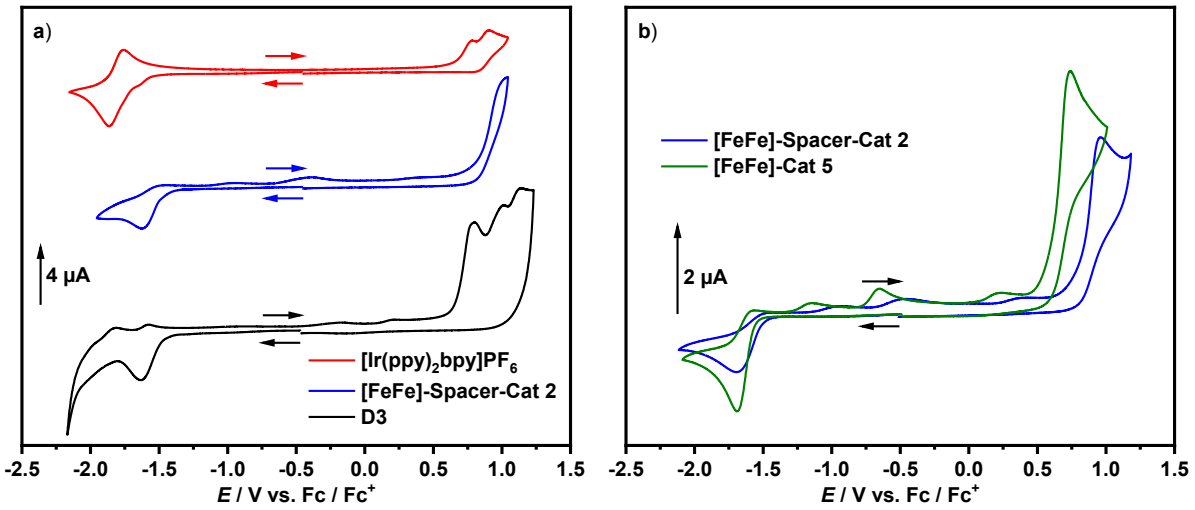

Fig. 62 Cyclic voltammograms of **a) [Ir(ppy)$_2$bpy]PF$_6$** (1 mM), **[FeFe]-Spacer-Cat 2** (1 mM) and **D3** (1 mM), **b) [FeFe]-Spacer-Cat 2** (1 mM) and **[FeFe]-Cat 5** (1 mM) in an acetonitrile solution (0.1 M TBAHFP) at 298 K. Experimental setup: Pt as WE, Pt as CE, Ag/AgCl as reference, scan rate: v = 100 mV s^{-1}.

Starting with the iridium photosensitiser, the obtained curve of **[Ir(ppy)$_2$bpy]PF$_6$** shows two irreversible oxidation waves at $E_{pa\text{-}1}$ [PS$^+$/PS] = 0.79 V *vs.* Fc/Fc$^+$ and $E_{pa\text{-}2}$ [PS$^+$/PS] = 0.91 V *vs.* Fc/Fc$^+$ and one reversible reduction wave at $E_{1/2}$ [PS/PS$^-$] = –1.81 V *vs.* Fc/Fc$^+$. The irreversible oxidations can be assigned to metal-centred processes because the metal-carbon bonds in the cyclometalated complexes generally have relatively strong σ-donor properties and, in addition, bpy and ppy would usually exhibit higher oxidation potentials.[17] Furthermore, a change in the oxidation signals was observed in the course of the measurements. While the second signal persisted, the first disappeared almost completely after a few cycles. In combination with the irreversibility of both signals, which speaks for the formation of by-products or decay products during the measurement, an interaction with ligating acetonitrile molecules during the measurement resulting in the formation of such by-products can be assumed here. Therefore, only the first oxidation signal is referred in the following. The reversible reduction wave, on the other hand, can be assigned to a bpy-centred process.[17] The already in the previous chapter discussed cyclic voltammogram of **[FeFe]-Spacer-Cat 2** shows the typical irreversible signals for such a [FeFe] complex in acetonitrile, also caused by the formation of solvent involved by-products.[95,96] The oxidation signal at E_{pa} [Cat$^+$/Cat] = 0.96 V *vs.* Fc/Fc$^+$ refers to the iron-centred Fe^{II}Fe^{I}/Fe^{I}Fe^{I} redox couple and the reduction at E_{pc} [Cat/Cat$^-$] = –1.70 V *vs.* Fc/Fc$^+$ to the corresponding Fe^{I}Fe^{I}/Fe^{0}Fe^{I} redox couple.[95] **Fig. 62b** shows the direct comparison between the cyclic voltammograms of both diiron complexes **[FeFe]-Spacer-Cat 2** and **[FeFe]-Cat 5**. Here, the influence of the attached aromatic spacer

on the position of the iron-centred redox potentials can be observed directly. As can be seen, the additional spacer unit leads to a significant cathodic shift of the oxidation signal, while the for the photocatalysis more important reduction remains unaffected.

The redox waves of the contained constituents can be clearly seen in the cyclic voltammogram of the dyad **D3**. At E_{pa} [D3-PS$^+$/D3-PS] = 0.80 V *vs.* Fc/Fc$^+$ appears the iridium-based oxidation, at E_{pa} [D3-Cat$^+$/D3-Cat] = 1.01 V *vs.* Fc/Fc$^+$ the iron-centred $Fe^{II}Fe^{I}/Fe^{I}Fe^{I}$ oxidation and at E_{pc} [D3-Cat/D3-Cat$^-$] = –1.63 V *vs.* Fc/Fc$^+$ the iron-centred $Fe^{I}Fe^{I}/Fe^{0}Fe^{I}$ reduction. When comparing the individual **D3** signals with the processes of the corresponding single molecules, only slight changes in the position of the potentials can be seen through the linkage to the dyad. The iridium-based oxidation of **D3** shows a negligible anodic shift (0.01 V) compared to the first oxidation of **[Ir(ppy)$_2$bpy]PF$_6$**. The two iron-centred redox processes of **D3** also show anodic shifts compared to the corresponding processes of **[FeFe]-Spacer-Cat 2**. The $Fe^{II}Fe^{I}/Fe^{I}Fe^{I}$ oxidation exhibits a shift of 0.05 V and the $Fe^{I}Fe^{I}/Fe^{0}Fe^{I}$ reduction a 0.07 V shift. Since the complete bpy-centred reduction could not be measured in the cyclic voltammetry measurement of **D3** due to the limiting solvent window, it is difficult to compare the reduction potential with the related one of **[Ir(ppy)$_2$bpy]PF$_6$**. However, this reduction with a peak potential at E_{pa} [D3-PS/D3-PS$^-$] = –1.83 V *vs.* Fc/Fc$^+$ seems to have undergone a cathodic shift compared to **[Ir(ppy)$_2$bpy]PF$_6$**. Since the redox potentials in the excited state are also required to assess the processes taking place in the electron cascade, this will be dealt with in the next section.

Table 8 Electrochemical data of **[Ir(ppy)$_2$bpy]PF$_6$**, **[FeFe]-Spacer-Cat 2**, **[FeFe]-Cat 5** and **D3** measured by cyclic voltammetry in acetonitrile solutions with 0.1 M TBAHFP at 298 K.

Compound	E_{red} (V *vs.* Fc/Fc$^+$)		E_{ox} (V *vs.* Fc/Fc$^+$)	
	E_{pc-2}	E_{pc-1}	E_{pa-1}	E_{pa-2}
[Ir(ppy)$_2$bpy]PF$_6$	–1.81[a]		0.79	0.91
[FeFe]-Spacer-Cat 2		–1.70	0.96	
[FeFe]-Cat 5		–1.69	0.74	
D3	–1.83[b]	–1.63[b]	0.80	1.01

[a] $E_{1/2}$ of reversible reduction. [b] Quasi-reversible reduction.

5.2.4 Estimation of Excited State Redox Potentials

As with the ruthenium compounds in the previous chapter, the electron transfer processes taking place with the participation of the iridium compounds during photocatalysis are to be examined and assessed from a thermodynamic point of view. Assuming that the contemplated electron cascade can run either under the RQ or the OQ mechanism, in addition to the ground state redox potentials of the catalysts involved, the excited state redox potentials of the photosensitisers are required. As already described in the ruthenium dyad chapter, these excited state redox potentials can be estimated, according to the method of Bernhard *et al.*,

using the electrochemical data from the cyclic voltammetry measurements and the 0-0 energies determined from the emission spectra of the corresponding iridium containing compounds (see **Fig. 63**).[24,113] The results are reported in **Table 9**.

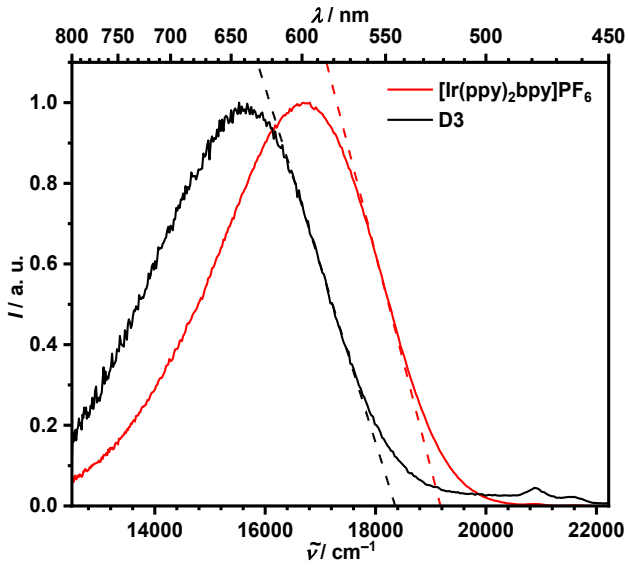

Fig. 63 Normalised emission spectra of **[Ir(ppy)$_2$bpy]PF$_6$** and **D3** in degassed acetonitrile solution at 298 K. The samples were excited at λ_{ex} = 23900 cm^{-1} (419 nm). Tangents for the 0-0 energy estimations are given in dashed lines.

Table 9 Excited state redox properties of **[Ir(ppy)$_2$bpy]PF$_6$** and **D3**.

Compound	$E^{0'}$ [PS$^+$/PS*] (V *vs.* Fc/Fc$^+$)	$E^{0'}$ [PS*/PS$^-$] (V *vs.* Fc/Fc$^+$)	0-0 energy[a] (eV)
[Ir(ppy)$_2$bpy]PF$_6$	–1.59	0.57	2.38
D3	–1.48	0.45	2.28

[a] Estimation from emission spectrum (see **Fig. 63**).

An excited state oxidation potential of $E^{0'}$ [PS$^+$/PS*] = –1.59 V *vs.* Fc/Fc$^+$ and an excited state reduction potential of $E^{0'}$ [PS*/PS$^-$] = 0.57 V *vs.* Fc/Fc$^+$ could be appraised for the **[Ir(ppy)$_2$bpy]PF$_6$** photosensitiser using the electrochemical data from **Table 8** and a 0-0 energy of 2.38 eV, which was determined using the tangential method from the emission spectrum of the photosensitiser (see **Fig. 63**). The conditions for thermodynamically feasible electron transfers listed in the section on estimating the excited state redox potentials of the ruthenium compounds naturally also apply to photocatalytically active systems with iridium photosensitisers. Therefore, assuming the corresponding 3CS operates *via* the RQ mechanism, the following applies for the initial electron transfer:

$$E^{0'}\,[SD^+/SD] < E^{0'}\,[PS^*/PS^-] \qquad (3)$$

The oxidation potential $E_{1/2}$ [SD$^+$/SD] for TEA as the sacrificial electron donor is 0.29 V *vs.* Fc/Fc$^+$.[125] With that the thermodynamic requirement of equation 3 is clearly fulfilled with ΔE_{RQ1} = 0.28 V. The condition for the subsequent electron transfer from the now reduced photosensitiser to the catalyst in the RQ-operating 3CS can be described as follows:

$$E^{0'}\,[PS/PS^{-}] < E^{0'}\,[Cat/Cat^{-}] \quad (4)$$

With the abovementioned data of **[Ir(ppy)$_2$bpy]PF$_6$** and **[FeFe]-Spacer-Cat 2** this is also fulfilled by the 3CS with ΔE_{RQ2} = 0.11 V (cf. **Table 8**). However, if the 3CS performs *via* the OQ mechanism, the initial redox process would consist of the reduction of the catalyst by the excited photosensitiser. Therefore, the following thermodynamic requirement applies for a feasible electron transfer:

$$E^{0'}\,[PS^{+}/PS^{*}] < E^{0'}\,[Cat/Cat^{-}] \quad (5)$$

Since only irreversible signals for the oxidation of **[Ir(ppy)$_2$bpy]PF$_6$** and the reduction of **[FeFe]-Spacer-Cat 2** were detected in the cyclic voltammetry measurements, the underlying redox potentials can only be roughly estimated. Nevertheless, the potential difference between $E^{0'}$ [PS$^+$/PS*] = –1.59 V *vs.* Fc/Fc$^+$ and E_{pc} [Cat/Cat$^-$] = –1.70 V *vs.* Fc/Fc$^+$ is with ΔE_{OQ} = –0.11 V definitively too large for a thermodynamically feasible process.

For the Dyad **D3**, considering the photosensitiser and catalyst moieties separately, the electrochemical data from **Table 8** and the 0-0 energy obtained from the emission spectrum (see **Fig. 63**) result in an oxidation potential of the excited photosensitiser moiety of $E^{0'}$ [D3-PS$^+$/D3-PS*] = –1.48 V *vs.* Fc/Fc$^+$ and a reduction potential of the excited photosensitiser moiety of $E^{0'}$ [D3-PS*/D3-PS$^-$] = 0.45 V *vs.* Fc/Fc$^+$. Since the abovementioned thermodynamic conditions must also apply to the corresponding 2CS, the **D3** containing system fulfils the prerequisite specified in equation 3 for the first RQ electron transfer with ΔE_{RQ1} = 0.16 V. The expression given in equation 4 for the second RQ electron transfer, which takes place intramolecularly in the 2CS from the photosensitiser moiety of the dyad to the associated catalyst moiety, is very clearly fulfilled by the **D3** system with ΔE_{RQ2} = 0.20 V. Amazingly, the difference here is almost twice that of the 3CS. Analogous to the 3CS, the **D3** containing system does not meet the condition for the OQ electron transfer from the excited photosensitiser to the catalyst, which is listed in equation 5. With ΔE_{OQ} = –0.15 V, the potential difference is too large here, too.

Thus, the iridium containing systems clearly prefer the RQ mechanism in photocatalysis over the OQ mechanism and thus show a similar behaviour as the ruthenium containing systems. In addition, it can be seen that in the **[Ir(ppy)$_2$bpy]PF$_6$** containing 3CS, the initial electron transfer from the sacrificial electron donor to the excited photosensitiser is more favourable than the corresponding process in the **D3** containing 2CS. In contrast, the subsequent intramolecular electron transfer from the reduced photosensitiser part to the catalyst part in the 2CS is more favourable from a thermodynamic point of view than the corresponding intermolecular process in the 3CS. Therefore, this process represents the driving force of the 2CS and the initial electron transfer that of the 3CS.

5.2.5 Emission Quenching Studies

In order to better classify the initial redox process of the photocatalytically active iridium systems and also to gain further evidence for the RQ mechanism in these systems, the electron transfer from TEA as the sacrificial electron donor to the corresponding excited iridium photosensitisers was investigated from a kinetic point of view. To this end, the dynamic quenching of the excited state of both the **[Ir(ppy)$_2$bpy]PF$_6$** photosensitiser and the photosensitiser moiety of **D3** by TEA was investigated. The phosphorescence spectrum and corresponding emission lifetime of each of both iridium compounds were measured in degassed acetonitrile at 298 K first without and then with increasing TEA amount. The phosphorescence spectra measured are displayed in **Fig. 64**, the emission decay curves recorded are shown in **Fig. 65** and the lifetimes obtained are listed in **Table 10**.

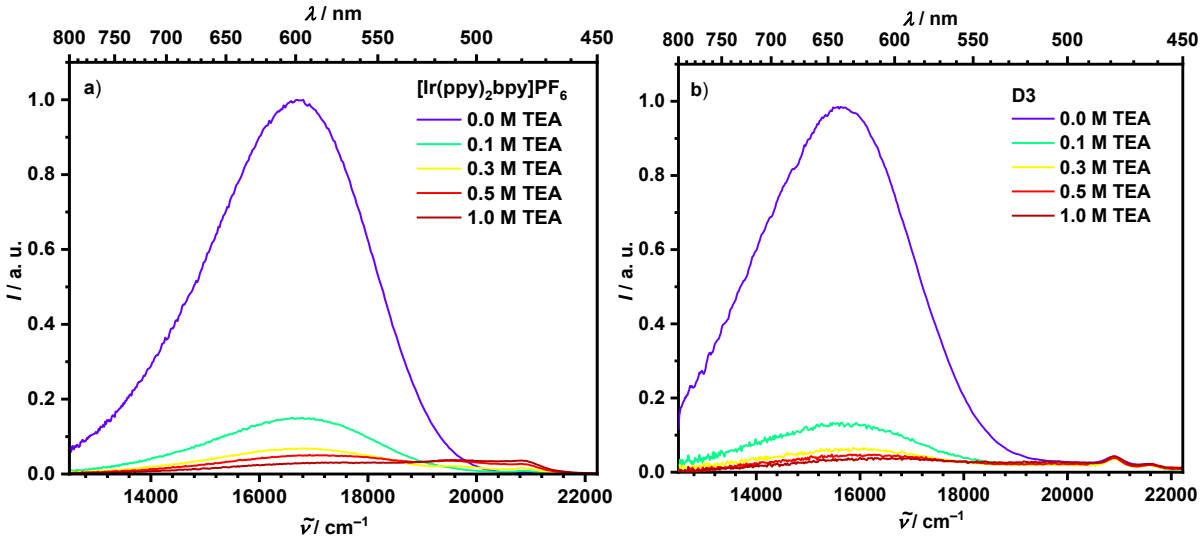

Fig. 64 Normalised emission spectra of **a) [Ir(ppy)$_2$bpy]PF$_6$** and **b) D3** in degassed acetonitrile solution with increasing amount of TEA as quencher at 298 K. The samples were excited at λ_{ex} = 23900 cm^{-1} (419 nm).

Table 10 Luminescence lifetimes of **[Ir(ppy)$_2$bpy]PF$_6$** and **D3** without a quencher (TEA) and with subsequent increasing quencher concentration in acetonitrile at 298 K. The samples were excited at λ_{ex} = 23900 cm^{-1} (419 nm).

Compound	*c* (TEA)				
	0.0 M	0.1 M	0.3 M	0.5 M	1.0 M
[Ir(ppy)$_2$bpy]PF$_6$	289 ns	49.2 ns	20.6 ns	14.2 ns	7.64 ns
D3	123 ns	18.2 ns	7.66 ns	5.36 ns	2.56 ns

In order to obtain the underlying emission lifetimes from the decay curves shown in **Fig. 65**, they were fitted using the exponential term given in equation 13. The respective lifetime τ and the value of the goodness of fit χ^2 can be found in the corresponding diagram in **Fig. 65**. The post-pulse-like artefact that appeared in the time-resolved phosphorescence measurements of **D3** 1.39 ns after excitation was not taken into account.

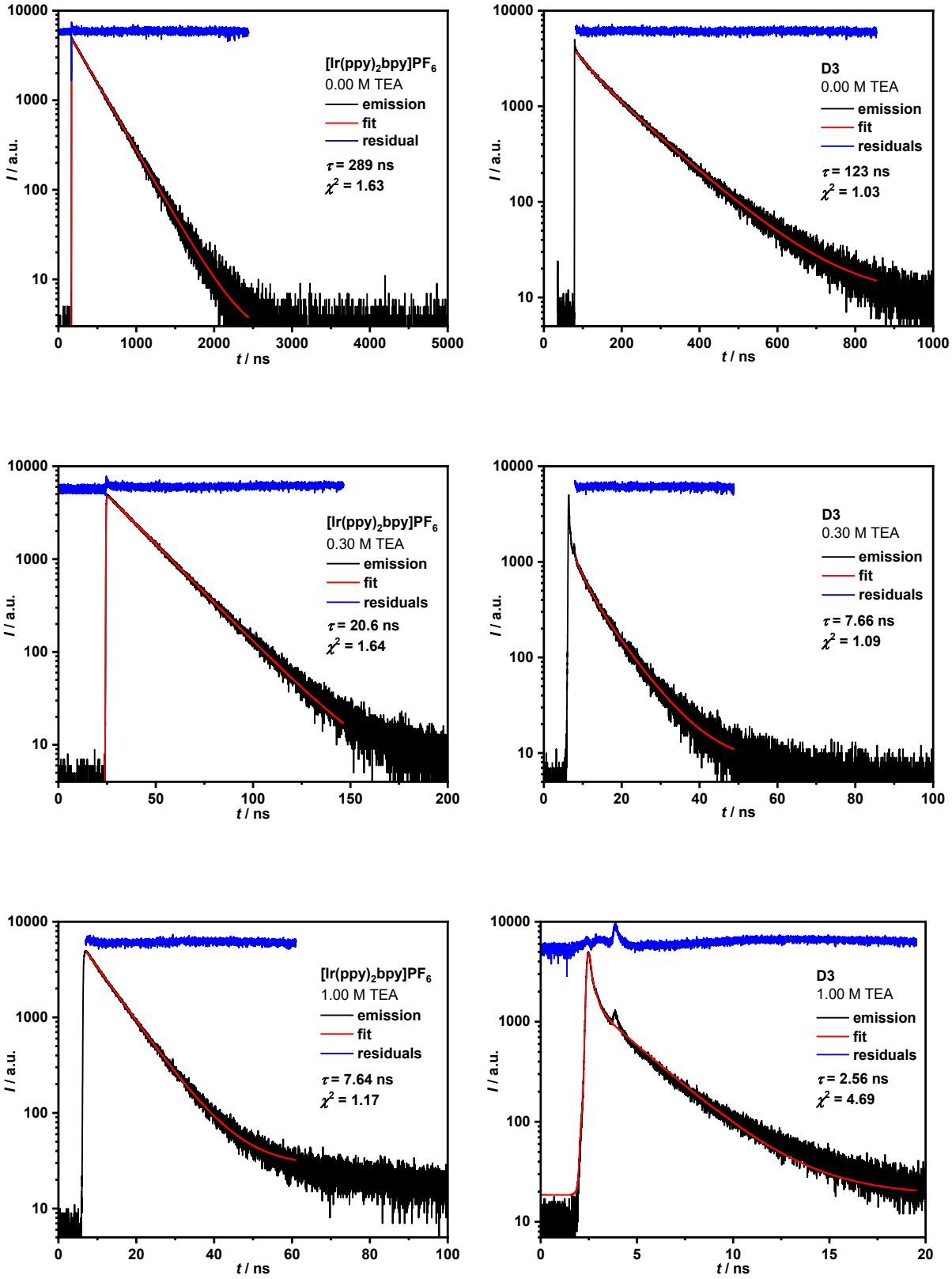

Fig. 65 Phosphorescence kinetics of **[Ir(ppy)$_2$bpy]PF$_6$** (left side) and **D3** (right side) without a quencher (first line), with 0.30 M TEA (second line) and with 1.00 M TEA (third line) in acetonitrile at 298 K. The samples were excited at λ_{ex} = 23900 cm^{-1} (419 nm). The kinetic traces were fitted to a first order decay by deconvolution or tail fitting, respectively.

Along with the decrease in phosphorescence intensity (see **Fig. 64**), its lifetime also decreases with increasing quencher concentration. For **[Ir(ppy)$_2$bpy]PF$_6$** it drops from 289 ns to 7.64 ns and for the Dyad **D3** from 123 ns to 2.56 ns. Since all iridium containing compounds exhibit a monoexponential decay behaviour, it is now possible to assess the occurring process from a kinetic point of view directly using the Stern-Volmer equation for dynamic emission quenching given in equation 10. The rate for dynamic quenching k_d can be calculated from the ratio of the unquenched lifetime to the quenched excited state lifetime (τ_0/τ) and the associated quencher concentration [Q]. The resulting data are reported in **Table 11** and the Stern-Volmer plots arising from equation 10 are shown in **Fig. 66**.

Table 11 Quenching kinetics of **[Ir(ppy)$_2$bpy]PF$_6$** and **D3** with TEA as quencher in acetonitrile at 298 K.

Compound	τ_0 (ns)	k_d (M^{-1} s^{-1})
[Ir(ppy)$_2$bpy]PF$_6$	289	$1.3 \cdot 10^8$
D3	123	$3.8 \cdot 10^8$

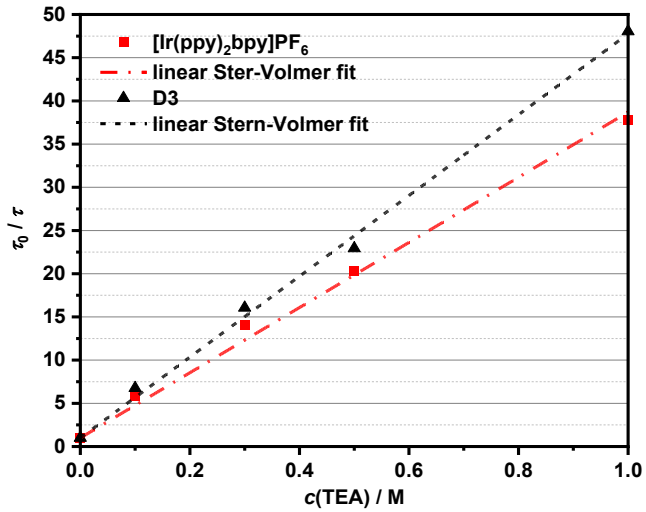

Fig. 66 Dynamic quenching studies of **[Ir(ppy)$_2$bpy]PF$_6$** and **D3**. All linear fits in the Stern-Volmer plot have $R^2 > 0.99$.

In view of the lifetimes measured, it is noticeable that those of **D3** are considerably shorter than those of **[Ir(ppy)$_2$bpy]PF$_6$**. This indicates a more rapid deactivation within the dyad. Whether this is due to a subsequent electron transfer to the catalyst or a respective energy transfer to it cannot be further verified at this point. However, since, as shown in the previous sections, there is a certain, albeit relatively weak, coupling between the dyad components in **D3** despite the presence of the π-conjugation blockers, a partial energy transfer from the excited photosensitiser to the catalyst within the dyad cannot be completely ruled out, especially in the case of the TEA-free solution. As can be seen in the illustration of the Stern-Volmer plots, both compounds show a linear course in the relation to the inverse lifetime *vs.*

the quencher concentration. With k_d = 1.3·10^8 M^{-1} s^{-1}, **[Ir(ppy)$_2$bpy]PF$_6$** shows a lower rate constant than the dyad with k_d = 3.8·10^8 M^{-1} s^{-1}. Surprisingly, however, both compounds have significantly higher values than comparable iridium photosensitisers in the literature.[24] Since the determined rate constants are also clearly lower than the typical diffusion rate in acetonitrile (ca. 2·10^{10} M^{-1} s^{-1}), this indicates that the reduction of the excited iridium complexes in both systems is not diffusion-controlled, but is determined by the surprisingly small intrinsic electron transfer barriers.[117] In addition, this barrier appears to be somewhat lower in the dyad than in the corresponding 3CS, which contradicts the results of the previous section, which attested the dyad to have a lower thermodynamic driving force for this electron transfer. As already mentioned, this could probably be the result of a parallel energy transfer within the dyad molecule. Basically, however, the results of this series of measurements clearly confirm the RQ mechanism in both systems.

5.2.6 ns-Transient Absorption Spectroscopy

In order to obtain further information about the temporal sequence during the photocatalytic electron cascade in the iridium containing 2CS and 3CS, transient absorption spectroscopic measurements were carried out using a ns-laser setup. Analogously to the TA measurements of the ruthenium containing systems, the excitation wavelength of the laser was chosen in such a way that the photosensitiser-based MLCT transitions that are crucial for photocatalysis were excited.

In the present case of the [Ir(ppy)$_2$bpy]$^+$ systems, the photosensitiser moieties were excited at 25100 cm^{-1} (398 nm).[126] In order to ensure the comparability of both systems examined the same concentration (0.13 mM) of **[Ir(ppy)$_2$bpy]PF$_6$** and **[FeFe]-Spacer-Cat 2** in the 3CS and of **D3** in the 2CS was used. TEA was deployed in excess (3.14 mM) as the sacrificial electron donor in both systems. To achieve its sufficient and rapid decomposition in the aqueous medium after the electron transfer to the photosensitiser, a solvent mixture consisting of acetonitrile and water (*v*/*v* = 9:1) was used for the measurements.[14] **Fig. 67** shows the obtained TA spectra of the 3CS and the 2CS.

Starting with the **[Ir(ppy)$_2$bpy]PF$_6$** and **[FeFe]-Spacer-Cat 2** containing 3CS, a dominant ESA at 20000 cm^{-1} (500 nm) with a shoulder at 22700 cm^{-1} (440 nm) as well as at 13000 cm^{-1} (770 nm) is visible. This spectral feature arises immediately after excitation. By comparison with TA measurements of only the **[Ir(ppy)$_2$bpy]PF$_6$** photosensitiser (see **Fig. 68a**) or only **[FeFe]-Spacer-Cat 2** (see **Fig. 68b**) under similar conditions, it can be concluded that this signal clearly originates from the excited [Ir(ppy)$_2$bpy]$^+$ species. In the literature, it is assigned to the ILCT (interligand-charge-transfer) transition between a ppy and the bpy ligand.[126]

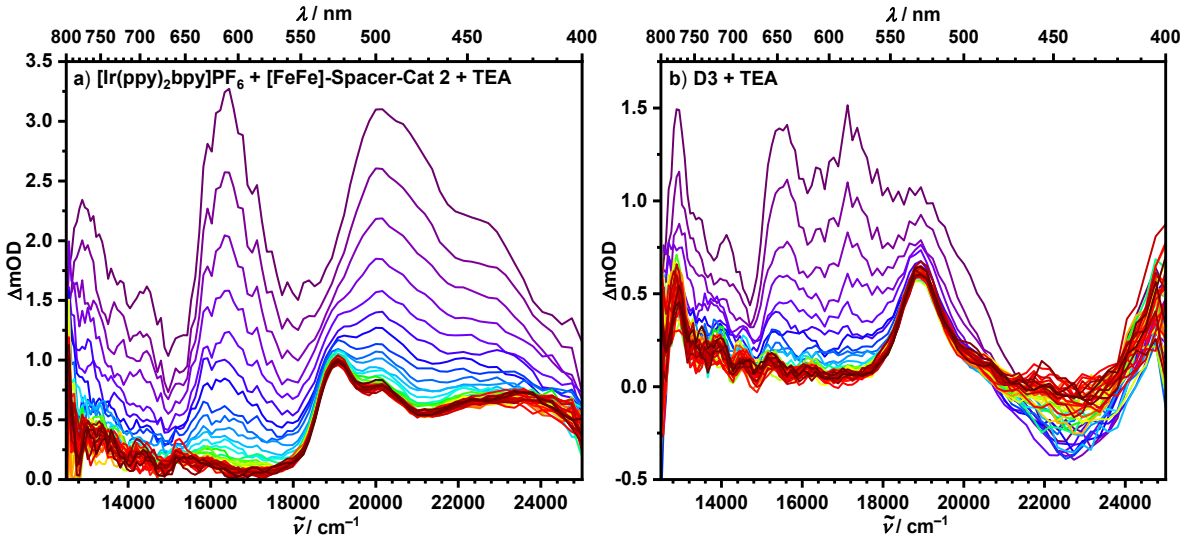

Fig. 67 UV/Vis transient absorption (TA) spectra of **a) [Ir(ppy)$_2$bpy]PF$_6$** (0.13 mM), **[FeFe]-Spacer-Cat 2** (0.13 mM) and TEA (3.14 mM) in MeCN/H_2O (*v*/*v* = 9:1) at 298 K and of **b) D3** (0.13 mM) and TEA (3.14 mM) in MeCN/H_2O (*v*/*v* = 9:1) at 298 K. TA spectra were obtained between 0 ns (purple) and 1.72 µs (dark red) after excitation at λ_{ex} = 25100 cm^{-1} (398 nm). The time delay between each curve is 40.0 ns.

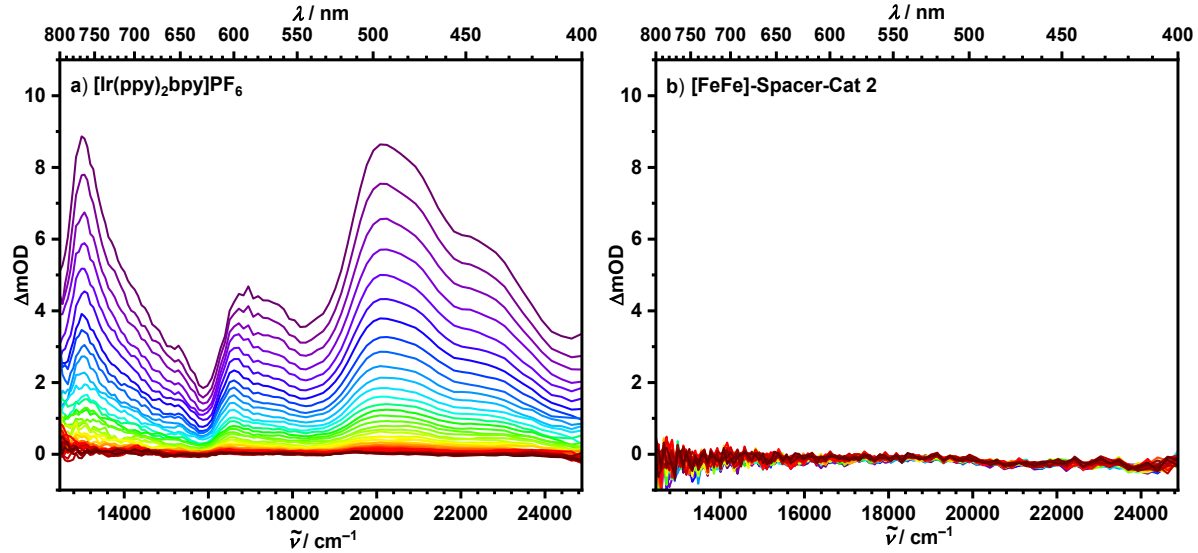

Fig. 68 UV/Vis transient absorption (TA) spectra of **a) [Ir(ppy)$_2$bpy]PF$_6$** (0.13 mM) in MeCN/H_2O (*v*/*v* = 9:1) at 298 K and of **b) [FeFe]-Spacer-Cat 2** (0.13 mM) in MeCN/H_2O (*v*/*v* = 9:1) at 298 K. TA spectra were obtained between 0 ns (purple) and 1.72 µs (dark red) after excitation at λ_{ex} = 21700 cm^{-1} (460 nm). The time delay between each curve is 40.0 ns.

The conspicuous absorption band at 16400 cm^{-1} (610 nm) in the TA spectra of the 3CS (see **Fig. 67a**) does not arise from an ESA but from an insufficient (overcompensated) correction of the strong **[Ir(ppy)$_2$bpy]PF$_6$** phosphorescence in this spectral area. That is why this signal will be disregarded for the further contemplation. When considering the spectra with a longer time interval to the excitation, the formation of a characteristic ESA at 19000 cm^{-1} (527 nm) and 20200 cm^{-1} (495 nm) is striking. To determine its origin, a UV/Vis spectroelectrochemistry

experiment of **[Ir(ppy)$_2$(bpy)]PF$_6$** in acetonitrile was carried out. **Fig. 69** shows the resulting spectra after applying and gradually increasing negative voltage to the sample.

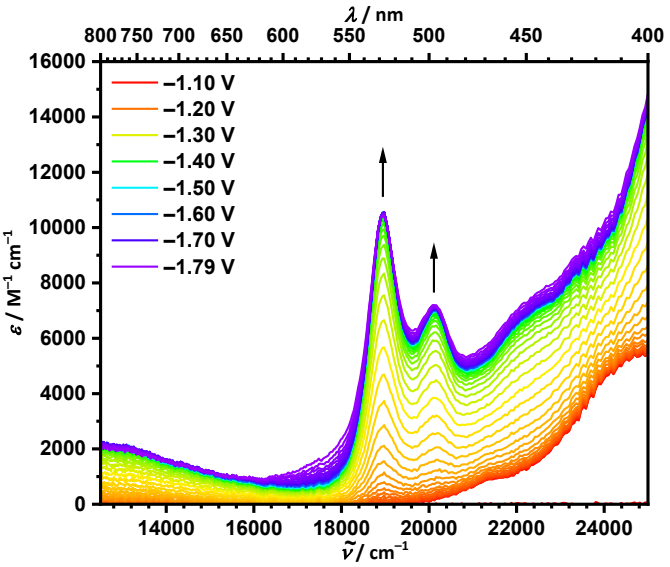

Fig. 69 Spectroelectrochemistry measurement of **[Ir(ppy)$_2$bpy]PF$_6$** ($4.13 \cdot 10^{-5}$ M) in an acetonitrile solution (0.1 M TBAHFP) at 298 K. Experimental setup: Pt as WE, Pt as CE, Ag/AgCl as Reference. All given voltages are referenced against Ag/AgCl.

Since the same absorption signals occur in the TA spectra as in the spectroelectrochemistry measurement, they can be assigned to the reduced iridium photosensitiser. This provides further proof of the RQ mechanism in the 3CS. Because of this and in view of the TEA excess in the solution under consideration, the presence of an $[Ir(ppy)_2bpy]^{2+}$ species cannot be assumed. Therefore, a spectroelectrochemistry measurement of **[Ir(ppy)$_2$(bpy)]PF$_6$** in the positive potential range was omitted.

In order to get a deeper insight into the temporal processes during photocatalysis and especially into the formation of the reduced $[Ir(ppy)_2bpy]^{+}$ species due to the initial reduction, the TA time traces of the intense ILCT band of the 3CS TA spectra (see **Fig. 67a**) at 20200 cm^{-1} (496 nm) were also measured. After fitting it by the single exponential mentioned in equation 13, a lifetime of τ = 165 ns could be determined for this feature. With the help of the Stern-Volmer relationship given in equation 10 and the data of **[Ir(ppy)$_2$bpy]PF$_6$** on k_d and τ_0 given in chapter 5.2.5, the expected phosphorescence lifetime of the photosensitiser in combination with 3.14 M TEA can be calculated. With τ = 259 ns, this is somewhat longer than that of the ILCT band measured. Since the diiron complex was also present in the solution of the TA measurement, this could indicate a possible parallel energy transfer between the photosensitiser and the catalyst, as was already suspected for **D3** in chapter 5.2.5. The result of the transient absorption kinetics determination including the coefficient B and the value for the goodness of fit χ^2 is shown in **Fig. 70**.

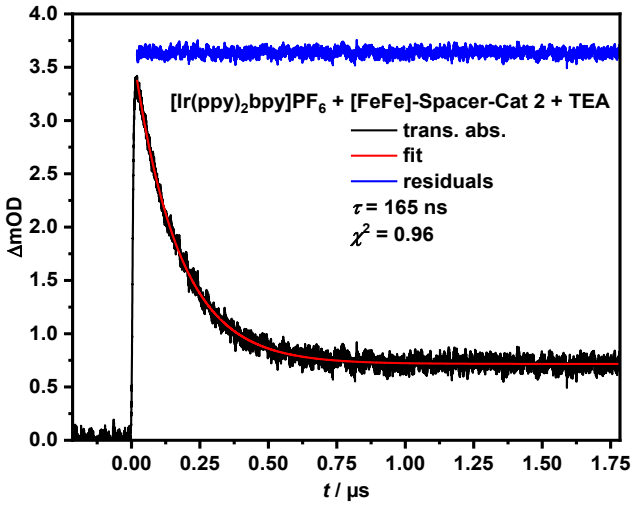

Fig. 70 Transient absorption (TA) kinetics of **[Ir(ppy)$_2$bpy]PF$_6$** (0.13 mM), **[FeFe]-Spacer-Cat 2** (0.13 mM) and TEA (3.14 mM) in MeCN/H_2O (*v*/*v* = 9:1) recorded at 20200 cm^{-1} (496 nm) at 298 K after excitation at λ_{ex} = 25100 cm^{-1} (398 nm). The TA kinetic traces were fitted to a first-order decay with a lifetime of 165 ns.

The characteristic ESA of the reduced [Ir(ppy)$_2$bpy]$^+$ species at 19000 cm^{-1} (527 nm) and at 13000 cm^{-1} (770 nm) can also be seen in the TA spectra of the 2CS (see **Fig. 67b**) at later times. As in the 3CS, this signal remains for at least several µs. This shows that, even in the dyad, the electron transfer from the photosensitiser to the catalyst is obviously very slow. In addition, there is also an artefact signal between 15000 cm^{-1} (667 nm) and 18000 cm^{-1} (556 nm) due to the insufficient phosphorescence compensation at this point, which will be not considered for further considerations, too. Furthermore, there is a relative broad and undefined negative signal at 22700 cm^{-1} (440 nm) in the 2CS TA spectra. This bleaching signal is probably caused by the simultaneous excitation of the diiron catalyst part of the dyad during the experiments. TA measurements of **D3** and TEA in acetonitrile with an exclusive excitation of the [FeFe] catalyst part at 21700 cm^{-1} (460 nm) support this presumption by the formation of a broad bleaching signal (see **Fig. 71**). As can be seen from the dyad absorption spectrum in **Fig. 60**, this spectral feature can presumably be assigned to the iron-centred Fe(t_{2g})-Fe(σ^*) transition. As can also be seen in **Fig. 60**, both the photosensitiser moiety and the catalyst moiety of the dyad have almost the same absorbance at the excitation wavelength of the laser. A parallel excitation of both parts of the molecule during the TA measurements is therefore relatively likely. Accordingly, this should also apply to the 3CS. However, the bleaching signal is probably covered there by the much more intense ILCT band (see **Fig. 67a**). In the dyad, on the other hand, the negative charge is probably stabilised at the bpy ligand by the amide group attached to the bpy ligand, which means that the corresponding ILCT transition in the 2CS can no longer take place to the same extent as in the 3CS.

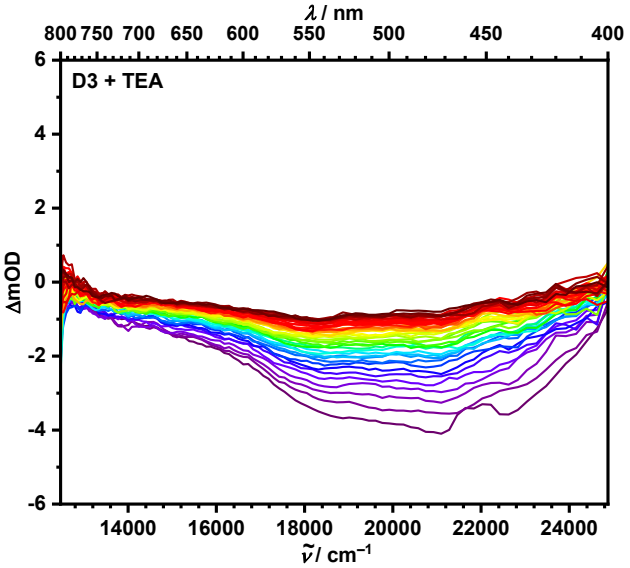

Fig. 71 UV/Vis transient absorption (TA) spectra of **D3** (0.13 mM) and TEA in MeCN/H_2O (*v*/*v* = 9:1) at 298 K. TA spectra were obtained between 0 ns (purple) and 1.72 µs (dark red) after excitation at λ_{ex} = 21700 cm^{-1} (460 nm). At this wavelength an almost exclusive excitation of the diiron part of the dyad molecule occurs. The time delay between each curve is 40.0 ns.

For a final and holistic assessment of the photophysical processes during the photocatalysis and for further elucidation of all observed bands in the respective TA spectra, the [FeFe] catalysts must also be considered. Unfortunately, due to the irreversible redox behaviour of all [FeFe] complex compounds in acetonitrile, it was not possible to carry out spectroelectrochemistry measurements of **[FeFe]-Spacer-Cat 2** and **D3** in order to determine the associated absorption bands of the corresponding reduced or oxidised species. Therefore, such bands, which could possibly appear in the TA spectra, could not be further taken into account. Apart from this, the 2CS and 3CS behave in comparison very similarly in the TA measurements with regard to the long time the negative charge remains on the photosensitiser. This is surprising given the higher thermodynamic driving force of the initial electron transfer in the dyad mentioned above.

5.2.7 Photocatalysis

To determine the photocatalytic performance of the iridium systems examined, photocatalytic hydrogen evolution reactions were carried out using the corresponding 3CS, consisting of the **[Ir(ppy)$_2$bpy]PF$_6$** photosensitiser, the **[FeFe]-Spacer-Cat 2** catalyst and TEA as the sacrificial electron donor, or the 2CS, consisting of the photocatalytically active dyad **D3** and TEA. As already mentioned at the beginning of the chapter, photocatalytic preliminary examinations were first carried out after the synthesis of the corresponding system components to determine their suitability in photocatalysis. Since the previously discussed ruthenium systems were used as a reference and starting point for this study, the measurement conditions and parameters for photocatalysis, which could be successfully used for them, were first tested on the new

iridium containing systems. The corresponding 3CS and 2CS, each with ascorbic acid as the sacrificial electron donor, were irradiated with light at 21500 cm^{-1} (465 nm) in pure water at 293 K for 17 h. In both systems, the water-insoluble components were solubilised using the poly(2-oxazoline) polymer shown in **Fig. 14**. Unlike the ruthenium containing 3CS with its water-soluble photosensitiser, in the iridium containing 3CS, in addition to the diiron catalyst, also the water-insoluble **[Ir(ppy)$_2$bpy]PF$_6$** photosensitiser had to be solubilised by the polymer micelles. For the 3CS, the photosensitiser was used in a 4-fold excess compared to the catalyst, in order to use the optimal ratio of the two components determined in chapter 4. By gas-chromatographic analysis of the supernatant gas phases, the amounts of hydrogen generated in each case could be detected and thus the catalytic productivity could be determined. A TON value of 45 was identified for the 3CS and a TON value of 13 for the 2CS. The results can be seen in **Fig. 72**.

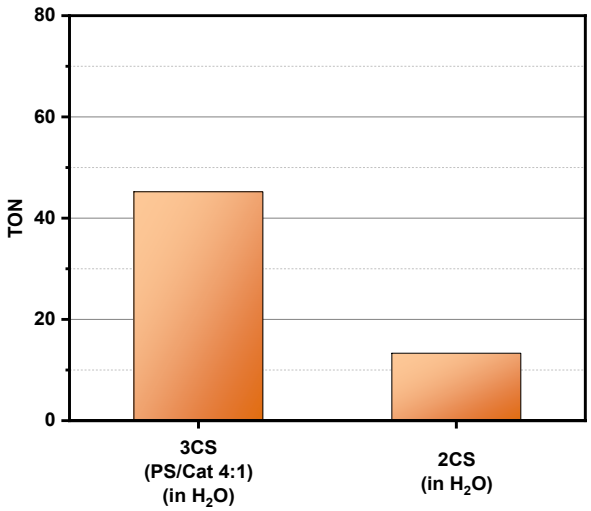

Fig. 72 Photocatalytic hydrogen evolution in aqueous poly(2-oxazoline) solution (pH = 4, polymer concentration: 2.0 mg ml^{-1}) at 293 K after 17 h irradiation with light at 21500 cm^{-1} (465 nm). Stoichiometric proportions: (left column) 0.08 mM **[Ir(ppy)$_2$bpy]PF$_6$**, 0.02 mM **[FeFe]-Spacer-Cat 2** and 0.36 M ascorbic acid; (right column) 0.02 mM **D3** and 0.36 M ascorbic acid.

At first glance, the 3CS achieves a productivity that is comparable to that of the corresponding 3CS of the examined ruthenium systems (see **Table 7**). However, equimolar amounts of photosensitiser and catalyst were used in the ruthenium systems, which, as shown in chapter 4, has a negative effect on catalytic productivity. It can therefore be assumed that the iridium containing 3CS performs significantly worse in the aqueous medium under the conditions mentioned above. The direct comparison of the 2CS with the corresponding ruthenium containing 2CS (see **Table 7**) confirms this assumption. In comparison to photocatalytic systems with iridium photosensitisers known from the literature, the systems tested also show comparatively poor performance.[5,9,53,67,127] Even if there is no comparison value in the literature for photocatalytic systems in pure water with molecular iridium photosensitisers.

Reasons for this behaviour could be, on the one hand, that the redox potentials of the $[Ir(ppy)_2bpy]^+$ complex are different compared to those of the $[Ru(bpy)_3]^{2+}$ complex and which in combination with water as a solvent may no longer optimally match those of the other system components for an optimal electron cascade during photocatalysis. On the other hand, a negative influence of the polymer micelles used on the various electron transfer processes, especially on the reductive quenching of the photosensitiser by the sacrificial electron donor, cannot be excluded at this point, since, as already mentioned above, not only the catalyst but also the photosensitiser was solubilised this time.

In the past, several bimolecular iridium systems in combination with TEA as the sacrificial electron donor in aqueous solvent mixtures have been successfully tested in the literature.[5,53] For this reason, TEA was used as the sacrificial electron donor in both systems due to the better matching redox potentials (see chapter 5.2.4). In combination with the poly(2-oxazoline) micelles used, however, the corresponding iridium and TEA containing systems showed in pure water no activity in photocatalytic preliminary examinations. Therefore, the solvent for the photocatalysis was additionally changed from pure water to a mixture of acetonitrile and water in a ratio of *v*/*v* = 9:1 (pH = 10). The water content is required for a quick and efficient degeneration of TEA after the photosensitiser has been reduced.[14] In this way, additional solubilisation additives no longer had to be used, which eliminates their potentially disruptive influence on the performance of the iridium systems. In order to compare the performance of the 3CS and the 2CS, an equimolar amount (0.02 mM) of **$[Ir(ppy)_2bpy]PF_6$** and **[FeFe]-Spacer-Cat 2** was used in the 3CS and of **D3** in 2CS. TEA was used in a concentration of 0.36 M in both systems. As before, the samples were irradiated at 293 K with light at 21500 cm^{-1} (465 nm) for 17 h and then the supernatant gas phases were analysed by gas chromatography. The catalytic productivity of the systems was determined using the detected amount of hydrogen generated. With the help of pressure sensors attached to the reaction vessels, the temporal progress of the hydrogen evolution reactions was also recorded. The results are shown in **Fig. 73** and listed in **Table 12**.

Table 12 Photocatalytic hydrogen evolution data of the 2CS and the 3CS in MeCN/H_2O (*v*/*v* = 9:1, pH = 10) at 293 K.

System	TON[a]	TOF[b] (s^{-1})
2CS	111	0.008
3CS (PS/Cat = 1:1)	342	0.019
3CS (PS/Cat = 4:1)	981	0.074

[a] After 17 h irradiation with light at 21500 cm^{-1} (465 nm). [b] Determined by maximum slope in the temporal progress of hydrogen evolution reactions.

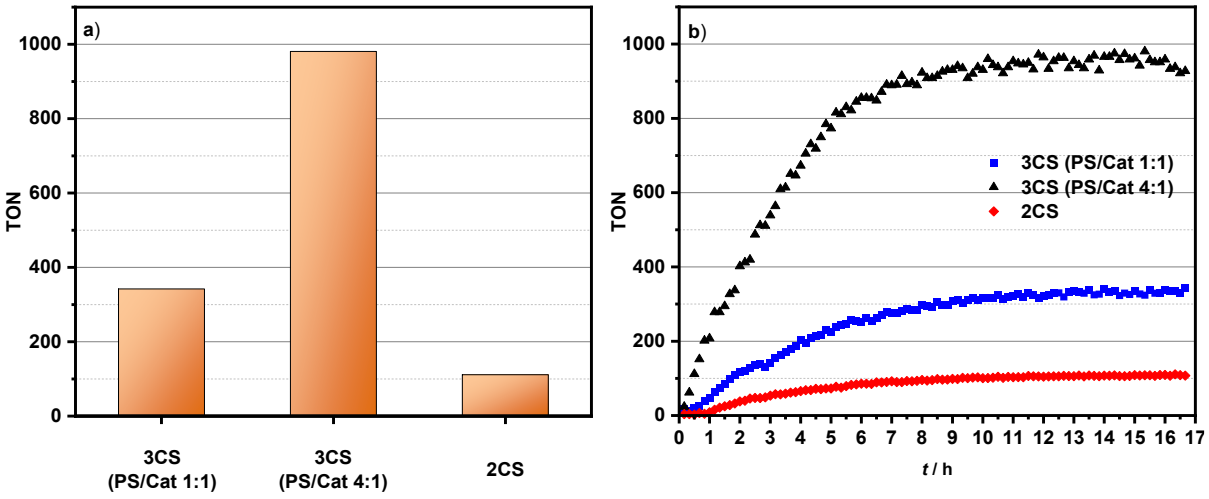

Fig. 73 Photocatalytic hydrogen evolution in MeCN/H_2O (*v*/*v* = 9:1, pH = 10) at 293 K after 17 h irradiation with light at 21500 cm^{-1} (465 nm). **a)** Turnover numbers (TON). Stoichiometric proportions: (left column) 0.02 mM **[FeFe]-Spacer-Cat 2**, 0.02 mM **[Ir(ppy)$_2$bpy]PF$_6$** and 0.36 M TEA; (middle column) 0.02 mM **[FeFe]-Spacer-Cat 2**, 0.08 mM **[Ir(ppy)$_2$bpy]PF$_6$** and 0.36 M TEA; (right column) 0.02 mM **D3** and 0.36 M TEA. **b)** Temporal progress of hydrogen evolution reactions.

First of all, as expected, both systems also showed photocatalytic activity in the acetonitrile/water mixture. A relatively high TON of 342 and a maximum TOF of 0.019 s^{-1} could be determined for the 3CS, which is a similar value in the case of photocatalytic productivity in relation to comparable iridium containing multicomponent systems.[5,53] In the literature, however, in contrast to the photocatalysis experiments carried out in this work, excitation was carried out with a broadband light source emitting below 25000 cm^{-1} (> 400 nm). Due to the absorption behaviour of the components involved, the authors could thus ensure that significantly more photons were absorbed by the photosensitiser than by the [FeFe] catalyst involved. As shown in chapter 5.2.2, this could not be guaranteed in the experiments carried out in this work due to the approximately equal absorbance of the MLCT bands of the photosensitiser, which are important for the photocatalytic electron cascade, and the Fe(t_{2g})-Fe(σ^*) transition of the catalyst at 21500 cm^{-1} (465 nm). In view of this, however, this does not seem to have a particularly negative effect on the photocatalytic performance since, as already mentioned, the productivity achieved is absolutely comparable to that of the literature systems. In order to evaluate how the redox potential of the diiron catalyst changed by an excitation affects the photocatalysis, the corresponding redox potential would have to be estimated or calculated accordingly. Due to the non-existent emission of the [FeFe] complexes, this could not be included in this analysis in the context of this work.

Furthermore, the 2CS with a TON of 111 and a maximum TOF of 0.008 s^{-1} shows significantly lower performance data than the 3CS, as was the case with the ruthenium systems. This is a little surprising since the data appear to contradict the findings of both the electrochemical and emission quenching experiments. On the other hand, the performance of the 2CS is

comparable to that of the similar dyad system by Chen *et al*.[6] In addition, the result is in line with the observations of the TA experiments, which showed that the dyad cannot take advantage of the covalent bond between the photosensitiser and the catalyst. Instead, the negative charge transferred to the iridium complex remains on the photosensitiser moiety for a relatively long time despite the presence of an intramolecular electron acceptor. As before with the ruthenium systems, the initial electron transfer from the sacrificial electron donor to the photosensitiser does not appear to be the rate-determining step in photocatalysis. Instead, the electron transfer capability of the same bridge unit built into the dyad also plays a decisive role here. If the intramolecular electron transfer from the reduced photosensitiser to the catalyst is insufficient, the dyad would still have the opportunity to go through an intermolecular redox process analogous to the 3CS. With this, however, the 2CS would be at a disadvantage due to the steric hindrance of the dyad compared to the single molecules in the 3CS, which could explain the lower photocatalytic performance of the 2CS. The resulting superiority of the 3CS over the 2CS would accordingly correspond to Sun's observations on the subject.[9]

In order to check the assumed functionality of the components involved in the respective systems, control experiments were carried out in which one component was removed in each case. No hydrogen evolution could be detected in any of these experiments, so that the presence of all components involved could be demonstrated as a necessary prerequisite for the functioning of the photocatalytic systems and, additionally, their assumed functionality could be confirmed.

The investigations of the various [FeFe] complexes in Chapter 4.4 have shown that the catalytic productivity of a multi-component system can be increased significantly by increasing the proportion of the photosensitiser. Increasing the local concentration of reduced photosensitisers probably compensates or even overcompensates for their losses due to photolability. For the diiron complexes investigated, an optimum could be achieved by using a fourfold excess of the photosensitiser. Applied to the iridium containing 3CS, an exceptionally high TON of 981 was achieved after 17 h of irradiation. In addition, this system showed a maximum TOF of 0.074 s^{-1}. It can be seen in the temporal progress of the hydrogen evolution reaction shown in **Fig. 73b** that over 80 % of the final amount of hydrogen has already been converted after the first 6 h. Thereafter, the photocatalytic activity drops significantly and the TON curve reaches its characteristic plateau.

5.2.8 Conclusion

In the course of this study on iridium containing photocatalysis systems, a photocatalytically active dyad consisting of an iridium 2-phenylpyridine 2,2'-bipyridine photosensitiser could be synthesised, which was covalently linked *via* a phenyl bridge to a $Ppyr_3$-substituted

propyldithiolate [FeFe] complex. As part of this, the associated single components **[Ir(ppy)$_2$bpy]PF$_6$** and **[FeFe]-Spacer-Cat 2** could also be produced. In combination with TEA as the sacrificial electron donor, the dyad **D3** formed the photocatalytic 2CS, TEA with the **[Ir(ppy)$_2$bpy]PF$_6$** photosensitiser and **[FeFe]-Spacer-Cat 2** as the catalyst the corresponding 3CS. In addition to the electrochemical investigation of the redox potentials of **D3**, **[Ir(ppy)$_2$bpy]PF$_6$** and **[FeFe]-Spacer-Cat 2** from both thermodynamic and kinetic aspects, the photocatalytic performance of both systems could also be determined. The absorption spectroscopic examination already showed as a result of comparably small shifts in the corresponding absorption bands in comparison with those of the single molecules, that there is only a slight interaction between the photosensitiser moiety and the catalyst moiety within the dyad. This finding was largely confirmed by the subsequent electrochemical investigations. With the exception of conspicuous anodic shifts in the iron-centred reductions, these also showed only small shifts in the **D3** peak potentials compared to those of **[Ir(ppy)$_2$bpy]PF$_6$** and **[FeFe]-Spacer-Cat 2**. As a result, the bridge unit built into the dyad appears to significantly hinder the electronic interaction between the dyad components. Specifically, this applies above all to the amide and ester bonds between the individual dyad building blocks originally used to reduce the electronic coupling as π-conjugation blockers. This situation could also be detected in the TA measurements. The surprisingly long-lived ESA for the reduced iridium photosensitiser that emerged in the measurements of **D3** indicates that the intramolecular electron transfer to the catalyst moiety is strongly inhibited during photocatalysis and instead the negative charge remains on the photosensitiser for a relatively long time. In the TA measurements, the 2CS therefore behaves very similarly to the 3CS, which, as expected, also shows a long residence time of the negative charge on the photosensitiser due to the intermolecular electron transfer to the catalyst. It is therefore assumed that the electronic hindrance within the dyad, presumably caused by the built-in π-conjugation blockers, leads to the fact that it bypasses the electronic barrier and instead transfers an electron from the reduced photosensitiser moiety to the catalyst moiety of another dyad molecule and thus behaves analogously to the 3CS. Accordingly, contrary to what was originally expected, the dyad would not benefit from the covalent bond between its two components. This was also reflected in the photocatalytic performance of the two systems examined. With a TON of 111, the 2CS showed only around a third of the catalytic productivity of the 3CS with a TON of 342. In addition, a maximum TOF of 0.008 s^{-1} could be achieved for the **D3** containing 2CS, while the 3CS showed a TOF of 0.019 s^{-1}. In the light of the situation just mentioned, it is assumed that the 2CS additionally has steric disadvantages in the processes during photocatalysis due to the larger dyad compared to the single **[Ir(ppy)$_2$bpy]PF$_6$** photosensitiser. These could therefore explain the performance losses compared to the 3CS.

As already described at the beginning of this chapter, the ruthenium containing dyads **D1** and **D2**, which represent the basis for **D3**, show a very similar behaviour in the photocatalysis (see chapter 5.1.7). In addition, the TA measurements of the **D1** containing 2CS also indicate a relatively long residence time of the negative charge on the photosensitiser moiety (see chapter 5.1.6). Although no comparison could be made with the corresponding 3CS, an analogy to the iridium containing 2CS can be drawn, since the same π-conjugation blockers as in **D3** are also used in the bridge units of **D1** and **D2**. Based on the results of the study on the iridium systems, it can therefore be concluded that the **D1** and **D2** containing systems presumably behave analogously to the iridium containing 2CS and that they also circumvent the intramolecular electronic barrier through an intermolecular electron transfer.

From a thermodynamic point of view, the electrochemical examination of the individual components and the subsequent estimation of the redox potential of the excited iridium photosensitisers showed a clear preference for the RQ mechanism for both iridium containing systems. In addition, this was also confirmed by the emission quenching experiments with TEA as the quencher and the TA measurements.

Since the iridium containing 3CS showed in the acetonitrile/water mixture a much better photocatalytic performance than the corresponding ruthenium containing 3CS in the aqueous medium during the photocatalytic investigations, attempts were made to further optimise the iridium containing multicomponent system in order to achieve an even better performance. Using the knowledge from Chapter 4.4, the composition of the 3CS was adjusted to a photosensitiser/catalyst ratio of 4:1, thus achieving a remarkably high catalyst-related TON of 981 and a maximum TOF of 0.074 s^{-1}.

6 SUMMARY AND OUTLOOK

Within the scope of this work, a number of different [FeFe]-hydrogenase biomimics were first tested for their functionality as catalysts in photocatalytic multicomponent systems for hydrogen evolution under light irradiation in an aqueous medium. Since some examples of the successful integration of such diiron complexes in aqueous systems with $[Ru(bpy)_3]^{2+}$ photosensitisers in combination with ascorbic acid as sacrificial electron donor are already known in the literature, these two components were also integrated into the corresponding systems for the investigations on their photocatalytic performance.[5,8,9,18,35,52,68,69,99] Due to the water insolubility of the diiron catalyst complexes, they were solubilised in water in this work using a poly(2-oxazoline) polymer shown in **Fig. 14**. The aqueous micelle system thus formed represents the significant difference to the known photocatalytic multicomponent systems in aqueous organic solutions. An important aspect of this study was therefore not only the characterisation and comparison of the various [FeFe] complexes on the basis of their photocatalytic performance and their spectral and electrochemical properties, but also, if possible, in the examination of existing structure-property relationships in this new aqueous environment in order to include the knowledge gained in the subsequent development of the photocatalytic dyad systems.

In the study on the diiron compounds, fourteen different [FeFe] complexes were synthesised, each with different dithiolate ligands and phosphine substituents (see **Fig. 15**). All of them showed photocatalytic activity in the aqueous micellar medium in combination with the **$[Ru(bpy)_3]Cl_2$** photosensitiser and ascorbic acid and generated hydrogen when exposed to light. In addition, some structure-property relationships discussed in the literature could also be demonstrated in this study. Thus, the spectroscopic and electrochemical investigations showed that, although the dithiolate ligands have an influence on the electronic properties of the complexes, these are primarily influenced by the phosphine substituents bound directly to the diiron core. This also applies to the photocatalytic performance of the systems tested. Although only the catalytic productivity was measured during the investigations, it was found that the various structural features of the [FeFe] catalysts evidently not only affect the activity of the systems, but also their productivity, which is normally associated with the stability of the components involved. This can probably be attributed to the fact that with otherwise identical measurement conditions and presumably comparable photolabilities of the components used, a higher activity of the system also leads to a higher output and thus to a higher catalytic productivity. For instance, electron-withdrawing dithiolate ligands, which lower the electron density on the diiron core and thus the protophilicity, have a negative influence on the TON value achieved. In contrast, the azadithiolate ligands have hardly any noteworthy influence in

terms of both the electronic properties and the photocatalytic performance. As already mentioned above, the phosphine substituents showed the greatest influence, both on the thermodynamic and on the photocatalytic properties of the catalysts. The $Ppyr_3$ substituent showed the best properties in the study for photocatalysis. Due to the electron-donating effect of a phosphine ligand, it has a positive impact on the protophilicity of the complex. At the same time, the internal pyrrole substituents prevent an excessive cathodic shift in the reduction potential, which would lead to a mismatch with the redox potentials of the photosensitiser.[9] Consequently, the $Ppyr_3$-substituted [FeFe] complexes also showed the highest catalytic productivity in the study. In addition, further parameters of the photocatalytic systems, such as their stoichiometric composition and pH-value, have also been optimised. In the next step, these findings were transferred together with the structure-property relationships obtained into the design of photocatalytically active dyad systems.

In the study about photocatalytic dyads, in which the photosensitiser is covalently linked to the catalyst, it should in principle be examined whether two-component systems (2CS) formed with them have a performance advantage over the conventional three-component systems (3CS) investigated in the previous chapter. In addition to the thermodynamic and kinetic properties of the dyads and the associated single components, the quenching mechanism under which the corresponding systems work during photocatalysis was also investigated. As Sun *et al.* have observed, the quenching mechanism appears to have an important factor in the performance of the dyad system compared to the corresponding bimolecular system.[9] Within the scope of this work it was therefore investigated whether this also applies to the dyad systems produced in this work. The dyads to be examined were built on the top-performing system of the abovementioned study on the [FeFe] catalysts. In this way, the knowledge gathered there has also been incorporated into the dyad design. In this work, a total of three dyads could be produced together with the associated single components. Two of them, **D1** and **D2**, include a $[Ru(bpy)_3]^{2+}$ photosensitiser and **D3** a $[Ir(ppy)_2bpy]^{+}$ photosensitiser. All have a $Ppyr_3$-substituted propyldithiolate [FeFe] complex as catalyst, which in the case of **D1** and **D3** are bridged *via* a phenyl spacer and in the case of **D2** *via* a biphenyl spacer to the photosensitiser. Based on the synthesis of Sun and Åkermark, all bridge units are connected to the photosensitiser *via* an amide bond and to the catalyst *via* an ester bond.[56] As π-conjugation blockers, these are intended to reduce the electronic coupling between the two dyad components and thus make it more difficult for electrons to be transported back quickly after the charge has been transferred from the photosensitiser to the catalyst, since the longevity of the reduced state of the catalyst should promote photocatalytic activity. As the absorption spectroscopic and electrochemical investigations showed, this inner-dyadic electronic decoupling works slightly better for **D3**. The ruthenium containing dyads, on the other hand, show a more pronounced interaction between the components. However, the

photocatalytic investigations showed that all dyads in the corresponding 2CS show a significantly poorer performance than the corresponding bimolecular 3CS. Transient absorption spectroscopy has shown that the iridium containing dyad **D3** behaves very similar to the associated multicomponent system during photocatalysis. The electron intended for the intramolecular transfer from the photosensitiser to the catalyst, as in the 3CS, remains on the photosensitiser for a relatively long time despite the covalently attached catalyst. This behaviour was also observed in the ruthenium containing dyad **D1**. It is therefore assumed that the suspected intramolecular electron transfer from the photosensitiser moiety to the catalyst moiety in the dyads during photocatalysis is probably prevented by the bridging units used and instead the system bypasses these by an intermolecular transfer to other surrounding dyad molecules. The extension of the bridge unit used, which is the structural difference between **D1** and **D2**, showed, apart from an expected slight reduction in the electronic coupling between the dyad components, no decisive effects on both the photocatalytic performance and the thermodynamic and kinetic properties. Apparently, this relatively small change has too little influence compared to that of the π-conjugation blockers used. In addition, the RQ mechanism could be clearly demonstrated for all systems examined by electrochemical investigations, including the redox potentials of the excited photosensitisers, which are important for the photocatalytic electron cascade, and emission quenching experiments. In combination with the photocatalysis results, the above-mentioned observations by Sun *et al.* about performance losses of dyads operating *via* the RQ mechanism are also confirmed for the photocatalytic dyads examined in this work.[9]

With the knowledge gained in this work, further research on new photocatalytic dyads, which would rely on a different connection between the individual components, would be very interesting for the future. In addition to direct bonds through C-C cross-coupling reactions, which would maintain the π-conjugation, completely different approaches would also be possible. For instance, a supramolecular approach of a photocatalytic system would be conceivable, which would represent an intermediate form between the classic 2CS and 3CS. A combination between a chelating organometallic photosensitiser and a catalyst with corresponding binding sites might be one such possibility. As early as 2008, Sun and Åkermark were able to show that such a system, which consisted of an isonicotinic acid-substituted azadithiolate [FeFe] complex that was supramolecularly bound to a zinc porphyrin, can generate hydrogen.[128] This opens up a whole new class of photocatalytically active systems with enormous performance potential. The impressive results of the iridium containing 3CS, consisting of the **[Ir(ppy)$_2$bpy]PF$_6$** photosensitiser, the **[FeFe]-Spacer-Cat 2** catalyst and TEA as the sacrificial electron donor, show that the components used in this work are fundamentally suitable for further investigations in this area. With this system, a remarkably high TON of 981 and a maximum TOF of 0.074 s^{-1} could be achieved under optimised conditions.

7 EXPERIMENTAL SECTION

7.1 Materials and Methods

7.1.1 Steady-State Absorption Spectroscopy

- JASCO V-670 UV/Vis/NIR spectrometer (software SpectraManager v. 2.08.04)
- Agilent Technologies Cary 5000 UV-Vis-NIR spectrophotometer (software Agilent Cary WinUV Analysis and Bio v.4.2)

All solvents were of spectroscopic grade and were used without further purification. Absorption spectra were recorded on one spectrometer listed above in 10 × 10 mm quartz-cuvettes from Starna (Pfungstadt, Germany) at r.t. Aggregation of the samples could be excluded by a concentration independent behaviour (10^{-6}–10^{-4} M).

7.1.2 Electrochemistry

Electrochemical measurements were performed in acetonitrile with tetrabutylammonium hexafluorophosphate (TBAHFP, 0.10 M) as supporting electrolyte. The solvent was dried by distillation from sodium hydride suspension and stored over activated molecular sieve prior use. TBAHFP was synthesised according to literature[129], recrystallised from ethanol/water and dried under high vacuum.

7.1.2.1 Cyclic Voltammetry (CV)

- Gamry Instruments Reference 600 Potentiostat/Galvanostat/ZRA (v. 6.2.2, Warminster, PA, USA)

Cyclic voltammograms were measured in argon atmosphere at r.t. with a sample concentration of 1 mM in acetonitrile. The used measuring cell was oven dried at 150 °C and flushed with argon gas prior use. For measurements a conventional three-electrode setup consisting of a platinum disk as working electrode (Ø = 1 mm), a platinum wire counter electrode and an Ag/AgCl “leak free” reference electrode (Warner Instruments, Hamden, CT, USA) was used in combination with a Reference 600 Potentiostat (Gamry Instruments, Warminster, PA, USA). The cyclic voltammograms were recorded at a scan rate of 100 mV s^{-1}. The reference electrode was referenced against the ferrocene/ferrocenium (Fc/Fc^+) redox couple. The electrochemical potential of the Fc/Fc^+ redox couple in MeCN/TBAHFP is 0.40 V *vs.* the saturated calomel electrode (SCE), 0.64 V *vs.* the normal hydrogen electrode (NHE) and

5.10 V *vs.* vacuum, respectively. Hence, the absolute respective redox potential $E^{0'}$ can be calculated by the following equation:

$$E^{0'} = -5.10\ \text{V} - E_{1/2}^{\text{red/ox}}$$

Half wave potentials $E_{1/2}$ were calculated as arithmetic mean of anodic peak potential E_{pa} and cathodic peak potential E_{pc}. For irreversible redox processes the corresponding peak potential was used as half wave potential by approximation and was signed accordingly. Chemical and electrochemical reversibility of the redox processes were checked in the CV measurements by multi thin layer experiments and measurements at different scan rates (from 50–1000 mV s^{-1}), respectively.

7.1.2.2 Spectroelectrochemistry (SEC)

- Agilent Technologies Cary 5000 UV-Vis-NIR spectrophotometer (software Agilent Cary WinUV Analysis and Bio v.4.2)
- Gamry Instruments Reference 600 Potentiostat/Galvanostat/ZRA (v. 6.2.2, Warminster, PA, USA)

UV/Vis/NIR-spectroelectrochemistry was performed in argon atmosphere at r.t. in a custom built three electrode quartz-cell sample compartment implemented in a Cary 5000 UV-Vis-NIR spectrometer from Agilent Technologies (Santa Clara, CA, USA). The cell consisted of a platinum disc working electrode (Ø = 6 mm), a platinum plate counter electrode (Ø = 1 mm) and an Ag/AgCl pseudo-reference electrode. All experiments were measured in reflexion mode with a path length of 100 µm and a solute concentration of 0.5 mM in acetonitrile. Measurements were performed by initially applying a starting voltage on the electrodes, followed by a stepwise voltage decrease of 0.01 V for each absorption scan. To ensure equilibrium conditions in the sample solution a dwell time of 15 s was bided after each voltage decrease and straight before starting the next absorption scan.

7.1.3 ns-Laser Flash Spectroscopy

- Edinburgh Instruments LP 920 laser flash spectrometer with a 450 W ozone-free Xe arc lamp including a photomultiplier (Hamamatsu R955), digital storage oscilloscope (Tektronix TD3012B) and software (L900 v. 7.3.5)
- EKSPLA NT 342A Nd:YAG laser operating at 10 Hz, 3–5 ns pulse duration, pulse energy 59 mJ at 28200 cm^{-1} (355 nm)

- OPO BBO II optical parametric oscillator for generating photon energies between 28200 cm^{-1} (355 nm) and 14300 cm^{-1} (700 nm)

Transient absorption (TA) spectroscopy was performed in 10 mm × 10 mm quartz cuvettes from Starna (Pfungstadt, Germany) at r.t. under argon atmosphere. All solvents were of spectroscopic grade and used without further purification. The prepared sample solutions were degassed by bubbling argon gas through the solutions for at least 15 min before each measurement. For aqueous micellar solutions this procedure was changed due to strong foaming of these surfactant containing mixtures. Here, the premium-grade EMSURE water from Merck Millipore was at first degassed for at least 30 min and after sample preparation the corresponding aqueous micellar solutions were additionally degassed for 5 min before each measurement. To ensure the further absence of oxygen during the measurements the used septum of the prepared samples was exchanged after degassing by a new one in a glove box with an oxygen-amount of < 1 ppm. The samples were excited with ca. 5 ns pulses from the 28200 cm^{-1} (355 nm) output of the EXSPLA NT 342A Nd:YAG shifted to 21700 cm^{-1} (460 nm) or 25100 cm^{-1} (398 nm) by an OPO BBO II optical parametric oscillator. The probe pulse was provided by a pulsed Xe flash lamp. All measurements were performed under activated fluorescence correction implemented in the L900 software. The measured time range was chosen such that the decay of the signal was complete, meaning that the signal intensity fell back to zero or proceeded at least parallel to the abscissa. The samples were prepared in different concentrations (10^{-6}–10^{-5} M) and were measured with different pulse energies (0.2–1.2 mJ) to avoid unwanted bimolecular self-deactivation processes. The stability of the samples was verified by recording the steady-state absorption spectra before and after the measurements. The transient maps were recorded by 160-fold averaging (10 × 16 shots) of measured temporal decay profiles in 4 nm steps between 12500 cm^{-1} (800 nm) and 25000 cm^{-1} (400 nm). The lifetimes of the particular decay curves were obtained by fitting with the tailfit function of the spectrometer software.

7.1.4 Steady-State Emission Spectroscopy

- Edinburgh Instruments FLS980 fluorescence lifetime spectrometer including a 450 W xenon lamp and a single photon counting photomultiplier (R928P) (software F980 version 1.2.2)

Steady-state emission spectra were recorded at r.t. in 10 mm × 10 mm quartz cuvettes from Starna (Pfungstadt, Germany). All solvents were of spectroscopic grade and were used without further purification. In order to avoid aggregation and self-absorption the samples were prepared in high dilution (ca. 10^{-6}–10^{-5} M). All samples containing organic solvents were also purged with argon for 10 min before each measurement to remove oxygen from the solutions.

For aqueous micellar solutions first the premium-grade EMSURE water from Merck Millipore was degassed with argon for at least 30 min. Due to strong foaming of these surfactant containing mixtures, the solutions prepared were then degassed again for only 5 min before each measurement. Steady-state emission spectra were recorded under magic angle conditions.

7.1.5 Time Dependent Emission Spectroscopy

- Edinburgh Instruments FLS980 fluorescence lifetime spectrometer including a high-speed single photon counting photomultiplier (H10720) (software F980 version 1.2.2)
- Edinburgh Instruments 23900 cm^{-1} (419 nm) pulsed Laser Diode

Sample preparation was the same as for steady-state emission spectroscopy. Emission lifetimes were determined by time-correlated single-photon counting (TCSPC). The samples were excited by a 23900 cm^{-1} (419 nm) pulsed laser diode with pulse lengths between 20.0 µs and 100 ns. The fluorescence was detected with a high-speed PMT detector (H10720). All measurements were recorded under magic angle conditions. The FAST software (version 3.4.2) was used to fit the decay curves with exponential decay functions in order to achieve the corresponding emission lifetimes. To achieve this, deconvolution of the data was accompanied by the measuring the instrument response function with a scatterer solution consisting of colloidal silica in deionised water (LUDOX AS-30).

7.1.6 Photocatalysis

- Self-made photoreactor consisting of a glass water basin with a severed LED board section in the middle and 10 separated reaction chambers, each equipped with a magnetic stirrer and illuminated by 10 LEDs at 21500 cm^{-1} (465 nm) and 3.00 V (1.58 A); temperature regulation by a LAUDA WK230 circulation chiller.
- Shimadzu Gas Chromatograph GC 2010 plus including a thermal conductivity detector (TCD), a Restek Q-Bond and a Restek molecular sieve (5 Å) column (software LabSolutions v. 5.51).
- Honeywell board mount pressure sensors (p_{max} = 2.07 bar) with PTFE sealed threaded glassware connection; sensor control and pressure detection by LABVIEW SignalExpress 2012 software from National Instruments (v. 6.0.0).

Photocatalysis was performed in a self-made photoreactor consisting of a glass water basin with a separated section in the middle, in which a LED board with 50 LEDs on each side was located. This setup ensured illumination from the middle to both sides of the basin. In order to

regulate the temperature during the experiment the water in the basin was temperature controlled by a WK230 circulation chiller from LAUDA (Lauda-Königshofen, Germany) connected to a glass tube on the ground of the basin. During photocatalysis the water temperature was adjusted to 293 K. Both sides of the basin were additionally separated by aluminium partitions into overall ten reaction chambers, each equipped with a magnetic stirrer to ensure an optimal mixing of the water and the reaction solutions during the experiment. Each chamber was illuminated by 10 LEDs (for emission spectrum see **Fig. 74**). With a surrounding rod system, it was possible to place reaction vessels in the chambers and adjust their mounting for an optimal illumination.

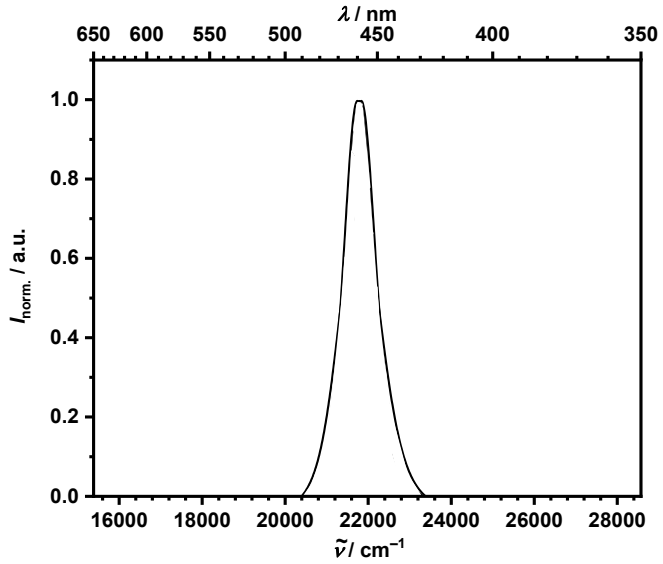

Fig. 74 Relative emission spectrum of InGaN-LEDs implemented in the self-made photoreactor for photocatalysis at 20 mA and 298 K. LEDs were obtained from Kingbright Electronic (Taipei, Taiwan).

All experiments were carried out in custom-build glass Schlenk tubes with two Young-valves, a glass thread for a septum screw fixing and a magnetic stirring bar inside. All solvents used for sample preparation were of spectroscopic grade and used without further purification. The aqueous solutions were prepared by the means of premium-grade EMSURE water from Merck Millipore. The solvents used for reaction solutions were degassed by bubbling argon through the solvent for at least 30 min prior use.

The sample preparation was carried out according to the following procedure. For experiments in pure water all water insoluble compounds were first dissolved together with a Poly(2-oxazoline) polymer[74-76] (see **Fig. 14**) as surfactant in DCM and filled in a photocatalysis Schlenk tube, in which the solvent was removed by carefully applying high vacuum. As a result, a polymeric thin film occurred at the glass wall of the vessel. In order to achieve a pure nitrogen atmosphere inside, the Schlenk tube was alternatingly evacuated and refilled with nitrogen gas for five times. All water-soluble compounds, including ascorbic acid as sacrificial donor, were separately dissolved in the degassed water under nitrogen atmosphere. After adjustment of

the pH value with diluted hydrochloric acid, 10.0 ml of the aqueous solution were extracted *via* a syringe and added in the photocatalysis Schlenk tube through the septum. After that, the Schlenk tube was shaken under exclusion of light until the magnetic stirring bar inside the vessel detached from the glass wall due to dissolving of the polymeric thin film. The overpressure inside the Schlenk tube was compensated by a brief vent on one Young valve on which a bubble counter was attached. Finally, the photocatalysis was initiated by switching on the LEDs. For experiments in mixtures of water and organic solvents the sample preparation changed regarding the absence of a surfactant and the fact that therefore first all compounds except the sacrificial donor were dissolved in DCM und then transferred into the photocatalysis Schlenk tube. After five evacuation and nitrogen refilling cycles, 10.0 ml of the beforehand prepared solvent mixture were added *via* a syringe through the septum. The preparation of the solvent mixture carried out according to the case of pure water experiments, except for triethylamine as sacrificial electron donor and therefore the corresponding pH value adjustment.

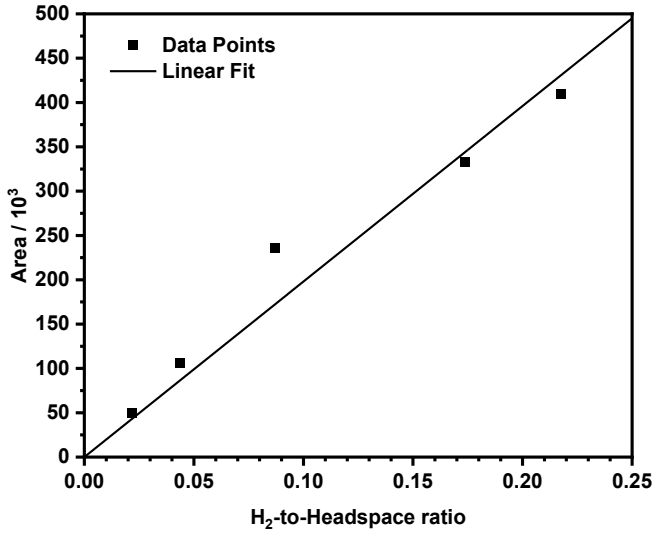

Fig. 75 Calibration curve for the determination of the produced H_2 amount with the area originating from the integration of the corresponding peak in the GC chromatogram. The headspace is the volume of the used Schlenk tube deducting the volume of the reaction solution.

All sample solutions were illuminated with light at 21500cm^{-1} (465 nm) under stirring for the indicated time. In order to determine the photocatalytic activity, the pressure development inside the Schlenk tube was measured by an attached board mount pressure sensor from Honeywell International (Morristown, NJ, USA). The pressure sensor was controlled and the signal detected by LABVIEW SignalExpress 2012 software from National Instruments (Austin, TX, USA). For the determination of the photocatalytic productivity 100 µl of the reaction's supernatant gas volume was analysed by a Shimadzu Gas Chromatograph GC 2010 plus. As carrier gas argon was purged over a Q-Bond and molecular sieve (5 Å) column from Restek with a total flow rate of 33.3 ml min^{-1}. The incoming gas was detected by a thermal conductivity

detector (TCD). Due to an unique dwell time of every gas kind on the column (4.0 min for hydrogen, 4.2 min for oxygen, 4.4 min for nitrogen) an individual gas detection was possible. With the generation of a calibration curve (see **Fig. 75**) by means of well-defined amounts of hydrogen-nitrogen mixtures, it was possible to deduce the amount of produced hydrogen from the intensity of the corresponding peak in the chromatogram and the volume of the used Schlenk tube. With that the calculation of the turnover number (TON) of the photocatalysis was accessible by dividing the amount of produced hydrogen per amount of inserted catalyst.

7.1.7 Recycling Gel Permeation Chromatography (GPC)

- JASCO Gel Permeation Chromatography System: interface box (LC-NetII ADC), HPLC pump (PU-2080 plus), in-line degasser (DG-2080-53), solvent selection valve unit (LV-2080-03), multi wavelength UV/Vis detector 195–700 nm (UV-2077), software Chrompass (v. 6.1)

- Shimadzu Gel Permeation Chromatography System: system controller (CBM-20A), solvent delivery unit (LC-20AD), online degasser (DGU-20A9), diode array detector (SPD-M20A), software LCsolution (v. 1.25)

Gel permeation chromatography (GPC) was performed with one of the setups listed above by using two preparative GPC columns (styrene-divinylbenzene-copolymer, 50 Å and 500 Å, 600 × 20.8 mm) from PSS (Mainz, Germany). The flow rate was 4 ml min^{-1} and the used solvent was HPLC grade $CHCl_3$ (Fisher Chemical or HiPerSolv Chromanorm from VWR Chemicals).

7.1.8 NMR Spectroscopy

- Bruker BioSpin Avance III HD 400 FT-Spectrometer (^{1}H: 400.13 MHz, ^{13}C: 100.61 MHz) with a Bruker Ultrashield magnet

- Bruker BioSpin Avance III HD 400 FT-Spectrometer (^{1}H: 400.03 MHz, ^{13}C: 100.59 MHz) with a Bruker Ascend magnet

^{1}H and ^{13}C NMR spectra were measured with one of the spectrometers listed above in deuterated solvents as indicated (e.g. acetone-d_6, chloroform-d ($CDCl_3$), dichloromethane-d_2 (CD_2Cl_2), dimethylsulfoxide-d_6 ($(CD_3)_2SO$) and methanol-d_4 (CD_3OD)). Samples were placed in frequency-adapted 5 mm glass sample tubes. Chemical shifts are given in ppm relative to residual non-deuterated solvent signal and naturally occurring isotope signal, respectively (^{1}H in ppm: $CHCl_3$: δ 7.26, $(CH_3)_2CO$: δ 2.05, CH_2Cl_2: δ 5.32, $(CH_3)_2SO$: δ 2.50, CH_3OH: δ 3.31; ^{13}C in ppm: $CHCl_3$: δ 77.16, $(CH_3)_2CO$: δ 29.84, CH_3OH: δ 49.00).[130] Deuterated solvents were

used as received (Deutero, Acros Organics). The spin multiplicities are abbreviated as follows: s = singlet, bs = broad singlet, d = doublet, dd = doublet of doublet, ddd = doublet of doublet of doublet, t = triplet, dt = doublet of triplet, quint = quintet, m = multiplet and AA' / BB'. Overlapping signals in proton NMR spectra of chemically noneqivalent protons are given as m'. The order of declaration for proton spectra is: Chemical shift (spin multiplicity, coupling constant, number of protons, correlation of the proton in the molecule if possible). The carbon signals are abbreviated as follows: CH_3 = primary, CH_2 = secondary, CH = tertiary, C_q = quaternary.

7.1.9 Mass Spectrometry

- microTOF focus from Bruker Daltonics (Bremen, Germany)

Mass spectra were recorded with a Bruker Daltonics microTOF focus (ESI). All mass spectrometry peaks are reported as m/z. For calculation of the respective mass values of the isotopic distribution, the software "Bruker Daltonics IsotopePattern" from the software Compass 1.1 from Bruker Daltonics GmbH, Bremen was used. Calculated (calc.) and measured (exp.) peak values always correspond to the most intense peak of the isotopic distribution.

7.1.10 Elemental Analysis (CHN)

- vario MICRO cube CHNS instrument from Elementar (Hanau, Germany)
- Euro EA CHNSO Elemental Analyser from HEKAtech (Wegberg, Germany)

Elemental analyses were either performed with a vario MICRO cube CHNS instrument for non-halogenated compounds or with Euro EA for halogenated compounds at the Institut für Anorganische Chemie, Universität Würzburg.

7.2 Synthesis

Commercial compounds including solvents were purchased from Acros Organics, Alfa Aesar, Chempur, Fisher Chemical, Fluorochem, Fluka, Merck, Sigma-Aldrich, VWR Chemicals and were used without further purification if not stated otherwise.

All reactions specified as being performed under nitrogen atmosphere were performed under air-free conditions (nitrogen, dried with Sicapent® from Merck, oxygen was removed by copper oxide catalyst R3-11 from BASF) using standard Schlenk techniques.[131] Solvent for oxygen and/or moisture sensitive reactions were dried according standard literature procedures[132] and stored under nitrogen atmosphere. Solvents for chromatography and work-up procedures

were of technical grade and distilled prior use. Flash chromatography[133] was performed on silica gel (Macherey-Nagel “Silica 60 M”, 40–63 µm) wet-packed in glass columns.

7.2.1 Synthesis of [FeFe]-Hydrogenase Biomimics

General procedure for the synthesis of [FeFe]-hydrogenase biomimics [$Fe_2(\mu\text{-}S_2X)(CO)_6$] according to literature[87-89,134] (GP I).

Under nitrogen atmosphere $Fe_3(CO)_{12}$ (1.0 eq.) and the appropriate dithiol (1.1–1.8 eq.) were dissolved in dry THF and heated under reflux for the indicated time period. Then, the solvent was removed from the solution under reduced pressure and the resulting residue was purified by flash column chromatography. The product was dried in high vacuum. Due to its light sensitivity the complex was stored in the dark.

General procedure for the synthesis of phosphine substituted [FeFe]-hydrogenase biomimics [$Fe_2(\mu\text{-}S_2X)(CO)_5PR_3$] according to literature[15,35,92,93,135] (GP II).

Under nitrogen atmosphere the appropriate [FeFe]-hydrogenase biomimic **[$Fe_2(\mu\text{-}S_2X)(CO)_6$]** (1.0 eq.) and trimethylamine *N*-oxide dihydrate (1.2 eq.) were dissolved in degassed acetonitrile and were stirred at r.t. for 5 min. Then, a solution of the appropriate phosphine (1.0–1.2 eq.) in degassed acetonitrile (10 ml) was added and the reaction mixture was stirred at r.t. for the indicated time period. After that, the solvent was removed under reduced pressure and the resulting residue was purified first by flash column chromatography and afterwards by GPC. The product was dried in high vacuum. Due to its light sensitivity the complex was stored in the dark.

[FeFe]-Cat 1 / [$Fe_2(\mu\text{-}S_2(CH_2)_3)(CO)_6$]

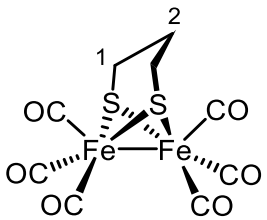

CAS: [70789-83-2].

Synthesis following GP I:

$Fe_3(CO)_{12}$ (2.00 g, 3.97 mmol), propanedithiol (420 µl, 4.19 mmol), THF (45 ml), reflux for 90 min; flash column chromatography (silica gel, petroleum ether).

Yield: 1.23 g (3.19 mmol, 76 %), red crystalline solid.

Formula: $C_9H_6Fe_2O_6S_2$ [385.96].

^{1}H-NMR (400.1 MHz, $CDCl_3$):

δ [ppm] = 2.14 (t, $^3J_{H\text{-}H}$ = 5.9 Hz, 4H, H-1), 1.83–1.78 (m, 2H, H-2).

^{13}C-NMR (100.6 MHz, $CDCl_3$):

δ [ppm] = 207.9 (C_q), 30.5 (CH_2), 23.4 (CH_2).

[FeFe]-Cat 2 / [Fe_2(μ-$S_2C_6H_4$)$(CO)_6$]

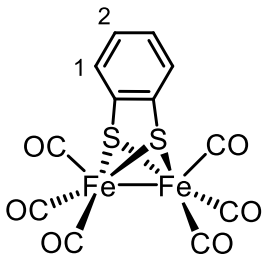

CAS: [84577-31-1].

Synthesis following GP I:

$Fe_3(CO)_{12}$ (2.77 g, 5.50 mmol), benzene-1,2-dithiol (860 mg, 6.05 mmol), THF (35 ml), reflux for 2 h; flash column chromatography (silica gel, petroleum ether).

Yield: 2.32 g (5.52 mmol, 91 %), red-brown crystalline solid.

Formula: $C_{12}H_4Fe_2O_6S_2$ [419.98].

^{1}H-NMR (400.1 MHz, $CDCl_3$):

δ [ppm] = 7.13 (m, 2H, H-1), 6.64 (m, 2H, H-2).

^{13}C-NMR (100.6 MHz, $CDCl_3$):

δ [ppm] = 207.6 (C_q), 147.6 (C_q), 128.1 (CH), 126.9 (CH).

[FeFe]-Cat 3 / $[Fe_2(\mu\text{-}S_2C_6H_2Cl_2)(CO)_6]$

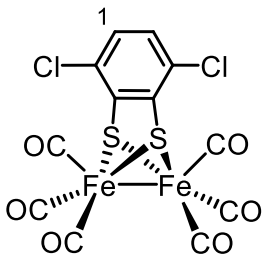

CAS: [1173464-48-6].

Synthesis following GP I:

$Fe_3(CO)_{12}$ (2.02 g, 4.01 mmol), 3,6-dichlorobenzene-1,2-dithiol (930 mg, 4.40 mmol), THF (35 ml), reflux for 2.5 h; flash column chromatography (silica gel, first column with petroleum ether, second column with *n*-hexane/MeOH = 95:5).

Yield: 444 mg (908 µmol, 21 %), red-brown solid.

Formula: $C_{12}H_2Cl_2Fe_2O_6S_2$ [488.87].

^{1}H-NMR (400.1 MHz, $CDCl_3$):

δ [ppm] = 6.63 (s, 2H, H-1).

3,4,5,6-Tetrachlorobenzene-1,2-dithiol

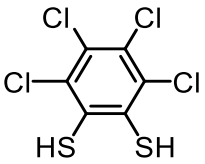

CAS: [13801-50-8].

Synthesis according to given literature.[89]

Under nitrogen atmosphere perchlorobenzene (5.00 g, 17.6 mmol), sodium hydrosulphide-x-hydrate (3.75 g, 66.9 mmol), iron powder (900 mg, 16.1 mmol) and sulphur (400 mg, 12.5 mmol) were dissolved in *N*,*N*-dimethylformamide (50 ml) and heated at 140 °C overnight. After cooling down to r.t., deionised water (100 ml) was added and the black precipitate was filtered and dried overnight. Then, the black solid was added to a solution of ZnO (2.00 g, 24.6 mmol) and sodium hydroxide (5.00 g, 125 mmol) in deionised water (50 ml) and methanol (50 ml). The mixture was heated under reflux for 2 h. After cooling down to r.t., the solution

was filtered and the filtrate was added to deionised water (100 ml) and sulphuric acid (18 M, 50 ml). The precipitate was filtered and washed with acidic water. The product was dried in high vacuum.

Yield: 4.85 g (17.3 mmol, 98 %), greenish-yellow solid.

Formula: $C_6H_2Cl_4S_2$ [280.02].

^{1}H-NMR (400.1 MHz, $CDCl_3$):

δ [ppm] = 5.97 (bs, 2H, SH).

[FeFe]-Cat 4 / [$Fe_2(\mu$-$S_2C_6Cl_4)(CO)_6$]

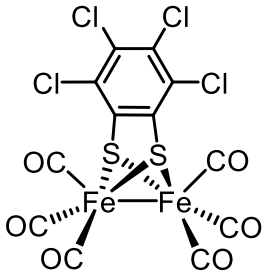

CAS: [1173464-48-6].

Synthesis following GP I:

$Fe_3(CO)_{12}$ (200 mg, 397 µmol), **3,5,6,7-tetrachlorobenzene-1,2-ditiol** (200 mg, 714 µmol), THF (35 ml), reflux for 90 min; flash column chromatography (silica gel, petroleum ether).

Yield: 47.0 mg (84.3 µmol, 14 %), red crystalline solid.

Formula: $C_{12}Cl_4Fe_2O_6S_2$ [557.76].

^{13}C-NMR (100.6 MHz, $CDCl_3$):

δ [ppm] = 206.5 (C_q), 148.4 (C_q), 131.6 (C_q), 131.4 (C_q).

***N*,*N*-Bis(chloromethyl)propan-1-amine**

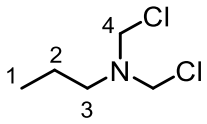

CAS: [/].

Synthesis based on given literature.[33]

A mixture of propan-1-amine (15.3 ml, 186 mmol) and paraformaldehyde (14.5 g, 483 mmol) in DCM (110 ml) was stirred for 16 h and then treated dropwise with thionyl chloride (54.0 ml, 740 mmol). After gas evolution has ceased (3 h after beginning of addition) the reaction mixture was heated at 40 °C for 20 min to complete the reaction. After cooling down to r.t., the solvent and unreacted thionyl chloride were removed under reduced pressure. The crude product was extracted from the oily residue with diethyl ether (4 × 100 ml). After that, the product was dried in high vacuum. Due to its sensitivity against air moisture the complex was stored under nitrogen atmosphere.

Yield: 16.6 g (106 mmol, 57 %), pale yellow liquid.

Formula: $C_5H_{11}Cl_2N$ [156.05].

^{1}H-NMR (400.1 MHz, $CDCl_3$):

δ [ppm] = 5.22 (s, 4H, H-4), 2.93 (t, $^3J_{H\text{-}H}$ = 7.4 Hz, 2H, H-3), 1.60 (m, $^3J_{H\text{-}H}$ = 7.4 Hz, 2H, H-2), 0.94 (t, $^3J_{H\text{-}H}$ = 7.4 Hz, 3H, H-1).

^{13}C-NMR (100.6 MHz, $CDCl_3$):

δ [ppm] = 71.7 (CH_2), 50.9 (CH_2), 20.0 (CH_2), 11.4 (CH_3).

***S*,*S*'-(Propylamino)bismethyl dithioacetate**

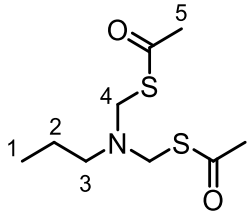

CAS: [/].

Synthesis based on given literature.[136]

Under nitrogen atmosphere potassium thioacetate (3.27 g, 28.6 mmol), which was dried before in high vacuum for 5 h, potassium carbonate (360 mg, 2.60 mmol) and ***N,N*-bis(chloromethyl)propan-1-amine** (2.03 g, 13.0 mmol) were dissolved in dry DCM (40 ml) and stirred at r.t. for 40 h. After that, the mixture was washed with deionised water (2 × 50 ml). The combined organic phases were dried over $MgSO_4$. After removing the solvent under reduced pressure, the resulting crude product was purified by flash column chromatography (silica gel, DCM/ethyl acetate = 1:1).

Yield: 1.93 g (8.20 mmol, 63 %), yellow liquid.

Formula: $C_9H_{17}NO_2S_2$ [235.37].

^{1}H-NMR (400.1 MHz, $CDCl_3$):

δ [ppm] = 4.58 (s, 4H, H-4), 2.46 (t, $^3J_{H\text{-}H}$ = 7.3 Hz, 2H, H-3), 2.37 (s, 6H, H-5), 1.47 (m, $^3J_{H\text{-}H}$ = 7.3 Hz, 2H, H-2), 0.88 (t, $^3J_{H\text{-}H}$ = 7.4 Hz, 3H, H-1).

^{13}C-NMR (100.6 MHz, $CDCl_3$):

δ [ppm] = 196.6 (C_q), 57.4 (CH_2), 51.7 (CH_2), 31.6 (CH_3), 20.2 (CH_2), 11.5 (CH_3).

ESI-MS (high resolution):

calc.: $[M+Na]^+$ 258.05929 m/z.

exp.: $[M+Na]^+$ 258.05985 m/z Δ = 2.17 ppm.

***N,N*-Bis(mercaptomethyl)propylamine**

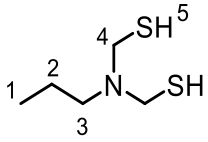

CAS: [/].

Synthesis based on given literature.[136]

Under nitrogen atmosphere a solution of ***S,S*'-(propylamino)bismethyl dithioacetate** (1.93 g, 8.20 mmol) in dry DCM (30 ml) was treated with pyrrolidine (1.48 ml, 17.7 mmol) at 0 °C. After stirring for 4 h, the ice bath was removed and the reaction mixture was stirred for additional 68 h. Then, the solvent was removed under reduced pressure and the resulting residue was purified by flash column chromatography (silica gel, DCM/ethyl acetate = 1:1).

Yield: 346 mg (2.29 mmol, 28 %), yellow liquid.

Formula: $C_5H_{13}NS_2$ [151.30].

^{1}H-NMR (400.1 MHz, $CDCl_3$):

δ [ppm] = 4.36 (s, 4H, H-4), 4.04 (s, 2H, H-5), 2.90 (t, $^3J_{H\text{-}H}$ = 7.4 Hz, 2H, H-3), 1.39 (m, $^3J_{H\text{-}H}$ = 7.4 Hz, 2H, H-2), 0.86 (t, $^3J_{H\text{-}H}$ = 7.4 Hz, 3H, H-1).

^{13}C-NMR (100.6 MHz, $CDCl_3$):

δ [ppm] = 58.4 (CH_2), 50.8 (CH_2), 20.3 (CH_2), 11.8 (CH_3).

[$Fe_2(\mu\text{-}S_2)(CO)_6$]

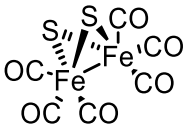

CAS: [58500-79-1].

Synthesis according to given literature.[90]

Under nitrogen atmosphere $Fe(CO)_5$ (10.0 ml, 76.1 mmol), methanol (50 ml) and freshly prepared aqueous potassium hydroxide solution (30 ml, 43 % (*w*/*w*)) were stirred at 0 °C for 60 min. Then, sulphur (13.4 g, 418 mmol) was slowly added and the mixture was stirred at 0 °C for 60 min. After that, water (100 ml), *n*-hexane (60 ml) and finally ammonium chloride (35.0 g, 654 mmol) were added. After removing of the ice bath, the mixture was stirred overnight. Then, the organic solvents were removed under reduced pressure and the resulting residue was extracted with diethyl ether (4 × 200 ml). The combined organic phases were filtered and the solvent was removed under reduced pressure. Finally, the obtained crude product was purified by flash column chromatography (silica gel, petroleum ether). Due to its light sensitivity the complex was stored in the dark.

Yield: 5.62 g (16.3 mmol, 43 %), red solid.

Formula: $C_6Fe_2O_6S_2$ [343.88].

^{13}C-NMR (100.6 MHz, $CDCl_3$):

δ [ppm] = 208.5 (C_q).

[FeFe]-Cat 11 / [$Fe_2(\mu$-$(SCH_2)_2NC_3H_7)(CO)_6$]

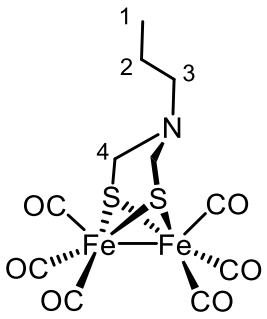

CAS: [933039-62-4].

Synthesis according to given literature.[35]

Under nitrogen atmosphere a solution of **[$Fe_2(\mu$-$S)_2(CO)_6$]** (1.50 g, 4.36 mmol) in dry THF (30 ml) was precooled to –78 °C and treated with $LiBHEt_3$ (8.82 ml, 8.82 mmol, 1 mol l^{-1} in THF). The dark green mixture was stirred at that temperature for 25 min and then treated with a solution of ***N,N*-bis(mercaptomethyl)propylamine** (5.11 g, 33.8 mmol) in THF (10 ml). After stirring for 30 min at –78 °C the reaction mixture was stirred for additional 18 h in the cooling mixture while slowly warming up to r.t. After filtration of the reaction mixture, the solvent was removed under reduced pressure from the filtrate and the resulting crude product was purified by flash column chromatography (silica gel, petroleum ether/DCM = 10:1). The product was dried in high vacuum. Due to its light sensitivity the complex was stored in the dark.

Yield: 578 mg (1.35 mmol, 31 %), red viscous liquid.

Formula: $C_{11}H_{11}Fe_2NO_6S_2$ [429.03].

^{1}H-NMR (400.1 MHz, $CDCl_3$):

δ [ppm] = 3.51 (s, 4H, H-4), 2.61 (t, $^3J_{H\text{-}H}$ = 7.2 Hz, 2H, H-3), 1.31 (m, $^3J_{H\text{-}H}$ = 7.2 Hz, 2H, H-2), 0.80 (t, $^3J_{H\text{-}H}$ = 7.3 Hz, 3H, H-1).

^{13}C-NMR (100.6 MHz, $CDCl_3$):

δ [ppm] = 208.0 (C_q), 59.3 (CH_2), 53.2 (CH_2), 21.0 (CH_2), 11.4 (CH_3).

ESI-MS (high resolution):

calc.: $[M+H]^+$ 429.87998 m/z.

exp.: $[M+H]^+$ 429.88091 m/z Δ = 2.16 ppm.

_N_,_N_-Bis(chloromethyl)benzenemethanamine

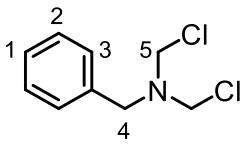

CAS: [845619-83-2].

Synthesis according to given literature.[33]

Under nitrogen atmosphere a mixture of benzylamine (7.50 ml, 68.7 mmol) and paraformaldehyde (5.37 g, 179 mmol) in dry DCM (60 ml) was stirred at r.t. for 23 h and then treated dropwise with thionyl chloride (20.0 ml, 274 mmol). The mixture was stirred at r.t. until the gas evolution has ceased (5 h after beginning of addition). Then, the solvent and unreacted thionyl chloride were removed under reduced pressure. After adding of diethyl ether (200 ml), the colourless solid was filtered. Finally, the solvent of the filtrate was removed under reduced pressure. Due to its sensitivity against air moisture and to avoid product polymerisation the complex was stored under nitrogen atmosphere at –30 °C.

Yield: 12.7 g (62.2 mmol, 91 %), pale yellow oil.

Formula: $C_9H_{11}Cl_2N$ [204.09].

^{1}H-NMR (400.1 MHz, $CDCl_3$):

δ [ppm] = 7.36 (m', 5H, H-1/2/3), 5.17 (s, 4H, H-5), 4.11 (s, 2H, H-4).

[FeFe]-Cat 13 / $[Fe_2(\mu\text{-}(SCH_2)_2NCH_2C_6H_5)(CO)_6]$

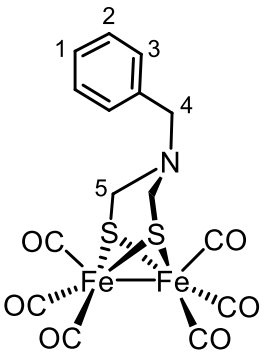

CAS: [403326-09-0].

Synthesis based on given literature.[90,91]

Under nitrogen atmosphere a solution of **[$Fe_2(\mu\text{-}S)_2(CO)_6$]** (480 mg, 1.40 mmol) in dry THF (20 ml) was precooled to –78 °C and threaded with $LiBHEt_3$ (3.22 ml, 3.22 mmol, 1 mol l^{-1} in THF). The dark green mixture was stirred at that temperature for 25 min and then treaded with a solution of ***N,N*-Bis(chloromethyl)benzenemethanamine** (1.74 g, 8.53 mmol) in THF (10 ml). After stirring at –78 °C for 30 min, triethylamine (390 µl, 2.80 mmol) was added and then the reaction mixture was stirred at –78 °C for additional 3 h. The reaction mixture was filtered by column filtration and then the solvent of the filtrate was removed under reduced pressure. The resulting crude product was purified by flash column chromatography (silica gel, petroleum ether/DCM = 10:1). Due to its light sensitivity the complex was stored in the dark.

Yield: 224 mg (470 µmol, 34 %), red-brown solid.

Formula: $C_{15}H_{11}Fe_2NO_6S_2$ [477.07].

^{1}H-NMR (400.1 MHz, $CDCl_3$):

δ [ppm] = 7.32–7.16 (m', 5H, H-1/2/3), 3.70 (s, 2H, H-4), 3.33 (s, 4H, H-5).

Tris(1*H*-pyrrol-1-yl)phosphine

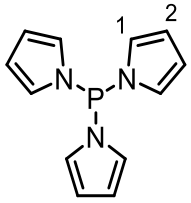

CAS: [60259-30-5].

Synthesis according to given literature.[137]

Under nitrogen atmosphere a solution of pyrrole (5.53 ml, 79.7 mmol) and triethylamine (12.1 ml, 86.8 mmol) in dry and degassed THF (40 ml) was cooled to –78 °C and was then treated with trichloro phosphine (1.75 ml, 20.1 mmol). A colourless solid precipitated immediately. After stirring for 60 min, the reaction mixture was allowed to warm up to r.t. and was stirred at that temperature for additional 30 min. Then, the mixture was heated at 65 °C for 21 h. After cooling down to r.t., the mixture was filtered and the filtered grey solid was washed with degassed THF (2 × 50 ml). Then, the solvent was removed under reduced pressure and the residue was diluted in degassed *n*-hexane (50 ml) under nitrogen atmosphere. After that, the *n*-hexane solution was concentrated *in vacuo* to about 10 ml and then slowly cooled to –78 °C under nitrogen atmosphere to crystallise the product. Due to its sensitivity to oxygen the complex was stored under nitrogen atmosphere.

Yield: 4.45 g (19.4 mmol, 97 %), colourless solid.

Formula: $C_{12}H_{12}N_3P$ [229.22].

^{1}H-NMR (400.1 MHz, $CDCl_3$):

δ [ppm] = 6.80 (m, 6H, H-1), 6.38 (m, 6H, H-2).

[FeFe]-Cat 12 / [Fe_2(μ-(SCH_2)$_2$$NC_3H_7$)(CO)$_5$Ppyr$_3$]

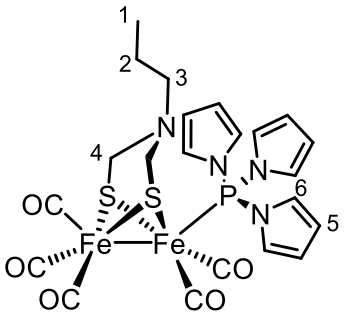

CAS: [/].

Synthesis following GP II:

[FeFe]-Cat 11 (100 mg, 233 µmol), trimethylamine *N*-oxide dihydrate (31.0 mg, 279 µmol), **tris(1*H*-pyrrol-1-yl)phosphine** (53.0 mg, 231 µmol), acetonitrile (30 ml), stirring for 3 h; flash column chromatography (silica gel, petroleum ether/DCM = 10:1).

Yield: 59.4 mg (94.2 µmol, 41 %), dark red solid.

Formula: $C_{22}H_{23}Fe_2N_4O_5PS_2$ [630.24].

^{1}H-NMR (400.1 MHz, $CDCl_3$):[*]

δ [ppm] = 6.89 (m, 6H, H-6), 6.38 (m, 6H, H-5), 3.01 (s, 2H, H-4), 2.58 (s, 2H, H-4), 2.07 (m, 2H, H-3), 1.08 (m, 2H, H-2), 0.65 (m, 3H, H-1).

^{13}C-NMR (100.6 MHz, $CDCl_3$):

δ [ppm] = 210.5 (C_q), 208.6 (C_q), 123.8 (CH), 113.4 (CH), 60.8 (CH_2), 51.8 (CH_2), 19.3 (CH_3), 11.6 (CH_2).

[*] Due to steric hindrance, the rotatability of the azadithiolate residue is probably hampered, which leads to the abolition of the chemical equivalence and splitting of the signal of the H-4 protons.

ESI-MS (high resolution):

calc.: $[M+H]^+$ 630.96198 m/z.

exp.: $[M+H]^+$ 630.96293 m/z Δ = 1.51 ppm.

[FeFe]-Cat 5 / $[Fe_2(\mu\text{-}S_2(CH_2)_3)(CO)_5Ppyr_3]$

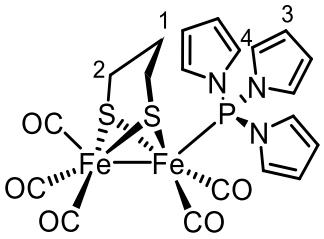

CAS: [1253526-95-2].

Synthesis following GP II:

[FeFe]-Cat 1 (500 mg, 1.30 mmol), trimethylamine *N*-oxide dihydrate (173 mg, 1.56 mmol), **tris(1*H*-pyrrol-1-yl)phosphine** (297 mg, 1.30 mmol), acetonitrile (50 ml), stirring for 3 h; flash column chromatography (silica gel, petroleum ether/DCM = 10:1).

Yield: 596 mg (1.02 mmol, 78 %), brown crystalline solid with metallic blaze.

Formula: $C_{20}H_{18}Fe_2N_3O_5PS_2$ [587.17].

^{1}H-NMR (400.1 MHz, $CDCl_3$):

δ [ppm] = 6.89 (m, 6H, H-3), 6.40 (m, 6H, H-4), 1.91 (m, 2H, H-1), 1.66 (m, 4H, H-2).

[FeFe]-Cat 6 / $[Fe_2(\mu\text{-}S_2C_6H_4)(CO)_5Ppyr_3]$

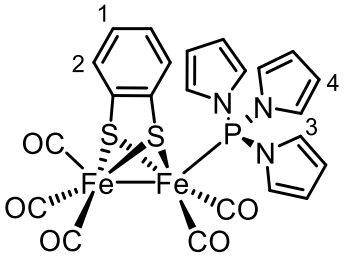

CAS: [/].

Synthesis following GP II:

[FeFe]-Cat 2 (1.00 g, 2.38 mmol), trimethylamine *N*-oxide dihydrate (318 mg, 2.86 mmol), **tris(1*H*-pyrrol-1-yl)phosphine** (546 mg, 2.38 mmol), acetonitrile (50 ml) stirring for 3 h; flash column chromatography (silica gel, petroleum ether/DCM = 10:1).

Yield: 857 mg (1.38 mmol, 58 %), dark red solid.

Formula: $C_{23}H_{16}Fe_2N_3O_5PS_2$ [621.19].

^{1}H-NMR (400.1 MHz, $CDCl_3$):

δ [ppm] = 6.83–6.77 (m, 6H, H-3), 6.72 (m, 2H, H-1), 6.41–6.37 (m, 6H, H-4), 6.30 (m, 2H, H-2).

^{13}C-NMR (100.6 MHz, $CDCl_3$):

δ [ppm] = 210.6 (C_q), 208.2 (C_q), 128.2 (CH), 126.5 (CH), 123.4 (CH), 113.4 (CH).

ESI-MS (high resolution):

calc.: $[M+Na]^+$ 643.88608 m/z.

exp.: $[M+Na]^+$ 643.88521 m/z Δ = 1.35 ppm.

[FeFe]-Cat 7 / $[Fe_2(\mu\text{-}S_2C_6H_2Cl_2)(CO)_5Ppyr_3]$

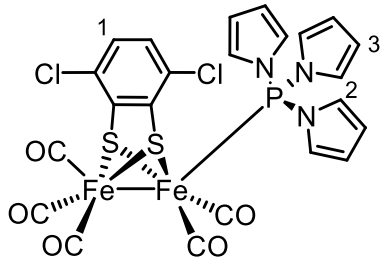

CAS: [/].

Synthesis following GP II:

[FeFe]-Cat 3 (200 mg, 409 µmol), trimethylamine *N*-oxide dihydrate (55.0 mg, 495 µmol) **tris(1*H*-pyrrol-1-yl)phosphine** (113 mg, 493 µmol), acetonitrile (30 ml), stirring for 3 h; flash column chromatography (silica gel, petroleum ether/DCM = 10:1).

Yield: 72.0 mg (104 µmol, 25 %), dark red solid.

Formula: $C_{23}H_{14}Cl_2Fe_2N_3O_5PS_2$ [690.08].

^{1}H-NMR (400.1 MHz, $CDCl_3$):

δ [ppm] = 6.75 (m, 6H, H-2), 6.38 (m, 2H, H-1), 6.34 (m, 6H, H-3).

^{13}C-NMR (100.6 MHz, $CDCl_3$):

δ [ppm] = 210.2 (C_q), 207.6 (C_q), 148.0 (C_q), 132.3 (C_q), 129.3 (CH), 123.4 (CH), 113.8 (CH).

ESI-MS (high resolution):

calc.: $[M+Na]^+$ 711.80826 m/z.

exp.: $[M+Na]^+$ 711.80661 m/z Δ = 2.32 ppm.

[FeFe]-Cat 14 / $[Fe_2(\mu\text{-}(SCH_2)_2NCH_2C_6H_5)(CO)_5Ppyr_3]$

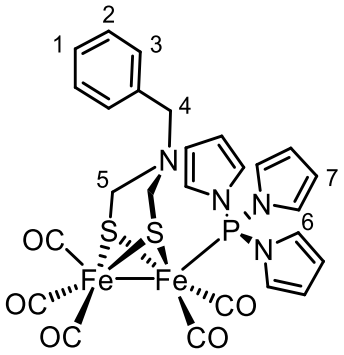

CAS: [1021186-12-8].

Synthesis following GP II:

$[Fe_2((\mu\text{-}SCH_2)_2NCH_2C_6H_5)(CO)_6]$ (206 mg, 432 µmol), trimethylamine *N*-oxide dihydrate (58.0 mg, 522 µmol), **tris(1*H*-pyrrol-1-yl)phosphine** (99.0 mg, 432 µmol), acetonitrile (40 ml), stirring for 3 h; flash column chromatography (silica gel, petroleum ether/DCM = 10:1).

Yield: 170 mg (251 µmol, 58 %), dark red solid.

Formula: $C_{26}H_{23}Fe_2N_4O_5PS_2$ [678.28].

^{1}H-NMR (400.1 MHz, $CDCl_3$):*

δ [ppm] = 7.41–7.04 (m', 5H, H-1/2/3), 6.83 (m, 6H, H-6), 6.31 (m, 6H, H-7), 3.18 (m, 2H, H-4), 2.98 (m, 2H, H-5), 2.26 (m, 2H, H-5).

[FeFe]-Cat 8 / [$Fe_2(\mu$-$S_2C_6H_4)(CO)_4(Ppyr_3)_2$]

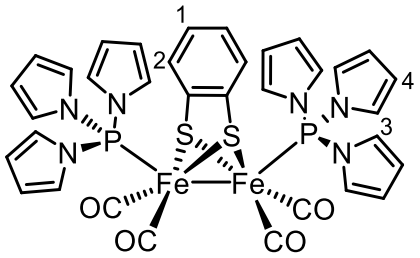

CAS: [/].

Synthesis based on given literature.[15]

Under nitrogen atmosphere **[FeFe]-Cat 6** (300 mg, 483 µmol) and **tris(1*H*-pyrrol-1-yl)phosphine** (221 mg, 964 µmol) were dissolved in dry toluene (30 ml) and the reaction mixture was refluxed under stirring for 24 h. After cooling down to r.t., the solvent was removed under reduced pressure and the resulting crude product was purified first by flash column chromatography (silica gel, petroleum ether/DCM = 4:1) and then by GPC. The product was dried in high vacuum. Due to its light sensitivity the complex was stored in the dark.

Yield: 80.5 mg (97.9 µmol, 20 %), dark red solid.

Formula: $C_{34}H_{28}Fe_2N_6O_4P_2S_2$ [822.40].

^{1}H-NMR (400.1 MHz, $CDCl_3$):

δ [ppm] = 6.87–6.21 (m', 24H, H-3/4), 6.52 (m, 2H, H-2), 6.16 (m, 2H, H-1).

^{13}C-NMR (100.6 MHz, $CDCl_3$):

δ [ppm] = 211.2 (C_q), 145.8 (C_q), 128.3 (CH), 126.1 (CH), 123.5 (CH), 114.7 (CH).

ESI-MS (high resolution):

calc.: $[M+Na]^+$ 844.96811 m/z.

* Due to steric hindrance, the rotatability of the azadithiolate residue is probably hampered, which leads to the abolition of the chemical equivalence and splitting of the signal of the H-5 protons.

exp.: $[M+Na]^+$ 844.96540 m/z Δ = 3.21 ppm.

[FeFe]-Cat 9 / $[Fe_2(\mu\text{-}S_2C_6H_4)(CO)_5PMe_3]$

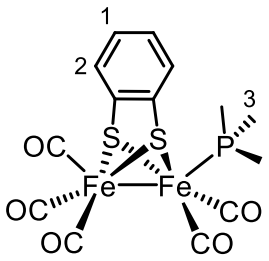

CAS: [/].

Synthesis following GP II:

[FeFe]-Cat 2 (400 mg, 952 µmol), trimethylamine *N*-oxide dihydrate (127 mg, 1.14 mmol), trimethyl phosphine (950 µl, 950 µmol, 1.0 M in THF), acetonitrile (50 ml), stirring for 2 h; flash column chromatography (silica gel, petroleum ether/DCM = 10:1).

Yield: 331 mg (707 µmol, 74 %), dark red solid.

Formula: $C_{14}H_{13}Fe_2O_5PS_2$ [468.05].

^{1}H-NMR (400.1 MHz, $CDCl_3$):

δ [ppm] = 7.07 (m, 2H, H-1), 6.56 (m, 2H, H-2), 1.54 (m, 9H, H-3).

^{13}C-NMR (100.6 MHz, $CDCl_3$):

δ [ppm] = 213.7 (C_q), 210.1 (C_q), 149.7 (C_q), 127.8 (CH), 126.1 (CH), 20.8 (CH_3).

Elemental Analysis (CHN):*

Calculated for $C_{14}H_{13}Fe_2O_5PS_2$:	C 35.93 %	H 2.80 %	S 13.70 %
found:	C 35.61 %	H 2.86 %	S 13.79 %

* Since no molecular peak could be found in the mass spectrometric investigation, an elemental analysis was carried out instead.

[FeFe]-Cat 10 / $[Fe_2(\mu\text{-}S_2C_6H_4)(CO)_5PPh_3]$

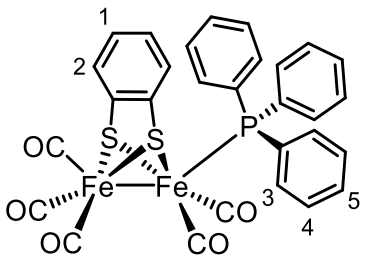

CAS: [1379801-43-0].

Synthesis following GP II:

[FeFe]-Cat 2 (400 mg, 952 µmol), trimethylamine *N*-oxide dihydrate (127 mg, 1.14 mmol), triphenyl phosphine (250 mg, 953 µmol), acetonitrile (50 ml), stirring for 3 h; flash column chromatography (silica gel, petroleum ether/DCM = 10:1).

Yield: 237 mg (362 µmol, 38 %), dark red solid.

Formula: $C_{29}H_{19}Fe_2O_5PS_2$ [654.26].

^{1}H-NMR (400.1 MHz, $CDCl_3$):

δ [ppm] = 7.50 (m, 6H, H-3), 7.38–7.30 (m', 9H, H-4/5), 6.49 (dd, $^3J_{H\text{-}H}$ = 5.4 Hz, $^4J_{H\text{-}H}$ = 3.2 Hz, 2H, H-1), 6.18 (dd, $^3J_{H\text{-}H}$ = 5.5 Hz, $^4J_{H\text{-}H}$ = 3.2 Hz, 2H, H-2).

Methyl 4-aminobenzoate

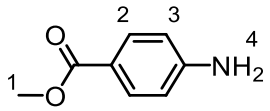

CAS: [619-45-4].

Synthesis according to given literature.[138]

To a solution of 4-aminobenzoic acid (500 mg, 3.65 mmol) in methanol (50 ml) thionyl chloride (665 µl, 1.08 g, 9.08 mmol) was added at 0 °C. The reaction mixture was stirred at 70 °C for 24 h. After cooling down to r.t., toluene (30 ml) was added and the solvent was removed under reduced pressure in order to remove the excess of thionyl chloride. After addition of ethyl acetate (150 ml) the solution was washed with sat. $NaHCO_3$ solution (2 × 100 ml) and dried over $MgSO_4$. Finally, the solvent was removed under reduced pressure.

Yield: 532 mg (3.52 mmol, 96 %), colourless crystals.

Formula: $C_8H_9NO_2$ [151.16].

^{1}H-NMR (400.1 MHz, $CDCl_3$):

δ [ppm] = 7.85 (AA', 2H, H-3), 6.64 (BB', 2H, H-2), 4.04 (bs, 2H, H-4), 3.85 (s, 3H, H-1).

Spacer 1 / 4-(*N*-*tert*-Butoxycarbonyl)aminobenzoic acid

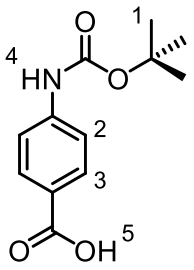

CAS: [66493-39-8].

Synthesis according to given literature.[55]

4-Aminobenzoic acid (2.74 g, 20.0 mmol) was suspended in water (40 ml) and *tert*-butanol (30 ml) was added. To this mixture di-*tert*-butyl dicarbonate (8.73 g, 40.0 mmol) and NaOH (880 mg, 22.0 mmol) were added and the reaction mixture was stirred at 60 °C for 24 h. Afterwards, water (100 ml) was added and the resulting mixture was washed with DCM (2 × 50 ml). The aqueous phase was separated and cooled with an ice bath. After addition of ethyl acetate (50 ml) the pH value was lowered down to 2 by addition of hydrochloric acid (2.0 M). After separation of the organic phase, the aqueous phase was extracted again with ethyl acetate (2 × 50 ml). The combined organic phases were dried over $NaSO_4$ and finally the solvent was removed under reduced pressure.

Yield: 3.64 g (15.3 mmol, 77 %), colourless solid.

Formula: $C_{12}H_{15}NO_4$ [237.25].

^{1}H-NMR (400.1 MHz, DMSO-d_6):

δ [ppm] = 12.46 (bs, 1H, H-5), 9.74 (s, 1H, H-4), 7.83 (AA', 2H, H-3), 7.56 (BB', 2H, H-2), 1.48 (s, 9H, H-1).

1,3-Dibromopropan-2-yl 4-((*tert*-butoxycarbonyl)amino)benzoate

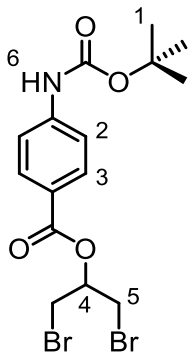

CAS: [551935-52-5].

Synthesis according to given literature.[55]

Under nitrogen atmosphere 4-dimethylaminopyridine (782 mg, 6.40 mmol) and 1,3-dibromopropan-2-ol (3.49 g, 15.9 mmol) were added to a suspension of **4-(*N*-*tert*-butoxycarbonyl)aminobenzoic acid** (3.80 g, 16.0 mmol) in dry DCM (50 ml). The resulting mixture was stirred at r.t. for 15 min and then a solution of *N*,*N*′-dicyclohexylcarbodiimide (5.61 g, 27.2 mmol) in dry DCM (20 ml) was added dropwise over a period of 15 min. After that, the reaction mixture was stirred at r.t. for 17 h. Then, the solvent was removed under reduced pressure and finally the resulting residue was purified by column chromatography (silica gel, toluene/ethyl acetate = 6:1).

Yield: 5.12 g (11.7 mmol, 74 %), colourless solid.

Formula: $C_{15}H_{19}Br_2NO_4$ [437.12].

^{1}H-NMR (400.1 MHz, $CDCl_3$):

δ [ppm] = 8.00 (AA', 2H, H-3), 7.45 (BB', 2H, H-2), 6.68 (s, 1H, H-6), 5.35 (m, 1H, H-4), 3.78–3.70 (m, 4H, H-5), 1.53 (s, 9H, H-1).

1,3-Bis(acetylthio)propan-2-yl 4-((*tert*-butoxycarbonyl)amino)benzoate

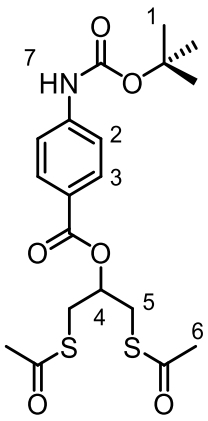

CAS: [551935-53-6].

Synthesis according to given literature.[55]

Under nitrogen atmosphere **1,3-dibromopropan-2-yl 4-((*tert*-butoxycarbonyl)amino)-benzoate** (5.00 g, 11.4 mmol) and potassium thioacetate (5.88 g, 51.5 mmol) were dissolved in acetone (50 ml) and the reaction mixture was stirred at r.t. for 16 h. After filtration of the formed KBr, the solvent was removed under reduced pressure and finally the obtained crude product was purified by column chromatography (silica gel, toluene/ethyl acetate = 6:1).

Yield: 4.25 g (9.94 mmol, 87 %), brown oil.

Formula: $C_{19}H_{25}NO_6S_2$ [427.54].

^{1}H-NMR (400.1 MHz, $CDCl_3$):

δ [ppm] = 7.93 (AA', 2H, H-3), 7.43 (BB', 2H, H-2), 6.65 (s, 1H, H-7), 5.29–5.23 (m, 1H, H-4), 3.36–3.23 (m, 4H, H-5), 2.33 (s, 6H, H-6), 1.53 (s, 9H, H-1).

1,3-Dimercaptopropan-2-yl 4-((*tert*-butoxycarbonyl)amino)benzoate

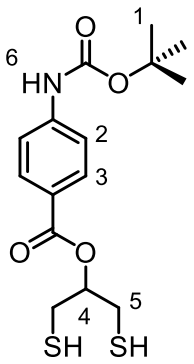

CAS: [551935-54-7].

Synthesis according to given literature.[55]

Under nitrogen atmosphere **1,3-bis(acetylthio)propan-2-yl 4-((*tert*-butoxycarbonyl)-amino)benzoate** (4.20 g, 9.82 mmol) was dissolved in dry DMF (20 ml). Hydrazine hydrate (1.08 ml, 34.7 mmol) was added dropwise at r.t. and the resulting mixture was stirred at this temperature for 10 min. Then, acetic acid (1.97 ml, 34.7 mmol) was added dropwise. After stirring for 1 h, the mixture was diluted with water (20 ml) and ethyl acetate (20 ml). Afterwards, the organic phase was washed with water (2 × 20 ml) and the combined aqueous phases were washed with ethyl acetate (20 ml). Finally, the combined organic phases were washed with water (10 ml), brine (10 ml) and dried over Na_2SO_4. After removing the solvent under reduced pressure, the obtained crude product was purified by column chromatography (silica gel, toluene/ethyl acetate = 6:1).

Yield: 3.04 g (8.85 mmol, 90 %), thick oil.

Formula: $C_{15}H_{21}NO_4S_2$ [343.46].

^{1}H-NMR (400.1 MHz, $CDCl_3$):[*]

δ [ppm] = 7.98 (AA', 2H, H-3), 7.45 (BB', 2H, H-2), 6.68 (s, 1H, H-6), 5.16 (quint, $^3J_{H\text{-}H}$ = 5.6 Hz, 1H, H-4), 3.01–2.97 (m, 4H, H-5), 1.53 (s, 9H, H-1).

[*] The signal for the thiol protons could not be detected with $CDCl_3$ as solvent.

[FeFe]-Spacer-Cat 1

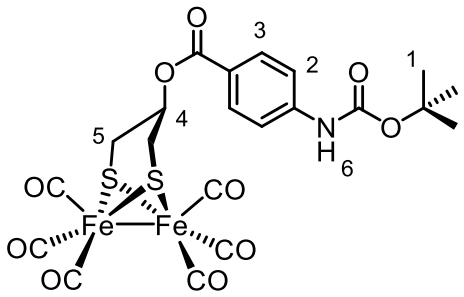

CAS: [551938-22-8].

Synthesis according to given literature.[55]

Under nitrogen atmosphere **1,3-dimercaptopropan-2-yl 4-((*tert*-butoxycarbonyl)amino)-benzoate** (3.00 g, 8.73 mmol) was dissolved in dry THF (30 ml) and triiron dodecacarbonyl (4.40 g, 8.74 mmol) was added and the reaction mixture was stirred at 67 °C for 3 h. After cooling down to r.t., the solvent was removed under reduced pressure and finally the obtained crude product was purified by column chromatography (silica gel, toluene/petroleum ether = 1:1). The product was dried in high vacuum. Due to its light sensitivity the complex was stored in the dark.

Yield: 3.64 g (5.86 mmol, 67 %), red viscous oil.

Formula: $C_{21}H_{19}Fe_2NO_{10}S_2$ [621.20].

^{1}H-NMR (400.1 MHz, $CDCl_3$):[*]

δ [ppm] = 7.87 (AA', 2H, H-3), 7.40 (BB', 2H, H-2), 6.65 (s, 1H, H-6), 4.49–4.41 (m, 1H, H-4), 2.92 (dd, $^2J_{H\text{-}H}$ = 13 Hz, $^3J_{H\text{-}H}$ = 4.2 Hz, 2H, H-5), 1.69 (dd, $^2J_{H\text{-}H}$ = 13 Hz, $^3J_{H\text{-}H}$ = 12 Hz, 2H, H-5), 1.52 (s, 9H, H-1).

[*] Due to steric hindrance, the rotatability of the benzoate residue is probably hampered, which leads to the abolition of the chemical equivalence and splitting of the signal of the H-5 protons.

[FeFe]-Spacer-Cat 2

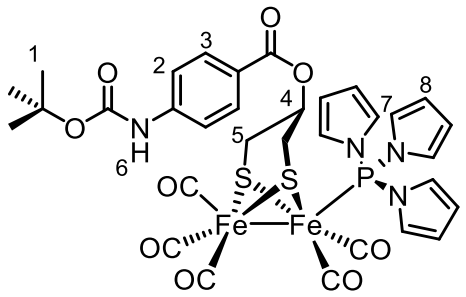

CAS: [/].

Synthesis based on given literature.[135]

Under nitrogen atmosphere **[FeFe]-Spacer-Cat 1** (1.80 g, 2.90 mmol) and trimethylamine *N*-oxide (261 mg, 3.47 mmol) were dissolved in degassed acetonitrile (20 ml) and stirred at r.t. for 5 min. Then, a solution of **tris(1*H*-pyrrol-1-yl)phosphine** (797 mg, 3.48 mmol) in degassed acetonitrile (10 ml) was added and the reaction mixture was stirred at r.t. for 3 h. After that, the solvent was removed under reduced pressure and finally the resulting residue was purified by flash column chromatography (silica gel, toluene). The product was dried in high vacuum. Due to its light sensitivity the complex was stored in the dark.

Yield: 2.37 g (2.88 mmol, 99 %), red solid.

Formula: $C_{32}H_{31}Fe_2N_4O_9PS_2$ [822.41].

^{1}H-NMR (400.1 MHz, $CDCl_3$):[*]

δ [ppm] = 7.75 (AA', 2H, H-3), 7.36 (BB', 2H, H-2), 6.89–6.91 (m, 6H, H 7), 6.61 (s, 1H, H-6), 6.38–6.41 (m, 6H, H-8), 3.54–3.61 (m, 1H, H-4), 2.69 (dd, $^2J_{H\text{-}H}$ = 13 Hz, $^3J_{H\text{-}H}$ = 4.5 Hz, 2H, H-5), 1.63 (dd, $^2J_{H\text{-}H}$ = 12 Hz, $^3J_{H\text{-}H}$ = 12 Hz, 2H, H-5), 1.51 (s, 9H, H-1).

^{13}C-NMR (100.6 MHz, $CDCl_3$):

δ [ppm] = 210.7 (C_q), 207.9 (C_q), 163.9 (C_q), 152.2 (C_q), 143.1 (C_q), 131.1 (CH), 123.7 (CH), 117.3 (CH), 114.7 (C_q), 113.9 (CH), 81.5 (C_q), 73.8 (CH), 28.4 (CH_3), 27.3 (CH_2).

[*] Due to steric hindrance, the rotatability of the benzoate residue is probably hampered, which leads to the abolition of the chemical equivalence and splitting of the signal of the H-5 protons.

ESI-MS (high resolution):

calc.: $[M+Na]^+$ 844.9862 m/z.

exp.: $[M+Na]^+$ 844.9846 m/z Δ = 1.89 ppm.

[FeFe]-Spacer-Cat 3

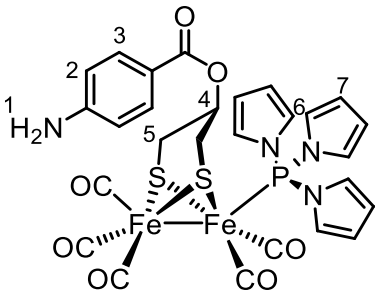

CAS: [/].

Synthesis based on given literature.[55]

Under nitrogen atmosphere **[FeFe]-Spacer-Cat 2** (650 mg, 790 µmol) was dissolved in dry DCM (25 ml) and trifluoroacetic acid (1.28 ml, 16.7 mmol) was added at r.t. The reaction mixture was stirred at that temperature for 5 h. Then, the solvent was removed under reduced pressure and finally the resulting residue was purified by column chromatography (silica gel, toluene/ethyl acetate = 6:1). Due to its light sensitivity the complex was stored in the dark.

Yield: 536 mg (742 µmol, 94 %), red solid.

Formula: $C_{27}H_{23}Fe_2N_4O_7PS_2$ [722.29].

^{1}H-NMR (400.1 MHz, $CDCl_3$):[*]

δ [ppm] = 7.73 (AA', 2H, H-3), 7.02–6.84 (m, 6H, H-6), 6.58 (BB', 2H, H-2), 6.50–6.27 (m, 6H, H-7), 3.57 (m, 1H, H-4), 2.79–2.54 (m, 2H, H-5), 1.70–1.53 (m, 2H, H-5).

[*] The signal for the amine protons could not be detected with $CDCl_3$ as solvent. Due to steric hindrance, the rotatability of the benzoate residue is probably hampered, which leads to the abolition of the chemical equivalence and splitting of the signal of the H-5 protons.

^{13}C-NMR (100.6 MHz, $CDCl_3$):

δ [ppm] = 210.8 (C_q), 208.0 (C_q), 164.2 (C_q), 151.2 (C_q), 131.8 (CH), 123.7 (CH), 118.9 (C_q), 113.87 (CH), 113.77 (CH), 73.6 (CH), 27.3 (CH_2).

ESI-MS (high resolution):

calc.: $[M+Na]^+$ 744.93378 m/z.

exp.: $[M+Na]^+$ 744.93402 m/z Δ = 0.32 ppm.

Methyl 4-bromobenzoate

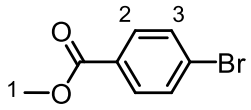

CAS: [619-42-1].

Synthesis based on given literature.[139]

To a solution of 4-bromobenzoic acid (1.00 g, 4.97 mmol) in methanol (30 ml) thionyl chloride (545 µl, 7.47 mmol) was added at 0 °C. The reaction mixture was stirred at 70 °C for 2 h. After cooling down to r.t., toluene (30 ml) was added and the solvent was removed under reduced pressure to discard the excess of thionyl chloride. After addition of ethyl acetate (150 ml) the solution was washed with sat. $NaHCO_3$ (2 × 100 ml) and brine (60 ml) and finally dried over Na_2SO_4. After that, the solvent was removed under reduced pressure.

Yield: 1.06 g (4.93 mmol, 99 %), colourless crystals.

Formula: $C_8H_7BrO_2$ [215.04].

^{1}H-NMR (400.1 MHz, $CDCl_3$):

δ [ppm] = 7.90 (AA', 2H, H-3), 7.58 (BB', 2H, H-2), 3.92 (s, 3H, H-1).

Methyl 4-(4,4,5,5-tetramethyl-1,3,2-dioxaborolan-2-yl)benzoate

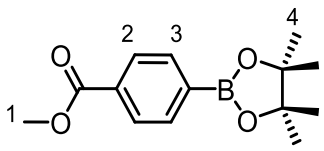

CAS: [171364-80-0].

Synthesis according to given literature.[108]

A mixture of **methyl 4-bromobenzoate** (2.00 g, 9.30 mmol), bis(pinacolato)diboron (2.60 g, 10.2 mmol), potassium acetate (2.74 g, 27.9 mmol) and Pd(dppf)Cl_2 (204 mg, 279 µmol) in dry acetonitrile (40 ml) was stirred at 80 °C for 48 h. After cooling down to r.t., water (10 ml) was added and the reaction mixture was extracted with DCM (3 × 50 ml). The combined organic phases were dried over anhydrous sodium sulphate. Then, the solvent was removed under reduced pressure and the obtained crude product was purified by column chromatography (silica gel, ethyl acetate/petroleum ether = 1:2).

Yield: 2.40 g (9.16 mmol, 98 %), colourless solid.

Formula: $C_{14}H_{19}BO_4$ [262.11].

^{1}H-NMR (400.1 MHz, $CDCl_3$):

δ[ppm] = 8.02 (AA', 2H, H-2), 7.87 (BB', 2H, H-3), 3.92 (s, 3H, H-1), 1.36 (s, 12H, H-4).

Methyl 4'-amino-2'-methyl-[1,1'-biphenyl]-4-carboxylate

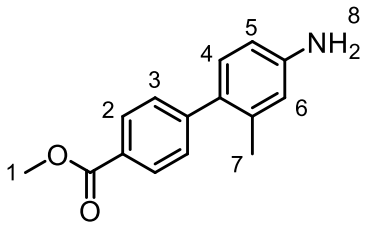

CAS: [188593-21-7].

Synthesis according to given literature.[107]

Under nitrogen atmosphere a mixture of **methyl 4-(4,4,5,5-tetramethyl-1,3,2-dioxaborolan-2-yl)benzoate** (1.80 mg, 6.87 mmol), 4-chloro-3-methylaniline (972 mg, 6.86 mmol) and potassium phosphate (7.29 g, 34.3 mmol) in 1,4-dioxane (24 ml) and water (6 ml) was

degassed for 10 min through nitrogen purging. Then, $Pd(OAc)_2$ (77.0 mg, 343 µmol) and 2-dicyclohexylphosphino-2′,4′,6′-triisopropylbiphenyl (655 mg, 1.37 mmol) were added and the reaction mixture was stirred at 80 °C for 20 h. After cooling down to r.t., the crude product was extracted with ethyl acetate (3 × 50 ml) and the combined organic layers were dried over Na_2SO_4. The solvent was removed under reduced pressure and the obtained crude product was purified by column chromatography (silica gel, petroleum ether/ethyl acetate = 2:1).

Yield: 1.62 g (6.71 mmol, 98 %), colourless solid.

Formula: $C_{15}H_{15}NO_2$ [241.29].

^{1}H-NMR (400.1 MHz, $CDCl_3$):[*]

δ [ppm] = 8.05 (AA', 2H, H-2), 7.37 (BB', 2H, H-3), 7.06 (dd, $^3J_{H\text{-}H}$ = 7.9 Hz, $^5J_{H\text{-}H}$ = 2.8 Hz, 1H, H-4), 6.99 (s, 1H, H-6), 6.69–6.64 (m, 1H, H-5), 3.93 (s, 3H, H-1), 2.22 (s, 3H, H-7).

^{13}C-NMR (100.6 MHz, $CDCl_3$):

δ [ppm] = 167.2 (C_q), 147.0 (C_q), 146.2 (C_q), 136.4 (C_q), 131.4 (C_q), 130.8 (CH), 129.5 (CH), 129.4 (CH), 127.9 (C_q), 117.0 (CH), 112.8 (CH), 52.1 (CH_3), 20.6 (CH_3).

4'-Amino-2'-methyl-[1,1'-biphenyl]-4-carboxylic acid

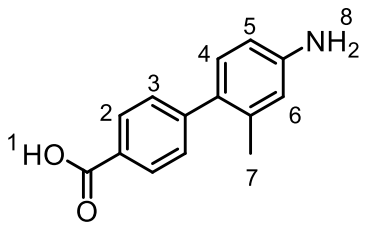

CAS: [180083-19-6].

Synthesis according to given literature.[140]

Methyl 4'-amino-2'-methyl-[1,1'-biphenyl]-4-carboxylate (850 mg, 3.52 mmol) was dissolved in a mixture of THF and MeOH (100 ml, *v*/*v* = 1:1). After addition of a KOH solution (2 M, 50 ml), the reaction mixture was heated at 90 °C overnight. After cooling down to r.t., the organic phase was evaporated under reduced pressure. The resulting aqueous phase was

[*] The signal for the amine protons could not be detected with $CDCl_3$ as solvent.

acidified with hydrochloric acid (6 M). The formed precipitate was filtered and washed with water. Finally, the product was dried in high vacuum.

Yield: 727 mg (3.20 mmol, 91 %), colourless solid.

Formula: $C_{14}H_{13}NO_2$ [227.26].

^{1}H-NMR (400.1 MHz, $CDCl_3$):[*]

δ [ppm] = 8.10 (AA', 2H, H-2), 7.43 (BB', 2H, H-3), 7.31 (d, $^3J_{H\text{-}H}$ = 8.0 Hz, 1H, H-5), 7.18–7.12 (m, 1H, H-4), 7.00 (s, 1H, H-6), 2.29 (s, 3H, H-7).

Methyl 4'-((*tert*-butoxycarbonyl)amino)-2'-methyl-[1,1'-biphenyl]-4-carboxylate

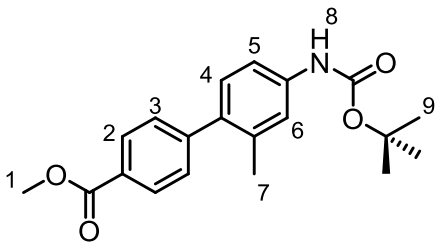

CAS: [/].

Synthesis based on given literature.[55]

Under nitrogen atmosphere **methyl 4'-amino-2'-methyl-[1,1'-biphenyl]-4-carboxylate** (670 mg, 2.78 mmol) was dissolved in dry THF (30 ml). To this solution triethylamine (770 µl, 5.52 mmol) and di-*tert*-butyl dicarbonate (1.21 g, 5.54 mmol) were added and the reaction mixture was stirred at r.t. for 15 h. Then, the solvent was removed under reduced pressure and the resulting residue was dissolved in DCM (30 ml). After washing with sat. $NaHCO_3$ solution (50 ml), water (50 ml) and brine (50 ml) the organic layer was dried over Na_2SO_4. The solvent was removed under reduced pressure and the obtained crude product was purified by column chromatography (silica gel, petroleum ether/ethyl acetate = 2:1).

Yield: 551 mg (1.61 mmol, 58 %), colourless solid.

Formula: $C_{20}H_{23}NO_4$ [341.40].

[*] The signal for both the carboxylic acid proton and the amine protons could not be detected with $CDCl_3$ as solvent.

^{1}H-NMR (400.1 MHz, $CDCl_3$):

δ [ppm] = 8.07 (AA', 2H, H-2), 7.39–7.33 (m', 3H, H-3/6), 7.21 (dd, $^{3}J_{H\text{-}H}$ = 8.3 Hz, $^{4}J_{H\text{-}H}$ = 2.2 Hz, 1H, H-5), 7.14 (d, $^{3}J_{H\text{-}H}$ = 8.3 Hz, 1H, H-4), 6.48 (s, 1H, H-8), 3.94 (s, 3H, H-1), 2.25 (s, 3H, H-7), 1.53 (s, 9H, H-9).

^{13}C-NMR (100.6 MHz, $CDCl_3$):

δ [ppm] = 167.2 (C_q), 152.9 (C_q), 146.5 (C_q), 138.0 (C_q), 136.3 (C_q), 135.8 (C_q), 130.3 (C_q), 129.54 (CH), 129.50 (CH), 128.5 (CH), 120.4 (CH), 116.2 (CH), 80.8 (C_q), 52.3 (CH_3), 28.5 (CH_3), 20.7 (CH_3).

ESI-MS (high resolution):

calc.: $[M+Na]^+$ 364.15193 m/z.

exp.: $[M+Na]^+$ 364.15331 m/z Δ = 3.79 ppm.

4'-((*tert*-Butoxycarbonyl)amino)-2'-methyl-[1,1'-biphenyl]-4-carboxylic acid

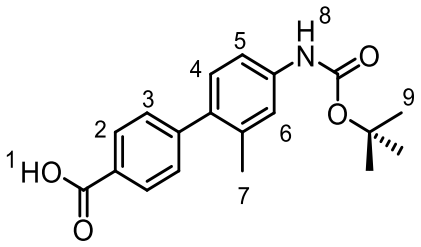

CAS: [/].

Synthesis based on given literature.[140]

Methyl 4'-((*tert*-butoxycarbonyl)amino)-2'-methyl-[1,1'-biphenyl]-4-carboxylate (850 mg, 2.49 mmol) was dissolved in a mixture of THF and MeOH (100 ml, *v*/*v* = 1:1). After addition of a KOH solution (2 M, 50 ml), the reaction mixture was heated at 90 °C for 60 min. After cooling down to r.t., the organic phase was evaporated under reduced pressure. The resulting aqueous phase was acidified with hydrochloric acid (6 M). The formed precipitate was filtered and washed with water. Finally, the product was dried in high vacuum.

Yield: 809 mg (2.47 mmol, 99 %), colourless solid.

Formula: $C_{19}H_{21}NO_4$ [327.38].

^{1}H-NMR (400.1 MHz, DMSO-d_6):

δ [ppm] = 13.0 (bs, 1H, H-1), 9.40 (s, 1H, H-8), 7.97 (AA', 2H, H-2), 7.44–7.41 (m', 3H, H-3/6), 7.34 (dd, $^{3}J_{H\text{-}H}$ = 8.5 Hz, $^{4}J_{H\text{-}H}$ = 2.2 Hz, 1H, H-5), 7.13 (d, $^{3}J_{H\text{-}H}$ = 8.4 Hz, 1H, H-4), 2.20 (s, 3H, H-7), 1.48 (s, 9H, H-9).

^{13}C-NMR (100.6 MHz, $CDCl_3$):

δ [ppm] = 207.3 (C_q), 171.1 (C_q), 147.3 (C_q), 138.2 (C_q), 136.3 (C_q), 135.7 (C_q), 130.3 (C_q), 130.2 (CH), 129.6 (CH), 127.6 (CH), 120.4 (CH), 116.2 (CH), 31.1 (C_q), 28.5 (CH_3), 20.8 (CH_3).

ESI-MS (high resolution):

calc.: $[2M+Na]^+$ 677.28334 m/z.

exp.: $[2M+Na]^+$ 677.28184 m/z Δ = 2.21 ppm.

Spacer 2

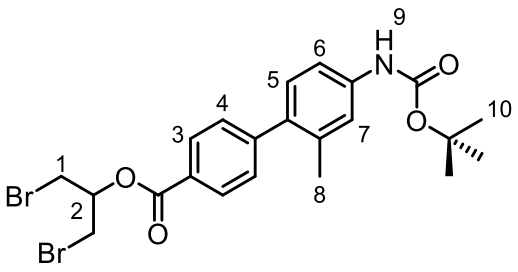

CAS: [/].

Synthesis based on given literature.[55]

Under nitrogen atmosphere 4-dimethylaminopyridine (92.0 mg, 753 µmol) and 1,3-dibromopropan-2-ol (410 mg, 1.88 mmol) were added to a suspension of **4'-((*tert*-butoxycarbonyl)amino)-2'-methyl-[1,1'-biphenyl]-4-carboxylic acid** (800 mg, 2.44 mmol) in dry DCM (50 ml). The resulting mixture was stirred at r.t. for 15 min and then a solution of *N*,*N*'-dicyclohexylcarbodiimide (659 mg, 3.19 mmol) in dry DCM (20 ml) was added dropwise over period of 15 min. The reaction mixture was stirred at r.t. for 17 h. Then, the solvent was removed under reduced pressure and finally the resulting residue was purified by column chromatography (silica gel, petroleum ether/ethyl acetate = 4:1).

Yield: 784 mg (1.49 mmol, 79 %), colourless solid.

Formula: $C_{22}H_{25}Br_2NO_4$ [527.25].

^{1}H-NMR (400.1 MHz, $CDCl_3$):

δ [ppm] = 8.10 (AA', 2H, H-3), 7.41 (BB', 2H, H-4), 7.35 (s, 1H, H-7), 7.22 (dd, $^3J_{H\text{-}H}$ = 8.3 Hz, $^4J_{H\text{-}H}$ = 2.1 Hz, 1H, H-6), 7.15 (d, $^3J_{H\text{-}H}$ = 8.5 Hz, 1H, H-5), 6.48 (s, 1H, H-9), 5.40 (quint, $^3J_{H\text{-}H}$ = 5.2 Hz, 1H, H-2), 3.81–3.73 (m, 4H, H-1), 2.26 (s, 3H, H-8), 1.53 (s, 9H, H-10).

^{13}C-NMR (100.6 MHz, $CDCl_3$):

δ [ppm] = 165.4 (C_q), 152.9 (C_q), 147.3 (C_q), 138.2 (C_q), 136.3 (C_q), 135.6 (C_q), 130.3 (C_q), 129.9 (CH), 129.7 (CH), 127.5 (CH), 120.4 (CH), 116.2 (CH), 80.8 (CH), 71.4 (C_q), 31.6 (CH_2), 28.5 (CH_3), 20.7 (CH_3).

Spacer 3

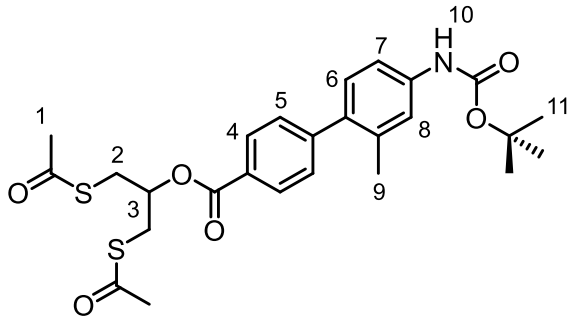

CAS: [/].

Synthesis based on given literature.[55]

Under nitrogen atmosphere **Spacer 2** (700 mg, 1.33 mmol) and potassium thioacetate (682 mg, 5.97 mmol) were dissolved in acetone (50 ml) and the reaction mixture was stirred at r.t. for 5 h. After filtration of the formed KBr, the solvent was removed under reduced pressure and finally the obtained crude product was purified by column chromatography (silica gel, petroleum ether/ethyl acetate = 4:1).

Yield: 675 mg (1.30 mmol, 98 %), brown oil.

Formula: $C_{26}H_{31}NO_6S_2$ [517.66].

^{1}H-NMR (400.1 MHz, $CDCl_3$):

δ [ppm] = 8.03 (AA', 2H, H-4), 7.38 (BB', 2H, H-5), 7.35 (s, 1H, H-8), 7.21 (dd, $^{3}J_{H\text{-}H}$ = 8.3 Hz, $^{4}J_{H\text{-}H}$ = 2.1 Hz, 1H, H-7), 7.14 (d, $^{3}J_{H\text{-}H}$ = 8.2 Hz, 1H, H-6), 6.49 (s, 1H, H-10), 5.31 (quint, $^{3}J_{H\text{-}H}$ = 5.8 Hz, 1H, H-3), 3.38–3.26 (m, 4H, H-2), 2.35 (s, 6H, H-1), 2.26 (s, 3H, H-9), 1.53 (s, 9H, H-11).

^{13}C-NMR (100.6 MHz, $CDCl_3$):

δ [ppm] = 194.6 (C_q), 165.6 (C_q), 152.9 (C_q), 146.8 (C_q), 138.1 (C_q),136.2 (C_q), 135.6 (C_q), 130.3 (CH), 129.7 (CH), 129.5 (CH), 127.9 (C_q), 120.4 (CH), 116.2 (CH), 80.7 (C_q), 71.5 (CH), 31.8 (CH_2), 30.6 (CH_3), 28.4 (CH_3), 20.7 (CH_3).

Spacer 4

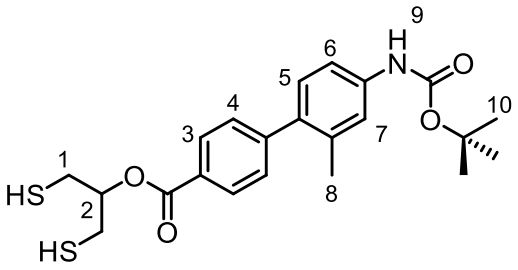

CAS: [/].

Synthesis based on given literature.[55]

Under nitrogen atmosphere **Spacer 3** (700 g, 1.35 mmol) was dissolved in dry DMF (20 ml). To this mixture hydrazine hydrate (133 µl, 4.27 mmol) was added dropwise at r.t. and the resulting mixture was stirred at r.t. for 10 min. Then, acetic acid (242 µl, 4.23 mmol) was added dropwise. After stirring for 18 h, the mixture was diluted with water (20 ml) and ethyl acetate (20 ml). After that, the organic phase was washed with water (2 × 20 ml) and the combined aqueous phases were washed with ethyl acetate (20 ml). Finally, the combined organic phases were washed with water (10 ml), brine (10 ml) and dried over Na_2SO_4. After removing the solvent under reduced pressure, the obtained crude product was purified by column chromatography (silica gel, petroleum ether/ethyl acetate = 2:1).

Yield: 460 mg (1.06 mmol, 79 %), brown oil.

Formula: $C_{22}H_{27}NO_4S_2$ [433.59].

^{1}H-NMR (400.1 MHz, $CDCl_3$):*

δ [ppm] = 8.09 (AA', 2H, H-3), 7.40 (BB', 2H, H-4), 7.35 (s, 1H, H-7), 7.23–7.20 (m, 1H, H-6), 7.16–7.14 (m, 1H, H-5), 6.49 (s, 1H, H-9), 5.14 (quint, $^{3}J_{H\text{-}H}$ = 5.7 Hz, 1H, H-2), 3.04–3.00 (m, 4H, H-1), 2.26 (s, 3H, H-8), 1.53 (s, 9H, H-10).

^{13}C-NMR (100.6 MHz, $CDCl_3$):

δ [ppm] = 165.8 (C_q), 152.9 (C_q), 147.0 (C_q), 138.2 (C_q), 136.3 (C_q), 135.7 (C_q), 130.3 (C_q), 129.70 (CH), 129.65 (CH), 128.0 (CH), 120.4 (CH), 116.2 (CH), 80.8 (CH), 75.5 (C_q), 28.5 (CH_3), 26.4 (CH_2), 20.8 (CH_3).

[FeFe]-Spacer-Cat 4

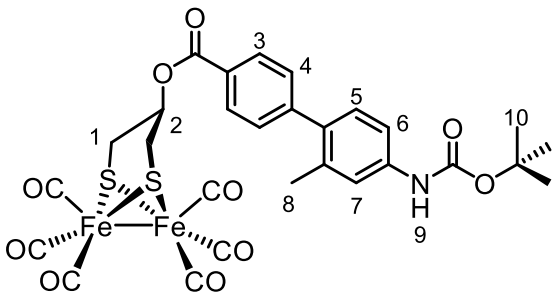

CAS: [/].

Synthesis based on given literature.[55]

Under nitrogen atmosphere **Spacer 4** (224 mg, 517 µmol) was dissolved in dry THF (30 ml) and triiron dodecacarbonyl (260 mg, 516 µmol) was added. The reaction mixture was stirred at 67 °C for 3 h. After cooling down to r.t., the solvent was removed under reduced pressure and finally the obtained crude product was purified by column chromatography (silica gel, petroleum ether). The product was dried in high vacuum. Due to its light sensitivity the complex was stored in the dark.

Yield: 293 mg (412 µmol, 80 %), red orange solid.

Formula: $C_{28}H_{25}Fe_2NO_{10}S_2$ [711.32].

* The signal for the thiol protons could not be detected with $CDCl_3$ as solvent.

^{1}H-NMR (400.1 MHz, $CDCl_3$):

δ [ppm] = 8.46 (s, 1H, H-9) 8.07 (AA', 2H, H-3), 7.54 (s, 1H, H-7), 7.51–7.46 (m', 3H, H-4/6) 7.17 (d, $^{3}J_{H\text{-}H}$ = 8.3 Hz, 1H, H-5), 6.05–6.00 (m, 1H, H-2), 3.58–3.44 (m, 4H, H-1), 2.26 (s, 3H, H-8), 1.50 (s, 9H, H-10)

^{13}C-NMR (100.6 MHz, $CDCl_3$):

δ [ppm] = 207.3 (C_q), 164.8 (C_q), 152.9 (C_q), 147.2 (C_q), 138.2 (C_q), 136.2 (C_q), 135.5 (C_q), 130.3 (CH), 129.67 (CH), 129.60 (CH), 127.5 (C_q), 120.4 (CH), 116.2 (CH), 80.8 (C_q), 74.5 (CH), 28.5 (CH_3), 27.2 (CH_2), 20.7 (CH_3).

[FeFe]-Spacer-Cat 5

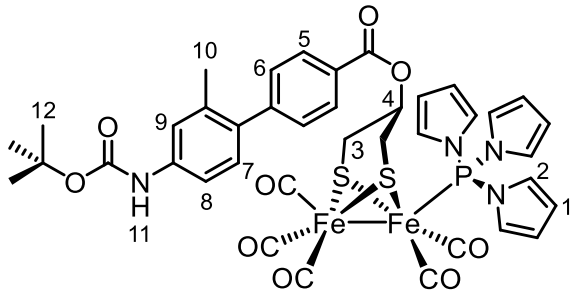

CAS: [/].

Synthesis based on given literature.[135]

Under nitrogen atmosphere **[FeFe]-Spacer-Cat 4** (280 mg, 394 mmol) and trimethylamine *N*-oxide (35.0 mg, 466 µmol) were dissolved in degassed acetonitrile (20 ml) and was stirred at r.t. for 5 min. Then, a solution of **tris(1*H*-pyrrol-1-yl)phosphine** (108 mg, 471 mmol) in degassed acetonitrile (10 ml) was added and the reaction mixture was stirred at r.t. for 21 h. After that, the solvent was removed under reduced pressure and finally the resulting residue was purified by flash column chromatography (silica gel, petroleum ether/DCM/acetone = 14:5:1). The product was dried in high vacuum. Due to its light sensitivity the complex was stored in the dark.

Yield: 283 mg (310 µmol, 79 %), red orange solid.

Formula: $C_{39}H_{37}Fe_2N_4O_9PS_2$ [912.53].

^{1}H-NMR (400.1 MHz, $CDCl_3$):

δ [ppm] = 8.45 (s, 1H, H-11), 7.89 (AA', 2H, H-5), 7.52–7.45 (m', 2H, H-8/9), 7.41 (BB', 2H, H-6), 7.13 (d, $^{3}J_{H\text{-}H}$ = 8.3 Hz, 1H, H-7), 7.00–6.98 (m, 6H, H-2), 6.49–6.45 (m, 6H, H-1), 3.80–3.72 (m, 1H, H-4), 2.88–2.80 (m, 4H, H-3), 2.22 (s, 3H, H-10), 1.49 (s, 9H, H-12).

^{13}C-NMR (100.6 MHz, acetone-d_6):

δ [ppm] = 212.2 (C_q), 212.1 (C_q), 164.6 (C_q), 153.7 (C_q), 147.8 (C_q), 140.4 (C_q), 136.3 (C_q), 135.4 (C_q), 130.2 (CH), 128.6 (C_q), 124.5 (CH), 123.9 (CH), 120.8 (CH), 116.7 (CH), 115.3 (CH), 114.7 (CH), 80.0 (C_q), 74.7 (CH), 28.5 (CH_3), 27.6 (CH_2), 20.8 (CH_3).

ESI-MS (high resolution):

calc.: $[2M+Na]^+$ 1847.0781 m/z.

exp.: $[2M+Na]^+$ 1847.0746 m/z Δ = 1.89 ppm.

[FeFe]-Spacer-Cat 6

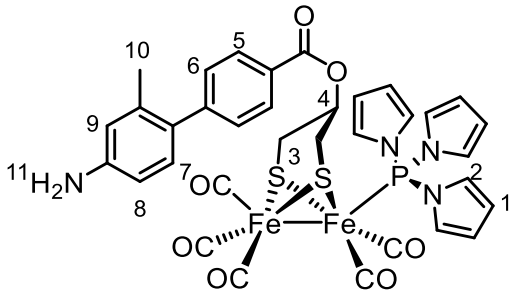

CAS: [/].

Synthesis based on given literature.[135]

Under nitrogen atmosphere **[FeFe]-Spacer-Cat 5** (218 mg, 239 µmol) was dissolved in dry DCM (25 ml) and trifluoroacetic acid (387 µl, 5.05 mmol) was added at r.t. The reaction mixture was stirred at that temperature for 24 h. Then, the solvent was removed under reduced pressure and finally the resulting residue was purified by column chromatography (silica gel, petroleum ether/ethyl acetate = 3:1). Due to its light sensitivity the complex was stored in the dark.

Yield: 125 mg (154 µmol, 64 %), red orange solid.

Formula: $C_{34}H_{29}Fe_2N_4O_7PS_2$ [812.41].

^{1}H-NMR (400.1 MHz, $CDCl_3$):[*]

δ [ppm] = 7.83 (AA', 2H, H-5), 7.36 (BB', 2H, H-6), 7.00–6.97 (m, 6H, H-2), 6.94–6.86 (m', 3H, H-7/8/9), 6.49–6.47 (m, 6H, H-1), 4.72–4.70 (m, 1H, H-4), 2.86–2.85 (m, 4H, H-3), 2.15 (s, 3H, H-10).

^{13}C-NMR (100.6 MHz, CD_2Cl_2):

δ [ppm] = 211.4 (C_q), 211.3 (C_q), 164.4 (C_q), 152.9 (C_q), 138.7 (C_q), 136.4 (C_q), 135.6 (C_q), 130.5 (CH), 128.0 (C_q), 124.0 (CH), 123.3 (CH), 120.4 (CH), 116.2 (CH), 114.8 (CH), 114.1 (CH), 74.2 (CH), 27.4 (CH_2), 20.7 (CH_3).

7.2.2 Synthesis of Photosensitisers

$[Ir(ppy)_2Cl]_2$

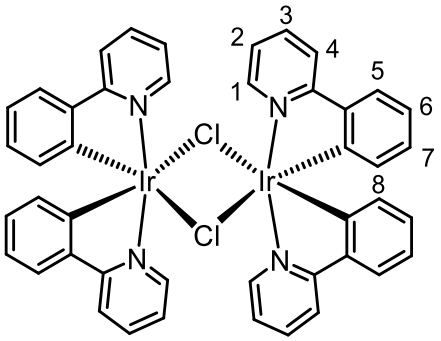

CAS: [92220-65-0].

Synthesis based on given literature.[121]

Under nitrogen atmosphere a mixture of iridium(III) chloride (299 mg, 1.00 mmol) and 2-phenylpyridine (357 ml, 2.50 mmol) in 2-ethoxyethanol (30 ml) and water (10 ml) was stirred at 150 °C for 20 h. After cooling down to r.t., the crude product was filtered and washed with diethyl ether (3 × 50 ml) and water (3 × 50 ml). The product was dried in high vacuum.

Yield: 394 mg (368 µmol, 74 %), yellow solid.

Formula: $C_{44}H_{32}Cl_2Ir_2N_4$ [1072.09].

[*] The signal for the amine protons could not be detected with $CDCl_3$ as solvent.

^{1}H-NMR (400.1 MHz, CD_2Cl_2):*

δ [ppm] = 9.25 (ddd, $^3J_{H\text{-}H}$ = 5.7 Hz, $^4J_{H\text{-}H}$ = 1.4 Hz, $^5J_{H\text{-}H}$ = 0.6 Hz, 4H), 7.94 (m, 4H), 7.80 (m, 4H), 7.56 (dd, $^3J_{H\text{-}H}$ = 7.8 Hz, $^4J_{H\text{-}H}$ = 1.3 Hz, 4H), 6.85–6.79 (m', 8H), 6.60 (m, 4H), 5.87 (ddd, $^3J_{H\text{-}H}$ = 7.8 Hz, $^4J_{H\text{-}H}$ = 1.2 Hz, $^5J_{H\text{-}H}$ = 0.3 Hz, 4H).

$[Ir(ppy)_2bpy]PF_6$

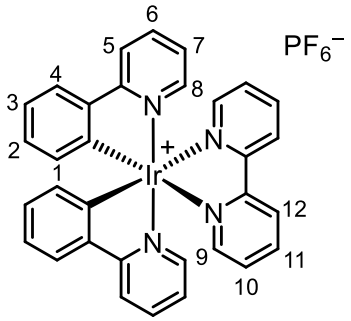

CAS: [106294-60-4].

Synthesis based on given literature.[120]

Under nitrogen atmosphere **$[Ir(ppy)_2Cl]_2$** (370 mg, 345 µmol) and 2,2'-bipyridine (119 mg, 762 µmol) in a mixture of DCM and MeOH (30 ml, *v*/*v* = 1:1) were stirred at 60 °C for 15 h. After cooling down to r.t., the reaction mixture was filtered to remove unreacted cyclometalated dimer. After that, a solution of ammonium hexafluorophosphate (563 mg, 3.45 mmol) in water (30 ml) was added to the filtrate and then the filtrate was concentrated under reduced pressure until precipitation of the crude product occurred. After filtration of the precipitate the solid was washed with water (2 × 50 ml) and diethyl ether (2 × 50 ml). The crude product was recrystallised from an acetonitrile-diethyl ether mixture.

Yield: 264 mg (329 µmol, 48 %), yellow solid.

Formula: $C_{32}H_{24}F_6IrN_4P$ [801.74].

^{1}H-NMR (400.1 MHz, CD_2Cl_2):

δ [ppm] = 8.49 (d, $^3J_{H\text{-}H}$ = 8.3 Hz, 2H, H-12), 8.13 (m, 2H, H-11), 8.03 (d, $^3J_{H\text{-}H}$ = 5.4 Hz, 2H, H-8), 7.96 (d, $^3J_{H\text{-}H}$ = 8.3 Hz, 2H, H-4), 7.79 (m, 2H, H-7), 7.74

* An exact proton assignment could not be made based only on the measured ^{1}H-NMR experiment.

(d, $^3J_{H\text{-}H}$ = 7.7 Hz, 2H, H-9), 7.50–7.45 (m', 4H, H-5/10), 7.08 (m, 2H, H-3), 7.00 (m, 2H, H-6), 6.94 (m, 2H, H-2), 6.31 (d, $^3J_{H\text{-}H}$ = 7.6 Hz, 2H, H-1).

4-(Methoxycarbonyl)pyridine 1-oxide

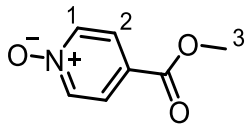

CAS: [3783-38-8].

Synthesis according to given literature.[105]

Under nitrogen atmosphere methyl isonicotinate (5.80 g, 42.3 mmol) and *meta*-chloroperoxybenzoic acid (14.6 g, 84.6 mmol) were dissolved in dry DCM (150 ml) and stirred at r.t. for 72 h. The solvent was removed under reduced pressure and the obtained crude product was purified by column chromatography (silica, ethyl acetate/MeOH = 96:4).

Yield: 6.32 g (41.3 mmol, 98 %), colourless solid.

Formula: $C_7H_7NO_3$ [153.14].

^{1}H-NMR (400.1 MHz, $CDCl_3$):

δ [ppm] = 8.22 (AA', 2H, H-1), 7.88 (BB', 2H, H-2), 3.94 (s, 3H, H-3).

4-(Methoxycarbonyl)-(2,2'-bipyridine) 1-oxide

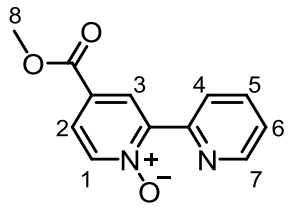

CAS: [1355019-38-3].

Synthesis according to given literature.[141]

Under nitrogen atmosphere **4-(methoxycarbonyl)pyridine 1-oxide** (6.00 g, 39.2 mmol), $Pd(OAc)_2$ (110 mg, 490 µmol), $[P(t\text{-}Bu)_3H]BF_4$] (426 mg, 1.47 µmol) and K_2CO_3 (2.71 g, 19.6 mmol) were charged in a flask. Then, a degassed solution of 2-bromopyridine (1.55 g, 9.81 mmol) in dry toluene (30 ml) was added *via* a syringe and the reaction mixture was stirred

at 110 °C for 24 h. After cooling down to r.t., the reaction mixture was filtered through a pad of celite and the solvent was removed under reduced pressure. The obtained crude product was purified by column chromatography (silica, ethyl acetate/MeOH = 96:4).

Yield: 1.79 g (7.78 mmol, 79 %), colourless solid.

Formula: $C_{12}H_{10}N_2O_3$ [230.22].

^{1}H-NMR (400.1 MHz, $CDCl_3$):

δ [ppm] = 8.82 (m, 1H, H-5), 8.80 (dd, $^4J_{H\text{-}H}$ = 2.6 Hz, $^5J_{H\text{-}H}$ = 0.4 Hz, 1H, H-3), 8.77 (ddd, $^3J_{H\text{-}H}$ = 4.8 Hz, $^4J_{H\text{-}H}$ = 1.8 Hz, $^5J_{H\text{-}H}$ = 0.9 Hz, 1H, H-7), 8.32 (dd, $^3J_{H\text{-}H}$ = 6.8 Hz, $^5J_{H\text{-}H}$ = 0.5 Hz, 1H, H-1), 7.88–7.83 (m', 2H, H-2/6), 7.39 (ddd, $^3J_{H\text{-}H}$ = 7.6 Hz, $^4J_{H\text{-}H}$ = 4.8 Hz, $^5J_{H\text{-}H}$ = 1.2 Hz, 1H, H-4), 3.96 (s, 3H, H-8).

Methyl (2,2'-bipyridine)-4-carboxylate

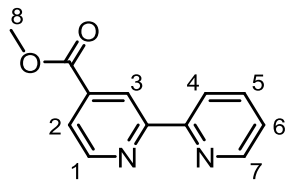

CAS: [98820-73-6].

Synthesis according to given literature.[141]

Under nitrogen atmosphere **4-(methoxycarbonyl)-(2,2'-bipyridine) 1-oxide** (1.50 g, 6.52 mmol) was dissolved in dry chloroform (15 ml) and PCl_3 (1.07 g, 7.79 mmol) was added. The reaction mixture was stirred at 60 °C for 17 h. After that, the reaction was quenched by dropwise addition of sat. aqueous Na_2CO_3 solution (20 ml) at 0 °C until neutralisation occurred. The product was extracted with DCM (5 × 15 ml). The combined organic phases were dried over Na_2SO_4 and the solvent was removed under reduced pressure. The obtained crude product was purified by column chromatography (silica, acetone/petroleum ether = 3:7).

Yield: 1.18 g (5.51 mmol, 85 %), colourless solid.

Formula: $C_{12}H_{10}N_2O_2$ [214.22].

^{1}H-NMR (400.1 MHz, $CDCl_3$):

δ [ppm] = 8.95 (m, 1H, H-3), 8.83 (dd, $^3J_{H\text{-}H}$ = 5.0 Hz, $^5J_{H\text{-}H}$ = 0.8 Hz, 1H, H-1), 8.73 (ddd, $^3J_{H\text{-}H}$ = 4.7 Hz, $^4J_{H\text{-}H}$ = 1.6 Hz, $^5J_{H\text{-}H}$ = 0.9 Hz, 1H, H-7), 8.43 (m, 1H, H-2), 7.88–7.83 (m', 2H, H-5/6), 7.36 (ddd, $^3J_{H\text{-}H}$ = 7.4 Hz, $^4J_{H\text{-}H}$ = 4.9 Hz, $^5J_{H\text{-}H}$ = 1.0 Hz, 1H, H-4), 3.99 (s, 3H, H-8).

(2,2'-Bipyridine)-4-carboxylic acid

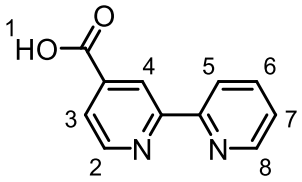

CAS: [1748-89-6].

Synthesis according to given literature.[141]

Under nitrogen atmosphere **methyl (2,2'-bipyridine)-4-carboxylate** (620 mg, 2.89 mmol) and KOH (585 mg, 10.4 mmol) were dissolved in MeOH (20 ml) and stirred at 60 °C for 17 h. After cooling down to r.t., the solvent was removed under reduced pressure. The crude product was dissolved in water (15 ml) and the aqueous layer was washed with ethyl acetate (10 ml). The product was precipitated by adjusting the pH to 3–4 with hydrochloric acid (1 M) while cooling to 4 °C. The product was filtered and washed with water and dried in high vacuum.

Yield: 540 mg (2.70 mmol, 93 %), colourless solid.

Formula: $C_{11}H_8N_2O_2$ [200.19].

^{1}H-NMR (400.1 MHz, $CDCl_3$):[*]

δ [ppm] = 8.86 (dd, $^3J_{H\text{-}H}$ = 5.0 Hz, $^5J_{H\text{-}H}$ = 0.7 Hz, 1H, H-2), 8.83 (dd, $^4J_{H\text{-}H}$ = 1.6 Hz, $^5J_{H\text{-}H}$ = 0.9 Hz, 1H, H-4), 8.73 (ddd, $^3J_{H\text{-}H}$ = 4.8 Hz, $^4J_{H\text{-}H}$ = 1.8 Hz, $^5J_{H\text{-}H}$ = 0.9 Hz, 1H, H-8), 8.42 (m, 1H, H-6) 7.98 (m, 1H, H-7), 7.86 (dd, $^3J_{H\text{-}H}$ = 4.9 Hz, $^4J_{H\text{-}H}$ = 1.6 Hz, 1H, H-3), 7.50 (ddd, $^3J_{H\text{-}H}$ = 7.5 Hz, $^4J_{H\text{-}H}$ = 4.8 Hz, $^5J_{H\text{-}H}$ = 1.2 Hz, 1H, H-5).

[*] The signal for the carboxylic acid proton could not be detected with $CDCl_3$ as solvent.

$[Ru(bpy)_2bpy\text{-}COOH](PF_6)_2$

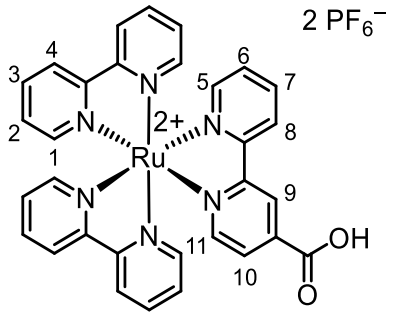

CAS: [218600-82-9].

Synthesis based on given literature.[106]

Under nitrogen atmosphere $[Ru(bpy)_2]Cl_2$ (660 mg, 1.36 mmol) and silver nitrate (463 mg, 2.73 mmol) were dissolved in dry MeOH (30 ml) and stirred at r.t. for 3 h. After filtration of the suspension, **(2,2'-bipyridine)-4-carboxylic acid** (300 mg, 1.50 mmol) was added to the filtrate and the reaction mixture was heated to 90 °C in the dark overnight. After cooling down to r.t., the solvents were removed under reduced pressure and the obtained residue was dissolved in a small amount of MeOH (3 ml). To the mixture a solution of ammonium hexafluorophosphate (888 mg, 5.45 mmol) in water (30 ml) was added dropwise. The formed precipitate was filtered, washed with water (4 ml) and diethyl ether (4 ml). The crude product was dried in vacuum and finally purified by column chromatography (alumina deactivated by 7 % (*w*/*w*) water, acetone/water = 8:2).

Yield: 896 mg (992 µmol, 73 %), red orange solid.

Formula: $C_{31}H_{24}F_{12}N_6O_2P_2Ru$ [903.56].

^{1}H-NMR (400.1 MHz, acetone-d_6):*

δ [ppm] = 8.99 (s, 1H), 8.94 (d, $^3J_{H\text{-}H}$ = 8.1 Hz, 1H), 8.86–8.82 (m', 4H), 8.23–8.16 (m', 5H), 8.09–8.00 (m', 5H), 7.84 (d, $^5J_{H\text{-}H}$ = 1.0 Hz, 2H), 7.63–7.51 (m', 5H).

* An exact proton assignment could not be made based only on the measured ^{1}H-NMR experiment.

[Ir(ppy)$_2$bpy-COOH]PF$_6$

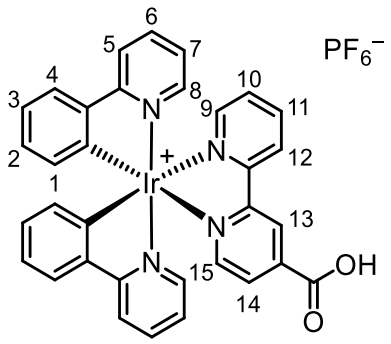

CAS: [/].

Synthesis based on given literature.[142]

Under nitrogen atmosphere **[Ir(ppy)$_2$Cl]$_2$** (370 mg, 345 µmol) and **(2,2'-bipyridine)-4-carboxylic acid** (152 mg, 759 µmol) in a mixture of DCM and MeOH (20 ml, *v*/*v* = 1:1) were stirred at 60 °C for 15 h. After cooling down to r.t., the reaction mixture was filtered to remove unreacted cyclometalated dimer. Then, a solution of ammonium hexafluorophosphate (563 mg, 3.45 mmol) in water (30 ml) was added to the filtrate and the mixture was stirred at r.t. for 30 min. Afterwards, the solvent volume was reduced to a third of the original volume under reduced pressure, so that the crude product was able to precipitate. After filtration of the precipitate the solid was washed with water (2 × 5 ml) and diethyl ether (2 × 5 ml). The crude product was dissolved in DCM and then the solvent was removed under reduced pressure.

Yield: 538 mg (636 µmol, 92 %), orange solid.

Formula: $C_{33}H_{24}F_6IrN_4O_2P$ [845.75].

^{1}H-NMR (400.1 MHz, $CDCl_3$):[*]

δ [ppm] = 9.00 (s, 1H, H-13), 8.58 (d, $^3J_{H\text{-}H}$ = 8.3 Hz, 1H, H-12), 8.15 (dd, $^3J_{H\text{-}H}$ = 5.6 Hz, $^5J_{H\text{-}H}$ = 0.7 Hz, 1H, H-15), 8.14 (m, 1H, H-11), 8.05 (ddd, $^3J_{H\text{-}H}$ = 5.4 Hz, $^4J_{H\text{-}H}$ = 1.5 Hz, $^5J_{H\text{-}H}$ = 0.7 Hz, 1H, H-9), 8.00 (dd, $^3J_{H\text{-}H}$ = 5.6 Hz, $^4J_{H\text{-}H}$ = 1.6 Hz, 1H, H-14), 7.97 (d, $^3J_{H\text{-}H}$ =8.4 Hz, 2H, H-8), 7.79 (m, 2H, H-7), 7.75 (d, $^3J_{H\text{-}H}$ = 8.0 Hz, 2H, H-4), 7.52–7.46 (m', 3H, H-5/10), 7.09 (m, 2H, H-3), 7.01–6.94 (m', 4H, H-2/6), 6.31 (dd, $^3J_{H\text{-}H}$ = 7.6 Hz, $^4J_{H\text{-}H}$ = 1.2 Hz, 2H, H-1).

[*] The signal for the carboxylic acid proton could not be detected with $CDCl_3$ as solvent.

^{13}C-NMR (100.6 MHz, $CDCl_3$):

δ [ppm] = 168.0 (C_q), 156.7 (C_q), 155.8 (C_q), 151.7 (CH), 151.2 (CH), 150.2 (C_q), 150.0 (C_q), 148.9 (CH), 144.04 (C_q), 143.97 (C_q), 139.8 (CH), 138.7 (CH), 132.0 (CH), 131.1 (CH), 128.9 (CH), 128.4 (CH), 125.3 (CH), 125.1 (CH), 124.5 (CH), 123.8 (CH), 123.2 (CH), 120.3 (CH).

ESI-MS (high resolution):

calc.: $[M–PF_6]^+$ 701.15246 m/z.

exp.: $[M–PF_6]^+$ 701.15235 m/z Δ = 0.16 ppm.

7.2.3 Synthesis of Photocatalytic Dyads

D1

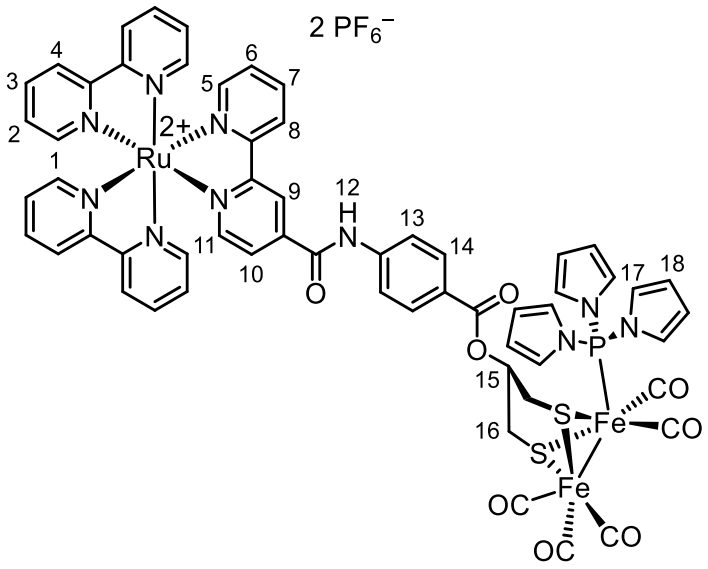

CAS: [/].

Synthesis based on given literature.[56]

Under nitrogen atmosphere **[Ru(bpy)$_2$bpy-COOH](PF$_6$)$_2$** (206 mg, 228 mmol) was dissolved in thionyl chloride (10 ml) and the reaction mixture was stirred at 100 °C for 3 h. After cooling down to r.t., the solvent was removed under reduced pressure. Then, the obtained residue was dissolved in dry acetonitrile (10 ml) and a solution of **[FeFe]-Spacer-Cat 3** (150 mg, 208 mmol) and dry triethylamine (360 µl, 2.58 mmol) in dry acetonitrile (20 ml) was added dropwise under stirring. The reaction mixture was stirred at r.t. for 20 h. After that, the solvent was removed under reduced pressure and the resulting residue was purified by column

chromatography (silica gel, acetonitrile/water/sat. $KNO_{3(aq)}$ = 90:5:5). After removing the solvent under reduced pressure, the crude product was redissolved in a small amount of acetone (3 ml) und precipitated by addition of ammonium hexafluorophosphate (151 mg, 926 µmol) in water (10 ml). After filtration, the product was dried under high vacuum. Due to its light sensitivity the complex was stored in the dark.

Yield: 167 mg (104 µmol, 50 %), red solid.

Formula: $C_{58}H_{45}F_{12}Fe_2N_{10}O_8P_3RuS_2$ [1607.83].

^{1}H-NMR (400.1 MHz, acetone-d_6):[*]

δ [ppm] = 10.4 (bs, 1H, H-12), 9.28 (s, 1H, H-9), 9.02 (d, $^3J_{H\text{-}H}$ = 9.28 Hz, 1H), 8.83–8.88 (m, 4H), 8.21–8.30 (m', 6H), 8.07–8.14 (m', 5H), 7.84–8.01 (m', 5H), 7.57–7.66 (m', 5H, H-2), 6.95–6.99 (m, 6H, H-17), 6.45–6.48 (m, 6H, H-18), 3.67–3.79 (m, 1H, H-15), 2.72–2.82 (m, 2H, H-16), 1.51–1.64 (m, 2H, H-16).

^{13}C-NMR (100.6 MHz, CD_2Cl_2):

δ [ppm] = 211.4 (C_q), 211.3 (C_q), 163.9 (C_q), 163.4 (C_q), 157.9 (C_q), 157.2 (C_q), 156.9 (C_q), 156.8 (C_q), 152.3 (CH), 152.1 (CH), 151.7 (CH), 151.5 (CH), 144.4 (C_q), 142.7 (C_q), 138.7 (CH), 138.6 (CH), 131.0 (CH), 128.9 (CH), 128.7 (CH), 128.6 (CH), 128.4 (CH), 126.1 (CH), 125.9 (C_q), 125.3 (CH), 124.7 (CH), 124.5 (CH), 124.0 (CH), 122.5 (CH), 120.0 (CH), 114.1 (CH), 74.2 (CH), 27.4 (CH_2).

ESI-MS (high resolution):

calc.: $[M–PF_6]^+$ 1462.9998 m/z.

exp.: $[M–PF_6]^+$ 1462.9997 m/z Δ = 0.07 ppm.

[*] Due to strong signal splitting and signal overlap, proton assignment was partially dispensed with. The rotatability of the photosensitiser-spacer residue around the C-O bond next to proton 15 is probably hampered due to steric hindrance. This leads to the abolition of the chemical equivalence and splitting of the signal of the H-16 protons.

D2

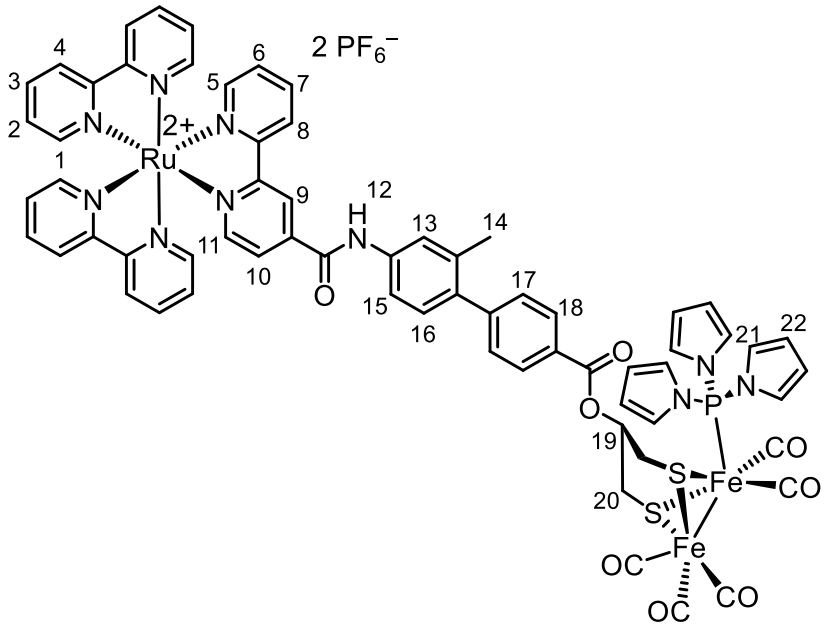

CAS: [/].

Synthesis based on given literature.[56]

Under nitrogen atmosphere **[Ru(bpy)$_2$bpy-COOH](PF$_6$)$_2$** (122 mg, 135 µmol) was dissolved in thionyl chloride (5 ml) and the reaction mixture was heated at 100 °C under stirring for 3 h. After cooling down to r.t. the solvent was removed under reduced pressure. Then, the obtained residue was dissolved in dry acetonitrile (10 ml) and a solution of **[FeFe]-Spacer-Cat 6** (100 mg, 123 µmol) and dry triethylamine (213 µl, 1.53 mmol) in dry acetonitrile (20 ml) was added dropwise under stirring. The reaction mixture was stirred at r.t. for 20 h. After that, the solvent was removed under reduced pressure and the resulting residue was purified by column chromatography (silica gel, acetonitrile/water/sat. $KNO_{3(aq)}$ = 90:5:5). After removing the solvent under reduced pressure the crude product was redissolved in a small amount of acetone (3 ml) und precipitated by addition of ammonium hexafluorophosphate (151 mg, 926 µmol) in water (10 ml). After filtration the product was dried under high vacuum. Due to its light sensitivity the complex was stored in the dark.

Yield: 88.1 mg (51.9 µmol, 42 %), red solid.

Formula: $C_{65}H_{51}F_{12}Fe_2N_{10}O_8P_3RuS_2$ [1697.96].

^{1}H-NMR (400.1 MHz, acetone-d_6):*

δ [ppm] = 11.01 (s, 1H), 9.45 (s, 1H), 9.12 (d, $^{3}J_{H\text{-}H}$ = 7.9 Hz, 1H), 8.87–8.83 (-, 5H), 8.26–8.15 (m', 5H), 8.09–8.07 (m', 5H), 8.00–7.99 (m', 1H), 7.92–7.90 (m', 4H), 7.62–7.59 (m', 5H), 7.47–7.45 (m', 2H), 7.22 (d, $^{3}J_{H\text{-}H}$ = 8.2 Hz, 1H), 7.00–6.98 (m, 6H), 6.49–6.48 (m, 6H), 3.79–3.76 (m, 1H), 3.32–3.26 (m, 4H), 2.27 (s, 3H).

^{13}C-NMR (100.6 MHz, acetone-d_6):

δ [ppm] = 211.4 (C_q), 211.3 (C_q), 164.4 (C_q), 163.0 (C_q), 157.9 (C_q), 157.2 (C_q), 157.0 (C_q), 156.8 (C_q), 152.3 (CH), 152.0 (CH), 151.7 (CH), 151.6 (CH), 151.5 (CH), 146.9 (C_q), 144.7 (C_q), 138.6 (CH), 137.9 (C_q), 137.8 (C_q), 136.5 (C_q), 130.4 (CH), 129.8 (CH), 129.7 (CH), 128.8 (CH), 128.6 (CH), 128.5 (CH), 128.4 (CH), 128.2 (C_q), 126.2 (CH), 125.4 (CH), 124.7 (CH), 124.5 (CH), 124.0 (CH), 122.6 (CH), 118.5 (CH), 114.1 (CH), 74.2 (CH), 27.4 (CH_2), 20.8 (CH), 8.9 (CH_3).

ESI-MS (high resolution):

calc.: $[M–2PF_6]^{2+}$ 704.04114 m/z.

exp.: $[M–2PF_6]^{2+}$ 704.04014 m/z Δ = 1.42 ppm.

* An exact proton assignment could not be made based only on the measured ^{1}H-NMR experiment.

D3

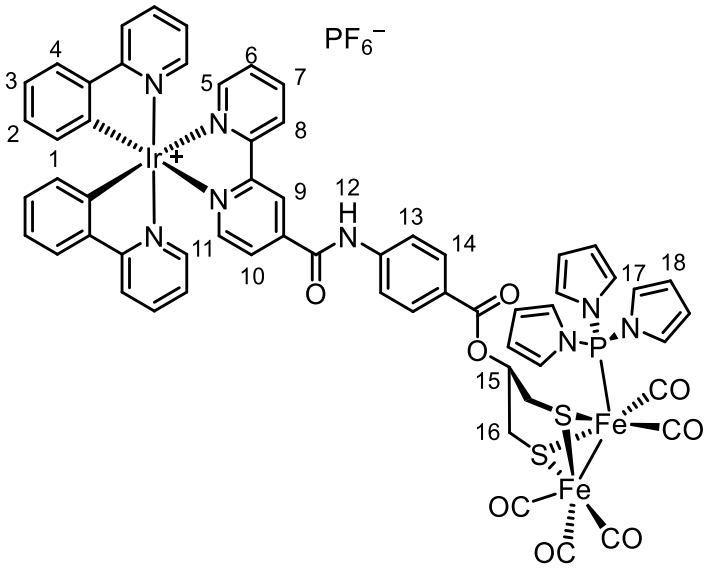

CAS: [/].

Synthesis based on given literature.[56]

Under nitrogen atmosphere **[Ir(ppy)$_2$bpy-COOH]PF$_6$** (193 mg, 228 mmol) was dissolved in thionyl chloride (10 ml) and the reaction mixture was stirred at 100 °C for 3 h. After cooling down to r.t., the solvent was removed under reduced pressure. Then, the obtained residue was dissolved in dry acetonitrile (10 ml) and a solution of **[FeFe]-Spacer-Cat 3** (150 mg, 208 mmol) and dry triethylamine (360 µl, 2.58 mmol) in dry acetonitrile (20 ml) was added dropwise under stirring. The reaction mixture was stirred at r.t. for 20 h. The solvent was removed under reduced pressure and the resulting residue was purified by column chromatography (silica gel, acetonitrile/water/sat. $KNO_{3(aq)}$ = 90:5:5). After removing the solvent under reduced pressure, the crude product was redissolved in a small amount of acetone (3 ml) und precipitated by addition of ammonium hexafluorophosphate (135 mg, 828 µmol) in water (10 ml). After filtration, the product was dried under high vacuum. Due to its light sensitivity the complex was stored in the dark.

Yield: 215 mg (139 µmol, 67 %), red solid.

Formula: $C_{60}H_{45}F_6Fe_2IrN_8O_8P_2S_2$ [1550.03].

^{1}H-NMR (400.1 MHz, CD_2Cl_2):*

δ [ppm] = 9.31–9.14 (m, 1H), 8.96–8.81 (m, 1H), 8.25–8.10 (m', 2H), 8.08–7.66 (m', 13H), 7.64–7.29 (m', 3H), 7.20–6.97 (m', 4H), 6.97–6.90 (m', 6H), 6.90–

* An exact proton assignment could not be made based only on the measured ^{1}H-NMR experiment.

6.74 (m', 2H), 6.46–6.39 (m', 6H), 6.38–6.36 (m, 1H), 6.30–6.09 (m, 1H), 3.64–3.52 (m, 1H), 2.76–2.69 (m, 1H), 2.33–2.15 (m, 1H), 1.75–1.65 (m, 2H).

^{13}C-NMR (100.6 MHz, CD_2Cl_2):

δ [ppm] = 211.4 (C_q), 211.3 (C_q), 164.3 (C_q), 163.9 (C_q), 151.8 (C_q), 142.6 (C_q), 139.8 (CH), 138.9 (CH), 138.83 (CH), 138.80 (CH), 138.7 (CH), 133.3 (C_q), 131.9 (CH), 131.0 (CH), 124.0 (CH), 120.42 (CH), 120.40 (CH), 120.17 (CH), 120.16 (CH), 118.8 (C_q), 114.9 (C_q), 114.8 (C_q), 114.7 (C_q), 114.6 (C_q), 114.1 (CH), 114.03 (CH), 113.96 (CH), 113.8 (CH), 113.4 (CH), 113.3 (CH), 74.2 (CH), 73.5 (CH), 27.5 (CH_2).

ESI-MS (high resolution):

calc.: $[M–PF_6]^+$ 1405.08667 m/z.

exp.: $[M–PF_6]^+$ 1405.08996 m/z Δ = 2.34 ppm.

8 REFERENCES

[1] C. J. Winter, J. Nitsch, *Wasserstoff als Energieträger: Technik, Systeme, Wirtschaft*, Springer, Berlin, **2013**.
[2] R. Victor, *Int. J. Hydrocarbon Eng.* **1999**, *4*, 82–83.
[3] S. Berardi, S. Drouet, L. Francàs, C. Gimbert-Suriñach, M. Guttentag, C. Richmond, T. Stoll, A. Llobet, *Chem. Soc. Rev.* **2014**, *43*, 7501–7519.
[4] M. Frey, *ChemBioChem* **2002**, *3*, 153–160.
[5] H. Junge, N. Rockstroh, S. Fischer, A. Brückner, R. Ludwig, S. Lochbrunner, O. Kühn, M. Beller, *Inorganics* **2017**, *5*, 14/1–14/21.
[6] H.-h. Cui, M.-q. Hu, H.-m. Wen, G.-l. Chai, C.-b. Ma, H. Chen, C.-n. Chen, *Dalton Trans.* **2012**, *41*, 13899–13907.
[7] K. Kalyanasundaram, J. Kiwi, M. Grätzel, *Helv. Chim. Acta* **1978**, *61*, 2720–2730.
[8] L. L. Tinker, N. D. McDaniel, S. Bernhard, *J. Mater. Chem.* **2009**, *19*, 3328–3337.
[9] M. Wang, L. Chen, X. Lia, L. Sun, *Dalton Trans.* **2011**, *40*, 12793–12800.
[10] L. Li, L. Duan, Y. Xu, M. Gorlov, A. Hagfeldt, L. Sun, *Chem. Commun.* **2010**, *46*, 7307–7309.
[11] L. Li, L. Duan, F. Wen, C. Li, M. Wang, A. Hagfeldt, L. Sun, *Chem. Commun.* **2012**, *48*, 988–990.
[12] Y. Gao, X. Ding, J. Liu, L. Wang, Z. Lu, L. Li, L. Sun, *J. Am. Chem. Soc.* **2013**, *135*, 4219–4222.
[13] Z. Ji, M. He, Z. Huang, U. Ozkan, Y. Wu, *J. Am. Chem. Soc.* **2013**, *135*, 11696–11699.
[14] Y. Pellegrin, F. Odobel, *C. R. Chim.* **2017**, *20*, 283–295.
[15] Y. Na, M. Wang, J. Pan, P. Zhang, B. Åkermark, L. Sun, *Inorg. Chem.* **2008**, *47*, 2805–2810.
[16] K. Kalyanasundaram, *Coord. Chem. Rev.* **1982**, *46*, 159–244.
[17] Y. Ohsawa, S. Sprouse, K. A. King, M. K. DeArmond, K. W. Hanck, R. J. Watts, *J. Phys. Chem.* **1987**, *91*, 1047–1054.
[18] M. Kirch, J. M. Lehn, J. P. Sauvage, *Helv. Chim. Acta* **1979**, *62*, 1345–1384.
[19] C. Costa-Coquelard, J. Hao, S. Jiang, C. He, L. Sun, L. Ruhlmann, I. Lampre, *Can. J. Chem.* **2008**, *86*, 1034–1043.
[20] S.-H. Wu, J.-W. Ling, S.-H. Lai, M.-J. Huang, C. H. Cheng, I. C. Chen, *J. Phys. Chem. A* **2010**, *114*, 10339–10344.
[21] A. D. Kirk, G. B. Portner, *J. Phys. Chem.* **1980**, *84*, 2998–2999.
[22] C. V. Krishnan, N. Sutin, *J. Am. Chem. Soc.* **1981**, *103*, 2141–2142.
[23] A. Juris, V. Balzani, F. Barigelletti, S. Campagna, P. Belser, A. v. Zelewsky, *Coord. Chem. Rev.* **1988**, *84*, 85–277.
[24] J. I. Goldsmith, W. R. Hudson, M. S. Lowry, T. H. Anderson, S. Bernhard, *J. Am. Chem. Soc.* **2005**, *127*, 7502–7510.
[25] L. L. Tinker, N. D. McDaniel, P. N. Curtin, C. K. Smith, M. J. Ireland, S. Bernhard, *Chem. - Eur. J.* **2007**, *13*, 8726–8732.
[26] S.-y. Takizawa, R. Aboshi, S. Murata, *Photochem. Photobiol. Sci.* **2011**, *10*, 895–903.
[27] E. D. Cline, S. E. Adamson, S. Bernhard, *Inorg. Chem.* **2008**, *47*, 10378–10388.
[28] P. N. Curtin, L. L. Tinker, C. M. Burgess, E. D. Cline, S. Bernhard, *Inorg. Chem.* **2009**, *48*, 10498–10506.
[29] L. L. Tinker, S. Bernhard, *Inorg. Chem.* **2009**, *48*, 10507–10511.
[30] F. Gärtner, A. Boddien, E. Barsch, K. Fumino, S. Losse, H. Junge, D. Hollmann, A. Brückner, R. Ludwig, M. Beller, *Chem. - Eur. J.* **2011**, *17*, 6425–6436.
[31] C. Orain, F. Quentel, F. Gloaguen, *ChemSusChem* **2014**, *7*, 638–643.
[32] Y. Nicolet, C. Piras, P. Legrand, C. E. Hatchikian, J. C. Fontecilla-Camps, *Structure* **1999**, *7*, 13–23.
[33] J. D. Lawrence, H. Li, T. B. Rauchfuss, *Chem. Commun.* **2001**, 1482–1483.
[34] T. Yu, Y. Zeng, J. Chen, Y. Y. Li, G. Yang, Y. Li, *Angew. Chem. Int. Ed.* **2013**, *52*, 5631–5635.

[35] T. Yu, Y. Zeng, J. Chen, X. Zhang, G. Yang, Y. Li, *J. Mater. Chem. A* **2014**, *2*, 20500–20505.
[36] P. Surawatanawong, J. W. Tye, M. Y. Darensbourg, M. B. Hall, *Dalton Trans.* **2010**, *39*, 3093–3104.
[37] S. Ghosh, A. Rahaman, G. Orton, G. Gregori, M. Bernat, U. Kulsume, N. Hollingsworth, K. B. Holt, S. E. Kabir, G. Hogarth, *Eur. J. Inorg. Chem.* **2019**, 4506–4515.
[38] S. Wang, A. Aster, M. Mirmohades, R. Lomoth, L. Hammarström, *Inorg. Chem.* **2018**, *57*, 768–776.
[39] G. A. N. Felton, C. A. Mebi, B. J. Petro, A. K. Vannucci, D. H. Evans, R. S. Glass, D. L. Lichtenberger, *J. Organomet. Chem.* **2009**, *694*, 2681–2699.
[40] A. G. Orpen, N. G. Connelly, *Organometallics* **1990**, *9*, 1206–1210.
[41] R. H. Crabtree, *The Organometallic Chemistry of the Transition Metals*, John Wiley & Sons, New York, **2009**.
[42] N. A. Carmo dos Santos, M. Natali, E. Badetti, K. Wurst, G. Licini, C. Zonta, *Dalton Trans.* **2017**, *46*, 16455–16464.
[43] J. L. Dempsey, B. S. Brunschwig, J. R. Winkler, H. B. Gray, *Acc. Chem. Res.* **2009**, *42*, 1995–2004.
[44] Y.-K. Jiang, J.-H. Liu, *Int. J. Quantum Chem.* **2012**, *112*, 2541–2546.
[45] R. Gueret, L. Poulard, M. Oshinowo, J. Chauvin, M. Dahmane, G. Dupeyre, P. P. Lainé, J. Fortage, M.-N. Collomb, *ACS Catal.* **2018**, *8*, 3792–3802.
[46] S. Varma, C. E. Castillo, T. Stoll, J. Fortage, A. G. Blackman, F. Molton, A. Deronzier, M.-N. Collomb, *Phys. Chem. Chem. Phys.* **2013**, *15*, 17544–17552.
[47] D. H. Macartney, N. Sutin, *Inorg. Chim. Acta* **1983**, *74*, 221–228.
[48] F. Wang, W. G. Wang, X. J. Wang, H. Y. Wang, C. H. Tung, L. Z. Wu, *Angew. Chem. Int. Ed.* **2011**, *50*, 3193–3197.
[49] R. Ziessel, J. Hawecker, J. M. Lehn, *Helv. Chim. Acta* **1986**, *69*, 1065–1084.
[50] A. Fihri, V. Artero, M. Razavet, C. Baffert, W. Leibl, M. Fontecave, *Angew. Chem. Int. Ed.* **2008**, *47*, 564–567.
[51] W. Iali, P.-H. Lanoe, S. Torelli, D. Jouvenot, F. Loiseau, C. Lebrun, O. Hamelin, S. Ménage, *Angew. Chem. Int. Ed.* **2015**, *54*, 8415–8419.
[52] D. Streich, Y. Astuti, M. Orlandi, L. Schwartz, R. Lomoth, L. Hammarström, S. Ott, *Chem. - Eur. J.* **2010**, *16*, 60–63.
[53] P. Zhang, M. Wang, Y. Na, X. Li, Y. Jiang, L. Sun, *Dalton Trans.* **2010**, *39*, 1204–1206.
[54] U. P. Apfel, W. Weigand, *ChemBioChem* **2013**, *14*, 2237–2238.
[55] S. Salyi, M. Kritikos, B. Åkermark, L. Sun, *Chem. - Eur. J.* **2003**, *9*, 557–560.
[56] H. Wolpher, M. Borgström, L. Hammarström, J. Bergquist, V. Sundström, S. Styring, L. Sun, B. Åkermark, *Inorg. Chem. Commun.* **2003**, *6*, 989–991.
[57] Y. Amao, I. Okura, *J. Mol. Catal. B: Enzym.* **2002**, *17*, 9–21.
[58] S. Ott, M. Borgström, M. Kritikos, R. Lomoth, J. Bergquist, B. Åkermark, L. Hammerström, L. Sun, *Inorg. Chem.* **2004**, *43*, 4683–4692.
[59] J. Ekström, M. Abrahamsson, C. Olson, J. Bergquist, F. B. Kaynak, L. Eriksson, L. Sun, H. C. Becker, B. Åkermark, L. Hammarström, S. Ott, *Dalton Trans.* **2006**, 4599–4606.
[60] H. Cui, M. Wang, L. Duan, L. Sun, *J. Coord. Chem.* **2008**, *61*, 1856–1861.
[61] L.-C. Song, L.-X. Wang, C.-G. Li, F. Li, Z. Chen, *J. Organomet. Chem.* **2014**, *749*, 120–128.
[62] A. K. Mengele, S. Kaufhold, C. Streb, S. Rau, *Dalton Trans.* **2016**, *45*, 6612–6618.
[63] G.-G. Luo, K. Fang, J.-H. Wu, J. Mo, *Chem. Commun.* **2015**, *51*, 12361–12364.
[64] S. Schönweiz, S. A. Rommel, J. Kübel, M. Micheel, B. Dietzek, S. Rau, C. Streb, *Chem. - Eur. J.* **2016**, *22*, 12002–12005.
[65] Y. Luo, M. Wächtler, K. Barthelmes, A. Winter, U. S. Schubert, B. Dietzek, *Chem. Commun.* **2018**, *54*, 2970–2973.
[66] R. Goy, W. Weigand, L. Bertini, G. Zampella, L. de Gioia, T. Rudolph, F. H. Schacher, S. Lin, K. Sakai, M. Schulz, B. Dietzek, *Chem. - Eur. J.* **2017**, *23*, 334–345.
[67] C. Lentz, O. Schott, T. Auvray, G. S. Hanan, B. Elias, *Dalton Trans.* **2019**, *48*, 15567–15576.

[68] W. N. Cao, F. Wang, H. Y. Wang, B. Chen, K. Feng, C. H. Tung, L. Z. Wu, *Chem. Commun.* **2012**, *48*, 8081–8083.
[69] W. Wang, T. Yu, Y. Zeng, J. Chen, Y. Li, *Chin. J. Chem.* **2014**, *32*, 479–484.
[70] H. Y. Wang, W. G. Wang, G. Si, F. Wang, C. H. Tung, L. Z. Wu, *Langmuir* **2010**, *26*, 9766–9771.
[71] X. Li, M. Wang, D. Zheng, K. Han, J. Dong, L. Sun, *Energy Environ. Sci.* **2012**, *5*, 8220–8224.
[72] S. Pullen, H. Fei, A. Orthaber, S. M. Cohen, S. Ott, *J. Am. Chem. Soc.* **2013**, *135*, 16997–17003.
[73] R. Luxenhofer, R. Jordan, *Macromolecules* **2006**, *39*, 3509–3516.
[74] R. Luxenhofer, A. Schulz, C. Roques, S. Li, T. K. Bronich, E. V. Batrakova, R. Jordan, A. V. Kabanov, *Biomaterials* **2010**, *31*, 4972–4979.
[75] Y. Han, Z. He, A. Schulz, T. K. Bronich, R. Jordan, R. Luxenhofer, A. V. Kabanov, *Mol. Pharm.* **2012**, *9*, 2302–2313.
[76] R. Luxenhofer, S. Huber, J. Hytry, J. Tong, A. V. Kabanov, R. Jordan, *J. Polym. Sci. A Polym. Chem.* **2013**, *51*, 732–738.
[77] M. M. Lübtow, L. Hahn, M. S. Haider, R. Luxenhofer, *J. Am. Chem. Soc.* **2017**, *139*, 10980–10983.
[78] H. Reihlen, A. v. Friedolsheim, W. Oswald, *Justus Liebigs Ann. Chem.* **1928**, *465*, 72–96.
[79] H. Reihlen, A. Gruhl, G. v. Hessling, *Justus Liebigs Ann. Chem.* **1929**, *472*, 268–287.
[80] W. Hieber, P. Spacu, *Z. Anorg. Allg. Chem.* **1937**, *233*, 353–364.
[81] W. Hieber, C. Scharfenberg, *Ber. Dtsch. Chem. Ges. B* **1940**, *73B*, 1012–1021.
[82] S. F. A. Kettle, L. E. Orgel, *J. Chem. Soc.* **1960**, 3890–3891.
[83] R. B. King, *J. Am. Chem. Soc.* **1962**, *84*, 2460.
[84] R. B. King, M. B. Bisnette, *Inorg. Chem.* **1965**, *4*, 1663–1665.
[85] N. S. Nametkin, V. D. Tyurin, M. A. Kukina, *J. Organomet. Chem.* **1978**, *149*, 355–370.
[86] A. Winter, L. Zsolnai, G. Huttner, *Z. Naturforsch.* **1982**, *37*, 1430–1436.
[87] L. Schwartz, P. S. Singh, L. Eriksson, R. Lomoth, S. Ott, *C. R. Chimie* **2008**, *11*, 875–889.
[88] D. Seyferth, G. B. Womack, M. K. Gallagher, M. Cowie, B. W. Hames, J. P. Fackler Jr., A. M. Mazany, *Organometallics* **1987**, *6*, 283–294.
[89] E. S. Donovan, J. J. McCormick, G. S. Nichol, G. A. N. Felton, *Organometallics* **2012**, *31*, 8067–8070.
[90] Ö. Erdem, M. Stein, S. Kaur-Ghumaan, E. J. Reijerse, S. Ott, W. Lubitz, *Chem. - Eur. J.* **2013**, *19*, 14566–14572.
[91] G. Eilers, L. Schwartz, M. Stein, G. Zampella, L. de Gioia, S. Ott, R. Lomoth, *Chem. - Eur. J.* **2007**, *13*, 7075–7084.
[92] F. Huo, J. Hou, G. Chen, D. Guo, X. Peng, *Eur. J. Inorg. Chem.* **2010**, 3942–3951.
[93] Y.-C. Liu, T.-H. Yen, Y.-J. Tseng, C.-H. Hu, G.-H. Lee, M.-H. Chiang, *Inorg. Chem.* **2012**, *51*, 5997–5999.
[94] A. T. Fiedler, T. C. Brunold, *Inorg. Chem.* **2005**, *44*, 1794–1809.
[95] D. Chong, I. P. Georgakaki, R. Mejia-Rodriguez, J. Sanabria-Chinchilla, M. P. Soriaga, M. Y. Darensbourg, *Dalton Trans.* **2003**, 4158–4163.
[96] R. Mejia-Rodriguez, D. Chong, J. H. Reibenspies, M. P. Soriaga, M. Y. Darensbourg, *J. Am. Chem. Soc.* **2004**, *126*, 12004–12014.
[97] T. R. Simmons, G. Berggren, M. Bacchi, M. Fontecave, V. Artero, *Coord. Chem. Rev.* **2014**, *270–271*, 127–150.
[98] G. A. N. Felton, A. K. Vannucci, J. Chen, L. T. Lockett, N. Okumura, B. J. Petro, U. I. Zakai, D. H. Evans, R. S. Glass, D. L. Lichtenberger, *J. Am. Chem. Soc.* **2007**, *129*, 12521–12530.
[99] S. Gao, Y. Liu, Y. Shao, D. Jiang, Q. Duan, *Coord. Chem. Rev.* **2020**, *402*, 213081.
[100] M. Mirmohades, S. Pullen, M. Stein, S. Maji, S. Ott, L. Hammarström, R. Lomoth, *J. Am. Chem. Soc.* **2014**, *136*, 17366–17369.
[101] Z.-C. Fu, C. Mi, Y. Sun, Z. Yang, Q.-Q. Xu, W.-F. Fu, *Molecules* **2019**, *24*, 1878.

[102] P. Li, M. Wang, C. He, G. Li, X. Liu, C. Chen, B. Åkermark, L. Sun, *Eur. J. Inorg. Chem.* **2005**, 2506–2513.
[103] P. Li, M. Wang, C. He, X. Liu, K. Jin, L. Sun, *Eur. J. Inorg. Chem.* **2007**, 3718–3727.
[104] D. Morvan, J.-F. Capon, F. Gloaguen, P. Schollhammer, J. Talarmin, *Eur. J. Inorg. Chem.* **2007**, 5062–5068.
[105] J. D. Vasta, R. T. Raines, *Bioorg. Med. Chem.* **2015**, *23*, 3081–3090.
[106] A. Baron, C. Herrero, A. Quaranta, M.-F. Charlot, W. Leibl, B. Vauzeilles, A. Aukauloo, *Inorg. Chem.* **2012**, *51*, 5985–5987.
[107] D. E. Levy, M. S. Smyth, R. M. Scarborough, Millennium Pharmaceuticals, Inc., USA, **2003**, p. 260 pp.
[108] Z. Chai, S. Wan, C. Zhong, T. Xu, M. Fang, J. Wang, Y. Xie, Y. Zhang, A. Mei, H. Han, Q. Peng, Q. Li, Z. Li, *ACS Appl. Mater. Inter.* **2016**, *8*, 28652–28662.
[109] L. Gooßen, A. Döhring, *Adv. Synth. Catal.* **2003**, *345*, 943–947.
[110] N. E. Tokel-Takvoryan, R. E. Hemingway, A. J. Bard, *J. Am. Chem. Soc.* **1973**, *95*, 6582–6589.
[111] N. E. Tokel, A. J. Bard, *J. Am. Chem. Soc.* **1972**, *94*, 2862–2863.
[112] A. J. Bard, L. R. Faulkner, *Electrochemical Methods: Fundamentals and Applications, 2nd Edition*, John Wiley & Sons, New York, **2000**.
[113] V. Balzani, P. Ceroni, A. Juris, *Photochemistry and Photophysics: Concepts, Research, Applications*, Wiley-VCH, Weinheim, **2014**.
[114] A. Mills, *Analyst* **1999**, *124*, 1301–1307.
[115] B. Zelent, J. Kuśba, I. Gryczynski, M. L. Johnson, J. R. Lakowicz, *J. Phys. Chem.* **1996**, *100*, 18592–18602.
[116] A. Sillen, Y. Engelborghs, *Photochem. Photobiol.* **1998**, *67*, 475–486.
[117] M. Montalti, A. Credi, L. Prodi, M. T. Gandolfi, *Handbook of Photochemistry*, CRC Press, Boca Raton, **2006**.
[118] S. Wallin, J. Davidsson, J. Modin, L. Hammarström, *J. Phys. Chem. A* **2005**, *109*, 4697–4704.
[119] Y. Na, J. Pan, M. Wang, L. Sun, *Inorg. Chem.* **2007**, *46*, 3813–3815.
[120] D. L. Ma, L. J. Liu, K. H. Leung, Y. T. Chen, H. J. Zhong, D. S. Chan, H. M. Wang, C. H. Leung, *Angew. Chem. Int. Ed.* **2014**, *53*, 9178–9182.
[121] C. D. Sunesh, G. Mathai, Y.-R. Cho, Y. Choe, *Polyhedron* **2013**, *57*, 77–82.
[122] S. I. Bokarev, O. S. Bokareva, O. Kühn, *J. Chem. Phys.* **2012**, *136*, 214305/214301–214305/214310.
[123] C. Tard, C. J. Pickett, *Chem. Rev.* **2009**, *109*, 2245–2274.
[124] T. Stoll, M. Gennari, I. Serrano, J. Fortage, J. Chauvin, F. Odobel, M. Rebarz, O. Poizat, M. Sliwa, A. Deronzier, M.-N. Collomb, *Chem. - Eur. J.* **2013**, *19*, 782–792.
[125] Y. L. Chow, W. C. Danen, S. F. Nelsen, D. H. Rosenblatt, *Chem. Rev.* **1978**, *78*, 243–274.
[126] S. Tschierlei, A. Neubauer, N. Rockstroh, M. Karnahl, P. Schwarzbach, H. Junge, M. Beller, S. Lochbrunner, *Phys. Chem. Chem. Phys.* **2016**, *18*, 10682–10687.
[127] C. Lentz, O. Schott, T. Auvray, G. Hanan, B. Elias, *Inorg. Chem.* **2017**, *56*, 10875–10881.
[128] X. Li, M. Wang, S. Zhang, J. Pan, Y. Na, J. Liu, B. Åkermark, L. Sun, *J. Phys. Chem. B* **2008**, *112*, 8198–8202.
[129] S. Dümmling, E. Eichhorn, S. Schneider, B. Speiser, M. Würde, *Curr. Sep.* **1996**, *15*, 53–56.
[130] G. R. Fulmer, A. J. M. Miller, N. H. Sherden, H. E. Gottlieb, A. Nudelman, B. M. Stoltz, J. E. Bercaw, K. I. Goldberg, *Organometallics* **2010**, *29*, 2176–2179.
[131] D. F. Shriver, M. A. Drezdzon, *The Manipulation of Air-Sensitive Compounds*, John Wiley & Sons, New York, **1968**.
[132] S. Hünig, P. Kreitmeier, G. Märkl, J. Sauer, *Arbeitsmethoden in der Organischen Chemie*, Verlag Lehmanns, Berlin, **2006**.
[133] W. C. Still, M. Kahn, A. Mitra, *J. Org. Chem.* **1978**, *43*, 2923–2925.
[134] J. A. Cabeza, M. A. Martínez-García, V. Riera, D. Ardura, S. García-Granda, *Organometallics* **1998**, *17*, 1471–1477.

[135] T.-T. Zhang, M. Wang, N. Wang, P. Li, Z.-Y. Liu, L.-C. Sun, *Polyhedron* **2009**, *28*, 1138–1144.
[136] H. Pfaendler, R. Hartung, G. Golz, S. Schlaf, G. Silvennoinen, K. Polborn, P. Mayer, *Synthesis* **2009**, *2009*, 495–501.
[137] K. G. Moloy, J. L. Petersen, *J. Am. Chem. Soc.* **1995**, *117*, 7696–7710.
[138] S. Hinsberger, J. C. de Jong, M. Groh, J. Haupenthal, R. W. Hartmann, *Eur. J. Med. Chem.* **2014**, *76*, 343–351.
[139] H. Kakuta, N. Yakushiji, R. Shinozaki, F. Ohsawa, S. Yamada, Y. Ohta, K. Kawata, M. Nakayama, M. Hagaya, C. Fujiwara, M. Makishima, S. Uno, A. Tai, A. Maehara, M. Nakayama, T. Oohashi, H. Yasui, Y. Yoshikawa, *ACS Med. Chem. Lett.* **2012**, *3*, 427–432.
[140] J. Park, D. Feng, H.-C. Zhou, *J. Am. Chem. Soc.* **2015**, *137*, 1663–1672.
[141] J. D. Vasta, R. T. Raines, *Biochemistry* **2016**, *55*, 3224–3233.
[142] K. Huang, A. A. Marti, *Anal. Chem.* **2012**, *84*, 8075–8082.

9 TABLE OF FORMULAS

9.1 [FeFe]-Hydrogenase Biomimics and Precursors

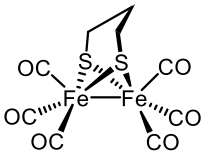

[FeFe]-Cat 1

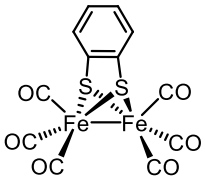

[FeFe]-Cat 2

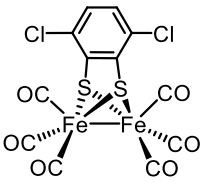

[FeFe]-Cat 3

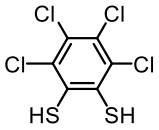

3,4,5,6-Tetrachloro-benzene-1,2-dithiol

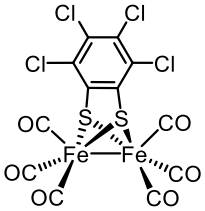

[FeFe]-Cat 4

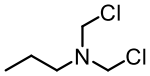

***N*,*N*-Bis(chloromethyl)-propan-1-amine**

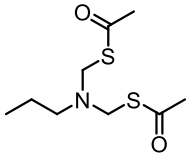

***S*,*S*'-(Propylamino)-bismethyl dithioacetate**

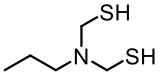

***N*,*N*-Bis(mercaptomethyl)-propylamine**

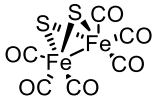

[$Fe_2(\mu\text{-}S_2)(CO)_6$]

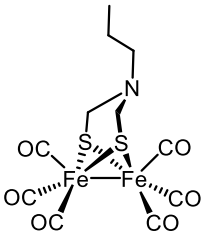

[FeFe]-Cat 11

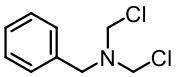

***N*,*N*-Bis(chloromethyl)-benzenemethanamine**

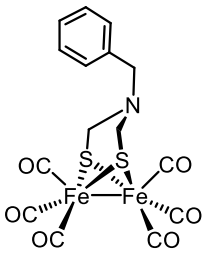

[FeFe]-Cat 13

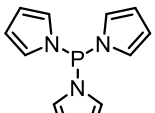

Tris(1*H*-pyrrol-1-yl)-phosphine

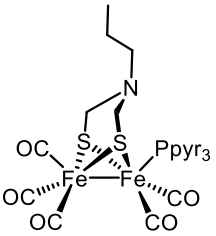

[FeFe]-Cat 12

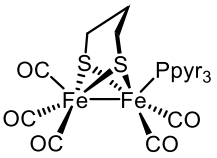

[FeFe]-Cat 5

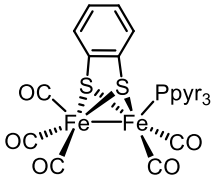

[FeFe]-Cat 6

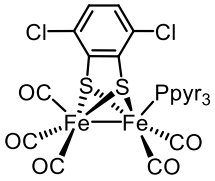

[FeFe]-Cat 7

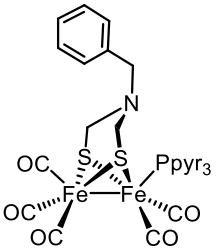

[FeFe]-Cat 14

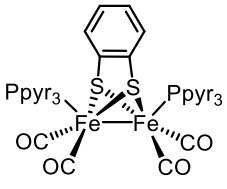

[FeFe]-Cat 8

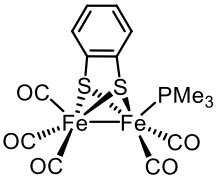

[FeFe]-Cat 9

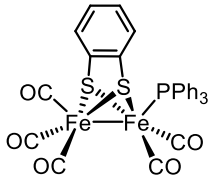

[FeFe]-Cat 10

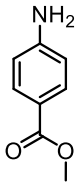

Methyl 4-aminobenzoate

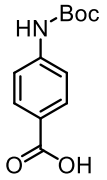

Spacer 1

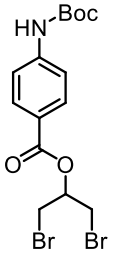

1,3-Dibromopropan-2-yl 4-((*tert*-butoxycarbonyl)amino)-benzoate

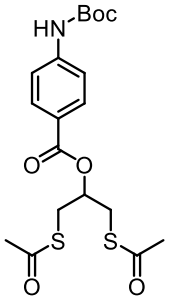

1,3-Bis(acetylthio)propan-2-yl 4-((*tert*-butoxycarbonyl)amino)-benzoate

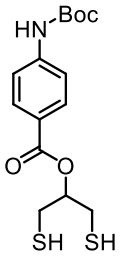

1,3-Dimercaptopropan-2-yl 4-((*tert*-butoxycarbonyl)-amino)benzoate

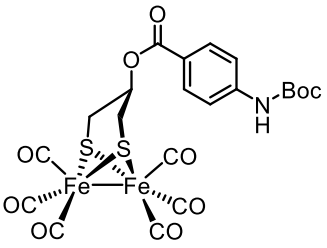

[FeFe]-Spacer-Cat 1

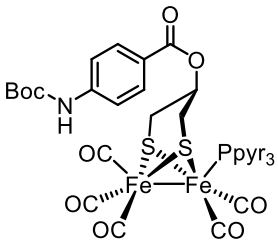

[FeFe]-Spacer-Cat 2

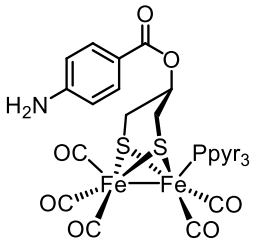

[FeFe]-Spacer-Cat 3

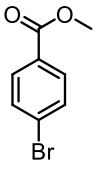

Methyl 4-bromobenzoate

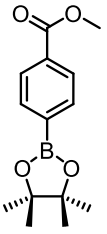

Methyl 4-(4,4,5,5-tetramethyl-1,3,2-dioxaborolan-2-yl)-benzoate

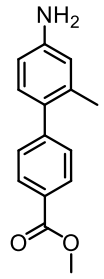

Methyl 4'-amino-2'-methyl-[1,1'-biphenyl]-4-carboxylate

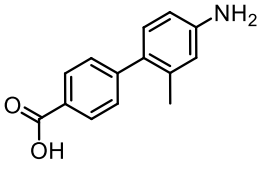

4'-Amino-2'-methyl-[1,1'-biphenyl]-4-carboxylic acid

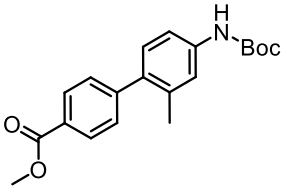

Methyl 4'-((*tert*-butoxycarbonyl)-amino)-2'-methyl-[1,1'-biphenyl]-4-carboxylate

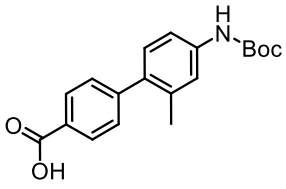

4'-((*tert*-Butoxycarbonyl)amino)-2'-methyl-[1,1'-biphenyl]-4-carboxylic acid

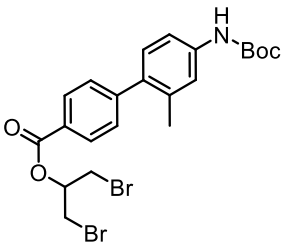

Spacer 2

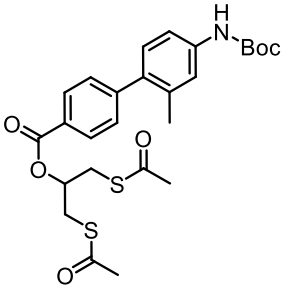

Spacer 3

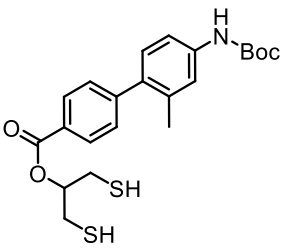

Spacer 4

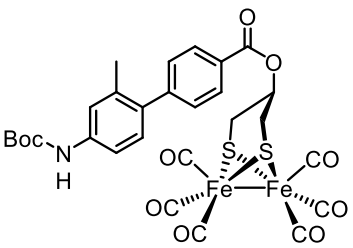

[FeFe]-Spacer-Cat 4

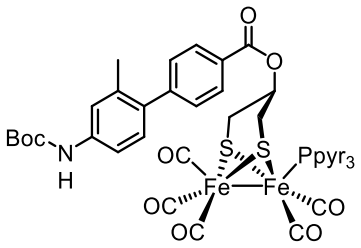

[FeFe]-Spacer-Cat 5

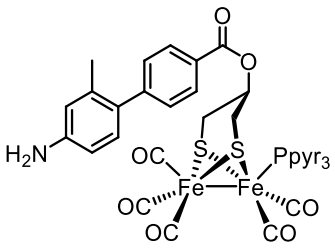

[FeFe]-Spacer-Cat 6

9.2 Photosensitisers and Precursors

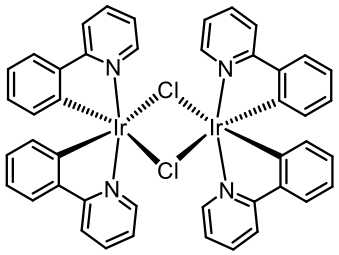

$[Ir(ppy)_2Cl]_2$

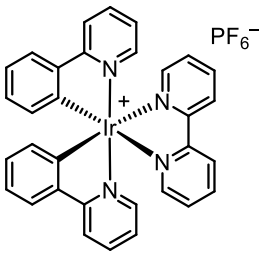

$[Ir(ppy)_2bpy]PF_6$

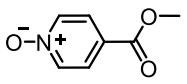

4-(Methoxycarbonyl)-pyridine 1-oxide

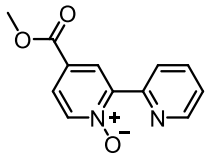

4-(Methoxycarbonyl)-(2,2'-bipyridine) 1-oxide

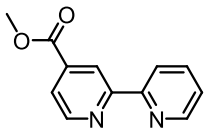

Methyl (2,2'-bipyridine)-4-carboxylate

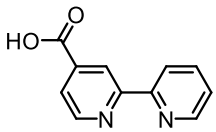

(2,2'-Bipyridine)-4-carboxylic acid

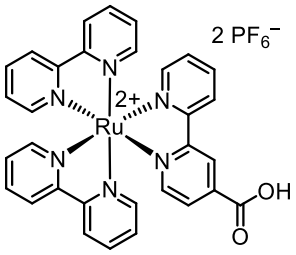

$[Ru(bpy)_2bpy\text{-}COOH](PF_6)_2$

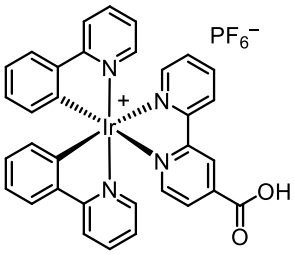

$[Ir(ppy)_2bpy\text{-}COOH]PF_6$

9.3 Photocatalytic Dyads

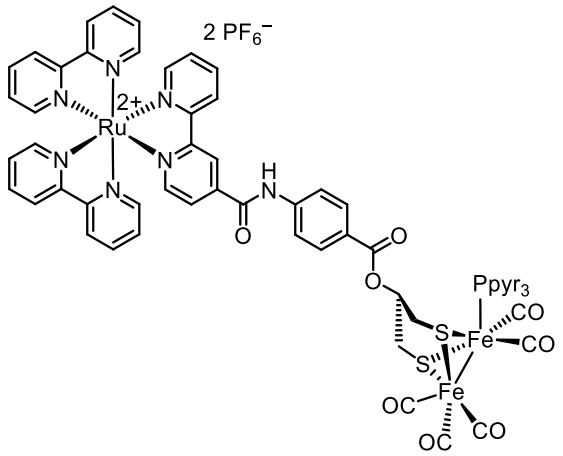

D1

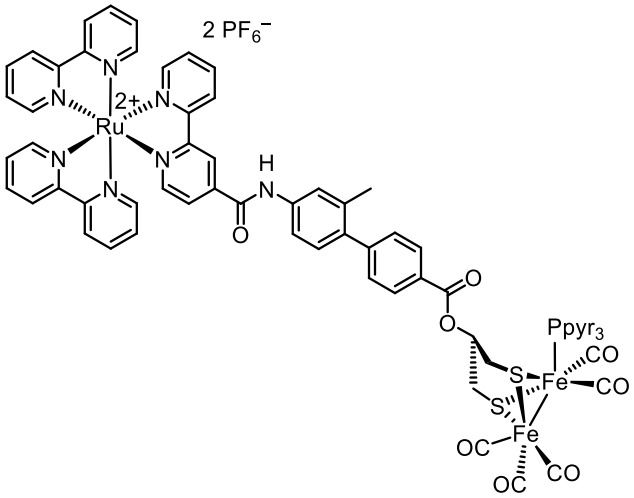

D2

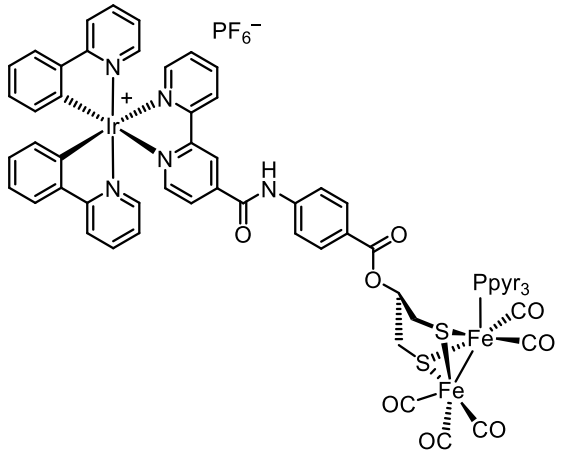

D3

10 ZUSAMMENFASSUNG

Im Rahmen dieser Arbeit wurden zunächst verschiedene biomimetische [FeFe]-Hydrogenase-Verbindungen auf ihre Funktionalität als Katalysatoren in photokatalytischen Mehrkomponentensystemen für die Wasserstoffentwicklung unter Lichtbestrahlung in einem wässrigen Medium getestet. Da in der Literatur bereits einige Beispiele für die erfolgreiche Integration solcher Dieisen-Komplexe in wässrigen Systemen mit $[Ru(bpy)_3]^{2+}$-Photosensibilisatoren in Kombination mit Ascorbinsäure als Opferelektronendonor bekannt sind, wurden diese beiden Komponenten auch in die entsprechenden Systeme zur Untersuchungen der photokatalytischen Leistungsfähigkeit integriert.[5,8,9,18,35,52,68,69,99] Aufgrund der Wasserunlöslichkeit der Dieisen-Katalysatorkomplexe wurden sie in dieser Arbeit unter Verwendung des in **Fig. 14** gezeigten und freundlicherweise von der Arbeitsgruppe Luxenhofer im Rahmen einer Kooperation zur Verfügung gestellten Poly(2-oxazolin)-Polymers in Wasser solubilisiert. Das so gebildete wässrige Mizellensystem stellt den signifikanten Unterschied zu den bisher bekannten photokatalytischen Mehrkomponentensystemen in wässrig-organischen Lösungen dar. Ein wichtiger Aspekt dieser Studie war daher nicht nur die Charakterisierung und der Vergleich der verschiedenen [FeFe]-Komplexe auf der Grundlage ihrer photokatalytischen Leistung und ihrer spektralen und elektrochemischen Eigenschaften, sondern nach Möglichkeit auch die Untersuchung bestehender Struktur-Eigenschafts-Beziehungen in dieser neuen wässrigen Umgebung, um die dabei gewonnenen Erkenntnisse in die nachfolgende Entwicklung der photokatalytischen Dyadensysteme einzubeziehen.

In der Studie über die Dieisen-Verbindungen wurden insgesamt vierzehn verschiedene [FeFe]-Komplexe mit jeweils unterschiedlichen Dithiolat-Cofaktoren und Phosphansubstituenten synthetisiert (siehe **Fig. 15**). Dabei zeigten alle im wässrigen Mizellenmedium in Kombination mit dem **$[Ru(bpy)_3]Cl_2$** Photosensibilisator und Ascorbinsäure photokatalytische Aktivität und generierten Wasserstoff unter Lichteinstrahlung. Darüber hinaus konnten in dieser Studie auch einige in der Literatur diskutierte Struktur-Eigenschafts-Beziehungen nachgewiesen werden. So zeigten die spektroskopischen und elektrochemischen Untersuchungen, dass die Dithiolat-Cofaktoren zwar einen Einfluss auf die elektronischen Eigenschaften der Komplexe haben, diese jedoch hauptsächlich durch die direkt an den Dieisen-Kern gebundenen Phosphansubstituenten beeinflusst werden. Dies gilt auch für die photokatalytische Leistungsfähigkeit der getesteten Systeme. Obwohl während der Untersuchungen nur die katalytische Produktivität vermessen wurde, konnte dabei festgestellt werden, dass die verschiedenen Strukturmerkmale der [FeFe]-Katalysatoren offenbar nicht nur die Aktivität der Systeme, sondern auch deren Produktivität, die normalerweise mit der Stabilität der beteiligten

Komponenten verbunden ist, beeinflussen. Dies ist wahrscheinlich darauf zurückzuführen, dass bei ansonsten identischen Messbedingungen und vermutlich vergleichbaren Photostabilitäten der verwendeten Komponenten eine höhere Aktivität des Systems gleichzeitig auch zu einer höheren katalytischen Produktivität im betrachteten Zeitraum führt. Beispielsweise haben elektronenziehende Dithiolat-Cofaktoren, die die Elektronendichte im Dieisen-Kern und damit die Protophilie senken, einen negativen Einfluss auf den erreichten TON-Wert. Im Gegensatz dazu zeigten die Azadithiolat-Cofaktoren kaum einen nennenswerten Einfluss sowohl auf die elektronischen Eigenschaften als auch auf die photokatalytische Leistungsfähigkeit. Wie bereits oben erwähnt, zeigten die Phosphansubstituenten den größten Einfluss sowohl auf die thermodynamischen als auch auf die photokatalytischen Eigenschaften der Katalysatoren. Der $Ppyr_3$-Substituent wies dabei in der Studie zur Photokatalyse die besten Eigenschaften auf. Zum einen wirkt sich die elektronenschiebende Wirkung des Phosphanliganden positiv auf die Protophilie des Komplexes aus, zum anderen verhindern die internen Pyrrolsubstituenten eine zu starke kathodische Verschiebung des Reduktionspotentials, was zu einer Diskrepanz mit den Redoxpotentialen des Photosensibilisators führen würde.[9] Folglich zeigten die $Ppyr_3$-substituierten [FeFe]-Komplexe auch die höchste katalytische Produktivität in der Studie. Darüber hinaus wurden auch noch weitere Parameter der photokatalytischen Systeme wie deren stöchiometrische Zusammensetzung und der pH-Wert der Lösungen optimiert. Im nächsten Schritt wurden diese Erkenntnisse zusammen mit den erhaltenen Struktur-Eigenschafts-Beziehungen in die Entwicklung photokatalytisch wirksamer Dyadensysteme übertragen.

In der Studie über photokatalytische Dyaden, bei denen der Photosensibilisator kovalent an den Katalysator gebunden ist, sollte grundsätzlich untersucht werden, ob mit ihnen gebildete Zweikomponentensysteme (2CS) einen Leistungsvorteil gegenüber den im vorherigen Kapitel untersuchten herkömmlichen Dreikomponentensystemen (3CS) aufweisen. Neben den thermodynamischen und kinetischen Eigenschaften der Dyaden und der zugehörigen Einzelkomponenten wurde auch der Quenching-Mechanismus, unter dem die entsprechenden Systeme während der Photokatalyse arbeiten, untersucht. Wie Sun *et al.* beobachtet haben, scheint der Quenching-Mechanismus einen wichtigen Faktor für die Leistung eines Dyadensystems im Vergleich zum entsprechenden bimolekularen System zu haben.[9] Im Rahmen dieser Arbeit wurde daher zusätzlich untersucht, ob dies auch für die in dieser Arbeit hergestellten Dyadensysteme gilt. Dabei basierten die zu untersuchenden Dyaden auf dem leistungsstärksten System der oben genannten Studie zu den [FeFe]-Katalysatoren, um auf diese Weise das dort gesammelte Wissen auch in das Dyadendesign einzubeziehen. In dieser Arbeit konnten insgesamt drei Dyaden zusammen mit den zugehörigen Einzelkomponenten hergestellt werden. Zwei von ihnen, **D1** und **D2**, umfassten einen $[Ru(bpy)_3]^{2+}$-

Photosensibilisator und **D3** einen $[Ir(ppy)_2bpy]^+$-Photosensibilisator. Alle beinhalteten einen $Ppyr_3$-substituierten Propyldithiolat-[FeFe]-Komplex als Katalysator, der im Fall von **D1** und **D3** über einen Phenyl-Abstandshalter und im Fall von **D2** über einen Biphenyl-Abstandshalter zum Photosensibilisator verbrückt war. Basierend auf der Synthese von Sun und Åkermark waren alle Brückeneinheiten über eine Amidbindung mit dem Photosensibilisator und über eine Esterbindung mit dem Katalysator verbunden.[56] Als π-Konjugationsblocker sollten diese die elektronische Kopplung zwischen den beiden Dyadenkomponenten verringern und damit einen schnellen Rücktransport von Elektronen nach erfolgtem Ladungstransport vom Photosensibilisator auf den Katalysator erschweren, da die Langlebigkeit des reduzierten Zustandes des Katalysators im Allgemeinen die photokatalytische Aktivität begünstigen sollte. Wie die absorptionsspektroskopischen und elektrochemischen Untersuchungen zeigten, funktioniert diese inner-dyadische elektronische Entkopplung besonders gut für **D3**. Die Ruthenium enthaltenden Dyaden zeigten dagegen eine leichte Wechselwirkung zwischen den Komponenten. Die photokatalytischen Untersuchungen zeigten jedoch, dass alle Dyaden im entsprechenden 2CS eine signifikant schlechtere Leistung aufweisen als das entsprechende bimolekulare 3CS. Durch transiente Absorptionsspektroskopie konnte gezeigt werden, dass sich die Iridium-haltige Dyade **D3** während der Photokatalyse dem zugehörigen Mehrkomponentensystem sehr ähnlich verhält. Das Elektron, das für den intramolekularen Transfer vom Photosensibilisator zum Katalysator vorgesehen war, verbleibt, analog zum 3CS, trotz des kovalent gebundenen Katalysators relativ lange beim Photosensibilisator. Dieses Verhalten wurde auch in der Ruthenium-haltigen Dyade **D1** beobachtet. Es wird daher angenommen, dass der vermutete intramolekulare Elektronentransfer von der Photosensibilisatoreinheit zur Katalysatoreinheit in den Dyaden während der Photokatalyse wahrscheinlich durch die verwendeten Brückeneinheiten behindert wird und stattdessen das System diesen durch einen intermolekularen Transfer auf andere Dyadenmoleküle in der direkten Umgebung umgeht. Die Verlängerung der verwendeten Brückeneinheit, die den einzigen strukturellen Unterschied zwischen **D1** und **D2** darstellte, zeigte, abgesehen von einer erwarteten leichten Verringerung der elektronischen Kopplung zwischen den Dyadenkomponenten, keine entscheidenden Auswirkungen sowohl auf die photokatalytische Leistung als auch auf die thermodynamischen und kinetischen Eigenschaften. Offensichtlich hat diese relativ kleine strukturelle Änderung im Vergleich zu dem Einfluss der verwendeten π-Konjugationsblockern einen zu geringen Einfluss. Darüber hinaus konnte klar das reduktive Quenchen (RQ) für alle untersuchten Systeme durch elektrochemische Untersuchungen, welche auch die für die photokatalytische Elektronenkaskade wichtigen Redoxpotentiale der angeregten Photosensibilisatoren berücksichtigten, und Emissionslöschexperimente nachgewiesen werden. In Kombination mit den Ergebnissen der Photokatalyse konnten die oben genannten Beobachtungen von Sun *et al.* zu Leistungsverlusten von Dyaden, welche

über den RQ-Mechanismus ablaufen, auch für die in dieser Arbeit untersuchten photokatalytischen Dyaden bestätigt werden.[9]

Mit den in dieser Arbeit gewonnenen Erkenntnissen wäre die weitere Erforschung neuer photokatalytischer Dyaden, die auf einer anderen Verbindung zwischen den einzelnen Komponenten beruhen würden, für die Zukunft sicher sehr interessant. Neben direkten Bindungen durch beispielsweise CC-Kreuzkupplungsreaktionen, die die π-Konjugation aufrechterhalten würden, wären auch völlig andere Ansätze möglich. Beispielsweise wäre ein supramolekularer Ansatz eines photokatalytischen Systems denkbar, der eine Zwischenform zwischen dem klassischen 2CS und 3CS darstellen würde. So könnte eine Kombination zwischen einem chelatisierenden metallorganischen Photosensibilisator und einem Katalysator mit entsprechenden Bindungsstellen eine solche Möglichkeit darstellen. Bereits 2008 konnten Sun und Åkermark zeigen, dass ein solches System, welches aus einem Isonicotinsäure-substituierten Azadithiolat-[FeFe]-Komplex bestand, der supramolekular an ein Zinkporphyrin gebunden war, Wasserstoff erzeugen kann.[128] Dies eröffnet eine völlig neue Klasse von photokatalytisch wirksamen Systemen mit einem enormem Leistungspotential. Die beeindruckenden Ergebnisse des Iridium-haltigen 3CS, bestehend aus dem **$[Ir(ppy)_2bpy]PF_6$** Photosensibilisator, dem **[FeFe]-Spacer-Cat 2** Katalysator und TEA als Opferelektronendonor, zeigen, dass die in dieser Arbeit verwendeten Komponenten grundsätzlich geeignet für weitere Untersuchungen in diesem Bereich sind. Mit diesem System konnte unter optimierten Bedingungen ein bemerkenswert hoher TON-Wert von 981 und ein maximaler TOF-Wert von 0.074 s^{-1} erreicht werden.

11 APPENDIX

Contributed Publication

Ultra-High to Ultra-Low Drug-Loaded Micelles: Probing Host-Guest Interactions by Fluorescence Spectroscopy

Michael M. Lübtow, Henning Marciniak, Alexander Schmiedel, Markus Roos, Christoph Lambert, and Robert Luxenhofer

Chem. Eur. J. **2019**, *25*, 12601–12610.

List of Conference Contributions

a. Oral presentations:

    1. 1st Solar Technologies Go Hybrid Symposium, October **2018**, Würzburg.
    2. 2nd Solar Technologies Go Hybrid Symposium, September **2019**, Erlangen.

b. Poster presentations:

    1. Chemie Symposium Studierender Mainfrankens, December **2016**, Würzburg.
    2. 6th Solar Technologies Go Hybrid Conference, October **2017**, Munich.
    3. 8th Solar Technologies Go Hybrid Conference, October **2019**, Nuremberg.

Pictorial Appendix

The following spectroelectrochemistry measurement was carried out to identify the spectral features that occurred during the TA investigations of the ruthenium containing photocatalytic systems in chapter 5.1.6.

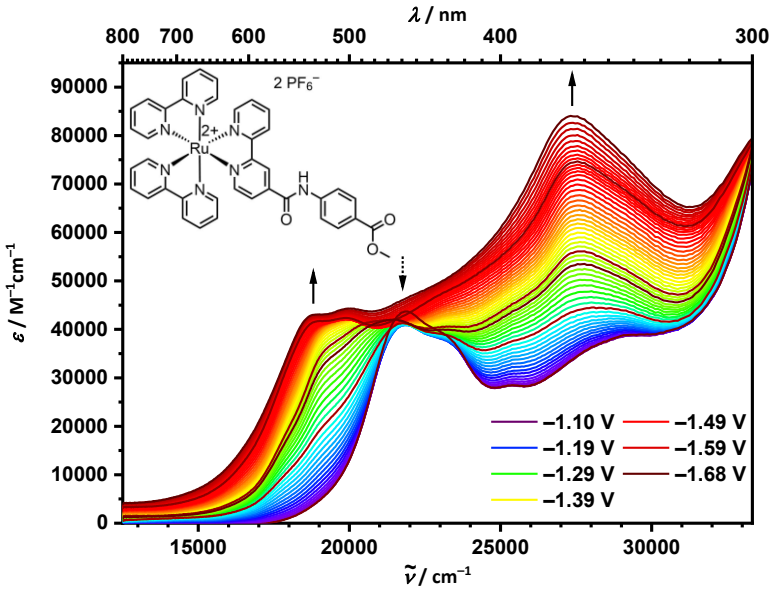

Fig. 76 Spectroelectrochemistry measurement of a methyl benzoate substituted tris(bipyridine)-ruthenium(II) photosensitiser ($5.52 \cdot 10^{-4}$ M, molecular structure displayed in diagram) in an acetonitrile solution (0.1 M TBAHFP) at 298 K. Experimental setup: Pt as WE, Pt as CE, Ag/AgCl as Reference. All given voltages are referenced against Ag/AgCl.